Electrochemical Studies and Modifications of CVD Diamond Electrodes

By

Liang Chen

Physical & Theoretical Chemistry, Department of Chemistry
&
Balliol College
Oxford

This thesis submitted to the University of Oxford for
the degree of Doctor of Philosophy
Trinity Term, 2013

Dedicated to my parents and my wife,

for offering warmest love in my life.

Electrochemical Studies and Modifications of CVD Diamond Electrodes

Liang Chen, Balliol College, Oxford, Doctor of Philosophy, Trinity Term 2013

Abstract

CVD diamond possesses certain attractive electrochemical properties *inter alia* low background current, broad potential window, chemical inertness and resistance to electrocorrosion and fouling. As a consequence its use in various areas of electrochemistry, such as electrochemical sensing, wastewater treatment and electrocatalysis is being explored. Unfortunately, alongside these attractive features, bare CVD diamond electrodes, in common with all other electrode materials, cannot be effectively applied in all electrochemical systems of interest, since for example it may not display useful electrochemical activity for the redox process of interest. In these circumstances it may be possible to modify the electrode by addition of other chemical species to the surface, to introduce the relevant activity. One of the main aims of this thesis was therefore to investigate the properties of certain chemical modifications to the diamond electrode surface. A second aim was also to explore for the first time the use of a practically useful form of single crystal diamond, so-called heteroepitaxial diamond, in electrochemistry.

The diamond electrodes used were boron-doped material grown by chemical vapour deposition. A range of electrochemical methods, including especially cyclic voltammetry, square-wave voltammetry, impedance spectroscopy and scanning electrochemical microscopy, were used to characterise electrode properties. Other physical methods employed included scanning electron and atomic force microscopy, X-ray photoelectron spectroscopy and dynamic light scattering techniques.

The electrochemical properties of heteroepitaxial single crystal diamond were explored and compared to polycrystalline counterparts. The single crystal diamond electrode was found to show superior properties in terms of wide potential window, low background current and homogeneous activity across the electrode surface, coupled with resistance to fouling. Heterogenous electron transfer rate constants were found to be lower than normally found on polycrystalline diamond; this was attributed to reduced density of states and absence of functional groups. An electrochemical route to the preparation of diamond electrodes, modified by PrO_x@Pt core-shell particles was demonstrated. It was observed that these electrode modifiers were far less susceptible to poisoning than bare Pt nanoparticles when used in the electrochemical oxidation of methanol. It was also shown that diamond electrodes with these core-shell particles deposited on them, displayed useful activity for the electrochemical oxidation of nitric oxide. The presence of the PrO_x layer was shown to impart useful selectivity against the oxidation of interfering compounds such as nitrite and ascorbic acid, without the loss of sensitivity which normally occurs if nafion coatings are used instead. Basic electrochemical characterisation of the PrO_x coating showed that the layer was chemically active and did not serve as a simple blocking layer when deposited on the electrode. The activity of Pt modified diamond electrodes for the oxidation of nitrite species was also studied. It was also shown that the addition of carbon black to a diamond electrode resulted in much enhanced electrochemical properties in the detection of riboflavin.

Acknowledgements

First and foremost, I would like to give my most sincere appreciation to my Supervisor Professor John S. Foord. It was a dream coming true when his effort finally took me on as a DPhil student at University of Oxford and a member in the group four years ago. I am very thankful for his leadership and guidance in the scientific research, his patience, understanding and enthusiasm throughout my studies here. I was motivated a lot by his support especially when I was stuck on the process of my second project due to the supplier failure. It was his consecutive encouragement that eventually supported me to overcome all the difficulties to be back on track. Everything would never have come to fruition without his rigorous scientific attitude, great personality and patient mentorship along with the delightful humour.

I am also indebted to the support from Dr. Jingping Hu, who is always enthusiastic and helpful in both science and life. The solid knowledge base and profound understanding from him always ignited abundant creative ideas and helped the researches proceeding methodically and rigorously. He is also one of my best senior friends in Oxford, the time we spent in playing table tennis, squash and cherries picking *etc.* will be another piece of joyful memories in my life. All other current and past Doctor and DPhil members in Foord group, Emina, Dong Myung, Geoff, Lulu, Sirikarn, Patrick, Inga, Adam, Celine, Chenbo, Montree helped me a lot throughout the past four years with their selfless supports and earnest advice. The harmony atmosphere in the groups calmed me, especially in my thesis writing-up and proof reading. I also want to thank all the past Part II students (Rowena, Vicky, Michael, Carl, Seb, Edward, Yu and Rhys) and visiting scholars and students (Professor Baixiang Liu, Dr. Xiao Lu, Dr. Jia Gong). The joining of them into the groups always brought fresh minds and funs, and their supports are very much appreciated. I am particularly thankful to Rowena, who contributed a lot in the investigations of PrO_x properties and carbon black applications with her earnest attitude and dedication. I would also like to give my gratitude to André Sartori and Dr. Matthias Schreck for their collaboration in the electrochemical characterisation of the highly boron doped single crystalline diamond. The diamond wafers synthesised by Schreck group gives exceptionally optimistic features, and the co-operative work turned out as one of most significant works in the thesis.

I want to thank Ms. Glynis Belham, the Academic Administrator of Balliol College, for her very kindly and efficient help on any requirement and issue to support my studies. I am also very appreciated to Dr. Maggie Charles, who is the tutor in EAP at Oxford University Language Centre and my teacher in Academic Writing Course. Her profound views and theories, enthusiastic teaching style and polite and patient attitude consolidated my fundamental of the academic writing, strengthened my understanding of writing skills and undoubtedly brought positive effects in smoothing my writing-up process.

The financial support is extremely necessary in my education here and I am grateful to my college, Balliol College for offering me the Jason Hu Scholarship throughout my DPhil study as this three-year funding source prominently alleviated my financial burden. Alongside, both Junior Maintenance Grant and Graduate Bursaries offered by Balliol College also significantly helped me to make up the difference in my tuition fees and living expenses. Without those help from my college, my education in Oxford would have been impossible, let alone the stage I reach so far.

Finally I am extremely grateful to my parents and my fiancée for their consecutive love, encouragement and patience throughout all these four years. No matter what I experienced, ups and downs, they stood beside me as always to offer me the warmest and most solid supports. I would like to thank my parents for raising me up, donating everything they could to perfect my education financially and mentally. Anything I have achieved would have never been realistic without standing on their strong shoulders. Thanks for my fiancée for the constant love for already seven years, letting us lean on each other and undergoing any difficulty and barrel in life together. I am very delightful to witness us approaching Doctoral and Master degree respectively, and this long adventurous journey saw both of us growing in personality and in spirit, but most preciously, in love. The faith and trust built up was beyond measuring by any manner and brought me the most reliable confidence.

Publications

Electrodeposition of a Pt-PrO_{2-x} electrocatalyst on diamond electrodes for the oxidation of methanol
L. Chen, J. Hu and J. S. Foord, *physica status solidi (a)* **2012**, *209*, 1792-1796.

Electrochemical characterisation of highly boron doped heteroepitaxial (001) single crystalline diamond
J. Hu, **L. Chen**, A. F. Sartori, M. Schreck and J. S. Foord
Ready for submission to *Advanced Functional Materials*

Electrochemical modification of diamond electrodes for the detection of nitric oxide (NO)
L. Chen and J. S. Foord
In preparation

Interaction of riboflavin (VB2) with carbon black (CB) modified diamond electrodes
L. Chen, R. Brugge and J. S. Foord
In preparation

Contents

Abstract i
Acknowledgements iii
Publications v
Contents vi
List of Abbreviations xi
List of Figures xiii
List of Tables xxi

Chapter 1 Introduction 1

1.1 Diamond: A Brief History 1
1.2 Development of CVD technique 3
1.3 Electrochemistry of diamond 6
1.4 Electroanalysis using diamond electrodes 7
1.5 Modifications of diamond electrode 9
1.6 Rare earth oxide and praseodymium oxide (PrO_x) 10
1.7 Aims and scope of this thesis 11
References 14

Chapter 2 Experimental Theories and Techniques 18

2.1 Introduction 18
2.2 Electrochemical characterisation 18
2.2.1 Overview 18
2.2.2 Electrochemical cells 19
2.2.3 Faradaic and Non-Faradaic processes 22
2.2.4 The fundamental theories of electrochemistry 24
2.3 Electrochemical techniques 29
2.3.1 Overview 29
2.3.2 Potential Sweep Techniques 30
2.3.3 Potential step methods - chronoamperometry 32

2.3.4 Pulse voltammetry 33
2.3.5 Rotating disc electrode (RDE) 34
2.3.6 Electrochemical impedance spectroscopy 35
2.3.7 Scanning electrochemical microscopy 37
2.4 Surface Characterisation Techniques 37
2.4.1 X-ray photoelectron spectroscopy (XPS) 38
2.4.2 Scanning electron microscopy 46
2.4.3 Dynamic light scattering combined with *zeta* potential 47
References 50

Chapter 3 Study on the electrochemical behaviours of highly boron doped heteroepitaxial (001) single crystalline diamond 52
3.1 Introduction 52
3.2 Experimental 56
3.2.1 Preparation of diamond electrodes 56
3.2.2 Electrochemical characterisations 58
3.2.3 Chemicals 59
3.3 Results and Discussion 60
3.3.1 CV and EIS characterisations 60
3.3.2 *Mott-Schottky* plot and energy diagram 72
3.3.3 Electrochemical characterisations of Methyl viologen and AQDS 75
3.3.4 Scanning electrochemical microscopy (SECM) 79
3.4 Summarising comments 86
References 88

Chapter 4 Electrodeposition of Pt-PrO_x Core-shell Catalyst on Boron Doped Diamond for Methanol Electro-oxidation 92
4.1 Introduction 92
4.2 Experimental 95
4.2.1 Materials, instruments and techniques 95
4.2.2 Electrodeposition of Pt and PrO_x 97
4.3 Characterisation of Pt and PrO_x-Pt/ BDDEs 98
4.3.1 Electrochemical characterisation of Pt-BDDE structures 98

4.3.2 Electrochemical characterisation of PrO_x-Pt deposited BDDEs..... 100
4.3.3 Surface characterisation of Pt and PrO_x/Pt coated BDD 103
4.3.4 XPS characterisation of Pt and PrO_x-Pt deposited BDDEs 107
4.4 Electrochemical oxidation of methanol on PrO_x-Pt/ BDD 109
4.4.1 The principle of methanol electro-oxidation 109
4.4.2 Methanol electrooxidation on Pt and PrO_x-Pt modified BDDEs..... 111
4.4.3 Methanol electro-oxidation on commercial catalyst based system ... 117
4.5 Summarising comments 119
4.6 Speculation concerning the 'spill-over' mechanism..... 120
Reference 125

Chapter 5 Electrodeposition of a PrO_x-Pt electrocatalyst on BDD electrode for the electrochemical detection of nitric oxide..... 129
5.1 Introduction 129
5.2 Experimental section 132
5.2.1 Chemicals and materials 132
5.2.2 Preparation of nitric oxide solution 132
5.2.3 Preparation of PrO_x/Pt-BDD electrodes 133
5.3 Results and discussion..... 133
5.3.1 Characterisation of Pt/BDD and PrO_x-Pt/BDD 133
5.3.2 Electrochemical detection of NO on bare-BDD and Pt-BDD 136
5.3.3 Interfering compounds in NO detection 140
5.3.4 Detection limit 150
5.3.5 Mechanism of NO electrochemical oxidation on PrO_x-Pt/BDD 151
5.4 Summarising comments 153
References..... 155

Chapter 6 Investigations on the Properties of Electrodeposited Praseodymium Oxide (PrO_x) 158
6.1 Introduction 158
6.2 Experimental..... 161
6.2.1 Materials, instruments and techniques..... 161
6.2.2 Electrodeposition of PrO_x 161

6.3 Results and discussion 162
6.3.1 Electrochemical characterisations of bare BDD 162
6.3.2 Electrochemical characterisations of PrO_x/BDD 165
6.3.3 Post-treatment of the deposited PrO_x film 172
6.3.4 XPS characterisations of PrO_x modified electrodes with different treatments 174
6.3.5 Dynamic light scattering (DLS) and *zeta* potential characterisation of the PrO_x suspension 179
6.3.6 Electrochemical detection of dopamine 181
6.4 Summarising comments 185
References 187

Chapter 7 Electrochemical detection of riboflavin (VB2) on carbon black modified BDD electrode 189
7.1 Introduction 189
7.2 Experimental 191
7.2.1 Materials, instruments and techniques 191
7.2.2 Deposition of CB on BDD 191
7.3 CV characterisations of CB modified BDD 192
7.3.1 Redox reaction of riboflavin 192
7.3.2 Effects of CB coating 193
7.3.3 Electrochemical behaviour of VB2 affected by exposure time 199
7.3.4 pH dependence 200
7.4 Detection limit and interfering effects 202
7.4.1 Detection limit 202
7.4.2 The simultaneous determination of VB2 with other vitamins 203
7.5 Summarising comments 204
References 206

Chapter 8 Electrodeposition of Pt nanoparticles on Boron-doped Diamond (BDD) for the electrochemical oxidation of nitrite..... 208
8.1 Introduction 208
8.2 Experimental 209

8.2.1 Chemicals and materials 209
8.2.2 Preparation of Pt modified BDD electrode 210
8.3 Results and discussion 210
8.3.1 Preparation and Electrochemical characterisations of Pt/BDD 210
8.3.2 Electrochemical oxidation of NO_2^- on bare BDD and Pt/BDD 212
8.3.3 pH effects in the NO_2^- detection on Pt modified electrode 214
8.3.4 Detection limit of NO_2^- on Pt modified BDD 216
8.3.5 Interferences in NO_2^- electrochemical detection 219
8.4 Summarising comments 221
References 223

List of Abbreviations

AA	.....	Ascorbic acid
AFM	.....	Atomic force microscopy
AQDS	.....	Anthraquinone-2,6-disulfonate
ASF	.....	Atomic sensitive factor
ASV	.....	Adsorptive stripping voltammetry
BDD	.....	Boron doped diamond
BE	.....	Binding energy
BEN	.....	Bias enhanced nucleation
CB	.....	Carbon black
CE	.....	Counter electrode
CME	.....	Chemically modified electrode
CMP	.....	Chemical-mechanical polishing
CV	.....	Cyclic voltammetry
CVD	.....	Chemical vapour deposition
DA	.....	Dopamine
DLS	.....	Dynamic light scattering
DMFC	.....	Direct methanol fuel cell
ECA	.....	Electrochemical active area
EDRF	.....	Endothelium-derived relaxing factor
EDX	.....	Energy dispersive X-ray analysis
EIS	.....	Electrochemical impedance spectroscopy
EPD	.....	Etch pit density
ESCA	.....	Electron Spectroscopy Chemical Analysis
ESR	.....	Electron spin resonance
FA	.....	Folic acid
FAT	.....	Fixed analyser transmission
FRA	.....	Frequency Response Analysis
FWHM	.....	Full width at half maximum
GC	.....	Glassy carbon
HFCVD	.....	Hot filament chemical vapour deposition

HPHT	.....	High-pressure high-temperature
HPLC	.....	High performance liquid chromatography
IHP	.....	Inner Helmholtz plane
MV	.....	Methyl viologen
MWCVD	.....	Microwave plasma chemical vapour deposition
NOS	.....	NO synthase
OHP	.....	Outer Helmholtz plane
PBS	.....	Phosphate buffered saline
PLD	.....	Pulsed laser deposition
PSD	.....	Potential step deposition
PTFE	.....	Polytetrafluoroethylene
RDE	.....	Rotating disc electrode
RE	.....	Reference electrode
RMS	.....	Root mean square
SCE	.....	Standard calomel electrode
SCR	.....	Selective catalytic reduction
SECM	.....	Scanning electrochemical microscopy
SEM	.....	Scanning electron microscopy
SHE	.....	Standard hydrogen electrode
SOFC	.....	Solid oxide fuel cell
SPM	.....	Scanning probe microscopy
SWV	.....	Square wave voltammetry
TMB	.....	Trimethylboron
UHV	.....	Ultra-high vacuum
UME	.....	Ultra-microelectrode
VB2	.....	Vitamin B2, riboflavin
WE	.....	Working electrode
XPS	.....	X-ray photoelectron spectroscopy
XRD	.....	X-ray diffractometer
YSZ	.....	Yttria stabilised zirconia

List of Figures

Figure 1.1 The pressure-temperature phase diagram for carbon..... 3

Figure 1.2 Examples of some of common types of low pressure CVD reactor. (*a*) A Hot filament CVD reactor, (*b*) a 'NIRIM-type' microwave plasma reactor, (*c*) a 'ASTEX-type' microwave plasma reactor, and (*d*) a DC arc jet (plasma torch) CVD reactor. 5

Figure 2.1 A schematic presentation of two-electrode (left) and three-electrode (right) electrochemical cells. 21

Figure 2.2 The electrical double layer on electrode/electrolyte interface 23

Figure 2.3 a) waveform and b) classic cyclic voltammogram of cyclic voltammetry 30

Figure 2.4 a) waveform and b) current response in potential step chronoamperometry 33

Figure 2.5 The time-potential waveform of SWV 34

Figure 2.6 The equivalent circuit of a typical reversible electron transfer process 36

Figure 2.7 *Nyquist* plot of EIS measurement 36

Figure 2.8 a) the photoelectron emission process in XPS b) the different energy levels in XPS 39

Figure 2.9 Electron mean free paths as a function of electron kinetic energy for several metals, this universal curve presents a minimum 2 - 5 Å at about 50 - 100 eV. 40

Figure 2.10 the schematic diagram of XPS comprising X-ray source and hemispherical analyser. 41

Figure 2.11 XPS spectrum of clean gold sample under monochromatic Al Kα X-ray .. 42

Figure 2.12 a) Chemical shifts of C 1s electrons for ethyl trifluoroacetate. The different chemical shifts can be roughly attributed to the varied electronegative values, b) Typical spin-orbit coupling of Au 4f electrons. 43

Figure 2.13 Schematic diagram of SEM 47

Figure 2.14 Schematic diagram of DLS 48

Figure 3.1 The multi-layer structure of heteroepitaxial (001) single crystal diamond 57

Figure 3.2 CVs of (001) heteroepitaxial, smooth and rough polycrystalline diamond electrodes in 0.1 M HNO_3 at a scan rate of 100 mV/s, for comparison of a) potential window and b) background current of these electrodes. 61

Figure 3.3 *Nyquist* impedance plot (-Im Z *vs.* Re Z) for (001) heteroepitaxial single crystal, smooth and rough polycrystalline BDD. Inset: the equivalent *Randles* circuit of electrodes where R_s is the series resistance, CPE is the constant phase element, R_{CT} is the charge transfer resistance and Z_w is the *Warburg* impedance respectively. 63

Figure 3.4 CVs of (001) heteroepitaxial, smooth and rough polycrystalline diamond electrodes in 1 mM $Ru(NH_3)_6^{3+}$ and 0.1 M KCl at a scan rate of 100 mV/s. 65

Figure 3.5 CVs of heteroepitaxial diamond in a) 1 mM RuHex and 0.1 M KCl at different scan rates from 0.02 V/s to 2 V/s and b) different concentrations of RuHex from 1 μM to 5 mM in 0.1 M KCl at a scan rate of 100 mV/s. 66

Figure 3.6 CVs of (001) heteroepitaxial, smooth and rough polycrystalline diamond electrodes in 1 mM $Fe(CN)_6^{4-}$/0.1 M KCl. 70

Figure 3.7 *Mott-Schottky* plot for heteroepitaxial (001) and polycrystalline diamonds at different frequencies of 25 k, 2.5 k, 250 and 80 Hz..... 72

Figure 3.8 Energy diagram of a) heteroepitaxial single crystal diamond and b) polycrystalline polished smooth diamond 75

Figure 3.9 CVs of heteroepitaxial (001) single crystal, smooth and rough polycrystalline diamond with 4 mM MV^{2+} in 0.1 M KCl at a scan rate of 100 mV/s. Inset: CV of heteroepitaxial (001) single crystal diamond in 1 mM MV^{2+} and 0.1 M KCl. 77

Figure 3.10 CVs of a) heteroepitaxial (001), smooth and rough polycrystalline diamond in 0.1 M $HClO_4$ at a scan rate of 50 mV/s after previous CVs in 1 mM AQDS and rinse and b) smooth polycrystalline diamond electrode in 0.1 M $HClO_4$ at different scan rates from 0.02 to 2 V/s after CV in 1 mM AQDS and rinse. 78

Figure 3.11 SECM of a) (001) heteroepitaxial BDD and b) smooth polycrystalline diamond, and (c,d) the corresponding approach curves at various areas on the diamond surface in $Ru(NH_3)_6^{3+}$ (middle) between two theoretical ideal positive (top) and negative (bottom) feedback curves. 81

Figure 3.12 SEM of (a,c) (001) heteroepitaxial BDD and (b,d) smooth polycrystalline diamond before and after platinum electrodeposition respectively. 83

Figure 3.13 AFM image shows the topography of epitaxial diamond with additional mechanical polishing step after the growth of a thin boron doped diamond layer with RMS roughness is only 0.12 nm in a scan area of 1×1 μm^2. 84

Figure 3.14 SECM of (a,b) smooth polycrystalline and (c,d) (001) heteroepitaxial diamond in (a,c) 1 mM $Ru(NH_3)_6^{3+}$/0.1 M KCl and (b,d) 1 mM $Fe(CN)_6^{4-}$/0.1 M KCl. 86

Figure 4.1 SEM of un-polished polycrystalline BDD electrode surface 96

Figure 4.2 CV of the Pt modified BDD following the two-stage electrodeposition process (i) to produce a loading of approximately 230 μg at a scan rate of 0.05 V/s. The other two traces correspond to lower Pt loadings using single stage of PSD method (ii) and potentiostatic deposition method (iii) 99

Figure 4.3 H-desorption peak current height from decorated Pt/BDD electrode in 0.5 M H_2SO_4 for differing PrO_x deposition scans. 101

Figure 4.4 CV of 1 mM a) $FcCH_2OH^{0/+}$ and b) $Ru(NH_3)_6^{2+/3+}$ in 0.1 M KCl on clean

BDD surface (i) and after 1,2 and 3 oxide deposition scans (ii, iii, iv) 102

Figure 4.5 CV of 1 mM $IrCl_6^{2-/3-}$ in 0.1 M KCl on clean BDD surface (i) and after 1,2 and 3 oxide deposition scans (ii, iii, iv). 103

Figure 4.6 Low resolution SEM of Pt deposited BDD electrode using single a) potentiostatic method and b) Potential step deposition. 104

Figure 4.7 SEM of Pt/BDD produced by the two-stage Pt deposition process at a) low and b) high resolution. 105

Figure 4.8 SEM of PrO_x-Pt/BDD produced by PrO_x electrodeposition for 10 CV scans under a) low and b) high resolution. 106

Figure 4.9 High resolution SEM of PrO_x-Pt/BDD produced by PrO_x electrodeposition for 3 CV scans. 106

Figure 4.10 XPS spectrum of Pt 4f peaks after two-stage electrodeposition process.. 107

Figure 4.11 XPS spectra of a) Pt 4f spectral region before (i) and after (ii) PrO_x electrodeposition, b) Pr 3d region after PrO_x electrodeposition. 108

Figure 4.12 Typical electrochemical oxidation of methanol on Pt modified electrodes 111

Figure 4.13 CVs of i) untreated Pt/BDD, ii) pre-treated Pt/BDD and iii) pre-treated Pt/BDD after 3 successive scans at a scan rate of 50 mV/s in 1 M CH_3OH and 0.5 M H_2SO_4. 112

Figure 4.14 CVs of i) pre-stringent cleaned Pt/BDD, ii) PrO_x/Pt-BDD in 1 M CH_3OH and 0.5 M H_2SO_4 at a scan rate of 50 mV/s with a) higher peak intensity and b) smaller peak intensity (correlating to slightly differing Pt loadings) variation. Insets: the onset potential variation after the PrO_x electrodeposition. 113

Figure 4.15 CV of i) Pt/BDD and ii) PrO_x-Pt/BDD in 1 M CH_3OH and 0.5 M H_2SO_4 at a scan rate of 50 mV/s without a stringent cleaning process applied on Pt-supported surface. 115

Figure 4.16 Chronoamperometric measurement in 1 M CH_3OH and 0.5 M H_2SO_4 at 0.6 V after successive electrodeposition of i) Pt and ii) Pt and PrO_x 117

Figure 4.17 CVs of nafion/Pt-CB/BDD i) before and ii) after the electrodeposition of PrO_x in 1 M CH_3OH and 0.5 M H_2SO_4 at a scan rate of 50 mV/s 118

Figure 4.18 The mechanism of indirect CO pathway in PrO_x-Pt system, in which (Vo^{--}) represents the oxygen vacancies. 123

Figure 5.1 CVs in 0.5 M H_2SO_4 on pure Pt and PrO_x-Pt coated BDD at a scan rate of 50 mV/s. 134

Figure 5.2 SEM of a) pure Pt coated BDD, b) lower and c) higher PrO_x coverage modified Pt/BDD electrodes. 135

Figure 5.3 XPS spectra of Pt 4f spectral region before i) and after ii) thicker PrO_x deposition by 40 CV scans with 0.5 mM $Pr(NO_3)_3$ and 5 mM H_2O_2 in 0.1 M KCl on Pt/BDD..... 136

Figure 5.4 CVs of 1.8×10^{-5}, 3.6×10^{-5} and 9.0×10^{-5} M NO in 0.1 M PBS (pH = 7.4) at a scan rate of 50 mV/s on a) bare and b) Pt-coated BDD. 138

Figure 5.5 CVs of 3.6×10^{-5} M NO in 0.1 M PBS (pH = 7.4) on Pt-coated BDD at different scan rates of 20, 50, 100 and 200 mV/s 139

Figure 5.6 SWV of NO at concentrations of 1.8×10^{-5}, 3.6×10^{-5}, 9.0×10^{-5} and 1.8×10^{-4} M in 0.1 M PBS (pH = 7.4) at a frequency of 10 Hz along with a 0.002 V step potential and a 0.05 V amplitude on a) bare and b) Pt-covered BDD 140

Figure 5.7 SWVs of 9.0×10^{-5} M NO, and its mixed solution with 1.8×10^{-3} M NO_2^- in 0.1 M PBS (pH = 7.4) at a frequency of 10 Hz along with a 0.002 V step potential and a 0.05 V amplitude on a) Pt/BDD and b) PrO_x-Pt/BDD after 40 cyclic scans in the electrodeposition of PrO_x..... 142

Figure 5.8 SWVs of 9.0×10^{-5} M NO, and its mixed solution with 1.8×10^{-3} M NO_2^- in 0.1 M PBS (pH = 7.4) at a frequency of 10 Hz along with a 0.002 V step potential and a 0.05 V amplitude on a) Pt/BDD and b) PrO_x-Pt/BDD after 20 cyclic scans in the electrodeposition of PrO_x..... 143

Figure 5.9 CVs of a) 5.4×10^{-5} M NO and b) 1.8×10^{-3} M AA in 0.1 M PBS (pH = 7.4) at a scan rate of 50 mV/s on Pt/BDD and PrO_x-Pt/BDD after 40 cyclic scans in the electrodeposition of PrO_x..... 144

Figure 5.10 CVs of the mixed solution of 9.0×10^{-5} M NO and 1.8×10^{-3} M AA in 0.1 M PBS (pH = 7.4) at a scan rate of 50 mV/s on i) pure Pt and Pt-PrO_x coated BDD electrode after ii) 20 and iii) 40 cyclic scans in the electrodeposition of PrO_x..... 145

Figure 5.11 SWVs of the mixed solution comprising of 1.8×10^{-3} M AA with a) 1.8×10^{-5} M, b) 3.6×10^{-5} M, c) 9.0×10^{-5} M and d) 1.8×10^{-4} M NO in 0.1 M PBS (pH = 7.4) at a frequency of 10 Hz along with a 0.002 V step potential and a 0.05 V amplitude on i) Pt and PrO_x-Pt coated BDD electrode after ii) 2 and iii) 40 cyclic scans in the electrodeposition of PrO_x..... 147

Figure 5.12 SWVs of the mixed solution of 1.8×10^{-3} M AA with a) 3.6×10^{-5} M and b) 9.0×10^{-5} M NO in 0.1 M PBS (pH = 7.4) at a frequency of 10 Hz along with a 0.002 V step potential and a 0.05 V amplitude on i) pure Pt and ii) Pt-PrO_x coated BDD electrode after 20 cyclic scans in electrodeposition..... 148

Figure 5.13 Chronoamperometric measurement at 0.8 V *vs.* Ag/AgCl in 0.1 M PBS (pH = 7.4) for 1000 seconds with successive injections of NO_2^-, NO and AA with varied concentrations on i) pure Pt/BDD and ii) Pt-PrO_x/BDD after 20 cyclic scans in electrodeposition. 149

Figure 5.14 Chronoamperometric measurement at 0.8 V *vs.* Ag/AgCl in 0.1 M PBS (pH = 7.4) for 600 seconds with successive injections of NO from its aqueous solution at a concentration of 1.8×10^{-5} M on i) Pt/BDD and ii) PrO_x-Pt/BDD after 20 cyclic scans in electrodeposition. 151

Figure 5.15 Supposed interaction mechanism between the PrO_x layer and anionic interfering compounds, *e.g.* NO_2^- 152

Figure 6.1 CVs of 100 μM a) $Ru(NH_3)_6Cl_3$ and b) $FcCH_2OH$ in 0.1 M KCl on bare BDD at varied scan rates from 0.02 to 1.0 V/s. 163

Figure 6.2 CVs of a) 100 μM $K_3Fe(CN)_6$ at varied scan rates from 0.02 to 1 V/s and b) 1 mM $K_3Fe(CN)_6$ after consecutive *n* scans (n = 5 to 500) at 0.1 V/s in 0.1 M KCl on bare BDD. 164

Figure 6.3 CVs of 100 μM K_2IrCl_6 in 0.1 M KCl at varied scan rates from 0.02 to 0.2 V/s on bare BDD..... 165

Figure 6.4 CVs of 100 μM a) $Ru(NH_3)_6^{3+}$, b) $FcCH_2OH$ and c) $Fe(CN)_6^{3-}$ in 0.1 M KCl at 0.05 V/s on bare and PrO_x coated BDD electrode after the electrodeposition in 25 mM $Pr(NO_3)_3$ and 5 mM H_2O_2 for 1 scan. 166

Figure 6.5 CVs of 100 μM a) $Ru(NH_3)_6^{3+}$, b) $FcCH_2OH$ and c) $Fe(CN)_6^{3-}$ in 0.1 M KCl at 0.1 V/s on i) bare and PrO_x coated BDD electrode after the electrodeposition in 5 mM $Pr(NO_3)_3$/1 mM H_2O_2 in 0.1 M KCl electrolyte for ii) 1 and iii) 6 scans. 168

Figure 6.6 CVs of a) 100 μM and b) 10 μM $Fe(CN)_6^{3-}$ in 0.1 M KCl at 0.1 V/s on bare and PrO_x modified BDD after varied cyclic numbers in the deposition of PrO_x at 0.05 V/s. 169

Figure 6.7 CVs of 100 μM $Fe(CN)_6^{3-}$ and $Fe(CN)_6^{4-}$ in 0.1 M KCl at a scan rate of 0.02 V/s on bare and modified BDD electrode after 20 cyclic numbers in the deposition of PrO_x at 0.05 V/s. 170

Figure 6.8 CVs of 100 μM $IrCl_6^{2-}$ in 0.1 M KCl on a) bare and PrO_x modified BDD (after 20 scans in CV electrodeposition) at 0.02 V/s and b) PrO_x modified BDD (after 20 scans in CV electrodeposition) with varing scan rates from 0.02 to 0.2 V/s, Inset: linear plot of cathodic currents *vs.* square root of scan rates. 171

Figure 6.9 CVs of 100 μM $Fe(CN)_6^{4-}$ at a scan of 20 mV/s on i) bare BDD and after several treatments: ii) PrO_x freshly deposited, iii) after air-exposured, annealed and iv) after annealed in hydrogen plasma. 173

Figure 6.10 CVs of 1 mM a) $Fe(CN)_6^{3-}$, b) $Ru(NH_3)_6^{3+}$, c) $FcCH_2OH$ in 0.1 M KCl at 0.02 V/s on i) bare BDD, and PrO_x coated and air-annealed BDD with ii) 20 scans and iii) 40 scans in CV electrodeposition of PrO_x..... 174

Figure 6.11 XPS survey spectrum of PrO_x film as freshly electrodeposited after 20 CV scans with 5 mM $Pr(NO_3)_3$/1 mM H_2O_2 in 0.1 M KCl at 0.05 V/s 175

Figure 6.12 Narrow scan XPS spectra of a) Pr 3d with three core components peaks *a*/*a*', *b*/*b*' and *c*/*c*' for Pr $3d_{5/2}$ and Pr $3d_{3/2}$ respectively and a rise *t*' on the higher binding energy value for $3d_{3/2}$ component due to the multiplet effect[32] and b) O1s with three component peaks for O^{2-}, OH^- and $O^{\delta-}$ after the PrO_x film was freshly electrodeposited after 20 CV scans with 5 mM $Pr(NO_3)_3$/1 mM H_2O_2 in 0.1 M KCl at 0.05 V/s..... 177

Figure 6.13 Narrow scan XPS spectra of Pr 3d with three core components peaks *A*/*A*',

B/*B*' and *C*/*C*' for $Pr3d_{5/2}$ and $Pr3d_{3/2}$ respectively for a) hydrogen annealed and b) air annealed PrO_x deposits on BDD produced after 20 CV scans in 5 mM $Pr(NO_3)_3$/1 mM H_2O_2 at 0.05 V/s..... 177

Figure 6.14 Narrow scan XPS spectra of O 1s with three component peaks for O^{2-}, OH^- and $O^{\delta-}$ for a) hydrogen annealed and b) air annealed PrO_x deposits on BDD produced after 20 CV scans in 5 mM $Pr(NO_3)_3$/1 mM H_2O_2 at 0.05 V/s..... 178

Figure 6.15 Dynamic light scattering histogram of PrO_x suspension prepared by fresh electrodeposition using 5 mM $Pr(NO_3)_3$ and 1 mM H_2O_2 in 0.1 M KCl at 0.05 V/s for 50 scans on pure Pt wire 180

Figure 6.16 *Zeta* potential distribution plot for fresh PrO_x suspension produced from 5 mM $Pr(NO_3)_3$ and 1 mM H_2O_2 in 0.1 M KCl at 0.05 V/s for 50 scans on pure Pt wire. 181

Figure 6.17 CVs of 10 mM AA and 1 mM DA in 0.1 M PBS at 0.1 V/s on (i) bare and (ii) PrO_x coated BDD (dashed line) produced by 10 cyclic scans in 5 mM $Pr(NO_3)_3$ and 1 mM H_2O_2 in 0.1 M KCl at 0.05 V/s..... 183

Figure 6.18 SWVs of AA and DA mixed solution with increasing concentrations of AA at 0.1, 0.2, 0.5 and 1 mM in the presence of a fixed DA concentration of 0.1 mM at a frequency of 10 Hz along with a 0.002 V step potential and a 0.05 V amplitude on a) un-modified bare and b) PrO_x coated BDD produced by 10 cyclic scans in 5 mM $Pr(NO_3)_3$ and 1 mM H_2O_2 in 0.1 M KCl at 0.05 V/s..... 184

Figure 6.19 Electrocatalytic oxidation of AA by oxidised DA 185

Figure 7.1 Survey XPS spectrum of native CB 192

Figure 7.2 The redox reactions of VB2 between its quinone and hydroquinone forms 193

Figure 7.3 CVs of a) anodically treated bare BDD and b) 30 μL CB coating modified BDD at varying scan rates from 20 to 200 mV/s in 0.1 mM VB2 and 0.5 M H_2SO_4. (Inset: linear fitting of cathodic peak currents against scan rates in the double logarithmic manners) 194

Figure 7.4 CVs of a) anodically treated bare BDD and b) 30 μL CB coating modified BDD in 0.5 M H_2SO_4 at varying scan rates from 20 to 200 mV/s after being characterised in 0.1 mM VB2 and 0.5 M H_2SO_4 and carefully rinsed. 195

Figure 7.5 CVs of modified BDD electrode with different CB loadings (10 to 30 μL) in 0.1 mM VB2 and 0.5 M H_2SO_4 at a scan rate of 50 mV/s..... 196

Figure 7.6 CVs of modified BDD with 40 μL CB loading in 0.1 mM VB2 and 0.5 M H_2SO_4 at varied scan rates from 20 to 200 mV/s. 197

Figure 7.7 CVs of anodically treated and 0.1 mM VB2-immersed BDD coated with 10 μL CB in 0.5 M H_2SO_4, with varing ultrasonication times of a few seconds, 10 and 30 minutes at a scan rate of 50 mV/s. 198

Figure 7.8 CVs of anodically treated and 0.1 mM VB2-immersed BDD coated with 10 μL CB in 0.5 M H_2SO_4, with varing VB2 immersion times of 15, 30 and 60 minutes at a scan rate of 50 mV/s. 199

Figure 7.9 CVs of a) un-modified bare and b) CB coated BDD over a pH range from 2.0 to 12.0 in 0.1 mM VB2 with 0.1 M phosphate buffer solution at a scan rate of 50 mV/s. 200

Figure 7.10 Plots of E_a against pH for 0.1 mM VB2 in 0.5 M H_2SO_4 on a) un-modified bare and b) CB coated BDD. 201

Figure 7.11 SWV of varying VB2 concentrations in 0.5 M H_2SO_4 on a) bare and b) 10 μL CB coated BDD from cathodic direction at a frequency of 10 Hz along with a 0.002 V step potential and a 0.05 V. Inset: SWV of VB2 at 2×10^{-8} to 4×10^{-7} M. 203

Figure 7.12 SWVs of 0.5 μM VB2, 1.0 μM FA and 50 μM AA in 0.5 M H_2SO_4 at a frequency of 10 Hz along with a 0.002 V step potential and a 0.05 V amplitude on a) un-modified bare and b) 10 μL CB coated BDD in cathodic direction. 204

Figure 8.1 CVs of modified BDD electrodes in 0.5 M H_2SO_4 at a scan rate of 0.05 V/s after i) 20-minute PSD, ii) 20-minute potentiostatic deposition and iii) 10-minute PSD followed by 10-minute potentiostatic deposition. 211

Figure 8.2 SEM of Pt modified BDD electrode with a) high and b) low resolution after the two-stage electrodeposition comprising of 10-minute PSD followed by 10-minute potentiostatic deposition. 212

Figure 8.3 CVs of 1×10^{-3} M NO_2^- in 0.1 M PBS (pH = 7.4) at a scan rate of 0.05 V/s on i) bare and modified BDD electrodes after ii) 20-minute PSD, iii) 20-minute potentiostatic deposition and iv) 10-minute PSD followed by 10-minute potentiostatic deposition. 213

Figure 8.4 CVs of 1×10^{-3} M NO_2^- in 0.1 M PBS (pH = 7.4) at i) 0.02 V/s, ii) 0.05 V/s, iii) 0.1 V/s and iv) 0.2 V/s on the Pt coated BDD electrode after 10-minute PSD followed by 10-minute potentiostatic deposition. Inset: linear fitting of peak current *vs.* square root of scan rate. 214

Figure 8.5 a) CVs of 1×10^{-3} M NO_2^- in phosphate buffer solution at different pH values from 3.0 to 10.0 at a scan rate of 0.05 V/s on Pt modified BDD after the two-stage electrodeposition of Pt nanoparticles. Inset: linear correlation between NO_2^- oxidation peak potential *vs.* pH from 3.0 to 6.0. b) The relationship between the NO_2^- oxidation peak current density *vs.* pH from 3.0 to 9.0. 216

Figure 8.6 CVs of 0.1 M PBS (pH = 7.4) in the presence of 1×10^{-4}, 2×10^{-4}, 4×10^{-4}, 6×10^{-4}, 8×10^{-4} and 1×10^{-3} M NO_2^- at a scan rate of 0.05 V/s on Pt/BDD electrode. Inset: linear correlation between the peak current density *vs.* the NO_2^- concentration. 217

Figure 8.7 SWVs of 0.1 M PBS (pH = 7.4) with different NO_2^- presenses from a) 2×10^{-5} to 4×10^{-3} M and b) 6×10^{-3} to 1×10^{-2} M in 0.1 M PBS (pH = 7.4) at a frequency of 10 Hz along with a 0.002 V step potential and a 0.05 V amplitude. a) Inset: linear relationship between the oxidation peak current density *vs.* the NO_2^- concentration. .. 218

Figure 8.8 CVs of a) 1×10^{-4} M NO_2^- i) without and ii) with 50-fold AA in 0.1 M PBS (pH = 7.4) at a scan rate of 0.05 V/s on Pt/BDD and b) SWV of 1×10^{-4} M NO_2^- and 50-fold AA in 0.1 M PBS (pH = 7.4) at a frequency of 10 Hz along with a 0.002 V step potential and a 0.05 V amplitude on Pt/BDD. 219

Figure 8.9 CVs of 1×10^{-4} M NO_2^- i) without and ii) with 50-fold I^- in 0.1 M PBS (pH = 7.4) at a scan rate of 0.05 V/s on Pt/BDD. 220

List of Tables

Table 1.1 Some outstanding properties of diamond. 2

Table 3.1 Estimated heterogeneous electron transfer rate constants for $Ru(NH_3)_6^{3+}$ and $Fe(CN)_6^{4-}$ using *Nicholson* method, Digisim fitting and impedance characterisations. . 67

Table 4.1 Characterisation of Pt electrodeposited on diamond surfaces applying differing techniques. 100

Table 4.2 The elemental composition of Pt and PrO_x-Pt decorated BDD surface a)After two-stage of Pt electrodeposition, b)After successive PrO_x electrodeposition by CV. 109

Table 4.3 Key parameters in CV of electrooxiation of methanol..... 114

Chapter 1
Introduction

1.1 Diamond: A Brief History

The word 'Diamond' is derived from the Greek *αδαμασ (adamas*), meaning unconquerable, unalterable and invincible[1]. It was used to describe the hardest material and later became the specific synonym of diamond.

It is generally believed that diamond was first recognised and mined in India around 4,000 years ago along the rivers Penner, Krishna and Godavari[2]. They were soon treasured as gemstones for religious icons and still remain as a symbol of wealth and prestige to date. Although these precious gemstones have been prized for their scarcity for quite a long history, the modern diamond era only came in the 19^{th} Century, when extremely large diamond deposits were discovered in South Africa, attracting a huge rush of European prospectors and changing the fates of many African countries[1].

Apart from the value as gemstones, diamond presents a broad range of exceptional physical properties. Acknowledged as the hardest known material along with the highest conductivity at low temperature, diamond also presents other distinctive properties such as transparency over a broad wavelength range, high stiffness and low compressibility. Considering it is fairly inert to most chemical reagents, diamond has been undoubtedly treated as an advantageous material in engineering applications. The material also has attractive dielectric and wide band gap semiconductor properties for electronic applications. Some of its outstanding properties are summarised in **Table 1.1**.

Table 1.1 Some outstanding properties of diamond. (Compiled from ref[3])

Extreme mechanical hardness (*ca*. 90 GPa) and wear resistance
Highest bulk modulus (1.2×10^{12} N m^{-2})
Lowest compressibility (8.3×10^{13} m^2 N^{-1})
Highest room temperature thermal conductivity (2×10^{13} W m^{-1} K^{-1})
Very low thermal expansion coefficient at room temperature (1×10^{-6} K)
Broad optical transparency from the deep ultraviolet to the far infrared
Highest sound propagation velocity (17.5 km s^{-1})
Very good electrical insulator (room temperature resistivity is *ca*. 10^{13} Ω cm)
Diamond can be doped, becoming a semiconductor with a wide band gap of 5.4 eV
Very resistant to chemical corrosion
Biologically compatible
Some surfaces exhibit very low or ‘negative’ electron affinity

However, unfortunately, most of these exceptional properties are extremely difficult to exploit due to the high price, natural variations and scarcity of large natural diamonds. Unsurprisingly there have been many attempts to make synthetic diamond. Since diamond was known to be a form of carbon allotrope, many works had been made to synthesise it artificially by using graphite, which is another commonly occurring form of carbon. According to the phase diagram in **Figure 1.1**, extremes of pressure and temperature are required to convert graphite into diamond. Work using this approach led to the so-called high-pressure high-temperature (HPHT) technique for diamond growth by Tracy Hall at General Electric in 1954[1]. A Belt press was used in the synthesis process, where graphite was compressed to tens of thousands of atmospheres and heated to over 2,000 K in the presence of a metal catalyst such as cobalt. This approach has been broadly applied to produce diamonds for industrial utilisations. However under HPHT conditions, the resulting diamond is always in a form of single crystals with diverse sizes and vulnerable to the contamination of catalyst metals. Whist the basis for the large-scale industrial production of diamond grit, the method is not readily adapted to large scale production of high quality diamond for more scientific uses.

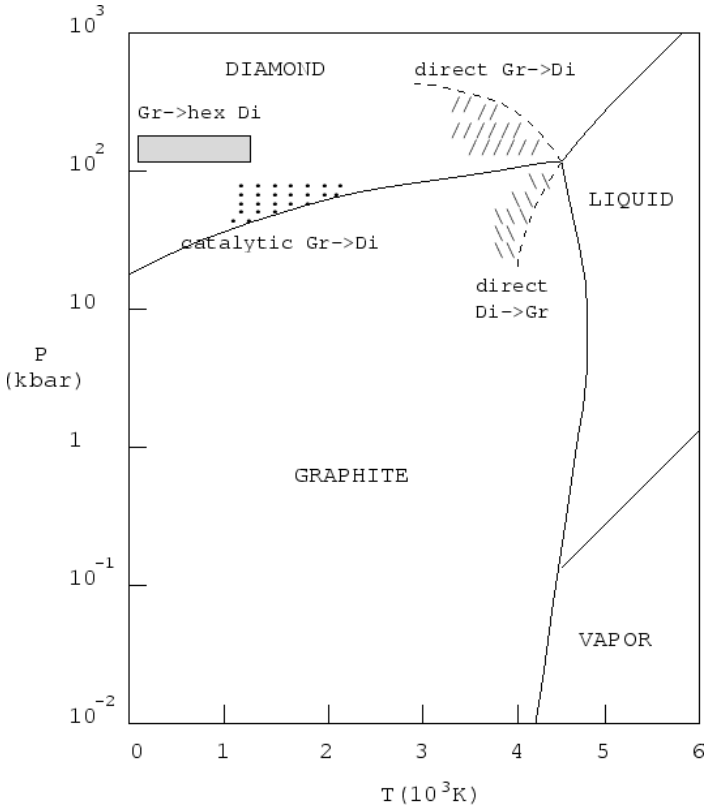


Figure 1.1 The pressure-temperature phase diagram for carbon[4]

1.2 Development of CVD technique

In order to address the issue, scientists started to investigate an alternative approach to nature's method of making diamond. One alternative is to dissociate carbon-containing gases to form metastable diamond phase (tetrahedral) under low pressure conditions using chemical vapour deposition (CVD). The earliest attempts were made by growing diamond on the surface of natural diamond crystals at 900 ˚C, along with reduced pressure, in the thermal decomposition process. However, those experiments were limited by the undesired competing process of graphite co-deposition, leading to the resulting diamond with mixed impure phases[5, 6]. The breakthrough came in the late 1960s, when atomic hydrogen was discovered to enable a much higher etching rate of

graphite than diamond[7, 8]. Saturated hydrogen termination of the diamond surface prohibits the re-construction of this graphite phase, significantly. In 1982, with the reconciliation of all these findings, Matsumoto's group in NIRIM (National Institute of Research in Inorganic Materials) designed the first hot filament assisted chemical vapour deposition (HFCVD) reactor, which could grow diamond of high quality on non-diamond substrates at significant rates[9, 10]. In the following year, the same group introduced another technique for diamond growth using a microwave plasma reactor, which was later recognised as MWCVD[11]. All these efforts above from NIRIM stimulated the worldwide interest in diamond CVD, and became the pioneering contributions for all the new diamond development and research afterwards to the present date.

Following the success of HFCVD and MWCVD, many other methods have been introduced for diamond synthesis, *inter alia* Laser-assisted CVD, RF-plasma CVD, DC arc plasma jet CVD and combustion flame technique *etc*. Some of the common types of low-pressure CVD reactors are exhibited in **Figure 1.2** as below. Today high quality CVD diamond is readily produced as coatings and as free-standing wafers at reasonably economic cost to enable various scientific applications in such areas as optical windows, electronics, heat sinks and NEMS (nanoelectromechanical systems).

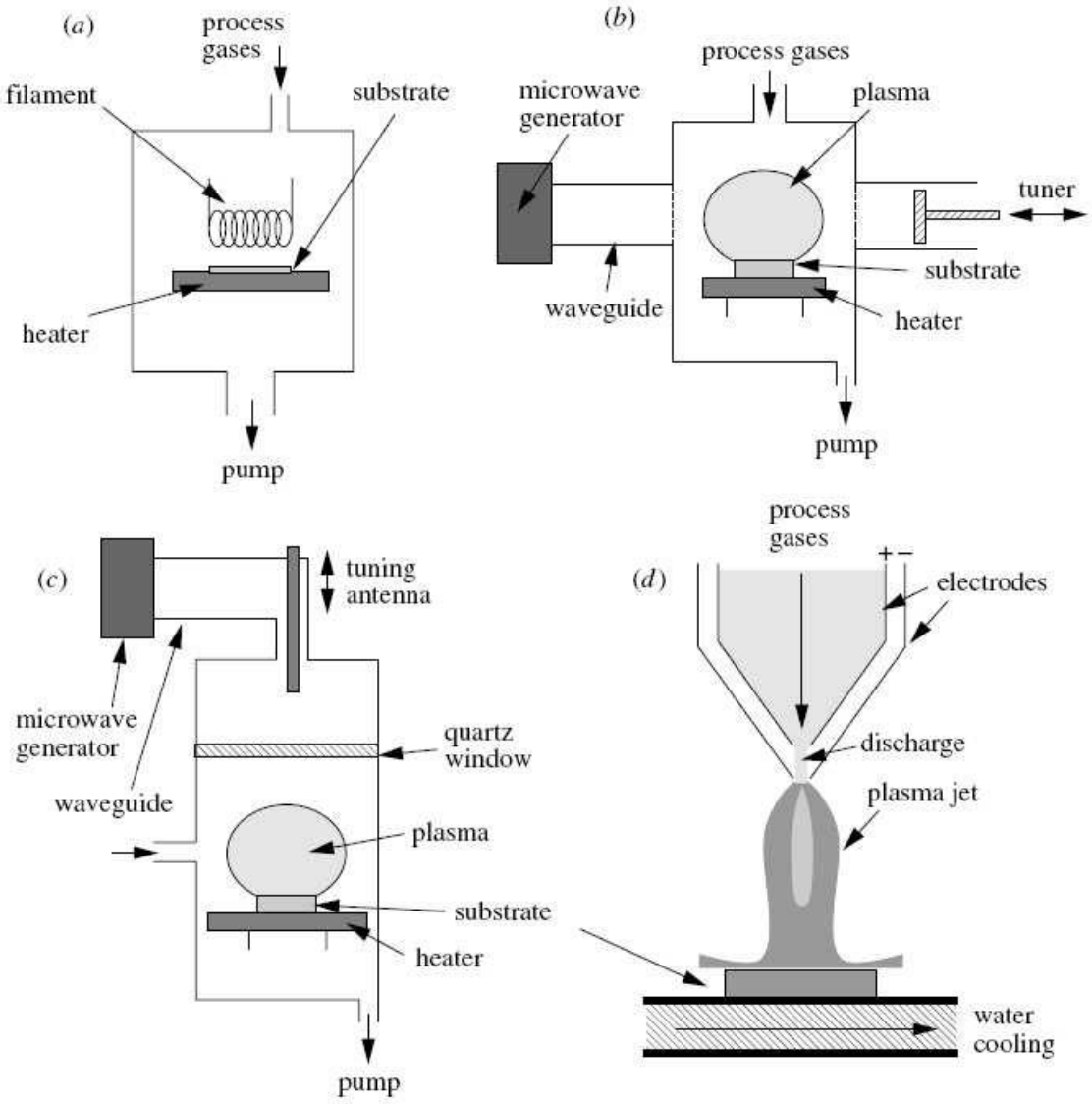


Figure 1.2 Examples of some of common types of low pressure CVD reactor. (*a*) A Hot filament CVD reactor, (*b*) a 'NIRIM-type' microwave plasma reactor, (*c*) a 'ASTEX-type' microwave plasma reactor, and (*d*) a DC arc jet (plasma torch) CVD reactor[1].

1.3 Electrochemistry of diamond

Apart from the applications noted above, CVD diamond also finds applications in electrochemistry, since it is readily produced with semimetal electrical properties, when heavily doped with boron. This in part stems from the well-recognised properties of diamond such as mechanical stability, chemical inertness and optical transparency[12]. This opens a new window for work under extreme conditions such as extremely high anodic potentials[13], chemically aggressive media[14], laser activation[15] and fast mass transport under high power ultrasound[16]. However, compared with other conventional electrodes, *e.g.* platinum, graphite and glassy carbon *etc.*, diamond presents two other distinct superior features: a low background current and a wide potential window[17]. It is even possible to achieve a 5 V window of polarisability of fluorinated diamond electrodes in aqueous solution[18]. Research has also shown that the material offers resistance to electrode fouling for use in biological media. These advantages can all be exploited in electroanalysis.

As mentioned earlier, the diamond electrode material was produced by CVD and doped with boron by addition of a volatile boron precursor to the reactor feedstock. Tshepe *et al* observed that at a high boron doping level of 3.92×10^{21} cm^{-3}, the metal to insulator transition occurs at lower temperatures[19]. However, good conductivity and electrochemical properties already can be achieved at room temperature with comparatively lower boron content[20] at approximately 10^{20} cm^{-3}. At this boron doping level, there is about one boron atom co-existing with 1000 carbon atoms[12]. A free-standing electrode made of this material offers low series resistance of a few hundred ohms, having thickness of about 0.5 mm. Although single crystal diamond can be grown, most diamonds for electrochemical work are polycrystalline or nanocrystalline

materials. The synthesised thin-film diamond electrodes are normally mixed with some non-diamond sp^2 carbon impurities. The more sp^2 species present, the narrower the potential window in aqueous solutions and *vice versa*[21]. The diamond electrode surface can be produced as either hydrogen-terminated or oxygen-terminated. The former yields a hydrophobic surface, which gradually becomes oxidised when used in aqueous media. The latter is hydrophilic and relatively stable over prolonged electrochemical usage.

The electrochemical behaviour of diamond electrodes is often explored under cyclic voltammetry (CV) in standard redox mediator systems such as $Ru(NH_3)_6^{2+/3+}$, $Fe(CN)_6^{3-/4-}$, $FcCH_2OH^{0/+}$ and $IrCl_6^{2-/3-}$. For so-called 'outer-sphere' redox couples such as $Ru(NH_3)_6^{2+/3+}$ as one of typical redox systems[22, 23], the rate constants for diamond tend to be comparable but somewhat slower than for other standard electrode materials such as graphite, which can be ascribed to a lower density of electronic states[21]. For these couples, the rate constant is largely independent of the exact properties of the diamond and the surface termination. On the other hand, in the other electron transfer process known as 'inner-sphere', *e.g.* for $Fe(CN)_6^{3-/4-}$, the reactions occur only through specific interactions with the electrode surface itself. The kinetics in this case on diamond is very sensitive to the surface chemistry and microstructure and phase purity of the electrode used[24, 25]. Diamond electrodes have attracted considerable interests for the purification of water and destruction of pollutants [26-28]. They have also attracted interests in electroanalysis as discussed below.

1.4 Electroanalysis using diamond electrodes

Many electrochemical investigations at the diamond electrode surface have been

concerned with its potential for electroanalytical use. With a fairly low capacitive current, diamond electrodes can produce an enhanced signal-to-noise ratio (S/N), which is directly correlated with the detection limit, especially at low concentrations of target analytes. The wide potential window also opens new opportunities for some applications requiring higher potentials that cannot be accomplished with other conventional electrode materials. Moreover, diamond presents low adsorption of contaminating species thereby appearing more resistive against the surface fouling. Unlike glassy carbon and other similar electrodes, diamond shows higher reproducibility without any essential regenerative treatment[17].

Diamond electrodes are broadly applied in amperometric detection in conjunction with other techniques such as electrophoresis, liquid chromatography and flow-injection analysis. For example, the detection limit for ascorbic acid, dopamine and 4-methylcatechol on a diamond electrode is comparatively lower than that achieved on its glassy carbon counterpart[17]. Cvačka *et al* reported the application of using boron-doped diamond microelectrodes in capillary electrophoresis for electrochemical detection of various analytes[29]. The diamond microelectrodes exhibited an extremely low background current (~ 100 pA) and noise level (~ 3 pA) without any pre-treatment along with precise detection limits for both catechol (2.6 fmol) and dopamine (1.7 fmol) respectively. Ivandini *et al* explored using liquid chromatography for the simultaneous detection of purine and pyrimidine at highly boron-doped diamond electrodes[30]. Those electrodes showed exceptionally high reproducibility as no fouling effect was observed. Low detection limits and well-resolved separation of various analytes were obtained at anodically oxidised surfaces, suggesting promising prospects for this electrode in biological analysis. A flow-injection analysis can also be combined with detection at

diamond electrodes for the determination of thiols, disulfides[31], sulfa-drugs[32] and some other compounds as reported. Moreover, owing to the outstanding resistance against corrosion exhibited by diamond electrodes, they are highly applicable in the stripping voltammetry technique, which is broadly applied for determining trace hazardous metal ions in drinkable water and food products. Detection limits of a few ppb can be achieved for Zn[33], Cd[34], and Pb[35] ions in solutions.

1.5 Modifications of diamond electrode

Although various advantageous properties have been demonstrated using diamond as the electrode material, it also has disadvantages as it does not drive all electrochemical reactions of interest. Also, its electrochemical selectivity can be low. To overcome these flaws, diamond surfaces can be effectively modified by plasma, chemical and electrochemical means, and by depositing or incorporating foreign materials such as metals, metal oxides and other thin films.

Some success has been achieved by binding enzymes to the surface to impart catalytic activity and selectivity. Notsu *et al* have reported using tyrosinase-modified boron doped diamond (BDD) electrodes for the determination of phenol and its derivatives[36]. The resulting modified electrode was very sensitive to target analytes and effectively alleviated the interfering effects from oxygen assigned to higher oxygen overpotentials achieved on such surface. Tatsuma *et al* studied the adsorption of heme undecapeptide and horseradish peroxidase (HRP) on diamond[37]. The modified electrode exhibited much less sensitivity against other interfering species such as ascorbic acid and uric acid, showing promising properties for the application to oxidase-based biosensors. Moreover, a broad range of organic molecules (*e.g.* amines, chlorines

and thiols) has been introduced to modify the diamond surface through photochemical process[38, 39]. Metallic nanoparticles such as Pt, Pd, Ag, Au and Cu can be electrodeposited onto the diamond surface to exploit higher catalytic activity of such particles, but with smaller concentrations compared to conventional bulk material[40]. Apart from these metallic deposits, some thin metal oxide films such as hydrous ruthenium oxide[41], hydrous iron oxide[42], zinc oxide[43] and tin oxide[44] *etc.* can also be effectively decorated onto the diamond surface and such modifications enable the surface to have distinctive features for specific electroanalysis. For instance, electrodeposited TiO_2 showed great photocatalytic activity for ethanol oxidation with a fairly low starting potential of 0.1 V *vs.* SCE, suggesting its promising aspects in relevant fuel cell applications[45]. When immobilised on the boron-doped diamond surface, iridium oxide exhibited optimistic electrocatalytic activity[46].

1.6 Rare earth oxide and praseodymium oxide (PrO_x)

During the recent decades, studies have been dedicated to discovering promising catalyst candidates in heterogeneous and electrocatalysis applications. Metals such as Pt has been proved for their excellent catalytic properties[47, 48] as stated earlier. However, they are vulnerable to the fouling and poisoning of the surface and suffer high prices. Rare earth oxides exhibit various characteristic features and properties, which make them attractive as alternative candidates in oxidation catalytic studies[49].

Among all the rare earth oxides, cerium oxide (CeO_2) was widely investigated and reported for its broad applications in a rich variety of electrochemical sensing. In contrast to most other rare earth oxide materials, whose trivalent oxidised state is confirmed as most stable[50], the fourth ionisation potential is more favourable for

cerium oxide[51]. The stoichiometric cerium oxide has a fluorite structure, which allows the rapid diffusion of oxygen atoms resulting in a high oxygen storage capacity[52]. In general analytical applications, cerium oxide is likely to be reduced to several non-stoichiometric phases, representing the oxygen-deficient states. With the co-existence of abundant oxygen vacancies, the mobility of oxygen atoms is enhanced, allowing this oxide material to play an active catalytic role[53].

Praseodymium oxide (PrO_x) possesses some similarities to CeO_2. It has the same physical fluorite structure, exhibiting high electrical conductivity which is assigned to the variation of ionic valence between Pr^{3+} and Pr^{4+} states[54] and its oxygen deficiencies. There are various limited reports [55-57] concerning its catalytic action, electrocatalytic action and catalyst promoter activity, which suggest applications competitive with CeO_2 could emerge for this material.

1.7 Aims and scope of this thesis

This thesis is broadly concerned with examining some new aspects of the electrochemical applications of diamond, including properties of diamond interfaces modified with PrO_x.

Chapter 2 introduces the experimental theories and techniques used in the projects. It explains the basic principles underlying electrochemical processes, and describes the characterisation techniques (*i.e.* XPS, SEM, and DLS) used.

Chapter 3 mainly focuses on the electrochemical investigations of synthesised heteroepitaxial (001) boron-doped single crystal diamond. The majority of diamond

electrodes used are polycrystalline/nanocrystalline in nature, and this brings several problems associated with pronounced heterogeneity across the surface in electrochemical activity, due to boron concentration fluctuations, sp^2 carbon, and defective material at grain boundaries, all of which may detract from performance. Homoepitaxially grown single crystal diamond is impractical to produce as an electrode material. The aim of this chapter was to compare heteroepitaxial single crystal diamond, a more practically useful material, with its homoepitaxial and polycrystalline counterparts.

Chapter 4 aims to explore diamond electrodes modified with Pt and PrO_x for the oxidation of methanol. In particular an aim is to identify if electrochemically deposited PrO_x can be effectively used as a catalyst promoter in such systems.

Chapter 5 studies an alternative application of the PrO_x-Pt/BDD structures noted above in biological systems for NO detection since NO is of interest as a neurotransmitter[58], immune system mediator[59], messenger molecule[60] and endothelium-derived relaxing factor (EDRF)[61] in physiological and psychological systems. This chapter aims to investigate whether the modified electrode can optimise the NO electrochemical detection, especially for achieving better selectivity against interfering compounds without harming the sensitivity.

Chapter 6 studies the electrochemical properties of deposited PrO_x thin film, without any incorporation of metallic Pt nanoparticles introduced in previous chapters. Several mediators with various charging states are measured to investigate the interactions between the modified surface and analytes. The aim is to understand electrochemical

interactions involving PrO_x coated electrodes.

Chapter 7 introduces the alternative surface modification of decorating carbon black (CB) onto BDD substrates for the electrochemical detection of riboflavin (Vitamin B2, VB2). Several factors that may affect the redox reaction of VB2, *e.g.* immersion time, homogeneity of CB coverage are explored. The modified electrode is also studied for its feasibility in simultaneous detection along with other vitamin species such as folic acid (Vitamin B9) and ascorbic acid (Vitamin C) in the complex system.

Chapter 8 extends the research on Pt/BDD electrodes to the electrochemical oxidation of NO_2^-. As another NO_x derivative, NO_2^- is frequently found as a pollutant or contaminant in the environment and food industries[62, 63].

References

[1] P.W. May, Philosophical Transactions of the Royal Society of London. Series A: Mathematical, Physical and Engineering Sciences 358 (2000) 473-495.

[2] http://en.wikipedia.org/wiki/Diamond.

[3] J.E. Field, The properties of natural and synthetic diamond, Academic Press, 1992.

[4] F.P. Bundy, Physica A: Statistical Mechanics and its Applications 156 (1989) 169-178.

[5] W.G. Eversole, Synthesis of diamond, US Patents 3030188, 1962.

[6] B.V. Derjaguin, D.V. Fedoseev, V.M. Lukyanovich, B.V. Spitzin, V.A. Ryabov, A.V. Lavrentyev, J. Cryst. Growth 2 (1968) 380-384.

[7] J.C. Angus, H.A. Will, W.S. Stanko, J. Appl. Phys. 39 (1968) 2915-2922.

[8] D.J. Poferl, N.C. Gardner, J.C. Angus, J. Appl. Phys. 44 (1973) 1428-1434.

[9] S. Matsumoto, Y. Sato, M. Tsutsumi, N. Setaka, J. Mater. Sci. 17 (1982) 3106-3112.

[10] S. Matsumoto, Y. Sato, M. Kamo, N. Setaka, Jpn. J. Appl. Phys. 21 (1982) L183-L185.

[11] M. Kamo, Y. Sato, S. Matsumoto, N. Setaka, J. Cryst. Growth 62 (1983) 642-644.

[12] R.G. Compton, J.S. Foord, F. Marken, Electroanalysis 15 (2003) 1349-1363.

[13] F. Montilla, P. Michaud, E. Morallon, J. Vazquez, C. Comninellis, Electrochim. Acta 47 (2002) 3509-3513.

[14] F. Okino, H. Shibata, S. Kawasaki, H. Touhara, K. Momota, M. Nishitani-Gamo, I. Sakaguchi, T. Ando, Electrochem. Solid-State Lett. 2 (1999) 382-384.

[15] F.L. Qiu, R.G. Compton, F. Marken, S.J. Wilkins, C.H. Goeting, J.S. Foord, Anal. Chem. 72 (2000) 2362-2370.

[16] C. Goeting, F. Marken, A. Gutierrez-Sosa, R. Compton, J. Foord, New Diamond Front. Carbon Technol. 9 (1999).

[17] Y.V. Pleskov, Russ. J. Electrochem. 38 (2002) 1275-1291.

[18] S. Ferro, A. De Battisti, Anal. Chem. 75 (2003) 7040-7042.

[19] T. Tshepe, J.F. Prins, M.J.R. Hoch, Diamond Relat. Mater. 8 (1999) 1508-1510.

[20] G.M. Swain, R. Ramesham, Anal. Chem. 65 (1993) 345-351.

[21] J.H.T. Luong, K.B. Male, J.D. Glennon, Analyst 134 (2009) 1965-1979.

[22] N. Vinokur, B. Miller, Y. Avyigal, R. Kalish, J. Electrochem. Soc. 143 (1996) L238-L240.

[23] M.C. Granger, M. Witek, J. Xu, J. Wang, M. Hupert, A. Hanks, M.D. Koppang, J.E. Butler, G. Lucazeau, M. Mermoux, Anal. Chem. 72 (2000) 3793-3804.

[24] N. Maleki, A. Safavi, F. Tajabadi, Anal. Chem. 78 (2006) 3820-3826.

[25] P. Chen, R.L. McCreery, Anal. Chem. 68 (1996) 3958-3965.

[26] D. Li, J. Qu, J. Environ. Sci. 21 (2009) 713-719.

[27] J. Iniesta, P. Michaud, M. Panizza, G. Cerisola, A. Aldaz, C. Comninellis, Electrochim. Acta 46 (2001) 3573-3578.

[28] D. Gandini, E. Mahé, P.A. Michaud, W. Haenni, A. Perret, C. Comninellis, J. Appl. Electrochem. 30 (2000) 1345-1350.

[29] J. Cvačka, V. Quaiserova, J. Park, Y. Show, A. Muck, G.M. Swain, Anal. Chem. 75 (2003) 2678-2687.

[30] T.A. Ivandini, K. Honda, T.N. Rao, A. Fujishima, Y. Einaga, Talanta 71 (2007) 648-655.

[31] N. Spătaru, B.V. Sarada, E. Popa, D.A. Tryk, A. Fujishima, Anal. Chem. 73 (2001) 514-519.

[32] T.N. Rao, B.V. Sarada, D.A. Tryk, A. Fujishima, J. Electroanal. Chem. 491 (2000) 175-181.

[33] E.A. McGaw, G.M. Swain, Anal. Chim. Acta 575 (2006) 180-189.

[34] C.E. Banks, M.E. Hyde, P. Tomčík, R. Jacobs, R.G. Compton, Talanta 62 (2004) 279-286.

[35] A. Manivannan, D.A. Tryk, A. Fujishima, Electrochem. Solid-State Lett. 2 (1999) 455-456.

[36] H. Notsu, T. Tatsuma, A. Fujishima, J. Electroanal. Chem. 523 (2002) 86-92.

[37] T. Tatsuma, H. Mori, A. Fujishima, Anal. Chem. 72 (2000) 2919-2924.

[38] T. Strother, T. Knickerbocker, J.N. Russell, J.E. Butler, L.M. Smith, R.J. Hamers, Langmuir 18 (2002) 968-971.

[39] J.B. Miller, Surf. Sci. 439 (1999) 21-33.

[40] J.-S. Gao, T. Arunagiri, J.-J. Chen, P. Goodwill, O. Chyan, J. Perez, D. Golden, Chem. Mater. 12 (2000) 3495-3500.

[41] K.J. McKenzie, F. Marken, Electrochem. Solid-State Lett. 5 (2002) E47-E50.

[42] K.J. McKenzie, D. Asogan, F. Marken, Electrochem. Commun. 4 (2002) 820-824.

[43] A. Chatterjee, J. Foord, Diamond Relat. Mater. 15 (2006) 664-667.

[44] M. Hyde, A.J. Saterlay, S.J. Wilkins, J.S. Foord, R.G. Compton, F. Marken, J. Solid State Electrochem. 6 (2002) 183-187.

[45] A. Manivannan, N. Spataru, K. Arihara, A. Fujishima, Electrochem. Solid-State Lett. 8 (2005) C138-C140.

[46] I. Duo, P.A. Michaud, W. Haenni, A. Perret, C. Comninellis, Electrochem. Solid-State Lett. 3 (2000) 325-326.

[47] M. Valden, X. Lai, D.W. Goodman, Science 281 (1998) 1647-1650.

[48] P.N. Rylander, Catalytic hydrogenation over platinum metals, Academic Press New York, 1967.

[49] M.P. Rosynek, Catal. Rev. - Sci. Eng. 16 (1977) 111-154.

[50] L. Marsella, V. Fiorentini, Phys. Rev. B 69 (2004) 172103.

[51] N. Haraguchi, Y. Okaue, T. Isobe, Y. Matsuda, Inorg. Chem. 33 (1994) 1015-1020.

[52] C.T. Campbell, C.H.F. Peden, Science 309 (2005) 713-714.

[53] S. Fabris, G. Vicario, G. Balducci, S. de Gironcoli, S. Baroni, J. Phys. Chem. B 109 (2005) 22860-22867.

[54] S. Chi Tsang, C. Bulpitt, Sens. Actuators, B: Chem. 52 (1998) 226-235.

[55] K. Asami, K.-i. Kusakabe, N. Ashi, Y. Ohtsuka, Appl. Catal., A: Gen 156 (1997) 43-56.

[56] Q. He, S. Mukerjee, S. Parres-Esclapez, A. Bueno-Lopez, J. Appl. Electrochem. 41 (2011) 891-899.

[57] W. Wang, P. Lin, Y. Fu, G. Cao, Catal. Lett. 82 (2002) 19-27.

[58] M.G. Belvisi, C. David Stretton, M. Yacoub, P.J. Barnes, Eur. J. Pharmacol. 210 (1992) 221-222.

[59] C. Bogdan, Nat. Immunol. 2 (2001) 907-916.

[60] E.M. Schuman, D.V. Madison, Science 254 (1991) 1503-1506.

[61] R. Palmer, A. Ferrige, S. Moncada, Nature (1987).

[62] M.J. Moorcroft, J. Davis, R.G. Compton, Talanta 54 (2001) 785-803.

[63] L. Jiang, R. Wang, X. Li, L. Jiang, G. Lu, Electrochem. Commun. 7 (2005) 597-601.

Chapter 2

Experimental Theories and Techniques

2.1 Introduction

In this thesis, electrochemistry is employed to modify electrodes using the electrodeposition method and to characterise the electrochemical properties in a range of systems using cyclic voltammetry (CV), chronoamperometry, square-wave voltammetry (SWV), scanning electrochemical microscopy (SECM) and electrochemical impedance spectroscopy (EIS). Relevant background, theories and methods will be explained. Theories of various other characterisation techniques will also be briefly introduced. In particular, X-ray photoelectron spectroscopy (XPS) is utilised to determine the elemental composition of the modified electrode, scanning electron microscopy (SEM) is employed for surface morphology and particle microstructure investigation and dynamic light scattering (DLS) is mainly used in measuring the surface charge of the nanoparticles or suspension.

2.2 Electrochemical characterisation

2.2.1 Overview

Electrochemistry is concerned with the study of charge transfer across an interface, most commonly a solid electrode - conductive solution interface, which accompanies chemical change represented by the oxidation or reduction of chemical species. This field is important, since it has applications in wide areas from corrosion and battery technology to fuel cells, electrocatalysis, electrochemical production of bulk chemicals, and chemical sensing[1]. Here, the basic principles of electrochemistry will be explained and discussed with reference to their utility for understanding electrochemical reactions.

2.2.2 Electrochemical cells

In electrochemical systems there is an interface between different phases, typically the electrode as the solid phase and the electrolyte as the liquid phase. As the transport of charge is attributed to the movement of electrons, it requires both electrode and electrolyte to be conductive. Some typical electrodes used in electrochemical reactions are Pt, Au, diamond, glassy carbon and graphite *etc.* The most frequently used electrolytes are aqueous solutions of ionic salts such as nitrate, chloride and sulphate, which also may contain redox active species. However, non-aqueous conductive solutions are also employed.

If a single electrode is inserted in such a solution, electrons will tend to move from one phase to the other so as to equalise the electrochemical potential until equilibrium is established, with a characteristic potential drop across the interface. This latter quantity cannot be easily determined, but if two electrodes are utilised, a high impedance voltmeter can readily measure the difference between these two potential drops, as the potential difference between the two conductive electrode materials. This gives rise to the concept of a simple electrochemical cell, the potential difference of which will be defined by the chemical reactions (so-called half reactions) occurring at two electrodes.

If the potential of one electrode within this two-electrode cell is kept constant, it can act as a reference electrode. This enables the potential of the other electrode to be measured with respect to this reference electrode. As is universally accepted, the *standard hydrogen electrode* (SHE) is the primary reference in electrochemical measurements[2] as shown below.

$$H^+(1\text{M}, aq)/H_2(1\text{ atm})/Pt(s) \quad 2.1$$

Although the free energy change of the chemical reaction associated with SHE corresponds to a potential of +4.44 ± 0.02 V at 25 °C[3], by convention, the potential of the SHE is defined as 0 V. In practical experiments, potentials are actually measured with respect to reference electrodes other than the SHE, as the SHE is not a convenient electrode to use. One well-known reference in wide use is the *silver-silver chloride electrode* with a potential of 0.197 V against SHE,

$$(Ag/AgCl)/KCl\ (saturated) \quad 2.2$$

A useful alternative is the *saturated calomel electrode* (SCE), having a potential of 0.242 V *vs.* SHE:

$$(Hg/Hg_2Cl_2)/KCl\ (saturated) \quad 2.3$$

Typically, reference electrodes are incorporated into two-electrode electrochemical cells comprising a working electrode (WE), conductive electrolyte, and a reference electrode, all connected to an electrical circuit. The measurement of the potential at the working electrode can be made with respect to the potential recorded at the reference electrode. Equilibrium electrochemistry is widely discussed in the field of inorganic chemistry to describe the stability of differing oxidation states in chemical systems and gives rise to the general field of potentiometry.

The behaviour of electrochemical cells when current is flowing through them is of even greater interest. For example, how does the potential difference across a battery relate to the current that is drawn from it? This gives rise to the concept of dynamic electrochemistry, the study of electrochemical cells during conditions of current flow. Again, this could be investigated in the two-electrode system outlined above. However the results would be hard to interpret since the performance of the cell would have a

sensitive dependence on the chemical processes taking place at each of the electrodes, coupled to the movement of charge in the connecting electrolyte. Modern research in electrochemistry is therefore typically carried out in an electrochemical cell comprising three electrodes as shown in **Figure 2.1,** with the addition of a counter electrode (CE)[1]. In brief the working electrode of interest is immersed in a conductive background electrolyte containing the redox species of interest. A current is then driven through the circuit comprising the WE and the CE, and the potential difference is measured between the WE and the RE under conditions of *zero* current flowing to the RE[2]. This is readily achieved using a potentiostat. If conducted correctly, the output of the experiment is a measurement of how the current flow at the WE is intimately linked to the chemistry and transport processes occurring in the vicinity of the WE and the potential drop occurring in this interfacial region. This fundamental knowledge can then be used in the design and development of more complicated electrochemical systems.

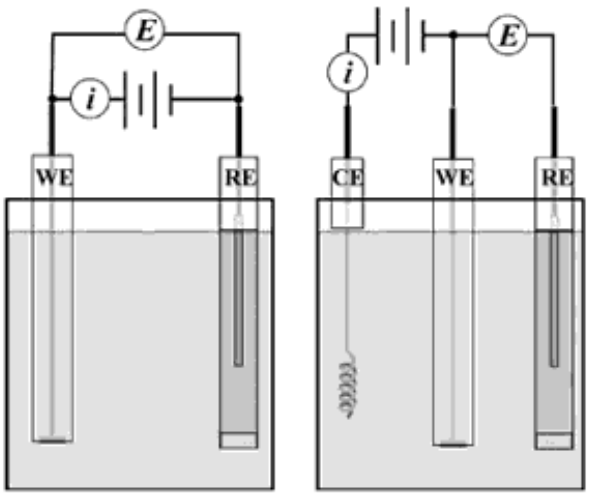


Figure 2.1 A schematic presentation of two-electrode (left) and three-electrode (right) electrochemical cells[1].

2.2.3 Faradaic and Non-Faradaic processes

In an electrochemical cell, there may be two types of current flowing at the same time. Currents which come from the oxidation or reduction of chemical species are defined as the faradaic currents as described below:

$$\frac{dQ}{dt} = \frac{d}{dt}(nFN) = nF\frac{dN}{dt} \qquad 2.4$$

where Q (C) is the charge passed through the cell, t (s) is the time, n is the number of transferred electrons involved in the oxidation or reduction of the chemical species of interest, F is the *Faraday* constant and N is the number of moles of the species in the cell. If oxidation and reduction are occurring simultaneously, then the net current flowing will be the difference between these two current sources. The faradaic current flowing at the WE described previously will normally depend on the potential applied, the electrode reaction kinetics and the supply of reacting chemical species to the electrode-electrolyte interface where the redox process takes place.

However non-faradaic currents also flow since the electrode-electrolyte interface corresponds to an electrical capacitor. As a consequence, charges builds up gradually as the potential drop across the interface changes, corresponding to a measured current flow in the external circuit. The electrical double layer which gives rise to the charge separation involved in this capacitance has a distinct and fairly well-understood chemical structure as shown in **Figure 2.2**. The first layer in this structure comprises both adsorbed ions and solvent molecules with electrical centres within the so-called *inner Helmholtz plane* (IHP), lying at the distance of χ_1 from the electrode surface. Charged species within this region are rigidly adhered to the electrode surface through chemical bonds. For example if the electrode surface has acidic groups on it, these will tend to dissociate at high pH, giving rise to a negative surface charge. Also, ions in

solution may become attracted to a charged surface. The second layer purely consists of solvated ions which are attached to the electrode because of the electrostatic fields which exist there. As the ions are almost completely surrounded by other solvent molecules in the solution, they may not be able to approach closer than a certain distance, χ_2. Compared with the first layer, in this case, the locus of the electrical centres is defined as the boundary of the *outer Helmholtz plane* (OHP). Due to charge conservation, the net charge in the inner and outer Helmholtz planes needs to be balanced by a net opposite charge distribution in the solution. Whilst in the solution phase, these balancing charged species will tend to be attracted to the electrode by electrostatic attraction, so will form a diffuse layer close to the electrode. The thickness of this 3D diffuse region will be a function of the electrostatic forces present, the thermal motion of the molecules concerned and the electrical screening properties of the electrolyte, as for example determined by the ionic strength[4].

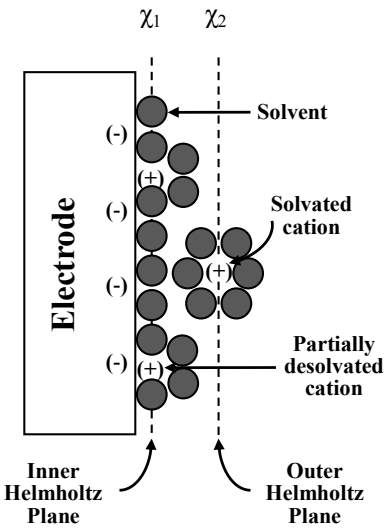


Figure 2.2 The electrical double layer on electrode/electrolyte interface[3]

2.2.4 The fundamental theories of electrochemistry

2.2.4.1 Electrochemical equilibrium, *Nernst* equation and *Gibbs* free energy

At equilibrium, where no current flows and constant potential is achieved, it is of interest to understand how the potential on the electrode relates to the concentration of chemical species in the cell. This is the purpose of the *Nernst* equation. Let the following reaction be considered.

$$O + ne^- \rightleftharpoons R \qquad 2.5$$

O is the oxidised species, R is the reduced species and n is the number of electrons exchanged in this reduction reaction. If the normal logarithmic free energy relationship between the activity of O species and R species and their chemical potential is adopted, the *Nernst* equation can be presented as below:

$$E = E^0 + \frac{RT}{nF}\ln\frac{a_O}{a_R} \qquad 2.6$$

where E^0 is the standard electrode potential defined as the electrode potential when the activity of O -species and R -species is unity, R is the ideal gas constant (8.314 J K^{-1} mol^{-1}), T is the *Kelvin* temperature, n is the number of electrons involved in the redox reaction, and F is the *Faraday* constant (9.6485 × 10^4 C mol^{-1}). The variables a_O and a_R are the activity of oxidised and reduced species, respectively. If the effects of non-ideality are ignored, the activity can be replaced by concentration terms (*i.e.* c_O and c_R).

2.2.4.2 Reaction rates and current in electrochemistry

The *Nernst* equation above readily predicts how the potential difference developed by electrochemical cells under conditions of *zero* current flowing relates to the concentration of chemical species which are present. However an understanding of the reaction kinetics of the underlying chemical processes, along with mass transport effects

in the cell is needed if the behaviour of the cell under conditions of chemical change, *i.e.* current flow is to be understood.

If no current flows at an electrode when the applied potential drop between the electrode and electrolyte is E_{eq}, then a quantity known as the overpotential (η) can be defined as the extent that the actual potential E exceeds E_{eq} as shown below:

$$\eta = E - E_{eq} \qquad 2.7$$

One fundamental aim of dynamic electrochemical theories is thus to explain how the current flowing relates to the applied overpotential.

2.2.4.3 *Butler-Volmer* Equation

The *Butler-Volmer* equation is a simple phenomenological model to explain the relevant behaviour. It is based on the idea that the reactant at the electrode is required to cross an energy barrier to be converted into reaction products, the magnitude of which will depend on the applied potential. Using transition state theory, the behaviour of reaction kinetics can thus be predicted. If we consider again the simple reaction in equation 2.5, it can be re-expressed as follows (n = 1 is generally assumed in *Butler-Volmer* equation):

$$O + e^- \overset{k_f}{\rightarrow} R \qquad 2.8$$

$$R \overset{k_b}{\rightarrow} O + e^- \qquad 2.9$$

where k_f (cm s^{-1}) and k_b (cm s^{-1}) are the rate constants for the forward (reduction) reaction (k_f) and backward (oxidation) reaction (k_b), respectively. The overall current i (A) can be predicted by the *Butler-Volmer* equation as the difference between the cathodic (reduction) and anodic (oxidation) reactions, which are presented as i_c and i_a

respectively in the equation below:

$$i = i_c - i_a \tag{2.10}$$

Both i_c and i_a are proportional to the respective rate constants and the concentration of the reacting species at the electrode surface as follows:

$$i_c = FAk_f C_O(0,t) \tag{2.11}$$

$$i_a = FAk_b C_R(0,t) \tag{2.12}$$

where F is the *Faraday* constant, A (cm^2) is the electrode area and $C_j(0,t)$ (mol cm^{-3}) is the concentration of species j measured at the electrode at the time t (s). The rate constants of the forward and backward reactions can be explained as a function of the standard heterogeneous rate constants, k^0 (cm s^{-1}) and the applied overpotential according to the following expressions:

$$k_f = k^0 e^{-\alpha f(E-E^{0\prime})} \tag{2.13}$$

$$k_b = k^0 e^{(1-\alpha) f(E-E^{0\prime})} \tag{2.14}$$

where α is known as the transfer coefficient which is usually estimated as 0.5 and $f = nF/RT$; α relates to where the transition state is located along the reaction coordinate, and this tends to be midway between reactants and products.

Based on the above equations, the net current flow at the electrode for an applied potential E can be described.

$$i = FAk^0\left[C_O(0,t)e^{-\alpha f(E-E^{0\prime})} - C_R(0,t)e^{(1-\alpha)f(E-E^{0\prime})}\right] \tag{2.15}$$

This equation predicts how the current flowing at the electrode depends on the applied overpotential and reactant concentrations at the electrode surface. The equation works qualitatively quite well, although quantitative agreement can be poor in view of the simplifications made in the derivation. Nowadays detailed modelling of electrochemical reactions is normally based on modern theories of electron transfer such as *Marcus*

theory and *Marcus-Hush-Chidsey* formalisms[5-9], which are capable of providing real chemical insights as to the huge variation in electrode reaction kinetics which is seen in chemical systems.

2.2.4.4 Equations governing mass transfer

Apart from reaction kinetics, mass transport also has an important effect in controlling the performance of electrochemical cells under dynamic conditions. Since chemical species are created and destroyed at the electrode surface, transport of species within the cell must take place. For example the *Butler-Volmer* equation derived above identifies the current flow as being dependent on the concentration of species at the electrode surface itself, so unless consumed reactants in this region are replenished, no current can be sustained. Mass transport can often be the rate-limiting factor governing the overall behaviour in the cell, since electron transfer is often on a much shorter timescale.

Mass transfer in electrochemical reactions can generally follow three different pathways or combinations of them. These three modes are defined as (1) migration, referring to movement of charged particles in an electric field; (2) diffusion, meaning the movement of species down the concentration gradient; (3) convection, correlating with the movement that may be induced in fluids, associated with density and temperature gradients or stirring operations.

The *Nernst-Planck* equation below correlates the flux of j species to migration, diffusion and convection in a single direction:

$$J_j(x) = -D_j \frac{\partial C_j(x)}{\partial x} - \frac{z_j F}{RT} D_j C_j \frac{\partial \emptyset(x)}{\partial x} + C_j v(x) \quad 2.16$$

$J_j(x)$ (mol cm^{-2} s^{-1}) is a unidirectional flux for species j at a distance of x (cm) from the electrode. D_j (cm^2 s^{-1}), z_j (C) and C_j (mol cm^{-3}) are the diffusion coefficient, the surface charge and the concentration of the species j, respectively. The variable $v(x)$ (cm s^{-1}) is the rate with which a volume element moves in the solution, while $\partial C_j(x)/\partial x$ represents the concentration gradient and $\partial \emptyset(x)/\partial x$ being the potential gradient. In this equation, the different terms are concerned with migration, diffusion and convection, respectively.

In many electrochemical experiments, migration is negligible since the experiments use a high concentration of supporting electrolyte which eliminates the occurrence of electric fields in the bulk solution. Similarly the experiments are carried out in a stagnant solution where convection effects are reduced on short timescales. Under these circumstances the main mode of transport of species to/from the bulk solution is by diffusion down the concentration gradients created by the electrochemical reaction. Two laws of diffusion in solution were proposed by *Fick* to describe the phenomena. *Fick's* first law explains the flux of a species *j*, as a function of the change in the concentration C_j (mol cm^{-3}), at a distance of x (cm) from the electrode surface at time *t* (s).

$$-J_j(x,t) = D_j \frac{\partial C_j(x,t)}{\partial x} \quad 2.17$$

where $J_j(x,t)$ is the flux of the species j while D_j is the diffusion coefficient of the solution. The second law describes the change of concentration as a function of time *t* (s).

$$\frac{\partial C_j(x,t)}{\partial t} = D_j \left(\frac{\partial^2 C_j(x,t)}{\partial x^2} \right) \quad 2.18$$

In many common situations where mass transport is the rate-limiting factor, these laws of diffusion can be employed to understand the electrochemical behaviour. For example, consider a situation where at some time $t = 0$, the potential on an electrode is switched to a large positive value such as to rapidly oxidise species at the surface. As a consequence, the concentration will be depleted at the surface, and a depleted "diffusion" layer will gradually extend into the bulk solution, as the reactant diffuses down the concentration gradient to the electrode surface. *Fick's* laws of diffusion can be used to calculate the reactant flux as a function of time t (s) at the electrode, and hence the current flowing $i(t)$, which is given by the *Cottrell* equation:

$$i(t) = \frac{nFA{D_j}^{1/2}C_j}{\pi^{1/2}t^{1/2}} \qquad 2.19$$

where n is the number of transferred electrons, F is the *Faraday* constant, A (cm^2) is the electrode area, D_j (cm^2 s^{-1}) is the diffusion coefficient of the species j, and C_j is the concentration of species j converted to the electrode. The equation correctly predicts that the current should decay to *zero* with an inverse relationship to the square root of the time, a good example of mass transport limitations. In practice, this behaviour is not precisely observed, due to capacitive charging at short timescale and natural convection at long timescales.

2.3 Electrochemical techniques

2.3.1 Overview

Based on the theoretical principles explained previously, a range of distinct electrochemical methods are used to probe electrochemical reactions. The important methods for this thesis will be briefly described.

2.3.2 Potential Sweep Techniques

2.3.2.1 Principles

The potential sweep technique is a broadly used method in electrochemical studies. In this technique, the current is recorded while the externally applied potential is changed linearly between two values E_1 and E_2. Normally E_1 is chosen at which no electrochemical activity exists and E_2 is defined as the state where the reaction is mass-transfer controlled.

2.3.2.2 Cyclic voltammetry

2.3.2.2.1 Fundamentals of cyclic voltammetry

Cyclic Voltammetry (CV) is perhaps the most typical potential sweep model, with the scan starting from E_1 towards E_2, before following a reversed direction until stopping at E_1. This represents one cycle of a cyclic voltammogram and multiple scans can be recorded following the same route. CV is almost always selected preferentially to study a new electrochemical system since the method presents a rapid way of assessing the main electrochemical features, which can then be studied in detail using other methods. The waveform and classic voltammogram of CV are shown in **Figure 2.3**.

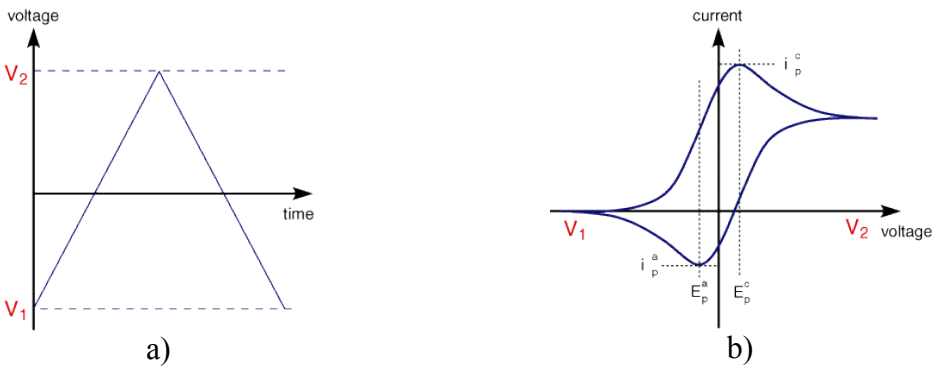


Figure 2.3 a) waveform and b) classic cyclic voltammogram of cyclic voltammetry[10]

CV is used to measure the resulting current passing through the WE in normally a stagnant solution. The applied potential on the working electrode is compared with the reference electrode such as Ag/AgCl or SCE. Kissinger and Heineman[11] suggested this potential could be defined as the *excitation signal*. The voltammogram is then represented as the function of the current against the linearly varied potential where the current is considered as the *response signal* to the *excitation signal*.

2.3.2.2.2 Characterisation of cyclic voltammetry

In a cyclic voltammogram, the magnitudes of the anodic peak potential (E_{pa}) and cathodic peak potential (E_{pc}) along with relevant anodic peak current (i_{pa}) and cathodic peak current (i_{pc}) are important parameters. In a redox couple reaction, if both species exchange electrons with the working electrode very fast, this system can be considered as electrochemically reversible. The formal potential (E^0) in this case is presented as below, centring between E_{pa} and E_{pc}:

$$E^0 = \frac{E_{pa} + E_{pc}}{2} \qquad 2.20$$

The peak-peak potential separation (ΔE_{pp}) between E_{pa} and E_{pc} is dependent on the electrons exchanged in the electrochemically reversible reactions and can be expressed as follows:

$$\Delta E_{pp} = E_{pa} - E_{pc} \cong \frac{0.059}{n} \ (at\ 298K) \qquad 2.21$$

where n is the number of transferred electrons. Therefore, for a reversible one-electron transfer, ΔE_{pp} should be about 0.059 V, which is independent of varied scan rates. However if the system is irreversible due to sluggish electron transfer at the electrode surface, the equation above is not applicable and the peak separation will increase. The peak current value can be estimated applying the *Randles-Sevčik* equation:

$$i_p = 0.4463 \frac{n^{3/2} F^{3/2}}{R^{1/2} T^{1/2}} A D^{1/2} C v^{1/2} \quad 2.22$$

or,

$$i_p = 2.69 \times 10^5 n^{3/2} A D^{1/2} C v^{1/2} \quad 2.23$$

As the number of transferred electrons (n), the electrode area (A) and the diffusion coefficient (D) are all constants in a practical experiment, i_p is directly proportional to the concentration of the solution and the square root of the scan rates. If a fixed concentration is used, i_p should be linearly correlated with $v^{1/2}$.

In an electrochemically reversible, diffusion-controlled system, simple and readily identifiable electrochemical behaviour is expected, with regard to the peak heights and peak separations. Complicating features such as adsorption at the electrode surface, or slow reaction kinetics will change the measured variables and the appearance of the voltammograms. As a consequence, a rapid qualitative picture of the dominant electrochemistry can be built up.

2.3.3 Potential step methods - chronoamperometry

The opposite approach to electrochemical systems is to use potential step methods. In potential step methods such as chronoamperometry, the potential is suddenly stepped from a potential where no electrochemical reaction takes place to one where the electrode reaction is driven to mass-transport conditions.[12]. The current-time behaviour is studied as a potential step or multi potential steps are applied. Suppose a species O is electro-inactive at the potential E_1in an electrochemical system and when the electrode potential is stepped down to E_2, the species O can be reduced rapidly following a basic charge transfer reaction.

$$O + e^- \rightarrow R \qquad 2.24$$

Figure 2.4 shows the typical waveform and current response in a chronoamperometric experiment, which as described should lead to a *Cottrell* type current response as noted above. This in principle can enable the determination of diffusion coefficients, number of electrons transferred, and bulk concentrations depending on what variables are known and unknown. In practice, the data tends to be inaccurate when the experiment is carried out at macroelectrodes, but is widely used instead at microelectrodes.

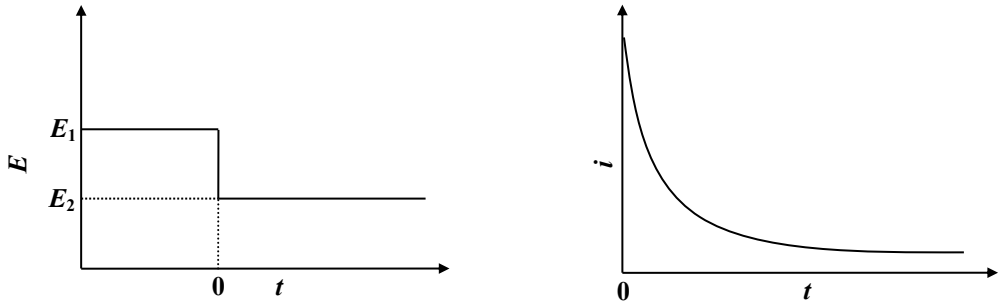


Figure 2.4 a) waveform and b) current response in potential step chronoamperometry[1]

2.3.4 Pulse voltammetry

In electroanalysis, a frequent problem which arises is to detect a small faradaic current in the presence of a large background current, which might arise for example from double layer capacitive charging or unwanted competing faradaic processes. In CV this might prove impossible to pull out the differing contributions. One solution is to use pulse voltammetric methods, where a particular pulsed potential waveform is applied to the electrode and the current flowing is measured at differing times in the programmed cycle.

A common example of this is square wave voltammetry (SWV). In this technique, a potential waveform as shown in **Figure 2.5** is applied. This represents a linear sweep

potential onto which a square wave potential is applied, defined by an amplitude and frequency. The current flowing is measured twice as i_1 and i_2. The first one in the forward part of the pulse is defined as $I_{forward}$ while the second one is termed as $I_{backward}$. The voltammogram is then plotted as a graph of the difference between these two currents as a function of applied potential. SWV offers some advantageous features in electrochemical measurements. In particular it serves to effectively eliminate capacitive background currents, and is thus invaluable in electroanalysis for measuring small signals at low analyte concentrations.

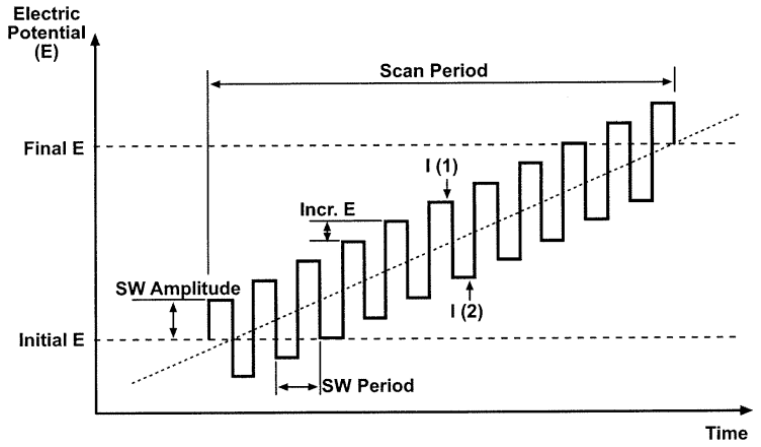


Figure 2.5 The time-potential waveform of SWV (compiled from ref[13])

2.3.5 Rotating disc electrode (RDE)

The methods described above are based on unforced diffusion of reactants to the electrode. Various electrochemical techniques are based on producing controlled forced diffusion of reactants to the electrode. Perhaps the original example of this is based on the rotating disc electrode[1, 2]. A typical RDE consists of a conductive disc in the central area, surrounded by a cylinder made by insulating materials such as PTFE (Polytetrafluoroethylene). A rotating speed ranging from 400 to 10000 rpm is generally applied. Due to friction between the RDE and the solution, the reactants are swept

towards the electrode then thrown outwards, leading to efficient transport to the electrode. The transport limited current (i_l) is presented as the function of the rotating speed ω (rad s^{-1}) as follows:

$$i_l = 0.621nFAD^{2/3}\nu^{-1/6}C\omega^{1/2} \quad 2.25$$

which is known as the *Levich* equation. This is just one example of numerous electrochemical techniques that can be used to enhance the mass transport of reactants to the electrode and hence overcome the limitations of unforced diffusion.

2.3.6 Electrochemical impedance spectroscopy

Electrochemical impedance spectroscopy (EIS), also called dielectric spectroscopy is a powerful technique for making precise measurements on electrochemical systems. In a simple modern faradaic EIS experiment, a small AC signal is applied to the WE in a three-electrode cell. The electrode is held at a potential where faradaic current flows due to the presence of the redox active species of interest in the solution. A frequency response analyser is then used to measure the AC current response which enables the resistance and capacitance of the electrochemical cell at that frequency to be determined. The experiment is repeated across a range of useful frequencies. The analysis of the data involves the design of an equivalent circuit, from knowledge of electrical circuit theory, which would accurately model the measured data.

In **Figure 2.6**, the simplest useful circuit is shown. It involves a so-called series resistance R_s, representing the resistance of the electrolyte and/or electrode in the cell. A second element is R_{ct}, the charge transfer resistance, which corresponds to the occurrence of faradaic processes. A capacitance C_d corresponds to the double layer capacitance, and finally a complex impedance known as the *Warburg* impedance Z_w

represents the resistance to charge transfer arising from mass transport limitations.

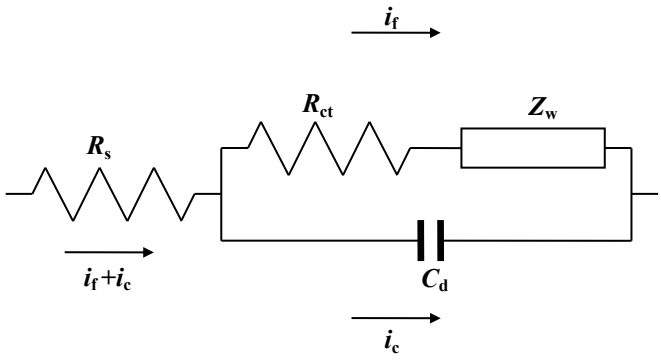


Figure 2.6 The equivalent circuit of a typical reversible electron transfer process[1]

The response of frequency in the cell which follows such an equivalent circle is often presented by plotting $-Z_{Im}$ against Z_{Re} which is known as *Nyquist* plot as shown in **Figure 2.7**.

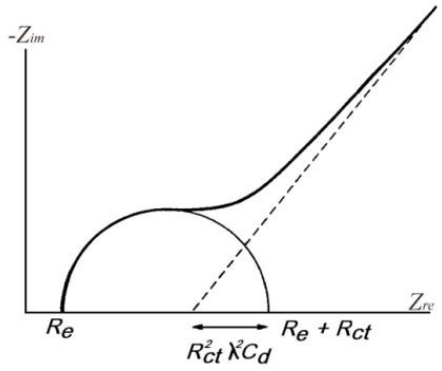


Figure 2.7 *Nyquist* plot of EIS measurement[14]

Data fitting enables precise determination of various kinetic and electrical parameters involving the cell. EIS is at its most powerful when measuring parameters for very well-understood electrochemical systems for which the equivalent circuit is thus well-known. It is more limited in more complex and poorly understood systems where more than one equivalent circuit could give an equally good fit.

2.3.7 Scanning electrochemical microscopy

Scanning electrochemical microscopy (SECM)[2, 15] is one type of scanning probe microscopies (SPM). It is carried out by scanning a tiny ultra-microelectrode (UME) tip across the electrode surface and displaying the ensuing variations in current response in 2D images, thereby mapping electrode activity at an interface. The method is superficially similar to other scanned probe methods such as atomic force microscopy (AFM) in operation. However the image arises in SECM from variations in electrochemical activity rather than for example variations in tip-substrate force of interaction. The lateral resolution tends to be measured in microns rather than the much higher resolution available to other scanned probe methods. Nevertheless, for probing electrochemical inhomogeneity on this length scale, SECM is the ideal method.

Various modes of electrochemical scanning exist in which differing potentials are applied to the WE and the tip to generate and detect electroactive species. For example, in negative feedback mode, the tip current measured is decreased if the tip passes close to an inactive part of the electrode since reactants can no longer diffuse to the tip surface. Conversely, a positive feedback occurs if the tip is close to an active region of the electrode. Much electrochemistry concerning inhomogeneous electrodes uses indirect methods to determine the surface electrochemical inhomogeneity. In contrast, SECM is one of the few direct methods which exist to look at these problems.

2.4 Surface Characterisation Techniques

Surface characterisation techniques are widely applied in this thesis. The mainly used techniques include X-ray photoelectron spectroscopy (XPS), Scanning Electron Microscopy (SEM) and Dynamic Light Scattering (DLS). Each of them is sensitive to

one or more particular surface features. XPS is utilised in surface elemental composition characterisation, SEM focuses on the surface morphology and DLS is applied for particle size determination, usually combined with the measurement using *zeta* potential technique to determine the surface charge of particles simultaneously.

2.4.1 X-ray photoelectron spectroscopy (XPS)

X-ray Photoelectron spectroscopy (XPS), otherwise known as Electron Spectroscopy Chemical Analysis (ESCA), is one of the most popular techniques applied for surface analysis. The photoelectric effect was initially observed by Heinric Hertz[16] in 1887 and then explained by Einstein[17] 18 years afterwards. With these initial efforts, XPS was firstly developed by Kai Siegbahn in 1960s[18] before he was awarded the *Nobel* Prize for his great contribution. With the rapid development in ultra-high vacuum and other complementary techniques, XPS is now applied commercially and broadly.

2.4.1.1 Introduction to XPS

The operation of XPS involves a process in which the electrons are ionised from core atomic orbitals by X-ray irradiation under ultra-high vacuum (UHV) conditions into the vacuum. The X-ray sources normally applied in XPS measurements are Al Kα (1486.6 eV, which is preferentially used in this thesis) and Mg Kα (1253.6 eV). After the material surface is irradiated by X-ray, core level electrons are ejected as photoelectrons as shown in **Figure 2.8** a). The kinetic energy of the ejected photoelectrons E_K can be determined from the following expression:

$$E_K = h\nu - E_B - \Phi_{sp} \qquad 2.26$$

where, $h\nu$ is the photon energy of X-ray source, E_B is the binding energy of the core atomic level, and Φ_{sp} is the spectrometer work function. As shown in **Figure 2.8** b), E_B

is the energy required to excite the bound core electron into the Fermi level.

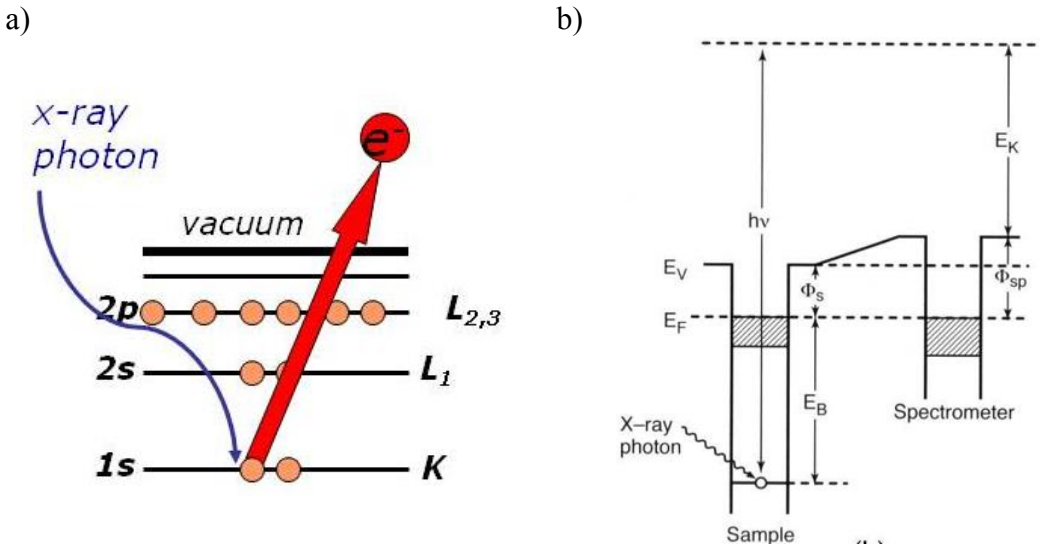


Figure 2.8 a) the photoelectron emission process in XPS b) the different energy levels in XPS[19, 20]

The X-ray photons can penetrate the sample surface to a distance of 1 to 10 μm and activate the photoelectrons. However, it is discovered that most photoelectrons cannot escape from the surface, with only those created in the top layers (< 20 Å) being ejected without energy loss, thus making XPS highly sensitive to the surface. Those electrons which are ejected without energy loss produce the characteristic peaks, while those that undergo inelastic scattering contribute to the background in the XPS spectrum. The electron mean free paths for some common metals[20] are plotted as a function of kinetic energy shown in **Figure 2.9**. It is confirmed that 20 Å is approximately the maximum elastic mean free path under classic XPS measurements, either using Al Kα or Mg Kα sources. The XPS spectrum is obtained by plotting the number of electrons per energy interval as a function of the correlated binding energy or kinetic energy. As described before, XPS can be used to determine the surface elemental composition as each element has unique core electron binding energy enabling the identification of the

emitting atom.

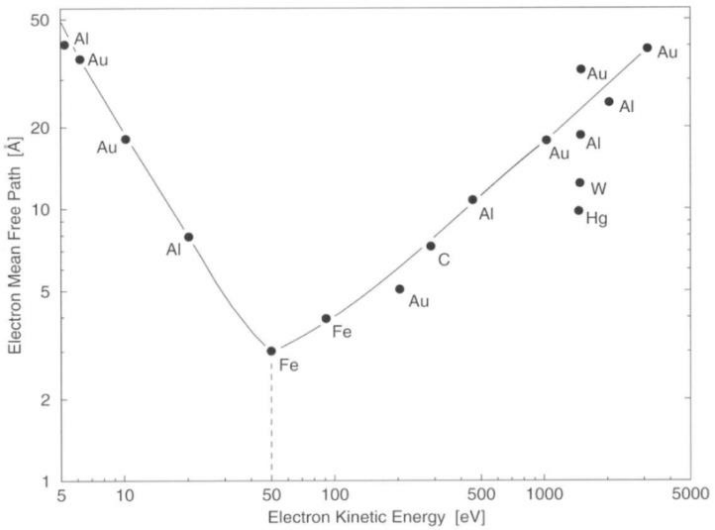


Figure 2.9 Electron mean free paths as a function of electron kinetic energy for several metals, this universal curve presents a minimum 2 - 5 Å at about 50 - 100 eV[20].

2.4.1.2 Important features in XPS

2.4.1.2.1 XPS Instrumentation

XPS measurements in this thesis are carried out using an X-ray photoelectron spectrometer under UHV conditions at 10^{-9} to 10^{-10} Torr. It comprises an X-ray source with Al Kα and Mg Kα twin anodes, a hemispherical energy analyser, and a photoelectron detection system. The XPS apparatus[21] is illustrated in **Figure 2.10**.

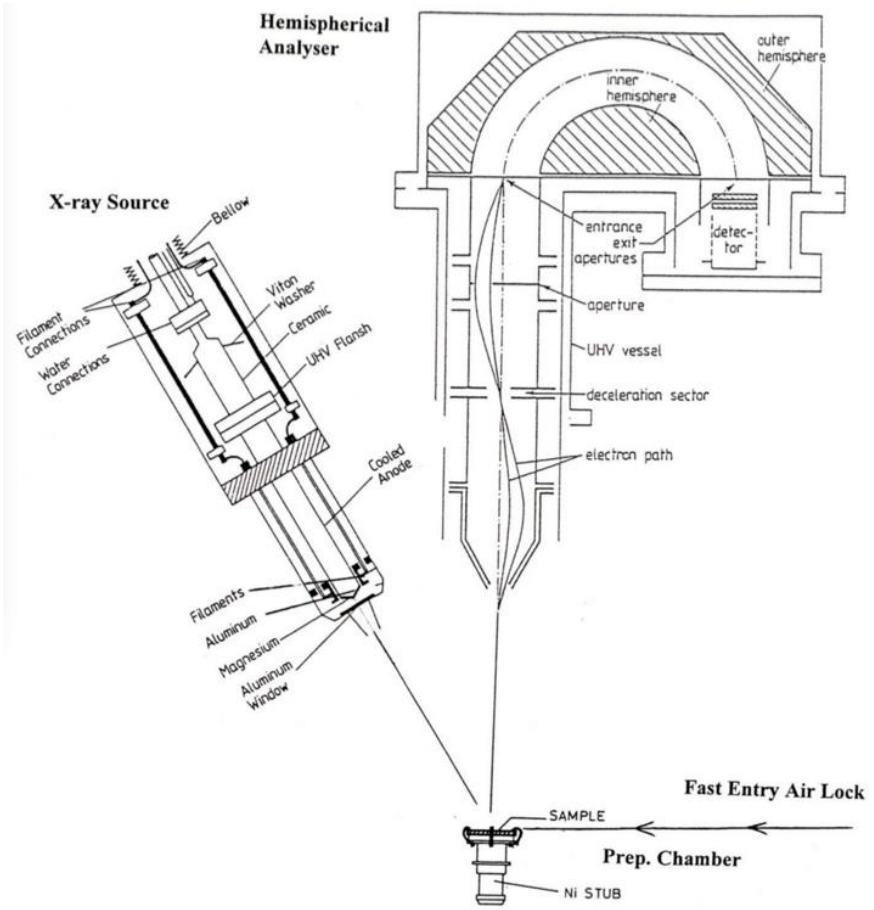


Figure 2.10 the schematic diagram of XPS comprising X-ray source and hemispherical analyser[21].

Figure 2.11 exhibits a typical XPS spectrum of a clean gold sample using Al Kα X-ray source. All the XPS experiments in this thesis were recorded with the Al Kα X-ray source (1486.4 eV) under 10^{-9} Torr. The fixed analyser transmission (FAT) mode was employed. 'Survey' and 'Narrow' scans were conducted with a pass energy of 50 eV and 25 eV, respectively. At least 20 scans were used in 'Narrow' scan for the region of interest. All the XPS data were plotted into CASAXPS software, the standard value of the C 1s peak (284.6 eV)[22] was used in peak calibration before analysis.

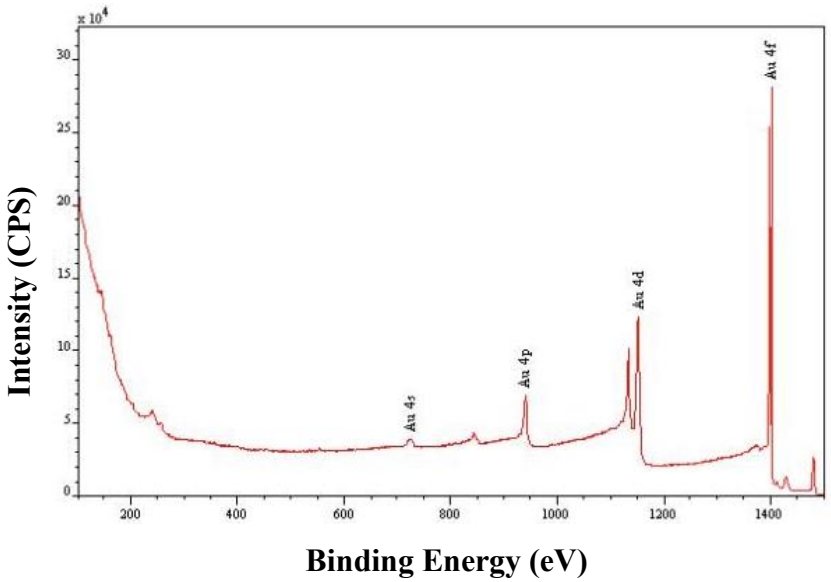


Figure 2.11 XPS spectrum of clean gold sample under monochromatic Al Kα X-ray[23]

2.4.1.2.2 Chemical shift

As noted above, the simple inspection of an XPS spectrum provides a surface elemental analysis since the binding energy of each characteristic peak is associated with an elemental core level. However, a chemical shift is observed in XPS when a small change is seen in the core level binding energy. It can be caused by either initial chemical bonding before the photoelectron ejection or post-photoemission processes *e.g.* relaxation of photoionisation, core hole screening, and polarisation of surrounding ions[20, 24-26]. **Figure 2.12** a) depicts the chemical shifts of the C 1s peak in ethyl trifuoroacetate[20]. There are 4 types of carbon atoms in this molecule structure. The one in the $-CF_3$ group is adjacent to three fluorine atoms along with one R-O-C=O group. All of the above are highly electronegative thus decreasing the electron density around the C. The bonding between the nuclei and 1s electrons is enhanced significantly for this carbon, resulting in the largest shift to higher binding energy. Comparatively, for the carbon atom in C=O group, the electron density is driven by two electronegative groups adjacently, accounting

for a reduced but still high binding energy shift. As for the carbon atoms in the -CH_2 and -CH_3 groups, as there is only one or no electronegative sites nearby, the smallest binding energy shift is observed instead.

2.4.1.2.3 Spin-orbit coupling

Apart from the chemical shift observed in the XPS spectrum, spin-orbit coupling is the other common phenomenon in XPS. Two different spin-orbit states will arise when a core level, other than the *s* orbital, is ionised. Since these states have differing stabilities, they represent varied binding energies. A typical splitting of Au 4f electrons due to spin-orbit coupling is shown in **Figure 2.12** b). As a result of interaction between the orbit l and the spin magnetic momentum, the total angular momentum j can be represented as:

$$j = l + 1/2\,, j' = l - 1/2 \qquad 2.27$$

The ratio of intensity of the electrons is associated with the ratio of the total quantum number and thereby can be represented as:

$$\frac{I_{l+1/2}}{I_{l-1/2}} = \frac{2j+1}{2j'+1} = \frac{l+1}{l} \qquad 2.28$$

a) b)

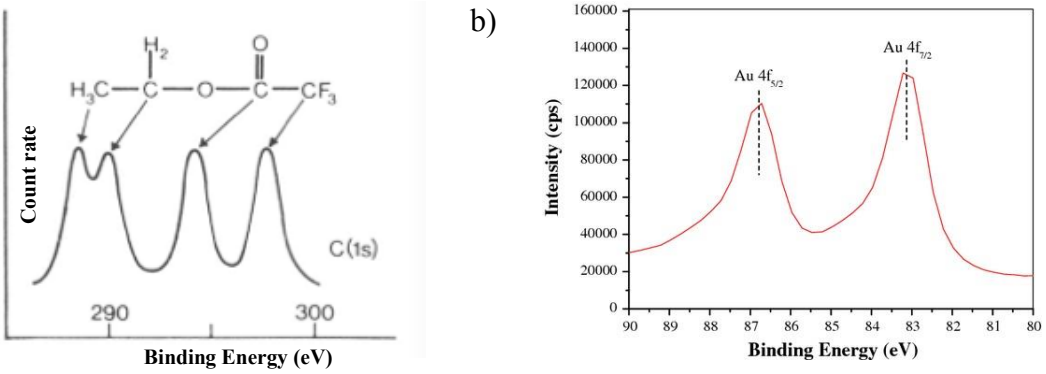


Figure 2.12 a) Chemical shifts of C 1s electrons for ethyl trifluoroacetate. The different chemical shifts can be roughly attributed to the varied electronegative values[20], b) Typical spin-orbit coupling of Au 4f electrons[27].

2.4.1.2.4 The Auger line

In the photoemission spectrum, additional peaks appear which do not have the characteristics of photoemission peaks, in which kinetic energy is independent of the photon energy. Auger lines are the result of a radiation-less relaxation process. An electron from a higher energy level can drop down to fill the vacant core hole; in doing so, energy is released which can cause a further electron, the Auger electron, to be ejected to the vacuum level. The most common types of Auger peaks are KLL, LMM, MNN and NOO series, where the letters denote the three core levels involved. In each series, the first letter represents the shell of initial vacancy after the photoelectron ejection while the latter two indicate the shells of the final vacancy[28]. Auger electron peaks are readily identified since their apparent binding energy shifts when the photon source is changed.

2.4.1.2.5 Satellite peaks

Although the picture presented so far shows that each spin-orbit core level component should produce a single peak, this is oversimplified. The ejected electron can lead to specific electronic excitations in the material, resulting in additional energy loss peaks at higher binding energy. This phenomenon can often be described in terms of a shake-up satellite[20, 29]. Shake-up satellites are observed, for example, due to anti-bonding ($\pi \rightarrow \pi^*$) transition in aromatic molecules. The plasmon loss peaks are prominent in metals when the freed photoelectrons excite plasmons in the metal valence band. As a result, these photoelectrons suffer an energy loss and show a satellite 15-30 eV higher in binding energy against the parent peak[30]. If unpaired electrons exist in the valence shell of the atom, the angular momentum can couple to the core hole created during photoemission giving rise to multiplet splitting. Again a

multiple peak structure will arise.

2.4.1.2.6 Multiplet splitting

Since an electron is freed from the atomic core, an unpaired electron will be left in the core hole. Unpaired electrons existing in the atom can interact with each other, resulting in various final-states with different kinetic energies. Multiplet splitting can be considered as the derivation of the spin-orbit splitting, contributing to the further separation of the doublet into several components asymmetrically.

2.4.1.3 The quantitative analysis of XPS

Apart from identifying qualitatively surface composition and chemical states, a useful aspect of XPS is quantitative elemental composition analysis. In an XPS spectrum from a sample with a uniform composition over the sampling depth, the intensity of a characteristic peak can be described as:

$$I = j\rho\sigma K\lambda \qquad 2.29$$

where j is the flux of photons, ρ is the concentration of atoms, σ is the photonionisation cross-section for photoelectron emission, K refers to instrumental parameters and λ represents the electron attenuation length. Quantitative analysis of XPS data can be achieved by determining the peak area (*i.e.* intensity I_i of a given peak after the subtraction of the background [31]. According to equation 2.29, the elemental concentration in a given sample will be equal to the peak intensity divided by a set of factors which should be constant from sample to sample. These factors are well-known and are tabulated as atomic sensitivity factors (ASF)[32]. The relative elemental proportion N_i is represented as:

$$N_i = \frac{I_i/S_i}{\sum(I_i/S_i)} \qquad 2.30$$

Use of this formula has many assumptions. Especially, it is assumed uniform composition over the XPS sampling depth (5 – 10 nm) and that the spectrometer in use performs in a similar way to the spectrometer which was used to determine the sensitivity factors. Nonetheless, the use of the formula is generally successful as long as excessive precision is not invoked.

2.4.2 Scanning electron microscopy

Scanning electron microscopy is an important technique for producing visual images of samples at a resolution in the 10 nm range which is unobtainable using optical microscopy. A schematic of an SEM is shown in **Figure 2.13**. In brief a high voltage (keV) electron gun is used to focus an electron beam onto the sample. This beam is rastered across the surface, and the secondary electrons which are produced from the interaction of the primary beam with the solid are detected and used to form the image. The result is similar to an optical micrograph of the sample, but at higher resolution. Differing imaging modes, such as the detection of back-scattered electrons, are possible. In addition X-rays are produced when the primary beam impacts the sample and these can be analysed for elemental determination as so-called EDX (energy dispersive X-ray analysis).

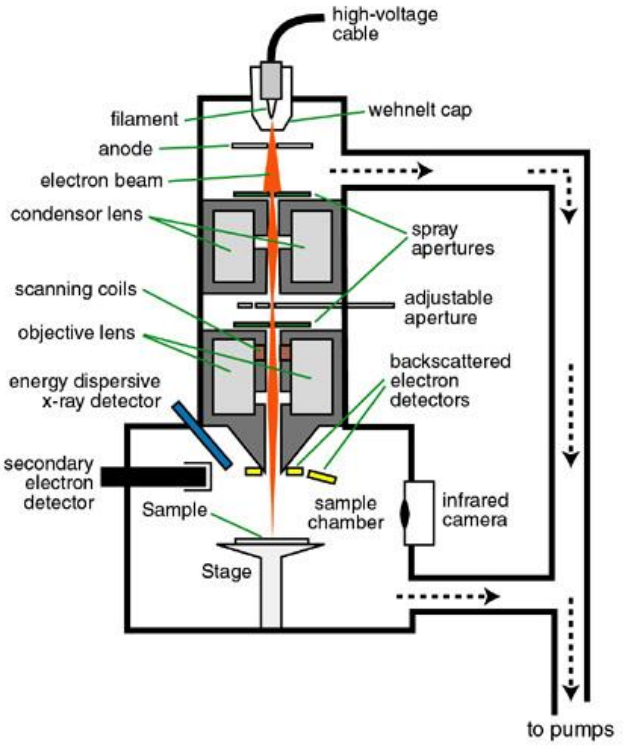


Figure 2.13 Schematic diagram of SEM[33]

2.4.3 Dynamic light scattering combined with *zeta* potential

Dynamic light scattering (DLS), also known as photon correlation spectroscopy or quasi-elastic light scattering, is a technique used to determine the particle size and its distribution in a suspension of particles in liquids. It is based on the light scattering of small solid particles under Brownian motion. Brownian motion refers to the random movement of small particles in the solution, which is attributed to the interaction between these particles and the surrounding fluids[34]. In DLS measurement, the Brownian motion of particles in the suspension results in the applied laser light being scattered at different intensities. The transitional diffusion coefficient can be featured with these fluctuated intensities and thereby the particle size can be determined following the *Stokes-Einstein* relationship[35].

In DLS measurement, the suspension of interest is first put into a cuvette. The monochromatic laser beam and the photon detector are placed at a 90˚ angle. Therefore, the particles undergoing Brownian motion will scatter some light perpendicularly to the laser. The scattered light is captured by the detector, and the optical signals will then be transferred into a correlator, determining the translational diffusion coefficient required for the particle size and distribution analysis. Ultimately, the particle size is calculated from the *Stokes-Einstein* equation and presented by the instrument software. **Figure 2.14** exhibits a typical schematic diagram of a DLS instrument.

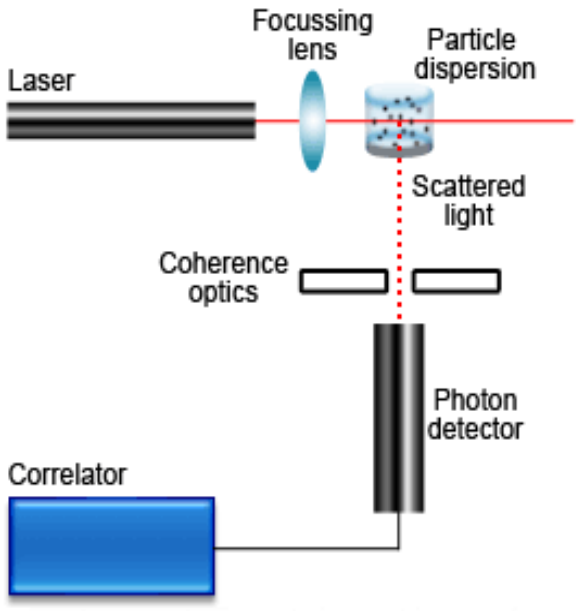


Figure 2.14 Schematic diagram of DLS[36]

Zeta potential is used to describe the potential difference across the diffuse region of the double layer associated with dispersed particles in the colloidal systems. The value of the *zeta* potential is used to understand the interactions between particles in the double layer, indicate the stability of the colloidal suspension, and identify the net charge on colloidal particles. It describes the repulsion between similarly charged particles in the

suspension. Generally, no matter whether the potential is positive or negative, higher values of *zeta* potential always correlate with better stability while lower ones relate with coagulation or flocculation. In this thesis, a Malvern Zetasizer Nano ZS instrument was operated to determine the particle size distribution along with the surface charge simultaneously by combining the *zeta* potential technique into DLS.

References

[1] C.G. Zoski, Handbook of Electrochemistry, Elsevier Science Limited, 2007.

[2] R.G. Compton, C.E. Banks, Understanding voltammetry, World Scientific, 2007.

[3] A.J. Bard, L.R. Faulkner, Electrochemical methods: fundamentals and applications, Wiley New York, 1980.

[4] P. Attard, Adv. Chem. Phys. 92 (1996) 1-160.

[5] R.A. Marcus, J. Chem. Phys. 24 (1956) 966-978.

[6] R.A. Marcus, N. Sutin, Biochim. Biophys. Acta (BBA)-Reviews on Bioenergetics 811 (1985) 265-322.

[7] N. Hush, J. Electroanal. Chem. 470 (1999) 170-195.

[8] N. Hush, J. Chem. Phys. 28 (1958) 962.

[9] C.E. Chidsey, Science 251 (1991) 919-922.

[10] http://www.ceb.cam.ac.uk/pages/linear-sweep-and-cyclic-voltametry-the-principles.html.

[11] P.T. Kissinger, W.R. Heineman, J. Chem. Educ. 60 (1983) 702-706.

[12] P.J. Gellings, H. Bouwmeester, Handbook of solid state electrochemistry, CRC press, 2010.

[13] A. Zhou, H. Dou, Electrochemical chip with miniaturized sensor array, US Patent, 2010.

[14] A. Lasia, Modern aspects of electrochemistry, Springer, 2002, pp. 143-248.

[15] A.J. Bard, M.V. Mirkin, Scanning electrochemical microscopy, CRC Press, 2012.

[16] H. Hertz, Annalen der Physik 267 (1887) 983-1000.

[17] A. Einstein, Annalen der Physik 322 (1905) 132-148.

[18] K. Siegbahn, K. Edvarson, Nucl. Phys. 1 (1956) 137-159.

[19] http://photonicswiki.org/index.php?title=Photoelectron_Spectrometer_XPS_and_UPS

[20] S. Hüfner, Photoelectron spectroscopy: principles and applications, Springer, 2003.

[21] E. Fuchs, H. Oppolzer, H. Rehme, Particle beam microanalysis: fundamentals, methods and applications, VCH, 1990.

[22] D. Ballutaud, N. Simon, H. Girard, E. Rzepka, B. Bouchet-Fabre, Diamond Relat. Mater. 15 (2006) 716-719.

[23] www.casaxps.com/help_manual/XPSInformation/IntroductiontoXPS.htm.

[24] N. Måtensson, A. Nilsson, J. Electron. Spectrosc. Relat. Phenom. 75 (1995) 209-223.

[25] L. Hedin, A. Johansson, J. Phys. B: At., Mol. Opt. Phys. 2 (1969) 1336.

[26] E. Pehlke, M. Scheffler, Phys. Rev. Lett. 71 (1993) 2338.

[27] X. Liang, Z.-j. Wang, C.-j. Liu, Nanoscale Res. Lett. 5 (2010) 124-129.

[28] J.F. Moulder, J. Chastain, R.C. King, Handbook of X-ray photoelectron spectroscopy: a reference book of standard spectra for identification and interpretation of XPS data, Physical Electronics, Eden Prairie, MN, 1995.

[29] M.A. Brisk, A. Baker, J. Electron. Spectrosc. Relat. Phenom. 7 (1975) 197-213.

[30] D. Briggs, J.T. Grant, Surface analysis by Auger and X-ray photoelectron spectroscopy, IM Publications, Chichester, UK, 2003.

[31] D.A. Shirley, Phys. Rev. B 5 (1972) 4709.

[32] C. Wagner, L. Davis, M. Zeller, J. Taylor, R. Raymond, L. Gale, Surf. Interface Anal. 3 (1981) 211-225.

[33] http://www4.nau.edu/microanalysis/Microprobe-SEM/Instrumentation.html.

[34] R. Brown, The Philosophical Magazine, or Annals of Chemistry, Mathematics, Astronomy, Natural History and General Science 4 (1828) 161-173.

[35] R. Pecora, Dynamic light scattering: applications of photon correlation spectroscopy, Springer, 1985.

[36] http://www.malvern.com/labeng/technology/dynamic_light_scattering/classical_90_degree_scattering.htm.

Chapter 3

Study on the electrochemical behaviour of highly boron doped heteroepitaxial (001) single crystalline diamond

3.1 Introduction

As mentioned earlier in *Chapter* 1, boron doped diamond (BDD) attracts increasing interest in electrochemical research. It has been considered as a unique advantageous electrode material with its superior properties, such as a low background current, a wide potential window, strong tolerance against poisoning and fouling effects, and chemical inertness and stability[1, 2]. Hereby BDD has been intensively investigated for its applications *inter alia* electro-organic synthesis[3, 4], electroanalytical sensing[5, 6] and water waste treatment[7-9]. However most studies mainly focused on using polycrystalline BDD but its electrochemical properties can be mainly affected by various factors such as (1) varied boron uptake in different crystallographic orientations of diamond grains, (2) the heterogeneous distribution of the surface density of states and local conductivity, (3) sp^2 carbon composition and other impure aggregation on grain boundaries and (4) other surface defects[10-13]. So the intrinsic electrochemical properties cannot be fully featured unless single crystal diamond electrodes are applied instead.

Homoepitaxial single crystal BDD has been generally grown on HPHT synthetic intrinsic single crystalline diamond and there have been several reports on electrochemistry studies of this surface[14-18]. Single crystal BDD provides a significantly lower background current, making it a more superior electrode material than polycrystalline diamond. Kondo *et al* studied homoepitaxial single crystal diamond

of (111) and (100) surfaces with boron doping levels of 2×10^{19} cm^{-3} and 2×10^{18} cm^{-3} respectively. Apparent outer-sphere electron-transfer was indicated for various redox systems except for $Fe(CN)_6^{3-/4-}$ on the (100) surface ascribed to the absence of specific chemical sites on this high quality surface which is supposed to catalyse the redox reaction for this couple[14]. Ramesham *et al* also observed similar phenomena by investigating the electrochemical properties of (100) orientated BDD in $Fe(CN)_6^{3-/4-}$, showing reversible but sluggish kinetics for this mediator[15]. Moreover, Lagemaat *et al* also investigated oxidised homoepitaxial single crystal diamond of (100) and (110) orientations and attributed the observed reversible electron transfer kinetics to the surface states distributed in the band gap. The flat band potential differed much on these two orientations, which is supposed to be determined by the presence of surface hydroxyl or carbonyl groups[16]. Pleskov *et al* compared homoepitaxial single crystal diamond grown by CVD deposition with polycrystalline diamond, showing both of them exhibit similar kinetic and impedance characteristics in a $Ce^{3+/4+}$ redox couple. The electrochemical behaviour of polycrystalline diamond was also reported as being influenced by the diamond crystallites properties of the surfaces rather than by disordered carbon of the inter-crystallite boundaries[17]. They also investigated single crystal diamond grown by HPHT method and found that a difference in electrochemical properties on individual crystal facets is mainly ascribed to varied boron acceptor concentrations in growth sectors that significantly affect the incorporation between facets and boron atoms during the synthesis[18].

Although high quality single crystal diamond with excellent electrochemical properties can be successfully deposited by HPHT methods or by CVD homoepitaxy as mentioned before, unfortunately, due to the size limitation of available substrates and expensive

price, this approach is not practically feasible for future diamond electrochemical applications[19]. An alternative approach to address the problem is to grow diamond on a non-diamond (also known as 'foreign') substrate, which is defined as a 'heteroepitaxy' process. If the atomic spacings match those in diamond crystals, the heteroepitaxial deposition can be therefore achieved[20]. During recent decades, epitaxial deposition of diamond crystals have been tried on various substrates[21-23], but iridium is the only material allowing successful growth of single crystal diamond film[24]. In particular, multilayer substrate structures using Si(100) as the base substrate, either yttria stabilised zirconia (YSZ)[25] or $SrTiO_3$ (100)[19] as an intermediate oxide buffer layer, and finally a heteroepitaxial single crystal iridium top layer have been proved viable for the heteroepitaxial growth of diamond films.

With such multi-layer structures, the heteroepitaxial single crystal diamond can be successfully synthesised with significantly reduced mosaicity. The initial mosaic spread of diamond films is $\geq 1°$ and further reduced as the subsequent textured growth proceeds. Since the small grains agglomerate, the angular spread decreases and tiny grain boundaries disappear, a final surface with a certain density of dislocations at around 10^9 cm^{-2} is estimated for a 34 μm thick film by assuming all the dislocations are located in regular arrays. This makes the synthesised diamond comparable against other defective single crystal films or even some natural type II diamonds[24].

In this work, substrates comprising highly boron doped (~ 10^{20} cm^{-3}) and moderately oxidised single crystal diamond with (001) orientation grown heteroepitaxially on Ir(001)/YSZ/Si(001) substrates were used. An intrinsic diamond layer of 70 μm to 80 μm was initially deposited upon iridium to guarantee the single crystalline transition

from the substrate underneath before a 3 μm thick boron doped diamond film was grown on the top. The typical dislocation density value for the intrinsic diamond layer was estimated as around 10^8 cm^{-2} from etch pit density (EPD) measurement. This value is several orders higher than that of type Ib synthesised diamond, *i.e.* $10^4 – 10^6$ cm^{-2} but very comparable to that of type IIa natural diamond as mentioned previously. The similar dislocation density was also observed in the BDD film on the top as it spreads consistently throughout two different layers.

Although homoepitaxial single crystal diamond has been studied in electrochemistry, there is no research on heteroepitaxial single crystal BDD, which could show differences due to factors such as differing dislocation densities and step bunching effects[26]. In this chapter, the electrochemical properties of this heteroepitaxial material were thus comprehensively characterised by cyclic voltammetry, impedance spectroscopy along with scanning electrochemical microscopy (SECM). Two different redox mediators, *i.e.* $Fe(CN)_6^{3-/4-}$ and $Ru(NH_3)_6^{2+/3+}$ were used to evaluate the heterogeneous transfer rate constant from peak-peak separation in CV, impedance data and approach curves during SECM measurements. The aim of the work was to enable comparison with homoepitaxial single crystal diamond on the one hand, and polycrystalline diamond on the other. All the results suggest the charge transfer kinetics is determined by the density of states originating from surface defects and functional groups. The varied heterogeneous rate constants are also affected by oxygen containing species on the diamond surface. The flat band potential is more positive for (001) orientated heteroepitaxial single crystal diamond than that of its polished polycrystalline counterparts. As expected, single crystal diamond also presents extremely weak adsorption and is found electrochemically as much more

uniform than polycrystalline material.

3.2 Experimental

3.2.1 Preparation of diamond electrodes

The boron doped heteroepitaxial single crystal diamond was grown on Ir(001)YSZ/Si(001) substrate as mentioned before within the group of Dr. Matthias Schreck at Augsburg and full growth steps and details were demonstrated in previous work[27]. Prior to the multi-layer growth procedure, a (001) orientated silicon wafer with a 3 mm thickness and a 4° off-axis angle was selected as the substrate. The growth of epitaxial YSZ film was firstly carried out by using pulsed laser deposition (PLD) with a krypton fluoride (KrF) excimer laser. In order to reduce the amount of local oxides on Si (001) surface, pulse deposition was originally conducted in vacuum before a further oxygen background pressure of about 5×10^{-4} mbar was applied afterwards. A YSZ oxide buffer layer with a thickness of 20 – 40 nm was achieved after the successive synthesis.

An iridium film with (001) orientation and a 150 nm thickness was then deposited upon the YSZ/Si(001) substrate through e-beam evaporation at 650 ℃. The deposition rate was stepped upwards as 0.004 nm/s was applied in the deposition for the first 20 nm while a 5 times higher value of 0.02 nm/s was used in the subsequent deposition process.

The nucleation of diamond crystals can be aligned excellently by the promotion of the bias enhanced nucleation (BEN) process[28]. Thereby a 80 μm thick intrinsic diamond film with (001) orientation was grown subsequently in a microwave plasma chemical vapour deposition (MWCVD) setup before a boron doped diamond layer of 3 μm was

finally synthesised on the very top of the multi-layer structure in a separate MWCVD chamber. The gases consisting of 2% CH_4 in H_2 were used as feedstock sources in the whole BEN process and a further 300 ppm trimethylboron (TMB) was added for the boron-doping step. The BDD layer coating was deposited at 750 °C, with a microwave power of 1100 W and a chamber pressure of 50 mbar also applied. The eventual multi-layer structure is exhibited in **Figure 3.1** as below.

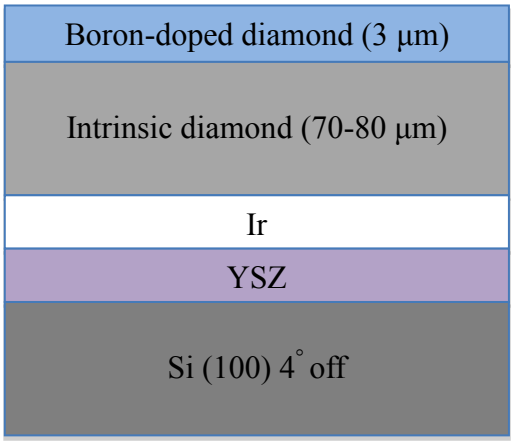


Figure 3.1 The multi-layer structure of heteroepitaxial (001) single crystal diamond

Once the intrinsic and boron doped diamond layers were deposited, the wafer was characterised using a high-resolution X-ray diffractometer (XRD). The rocking curves depict a full width at half maximum (FWHM) of 0.15°, confirming the higher crystalline quality of the deposited heteroepitaxial diamond films. From the atomic force microscopy (AFM) characterisation, the top BDD layer is found to be fairly smooth with a root mean square (RMS) roughness of about 0.7 nm in terrace free regions.

In order to compare the electrochemical properties of this multi-layer deposited heteroepitaxial single crystal BDD substrate, free-standing polycrystalline BDD wafers

([B] > 10^{20} cm^{-3}) of 10 × 10 × 0.6 mm were purchased from Element Six Co. Both as grown and polished polycrystalline diamond wafers were used, the latter with a RMS roughness less than 3 nm comparable to the value deduced from smooth single crystal substrate. All wafers were mounted into the same PTFE holder with around 0.454 cm^2 area exposed to the electrolytes in all electrochemical characterisations.

3.2.2 Electrochemical characterisations

All the CV related electrochemical characterisations were carried out using a μ-AUTOLAB III potentiostat (PGSTAT128N, Eco-Chemie, Netherlands) running GPES (Version 4.9) software at room temperature (21 °C). A standard three-electrode system consisting of the working electrode along with an Ag/AgCl reference electrode and a Pt wire auxiliary electrode was applied. SEM characterisation was operated using a Hitachi S530 SEM with a 20 kV acceleration voltage.

A similar cleaning process was carried out on all the BDD wafers prior to use. The electrodes were gently polished by alumina (1 μm and 0.3 μm) to remove most physically adsorbed impurities on the surface. All the wafers were subsequently immersed and cleaned in acetone using an ultrasonic bath to make sure alumina residues were stripped off before being carefully rinsed by distilled water and dried afterwards. In order to prepare a reproducible surface termination, they were then potential cycled between -1.8 and 2.5 V for at least 20 sweeps in 0.1 M HNO_3, enabling the surface of electrodes to display a very stable and reproducible state. With this electrochemical cleaning process, a reproducible concentration of oxygen containing functional groups bound onto the electrode surface can be achieved[29]. Electrochemical measurements were operated on the same work station with the Frequency Response Analysis (FRA)

module of type III μ-Autolab. A 10 mV modulation amplitude was applied and frequencies were varied between 0.1 and 500 kHz, supplied FRA software was utilised in data conversion and analysis.

Scanning electrochemical microscopy (SECM) was carried out with a commercial CHI 900B setup. Instead of using a three-electrode system stated in the electrochemical characterisation above, a four-electrode configuration was introduced. The BDD working electrode, an Ag/AgCl reference electrode along with a Pt wire counter electrode were all included plus a fourth probe electrode which is made of a Pt wire sealed into a quartz capillary using a laser puller. The electrode was delicately polished until a geometry of approximate 4 μm diameter and the ratio of insulation radius to the electrode disk radius lower than 5 were both achieved. This probe electrode was positioned around 2 μm above the BDD wafer surface, measuring the approaching curves at a rate of 0.1 μm/s. It was also effectively applied to map the electrochemical activity in different mediator electrolytes on a certain area of the electrode with *piezo* motors. A constant height along with a scan rate of 2.5 μm/s was selected in this feedback mode.

3.2.3 Chemicals

Hexaaminеruthenium(III) chloride ($Ru(NH_3)_6Cl_3$, 98%), potassium ferrocyanide ($K_4Fe(CN)_6$, 98.5%), potassium ferricyanide ($K_3Fe(CN)_6$, 99.99+%), methyl viologen (MV, 98%) and anthraquinone-2,6-disulfonate (2,6-AQDS, 90 %, mixture of isomers) were obtained from Sigma Aldrich and directly used as redox mediators in electrochemical experiments without any further purification. 0.1 M KCl was selected as a supporting electrolyte for $Ru(NH_3)_6^{3+}$, $Fe(CN)_6^{4-}$ and methyl viologen, and 0.1 M

$HClO_4$ was applied for AQDS. All the solutions were prepared with Milli-Q water (>18 MΩ cm) and deoxygenated in a nitrogen atmosphere sufficiently to remove dissolved oxygen prior to any measurement.

3.3 Results and Discussion

3.3.1 CV and EIS characterisations

Work commenced with characterisation by cyclic voltammetry in 0.1 M HNO_3 for heteroepitaxial (001) single crystalline BDD and for as-grown and polished smooth polycrystalline BDD, to compare the water hydrolysis potential window and background current of the electrodes. Scans were performed from -1.8 to 2.5 V and results are shown in **Figure 3.2**. If 200 μA/cm^2 is arbitrarily defined as the limiting current defining the potential window, it was discovered that polycrystalline BDDs present a similar potential window either with as-grown or polished smooth surface at around 2.9 V while single crystal diamond exhibits a comparatively wider range as quantified as approximately 3.3 V. The potential window for usable electrochemical applications such as in electrochemical sensors, of single crystal diamond is thus much wider than that of polycrystalline diamond. In **Figure 3.2** a), hydrogen evolution starts at a very negative potential on all crystalline diamond wafers but is particularly strongly inhibited on single crystal diamond substrate. A similar discovery has been reported by Kondo *et al*[14] on homoepitaxial diamond. The authors attributed the greater width of the potential window to a much lower boron concentration, *i.e.* 2×10^{18} cm^{-3}, which is about two orders of magnitude less than that of polycrystalline diamond. In this project, the typical boron dopant concentration is assessed as 1.18×10^{20} cm^{-3} from *Mott-Schottky* measurements, which will be discussed below. Although this is still lower than that of the polycrystalline BDD samples we employed, (7.49×10^{20} cm^{-3}), other

polycrystalline diamond of similar boron dopant concentration (1.7×10^{20} cm^{-3}) still shows the restricted potential window of around 2.5 V in 0.1 M H_2SO_4 [14]. The conclusion therefore is that the difference in boron doping level only at best partially contributes to the wider potential window, and that other factors must be involved. Studies of the hydrogen evolution reaction on diamond indicates the rate limiting step involves adsorption of H_3O^+ on the electrode surface. Presumably the comparative lack of grain boundaries and surface defects on the single crystal electrode surface significantly impedes this adsorption process, leading to the enhanced potential window at cathodic potentials.

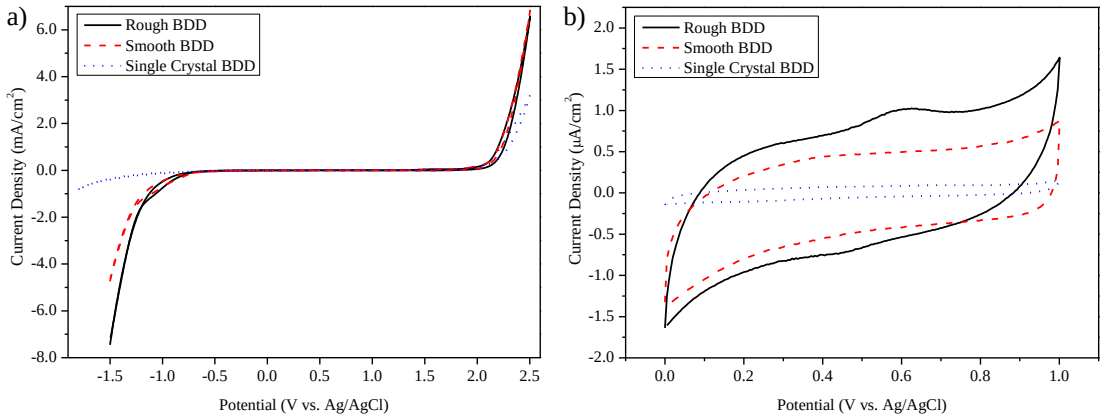


Figure 3.2 CVs of (001) heteroepitaxial, smooth and rough polycrystalline diamond electrodes in 0.1 M HNO_3 at a scan rate of 100 mV/s, for comparison of a) potential window and b) background current of these electrodes.

Apart from a wider potential window, heteroepitaxial single crystal diamond also exhibits an approximately 5 – 10 times lower background current value against polycrystalline diamond as being represented in **Figure 3.2** b) between 0 to 1.0 V. Both as-grown and polished smooth diamond substrates show a similar current density at about 0.9 to 1.4 $\mu A/cm^2$ throughout the measured potential range which is in line with the typical current width value in the literature[14, 30] while the signal arising from the

single crystal diamond wafer is negligible. This result is consistent with the observation on hydrogen terminated homoepitaxial diamond with a lower boron dopant concentration compared with its polycrystalline counterpart[14]. The featureless background current is mainly due to a much lower double layer capacitance on heteroepitaxial diamond originating from around 6 times lower boron dopant concentration along with a comparatively lower density of electrically active defect traps. Furthermore, the single crystal diamond surface has few redox active functionalities, which also contribute to the observed featureless profile. As for the two types of polycrystalline diamond wafers, as-grown rough diamond gives out a slightly larger background current density against the smooth one which is probably attributed to a larger actual electrode surface area correlating with a much higher degree of roughness on the un-polished substrate. Again these differences point to the advantages of using single crystal diamond in applications such as electrochemical sensors, where reducing background currents can lead to enhanced detection limits.

The double layer capacitance was further evaluated by impedance spectroscopy in 1 mM $Fe(CN)_6^{3-/4-}$ in 0.1 M KCl. The measured results are fitted to the *Randles* circuit comprising of an uncompensated series resistance, connected with a constant phase element in parallel with a charge transfer resistance and a *Warburg* constant in series connection as shown in **Figure 3.3**. Fitting parameters are shown in **Table 3.1**.

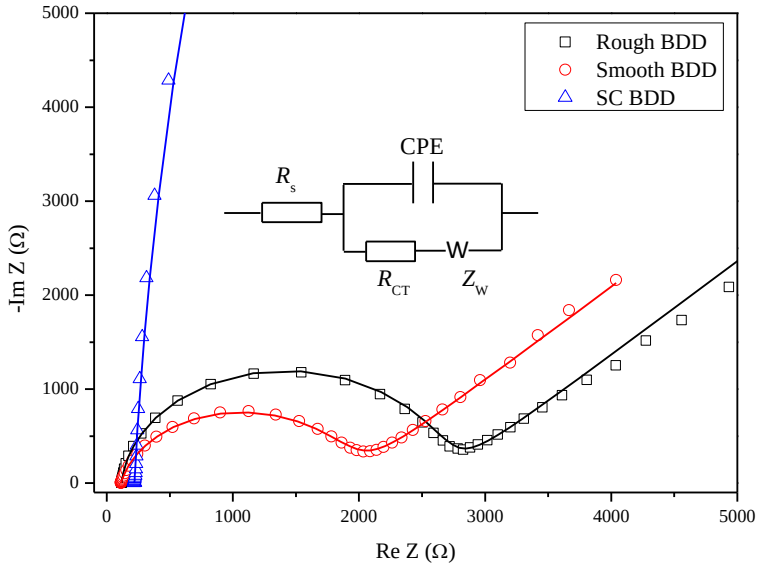


Figure 3.3 *Nyquist* impedance plot (-Im Z, imaginary part of impedance *vs.* Re Z, real part of impedance) for (001) heteroepitaxial single crystal, smooth and rough polycrystalline BDD. Inset: the equivalent *Randles* circuit of electrodes where R_s is the series resistance, CPE is the constant phase element, R_{CT} is the charge transfer resistance and Z_w is the *Warburg* impedance, respectively.

Comparing in particular the heteroepitaxial and smooth polycrystalline diamond films and focusing on the results in $Fe(CN)_6^{3-/4-}$ the fitting gives a capacitance of 0.8 μF for the single crystal diamond and nearly 10 times higher value, *i.e.* 7.66 μF for its polycrystalline counterpart as shown in **Table 3.1**, the latter of which is similar to the capacitance of polycrystalline diamond reported in the literature[31, 32]. The measured capacitance usually reflects the space charge capacitance (C_{SC}) at the semiconductor surface, as the double layer capacitance (C_H) at the electrolyte interface is usually an order of magnitude larger and can be neglected.[33] The capacitance differences are partially due to a lower density of carriers as a result of lower boron doping level in the heteroepitaxial film, and are also partially assigned to a strong depletion layer at the measured potential and a larger positive flat band potential from *Mott-Schottky* analysis discussed below.

In the impedance fitting, the *n* parameter in the constant phase element describes how far this circuit component can match the ideal capacitor. The deviation is usually due to the surface impurities and defects along with the inhomogeneous distribution of local electro-active regions on the surface[34]. The *n* value is observed as 0.975 in contrast to 0.862 for heteroepitaxial and polished smooth polycrystalline diamond, respectively. As the *n* value approaches unity, it suggests a homogeneous distribution of boron up-take and local electroactivity on heteroepitaxial single crystal diamond. This is in contrast to a much larger deviation from ideal capacitor like behaviour for polycrystalline smooth diamond as a result of varied boron concentrations on different grain facets and boundaries and inhomogeneous spatial distribution of local electro-activity on polycrystalline diamond[35, 36]. The uncompensated resistance is obtained as 213 Ω and 114 Ω for heteroepitaxial and polycrystalline diamond respectively as fitted to the theoretical model. As 0.1 M KCl was used as a quite conductive electrolyte in the series of experiments, the contribution to uncompensated resistance from the electrolyte is small and is rather mainly attributed to the resistance of the diamond film itself. The resistance value difference is consistent with the boron dopant levels in these two types of diamond materials. The evaluated uncompensated resistance will be widely applied in *iR* drop correction and the theoretical fitting using DigiSim commercial software later in this chapter. The impedance data in $Ru(NH_3)_6^{2+/3+}$ showed some differences but broadly similar trends.

The electrochemical behaviour of heteroepitaxial single crystal and polycrystalline diamond was further characterised by cyclic voltammetry with two different redox mediators, *i.e.* $Ru(NH_3)_6^{3+}$ and $Fe(CN)_6^{4-}$. Both types of polycrystalline diamond represent a similar peak position with an approximate 95 mV peak-peak separation and

a comparable peak current intensity at a scan rate of 100 mV/s for $Ru(NH_3)_6^{3+}$ as shown in **Figure 3.4**. However, in contrast, the peak current density observed on single crystal diamond is decreased by about 30% and shows a much higher peak-peak separation value at 171 mV, suggestive of relatively sluggish electron transfer kinetics on this substrate.

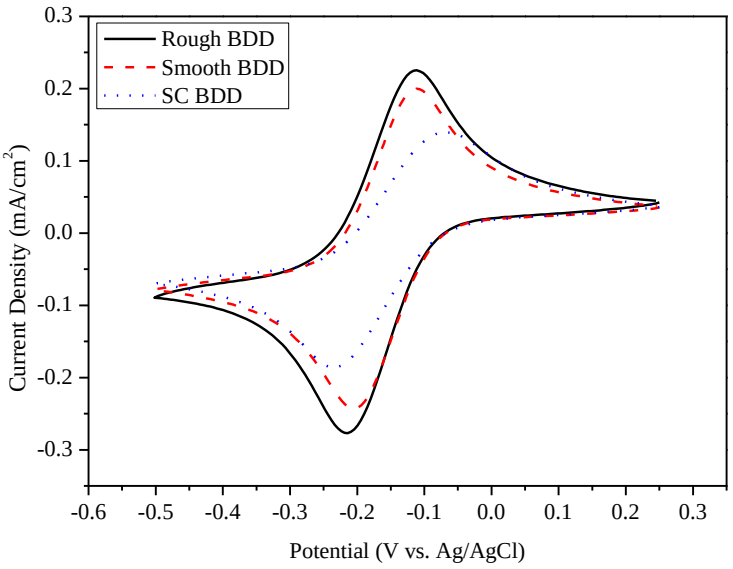


Figure 3.4 CVs of (001) heteroepitaxial, smooth and rough polycrystalline diamond electrodes in 1 mM $Ru(NH_3)_6^{3+}$ and 0.1 M KCl at a scan rate of 100 mV/s.

Further investigation was conducted by applying different scan rates using the same mediator concentration. A typical series of CV voltammograms on heteroepitaxial single crystal diamond with varied scan rates is shown in **Figure 3.5** a).The peak current density is found to be proportional to the square root of the scan rates on all three types of electrodes, suggesting planar diffusional control and Nernstian behaviour. This result is in contrast to the observation on polycrystalline diamond with lower boron dopant concentration[37], which exhibits nonlinear relationship between peak current density and the square root of scan rates.

For heteroepitaxial diamond, cyclic voltammetry was also carried out with different concentrations of $Ru(NH_3)_6^{3+}$ at a fixed scan rate of 100 mV/s as shown in **Figure 3.5** b). In a theoretical reversible diffusion-control model, the peak-peak separation will not be affected even though varied scan rates are applied. However, this value is found to increase steeply at higher concentrations of $Ru(NH_3)_6^{3+}$, indicating probably a significant contribution of the resistance of the diamond electrode to the voltammogram, especially at higher mediator concentrations. Therefore corrections to the measured peak-peak separation values in voltammograms are needed.

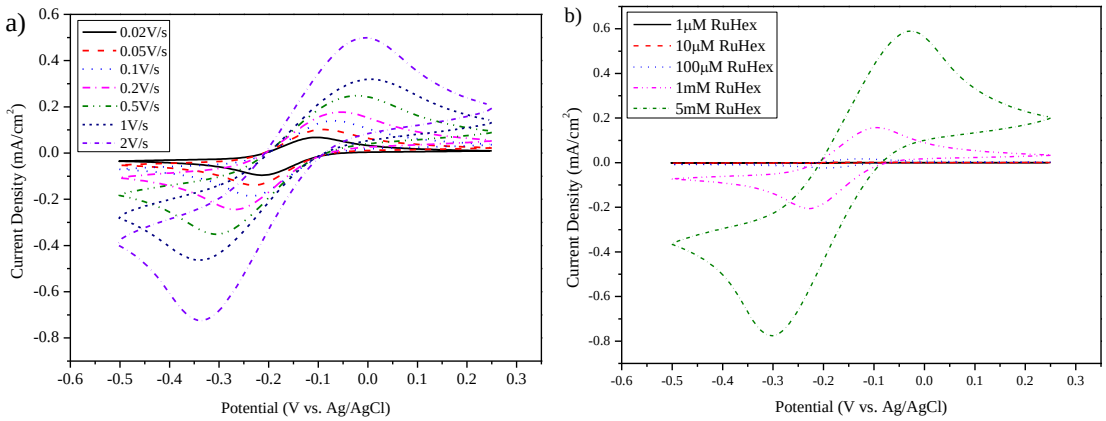


Figure 3.5 CVs of heteroepitaxial diamond in a) 1 mM RuHex and 0.1 M KCl at different scan rates from 0.02 V/s to 2 V/s and b) different concentrations of RuHex from 1 μM to 5 mM in 0.1 M KCl at a scan rate of 100 mV/s.

To consider this, the potential drop originating from the uncompensated resistance as determined from the impedance measurements was made. The resulting compensated peak-peak separation values, which became fairly independent of concentration, are around 260 mV, 99 mV and 110 mV compared with 347 mV, 209 mV and 201 mV for heteroepitaxial single crystal, polished smooth and as-grown rough polycrystalline diamond respectively in 1 mM $Ru(NH_3)_6^{3+}$ at a scan rate of 1.0 V/s as shown in **Table 3.1**, suggesting a quasi-reversible kinetics for all these electrodes. With the *iR*

compensated peak-peak separation, the electron transfer rates (k^0) can thus be calculated based on the *Nicholson* method[38] and are summarised in **Table 3.1** as well. With the smallest peak-peak separation, the smooth polycrystalline diamond exhibits the highest k^0 at 0.029 cm/s while its rough counterpart shows a relatively smaller rate constant at 0.0161 cm/s along with an approximately 10 mV higher compensated peak-peak separation. However, the k^0 value is evaluated as only 0.00245 cm/s on heteroepitaxial diamond, which is more than one order of magnitude lower than the smooth polycrystalline diamond attributed to the extremely high peak-peak separation, indicating much more sluggish kinetics on this type of electrode.

Table 3.1 Estimated heterogeneous electron transfer rate constants for $Ru(NH_3)_6^{3+}$ and $Fe(CN)_6^{4-}$ using *Nicholson* method, Digisim fitting and impedance characterisations.

		$Ru(NH_3)_6^{2+/3+}$			$Fe(CN)_6^{3-/4-}$		
		SC BDD	Poly Smooth	Poly rough	SC BDD	Poly Smooth	Poly Rough
	E_{pp} (mV)	347 [a]	209 [a]	201 [a]	/	234 [b]	244 [b]
Nicholson	E_{pp} (mV) after iR compensation [c]	260	99	110	/	219	211
	k^0 (cm s^{-1})	0.00245	0.029	0.0161	/	0.000920	0.00206
DigiSim Simulation	k^0 (cm s^{-1}) [d]	0.00252	0.032	0.0213	2.54E-5	5.84E-4	1.72E-3
	α	0.49	0.56	0.55	0.81	0.46	0.54
Impedance [e]	R_s (Ω)	213.3	113.4	108.8	213.3	114.5	119.0
	C_p (μF)	0.86	4.89	2.056	0.804	7.66	2.56
	n in CPE	0.965	0.90	0.967	0.975	0.8619	0.952
	R_{ct} (Ω)	657	11.52	41.3	121300	1820	2792
	k^0 (cm s^{-1})	0.00162	0.0924	0.0258	8.77E-6	5.77E-4	4.22E-4

All the data are specifically labelled with different conditions applied in the measuring process shown as below:

[a] The values measured at a scan rate of 1.0 V/s.
[b] The values measured at a scan rate of 0.1 V/s.
[c] The peak-peak separation values after the *iR* correction from uncompensated resistance.
[d] k^0 acquired at a scan rate of 500 mV/s, 1 V/s, 2 V/s using DigiSim fitting.
[e] Impedance conducted at the formal potential or open circuit potential in 1mM $Ru(NH_3)_6^{2+/3+}$ and a mixed solution of 0.5 mM $Fe(CN)_6^{4-}$ with 0.5 mM $Fe(CN)_6^{3-}$.

An alternative calculation of the electron transfer rate constant k^0 was also carried out by fitting experimental parameters into commercial simulation software, notably DigiSim 3.03 from Bioanalytical System Ltd. A homogeneous electrode with semi-infinite planar diffusion was assumed by the program throughout the fitting process when both uncompensated resistance and double layer capacitance were taken into account. The rate constant values for both heteroepitaxial and polished polycrystalline diamond electrodes in $Ru(NH_3)_6^{3+}$ from DigiSim fitting match those from the *Nicholson* method well, suggesting the appropriate *iR* correction is crucial to validate the *Nicholson* model in evaluating the kinetics. A slightly larger deviation of k^0 is however observed on the as-grown unpolished polycrystalline diamond, which is possibly due to the topographic effect with a larger degree of surface roughness. Apart from these two approaches mentioned before, the rate constants were also calculated from the electron transfer resistance from impedance measurements with both $Ru(NH_3)_6^{2+/3+}$ and $Fe(CN)_6^{3-/4-}$ using the equation as shown below[39]:

$$k^0 = RT/(n^2F^2A(C_{ox})^{\alpha}(C_{red})^{\beta}R_{CT}) \qquad 3.1$$

where R is the ideal gas constant, T is the temperature, n is the number of transferred electrons, F is the *Faraday* constant, A is the electrode surface area, C is the concentration of analyte, α, β are the transfer coefficients and R_{CT} is the charge transfer resistance. In the $Ru(NH_3)_6^{2+/3+}$ system, the rate constant values are quite similar to those from both the *Nicholson* method and DigiSim fitting as they are all in the same order of magnitude for all three different types of electrode materials even though heteroexpitaxial diamond exhibits a lower value which is more than 10 times smaller than polycrystalline diamond.

The rate constant of heteroepitaxial diamond for the $Ru(NH_3)_6^{2+/3+}$ redox couple is only slightly higher than that of (001) homoepitaxial single crystalline with a boron dopant concentration of 2×10^{18} cm^{-3} as reported[14] but still one order of magnitude lower than that of polycrystalline diamond of similar boron dopant level[37]. Meanwhile the rate constant of a polycrystalline diamond substrate also coincides with the typical value on this material with a similar boron level.[2, 37] The transfer coefficient α is observed to be around 0.5 in most of the calculations. This is consistent with all these three diamond materials behaving like semi-metals or degenerate semiconductors[33], due to the appreciable boron dopant concentration. $Ru(NH_3)_6^{3+}$ is well known as a typical outer-sphere electron transfer mediator[2, 40], which is insensitive to the content of surface functionalities, impurities and defects. The main reason attributed to the varied rate constants discovered for different diamond electrodes above is the variation of density of states at the band gap, which is comparatively lower for heteroepitaxial single crystal diamond correlating with a 6 times lower boron level in this material.

Similar to $Ru(NH_3)_6^{3+}$, 1 mM $Fe(CN)_6^{4-}$ was also applied as an inner-sphere mediator that has been reported as being sensitive to the material surface functionalities[41, 42]. In cyclic voltammograms shown in **Figure 3.6**, both polycrystalline diamond substrates represent approximately the same peak-peak separation although the polished smooth substrate exhibits a slightly a larger value. In contrast, an enormously wide peak-peak separation is discovered on the heteroepitaxial diamond.

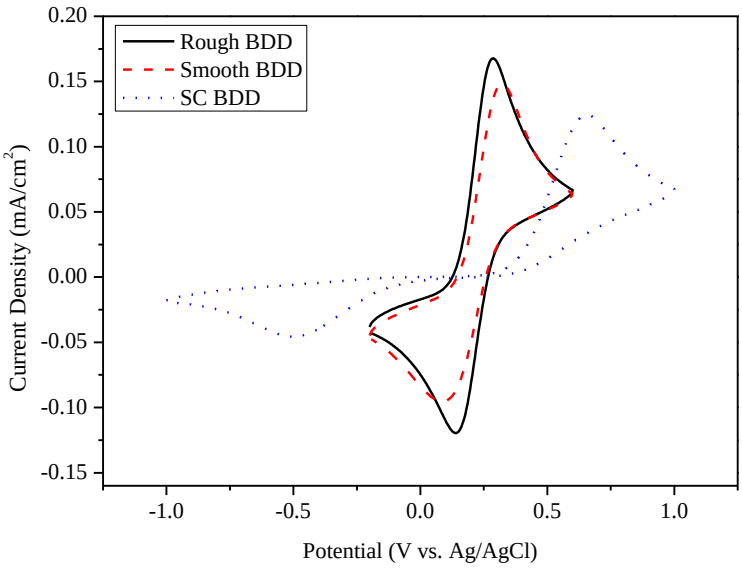


Figure 3.6 CVs of (001) heteroepitaxial, smooth and rough polycrystalline diamond electrodes in 1 mM $Fe(CN)_6^{4-}$/0.1 M KCl.

These values were fitted into the *Nicholson* model for the calculation of rate constants. DigiSim fitting and impedance measurements were also carried out to give a more accurate evaluation of the kinetics of these electrodes in this mediator.

As-grown rough polycrystalline diamond exhibited a higher rate constant value compared to its polished smooth counterpart in both the *Nicholson* method and DigiSim fitting. As mentioned previously, since the peak-peak separation is too big for heteroepitaxial diamond that exceeds the limitation of the *Nicholson* method, the rate constant can barely be assessed by this model. DigiSim gives the value for heteroepitaxial diamond at 2.54×10^{-5} cm s^{-1}, indicating sluggish kinetics for this material with an at least 20 times lower rate constant than polycrystalline diamond. Using the impedance fitting, all the rate constants seem to be underestimated except for a quite similar value for polished smooth polycrystalline diamond. It is noticeable that the rate constant of $Fe(CN)_6^{4-}$ on all these three electrode materials is nearly at least two

orders of magnitude lower than that achieved with $Ru(NH_3)_6^{3+}$. Different from the outer-sphere electron transfer process for $Ru(NH_3)_6^{3+}$, $Fe(CN)_6^{4-}$ exhibits inner-sphere features that makes it very sensitive to surface adsorbates and defects and is very dependent on specific chemical sites and functionalities to catalyse the electron transfer process. It has been found that the sp^2 carbon species can effectively catalyse the electron transfer on glassy carbon or HOPG electrodes[43, 44]. Hereby, due to there being low sp^2 carbon on heteroepitaxial single crystal diamond, this electron transfer process is significantly hindered. Moreover, the strong depletion layer in heteroepitaxial diamond also contributes to impeding the electron transfer. The rate constant obtained on heteroepitaxial diamond is 2.5×10^{-5} cm s^{-1}, which is very close to the value reported for homoepitaxial single crystal diamond[14, 15, 30], suggesting a similar state to the homoepitaxial diamond under electrochemical characterisations. However, this rate constant value is approximately two orders of magnitude lower than that of the polycrystalline diamond with a similar boron concentration[14]. The relatively sluggish kinetics is therefore not attributed to the comparable boron dopant concentrations for both materials but to considerably lower concentration of sp^2 carbon impurities, functionalities or defects on the heteroepitaxial diamond surface along with stronger band bending. Although both polycrystalline diamond electrodes exhibit much higher rate constants, the value is comparatively lower for the polished smooth electrode from both the *Nicholson* method and DigiSim fitting. This difference is probably mainly affected by the topography, as most of sp^2 carbon groups and other impurities aggregated near the grain boundaries are effectively removed during the polishing process, resulting in the deficiency of defects and functionalities on the smooth surface.

3.3.2 *Mott-Schottky* plot and energy diagram

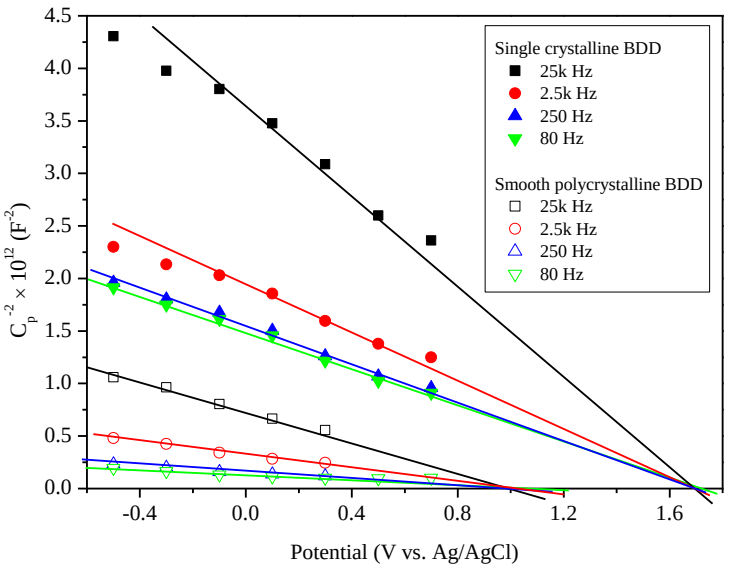


Figure 3.7 *Mott-Schottky* plot for heteroepitaxial (001) and polycrystalline diamond at different frequencies of 25 k, 2.5 k, 250 and 80 Hz.

Impedance measurements were conducted in 0.1 M KCl at various potentials ranging from -0.5 to 0.7 V, at which almost no faradaic current flows. The equivalent circuit (see above) parallel capacitance (C_p) is plotted as C_p^{-2} versus potential to give the *Mott-Schottky* plot, as shown in **Figure 3.7**. The slope of the plot strongly depends on the measuring frequency, indicating a frequency dispersion of capacitance for the diamond electrodes. The frequency dependence of the slope has been reported for diamond and other semiconductors before[45, 46]. It was attributed to the frequency dependence of dielectric relaxation or slow ionisation of deep acceptor levels in the space charge region, effect of surface states, or surface roughness of semiconductor materials.[47] From the slope of C_p^{-2} *versus* potential line at 80 Hz, the carrier concentration is evaluated using $N_A = -2/\{e\varepsilon_0\varepsilon_r A^2[\mathrm{d}(C_p^{-2})/\mathrm{d}E]\}$ where A is the electrode area, ε_0 is the permittivity of vacuum, ε_r is the relative permittivity of the material. From this equation, the carrier concentrations are 1.18×10^{20} cm^{-3} and 7.49×10^{20} cm^{-3} for heteroepitaxial

and smooth polycrystalline diamond, respectively. This acceptor concentration is in line with boron doping level from other measurements.

Although the capacitance is frequency dependent in the *Mott-Schottky* plot, the extrapolating lines converge to a similar value at the potential axis, which corresponds to the flat band potential. The nominal flat band potentials are 1.73 V and 0.90 V from this calculation for heteroepitaxial and smooth polycrystalline diamond respectively. This calculation assumes a potential-independent drop across the Helmholtz layer, which is true for typical non-degenerate semiconductors. For degenerate semiconductors with a high acceptor concentration, such as the single crystalline or polycrystalline diamond studied here, the extrapolation value at the potential axis is shifted by $e\varepsilon_0\varepsilon_r N_A^2/(2C_H^2)$ [48, 49]. As C_H is usually an order of magnitude larger than C_{SC}, the latter can be mostly neglected in impedance analysis[33]. In this calculation, a typical value of C_H of around 20 μF/cm^2 was used[50], which gives an offset of 0.011 V for single crystal and 0.073 V for polycrystalline diamond. After correction by the offset value, the true flat band potentials are 1.72 V and 0.83 V *vs.* Ag/AgCl reference electrode for heteroepitaxial and polycrystalline diamond, respectively, despite some uncertainty in the estimation of C_H. The flat band potential maps the energy of the valence band edge at the surface (E_{VS}) to the Fermi energy of the Ag/AgCl reference electrode on the scale of chemical potential in the solution: $E_{VS} = E_{FB} + E_F - E_{VB}$. Its sign and magnitude indicate the direction and extent of band bending when the electrode is in equilibrium with the solution. Based on the flat band potential, an interfacial energy diagram at equilibrium with the redox solution is proposed as illustrated in **Figure 3.8**. The flat band potential of polycrystalline diamond is similar to the value of 0.91 V *vs.* Ag/AgCl measured at 103 Hz in 0.5 M NaCl[51] and is within

the range of 0.45 to 1.00 V *vs.* SCE reported previously on polycrystalline diamond[50]. In contrast, the large positive flat band potential of heteroepitaxial single crystal diamond indicates a pronounced downward band bending, and a depletion of major carriers on the heteroepitaxial diamond surface. The heteroepitaxial diamond has a much lower density of defects and is more resistant to oxidisation although it was treated with potential cycling in dilute nitric acid under identical conditions. This flat band potential is similar to the value (1.2 V) of homoepitaxial diamond[47], but much smaller than the typical potential of around 4.0 V for heavily oxidised homoepitaxial (001) diamond of a lower boron doping level[49]. This discrepancy is attributable to the shift of the band edge to lower energies (*i.e.* more positive potentials) due to the dipole character of oxygen containing groups on the heavily oxidised diamond surface[49].

Although both types of diamond are highly boron doped, they still show diode like rectifying behaviour at extreme overpotentials, for example, for oxygen evolution above 2 V, the energy band bends up and an accumulation layer appears on the interface. As a consequence, both types of diamond electrodes show fast kinetics for oxygen evolution. In comparison, for the hydrogen evolution reaction, the energy band bends downwards and holes are almost depleted on the surface, so the electron transfer kinetics depends on the width of the space charge region that the electrons have to tunnel through. As the width of the space charge is influenced by the concentration of charge carriers in the bulk material, the less boron-doped single crystal sample exhibits a much lower current than polycrystalline diamond in our hydrolysis experiment, as shown in **Figure 3.2** b).

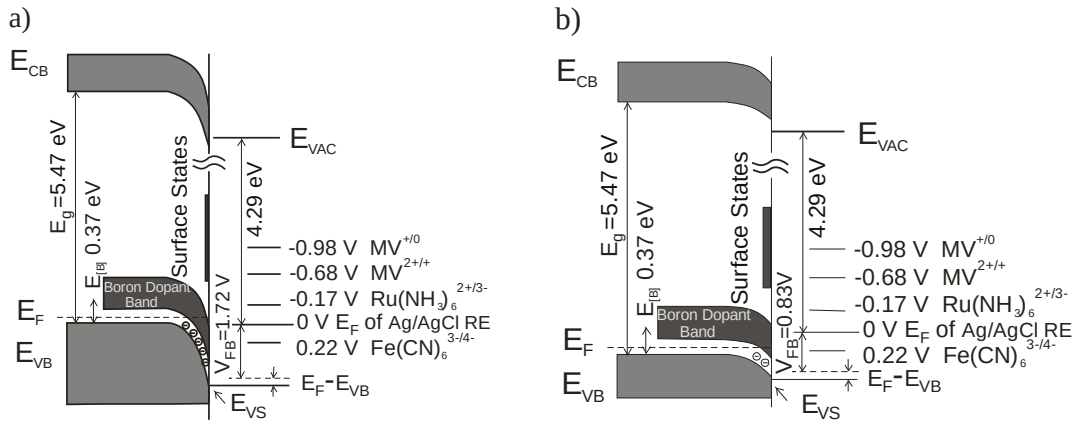


Figure 3.8 Energy diagram of a) heteroepitaxial single crystal diamond and b) polycrystalline polished smooth diamond

3.3.3 Electrochemical characterisations of methyl viologen and AQDS

3.3.3.1 Electrochemical characterisations of methyl viologen

The electrochemical properties of heteroepitaxial single crystal and polycrystalline (polished smooth and un-polished rough) diamonds were further investigated and characterised in methyl viologen (MV), a more complex electrochemical species displaying two successive one-electron transfer processes[52, 53] as shown below:

$$MV^{2+} + e^- \rightleftarrows MV^+ \quad 3.2$$

$$MV^+ + e^- \rightleftarrows MV^0 \quad 3.3$$

Figure 3.9 shows the CVs of different diamond electrodes in 4 mM MV^{2+} as the starting analyte in 0.1 M KCl at a scan rate of 100 mV/s. Two pairs of redox peaks are clearly visible for both types of polycrystalline diamond electrodes, as has been reported and interpreted previously[54]. The first redox peak in the cathodic scan at around -0.6 to -0.7 V is attributed to the one-electron transfer process between the initial MV^{2+} and reduced MV^+, while the other cathodic peak appearing at a comparatively lower potential of -1.1 V is the further reduction of MV^+ into MV^0 which can be associated with adsorption of the neutral molecule on the electrode surface. The asymmetric anodic

peak at -0.9 V in the anodic scan has a contribution from the electrochemical-stripping peak of such precipitation into MV^+. The higher current observed on rough polycrystalline diamond is probably partially attributed to the roughness and a large surface area as started earlier.

In contrast, the heteroepitaxial diamond shows a weak MV^0 precipitation peak at a very cathodic potential of -1.5 V, and absence of an expected stripping peak at -0.9 V. Instead, two anodic peaks are observed around -0.6 V, the typical potential for oxidisation from MV^+ to MV^{2+}. At a lower MV concentration (*i.e.* 1 mM), only one anodic peak can be seen besides the absence of a stripping peak around -0.9 V. Similar peaks have been observed on polycrystalline diamond and are attributed to a conproportionation process[54]. The peak at -0.6 V is attributed to the oxidisation of MV^+ from conproportionation, and the peak at -0.4 V is attributed to the stripping of MV^0 directly to MV^{2+}. The onset potential of the conproportionation process depends on various aspects, such as analyte concentration and scan rate. Here the conpropotionation process seems to only occur at a higher concentration, *i.e.* 4 mM MV, but independent of scan rates.

The absence of a stripping peak for MV^0 to MV^+ on heteroepitaxial diamond is associated with the semiconducting properties of this material. At the formal potential of $MV^{0/+}$, the energy band bends downwards strongly and the surface is depleted of dominant charge carriers, *i.e.* holes. At this condition, MV^{2+} can get reduced by receiving one electron from the electrode surface that is enriched with electrons although a large overpotential is required, but the stripping of MV^0 is strongly inhibited due to the lack of electron acceptors on the surface. Compared to heteroepitaxial

diamond of a relatively lower boron doping level, polycrystalline diamond shows a quite different profile. For polycrystalline diamonds, electrons can tunnel through the space charge region more easily due to a thinner space charge region at higher concentration of charge carriers; the presence of large amount of surface states also facilitates the electron transfer process.

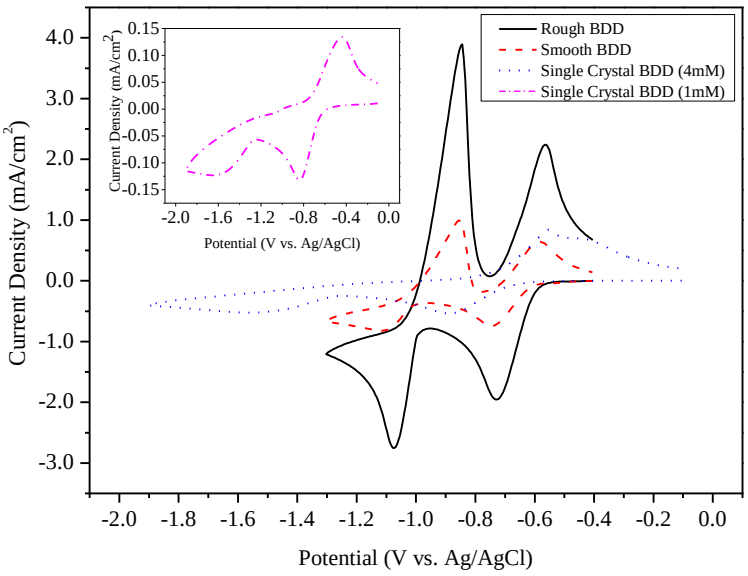


Figure 3.9 CVs of heteroepitaxial (001) single crystal, smooth and rough polycrystalline diamond with 4 mM MV^{2+} in 0.1 M KCl at a scan rate of 100 mV/s. Inset: CV of heteroepitaxial (001) single crystal diamond in 1 mM MV^{2+} and 0.1 M KCl.

3.3.3.2 Electrochemical characterisations of AQDS

Diamond has been reported for its strong resistance to fouling by polar adsorbates such as AQDS[55]. CVs of heteroepitaxial single crystal, polished smooth and un-polished rough polycrystalline diamond electrodes were conducted in 0.1 M $HClO_4$ supporting electrolyte after potential cycling in 1 mM AQDS and physically rinsing with Milli-Q water to remove weakly adsorbed species as shown in **Figure 3.10** a). The voltammogram of heteroepitaxial diamond is almost featureless, suggesting no adsorption of AQDS on

this electrode material after careful rinsing. This type of diamond still exhibits strong resistance even after initial potential cycling in diluted nitric acid as nearly no functionalities are attached onto the surface. However, for both types of polycrystalline diamond electrodes, different pictures are shown respectively. Due to the overwhelmingly large background current in the specific potential cycling region on rough polycrystalline diamond, the adsorption of AQDS cannot be neglected with a couple of small and broad peaks appeared at around 0.2 – 0.4 V. In contrast, its smooth polycrystalline counterpart exhibits a pair of symmetric peaks with an almost *zero* peak-peak separation at -0.1 V instead as specified in **Figure 3.10** b).

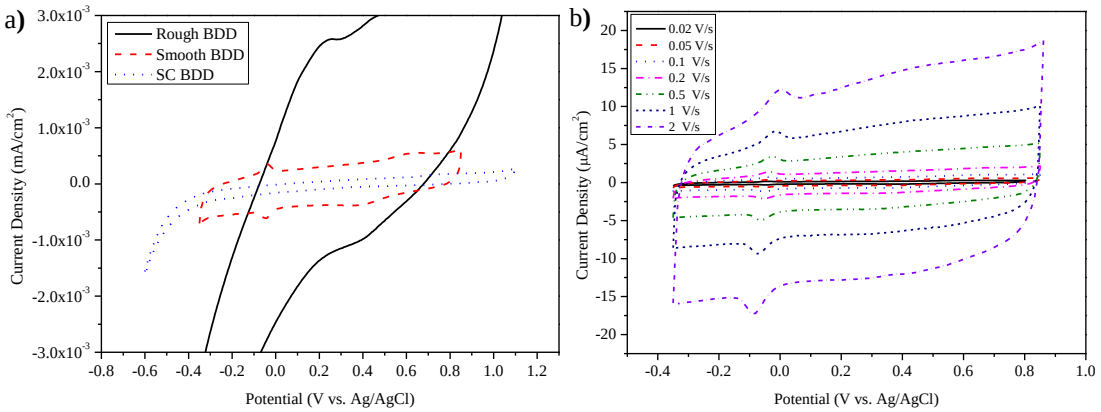


Figure 3.10 CVs of a) heteroepitaxial (001), smooth and rough polycrystalline diamond in 0.1 M $HClO_4$ at a scan rate of 50 mV/s after previous CVs in 1 mM AQDS and rinse and b) smooth polycrystalline diamond electrode in 0.1 M $HClO_4$ at different scan rates from 0.02 to 2 V/s after CV in 1 mM AQDS and rinse.

The peak current is observed to vary linearly along with different scan rates, indicating the electron process is adsorption controlled on this material surface. The total charge transferred during the faradaic electron transfer process is integrated as 1.6×10^{-3} mC/cm^2, which is independent of the scan rates. This evaluated value corresponds to 4.16×10^{-12} moles of AQDS adsorbed on the surface, in other words, approximate 6.5% of the surface sites are covered and occupied by the AQDS

adsorbates. If a flat orientation is assumed for all the AQDS molecules, an estimated molecular area of 1.307 nm^2 is achieved[56]. The adsorption of AQDS, although very weak on the smooth polycrystalline diamond surface, is proposed to come from a high density of surface defects from the mechanical polishing process[57]. The surface defects are acknowledged as the hosts for dipolar functionalities on the surface[58, 59], which is complementarily confirmed by a considerably large positive flat band potential for smooth polycrystalline diamond.

3.3.4 Scanning electrochemical microscopy (SECM)

SECM was conducted in feedback mode in 1 mM $Ru(NH_3)_6^{3+}$ to examine the heterogeneous electrochemical activity of diamond electrodes, which has been reported for polycrystalline and nanocrystalline diamond[60, 61]. During the SECM experiments, a platinum disc ultramicroelectrode of 4 μm diameter was positioned to around 2 μm above the substrate. The platinum probe and substrate were held at -0.4 and 0 V, corresponding to the reduction and oxidisation potential of $Ru(NH_3)_6^{2+/3+}$ respectively. $Ru(NH_3)_6^{3+}$ is reduced to $Ru(NH_3)_6^{2+}$ at the probe surface, the product diffuses to an electrochemical active substrate to get oxidised to $Ru(NH_3)_6^{3+}$ before being reduced to $Ru(NH_3)_6^{2+}$ again at the probe to finish a positive feedback loop. In contrast to an enhanced current on a conductive substrate, the hemisphere diffusion on the probe is hindered by an electrochemically inactive substrate and gives a lower steady state current, which is called the negative feedback mode. By positioning the probe close to the substrate, a current *vs.* distance plot is recorded as the approach curve, which reveals the characteristics of the substrate electrode[62]. As the probe scans at a fixed height over the substrate, the probe current reflects the local electrochemical activity of the substrate for a smooth electrode.

The resulting SECM images with the same width of current scale are shown in **Figure 3.11** a) and b), for heteroepitaxial single crystal and polished polycrystalline diamond, respectively. The polished polycrystalline diamond shows an inhomogeneous distribution of high and low feedback current which corresponds to a heterogeneous electrochemical activity, as the topographic effect can be excluded due to mechanical polishing to a root mean square (RMS) roughness less than 3 nm. The pattern of electrochemical activity is correlated with the distribution and shape of diamond grains in SEM images (**Figure 3.12** a) and b)). This heterogeneity is in line with similar observations on polycrystalline diamond of various doping levels and nanocrystalline diamond, and is attributable to different boron uptake at diamond grains of different crystallographic orientations and grain boundaries from combined SECM and conductive probe atomic force microscopy studies[60, 61]. Approach curves were recorded above sites of different electrochemical activity as shown in **Figure 3.11** c) and d), where L is the tip radius normalised to the distance between the tip and the substrate, and I is the current of tip normalised to the steady state current far away from the substrate. All the approach curves fall between the two theoretical positive and negative feedback curves, indicating finite charge transfer kinetics and a quasi-reversible process. Different approach curves are obtained above spots of different activity, suggesting a spatially distributed heterogeneous rate constant across the surface.

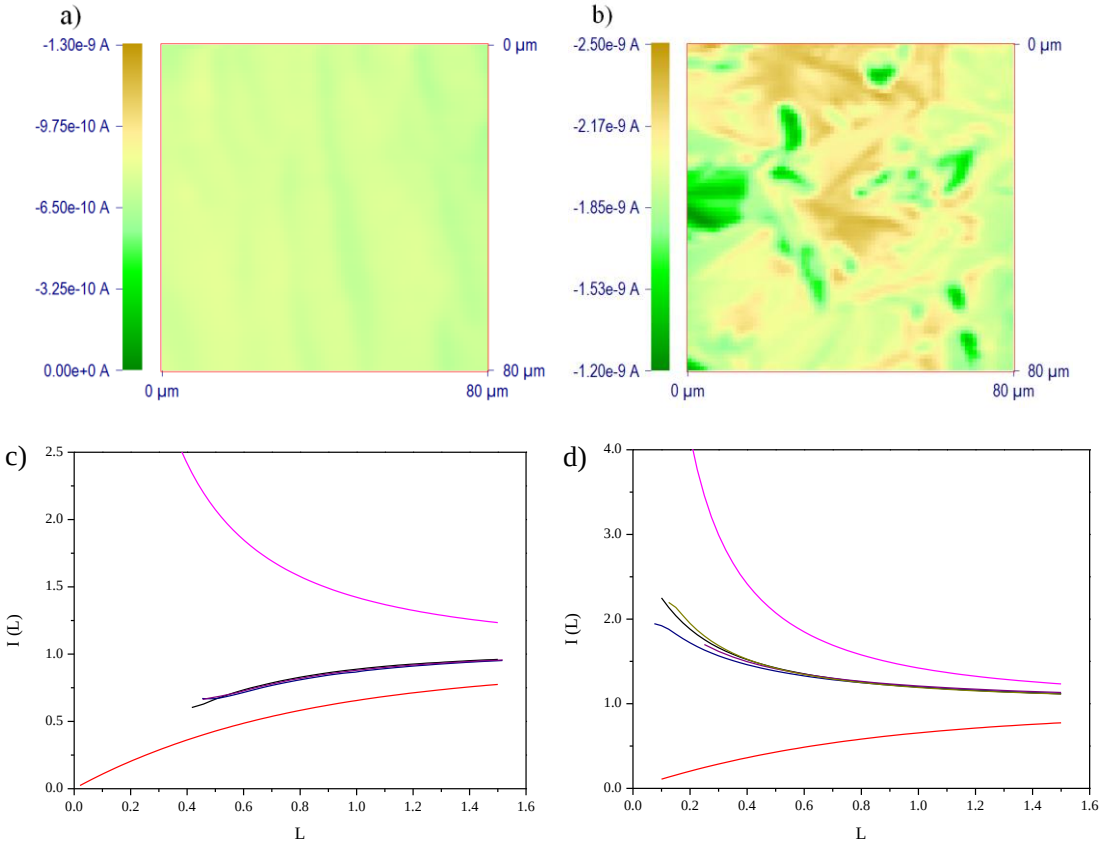


Figure 3.11 SECM of a) (001) heteroepitaxial BDD and b) smooth polycrystalline diamond, and (c,d) the corresponding approach curves at various areas on the diamond surface in $Ru(NH_3)_6^{3+}$ (middle) between two theoretical ideal positive (top) and negative (bottom) feedback curves.

The SECM image of heteroepitaxial single crystal diamond is plotted in **Figure 3.11** a). The feedback current is much more homogeneous compared to polycrystalline diamond. The current is lower than for the polycrystalline diamond due to the lack of 'hot spots' on this electrode. The current is lower when the probe approaches the substrate, indicating a negative feedback due to lower activity compared to the hot spots on the polycrystalline material which show positive feedback. The approach curves overlap each other when acquired at different regions of the diamond, as presented in **Figure 3.11** c), indicating homogeneous kinetics across the diamond surface. The homogeneous electrochemical activity demonstrates that prominent defects such as non-epitaxial

crystallites and twins are effectively suppressed and only (001)-oriented single crystalline diamond is grown heteroepitaxially on iridium. Despite the overall homogeneous activity, a slight variation of current is discernible at close examination. The vertical stripes of lower current are correlated to structures of similar shape and size in the SEM image (**Figure 3.12** a)). The silicon substrate used in the heteroepitaxial growth is cut at 4° off-axis to suppress non-epitaxial crystallites during the growth of the diamond layer, but it leads to the formation of macro steps on the surface due to a step bunching effect inherent to the growth mechanism in the presence of nitrogen during CVD. These macro steps increase in size with increasing thickness. During in-situ boron doping, these structures experience a significant smoothening due to different growth conditions. As a result of smoothing, the surface shows a wavy structure with maximum-minimum height variations of up to 100 nm within a typical AFM scan area of $20 \times 20\ \mu m^2$, although it shows a very low roughness (RMS = 0.7 nm) in a smaller scan area of $1 \times 1\ \mu m^2$. This suggests that the sample topography also partially attributes to the contrast in the SECM map.

Apart from the SECM measurements, the spatial variation in electrochemical activity was alternatively investigated by the electrodeposition of platinum nanoparticles. The deposition process was carried out in 2 mM $K_2PtCl_6^{2-}$ and 0.5 M H_2SO_4 by holding the potential at -0.2 V constantly for approximate 2 minutes until a 10 mC charge was passed to the substrate surface. With similar total Pt loading on their own surfaces, the two electrodes exhibit entirely different distributions of nanoparticles and morphology under SEM as shown in **Figure 3.12** c) and d) respectively.

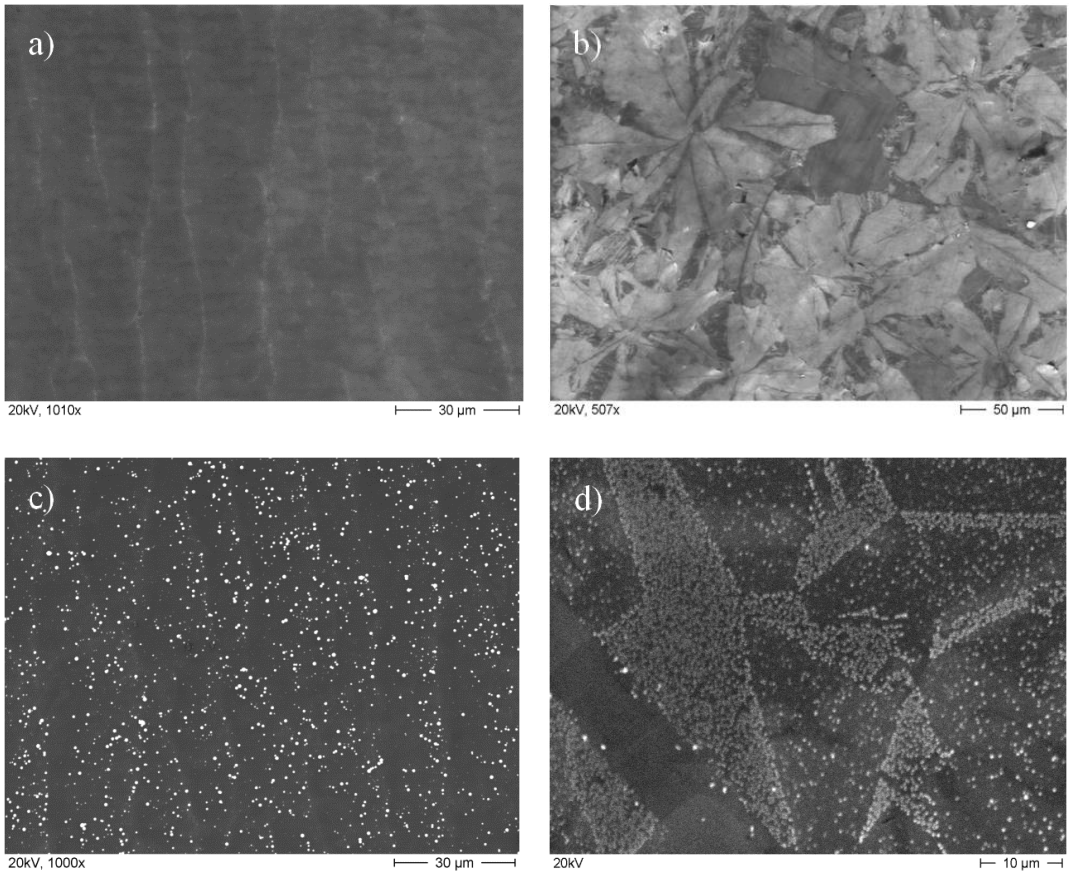


Figure 3.12 SEM of (a,c) (001) heteroepitaxial BDD and (b,d) smooth polycrystalline diamond before and after platinum electrodeposition respectively.

It is clear that Pt nanoparticles preferentially agglomerate on some regions of polycrystalline diamond substrate, leaving other adjacent surfaces with much lower coverage or even nearly bare. This is mainly attributed to the conductivity of different facets associated with varied boron uptakes, which is consistent with the spatial distribution of electrochemical active regions observed from previous SECM measurements. In contrast, a more homogeneous distribution of platinum nanoparticles is discovered on heteroepitaxial single crystal diamond substrate, which is also in line with the SECM results for this material.

The electrochemical activity of both types of diamond was studied further by mapping the electro-activity over an identical area with two different redox mediators: $Ru(NH_3)_6^{3+}$ and $Fe(CN)_6^{4-}$, as presented in **Figure 3.14**. To minimise the influence of topography to SECM imaging, the epitaxial diamond sample underwent chemical-mechanical polishing (CMP) to remove the wavy structure. AFM measurement confirms the smoothness, showing that the RMS roughness of the conductive epitaxial diamond surface is around 0.12 nm in a scan area of 1 × 1 μm^2 in **Figure 3.13**, in contrast to the RMS value of 0.7 nm without polishing.

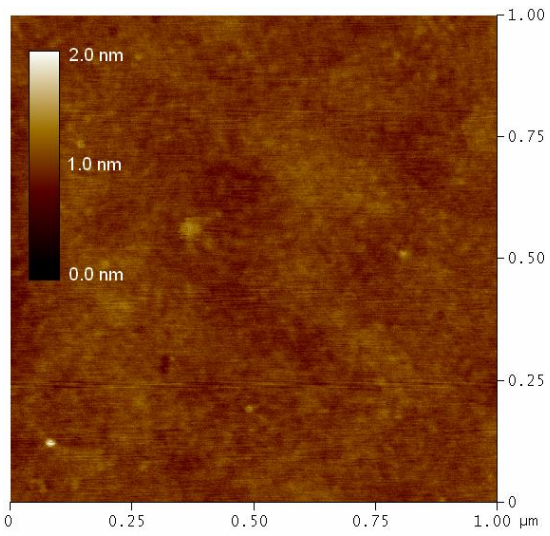


Figure 3.13 AFM image shows the topography of epitaxial diamond with additional mechanical polishing step after the growth of a thin boron doped diamond layer with RMS roughness is only 0.12 nm in a scan area of 1 × 1 μm^2.

The probe was held at -0.4 V and the substrate at 0 V for a $Ru(NH_3)_6^{3+}$ mediator for both types of diamond substrates, and the probe and substrate were biased at 0.4 V and 0 V for $Fe(CN)_6^{4-}$ on polycrystalline diamond, 0.4 V and -0.3 V respectively for $Fe(CN)_6^{4-}$ on single crystal diamond to take account of the wider overpotential for this type of electrode. For polished polycrystalline diamond, the most active region is quite different for $Ru(NH_3)_6^{3+}$ and $Fe(CN)_6^{4-}$, even when an identical area was imaged, as

shown in **Figure 3.14** a) and b). In some regions, such as the region marked with a square, the active areas are the same in both mediators, but in some regions such as the one marked with a circle, the active feature in $Ru(NH_3)_6^{3+}$ corresponds to an inactive feature in $Fe(CN)_6^{4-}$. This discrepancy has been observed before on nanocrystalline diamond, and was interpreted by different electric double layer structures locally on the surface[60]. As discussed previously, $Ru(NH_3)_6^{3+}$ is an outer-sphere electron transfer mediator, and the high electrochemical activity in the SECM image correlates with a high density of electronic states in that region. However, as an inner-sphere redox couple, the electron transfer of $Fe(CN)_6^{3-/4-}$ mostly depends on the surface termination and oxygen-containing functional groups instead of the density of electronic states of the electrode. Therefore the SECM image in $Fe(CN)_6^{4-}$ is a map of surface termination which is quite different from the image using $Ru(NH_3)_6^{3+}$ as the redox mediator.

Different from the behaviour of polycrystalline diamond, interestingly, the heteroepitaxial single crystalline diamond shows an identical region of high electrochemical activity in both $Ru(NH_3)_6^{3+}$ and $Fe(CN)_6^{4-}$ solutions, as presented in **Figure 3.14** c) and d). The horizontal strips are due to subtle bench vibrations when the probe scans over the diamond substrate. Probably this behaviour arises since $Fe(CN)_6^{4-}$ is very sensitive to surface termination and functional groups. On the polycrystalline surface, these vary markedly so the activity of $Fe(CN)_6^{4-}$ shows no correlation with the activity for 'Ruhex' which maps instead the density of states. In contrast the heteroepitaxial diamond has more uniform termination, so in this case both redox couples track variations in the density of states.

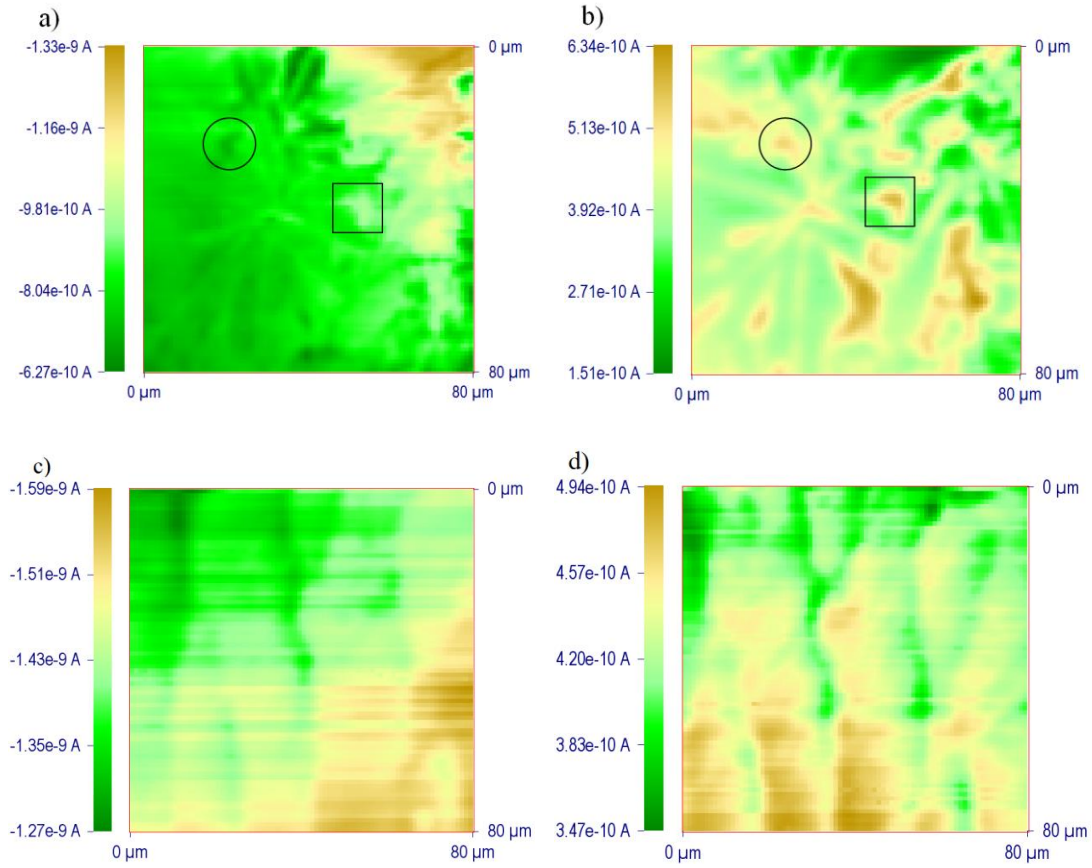


Figure 3.14 SECM of (a,b) smooth polycrystalline and (c,d) (001) heteroepitaxial diamond in (a,c) 1 mM $Ru(NH_3)_6^{3+}$/0.1 M KCl and (b,d) 1 mM $Fe(CN)_6^{4-}$/0.1 M KCl.

3.4 Summarising comments

Electrochemical properties of heteroepitaxial (001) single crystal diamond of a high boron doping level were studied and compared with as-grown and polished smooth polycrystalline diamond. It is observed that:

- The heteroepitaxial diamond exhibits superior merits of electrochemical properties similar to homoepitaxial conducting diamond reported in the literature, with regards to a wide potential window and a low background current.
- The heteroepitaxial diamond shows fairly homogeneous electrochemical activity from impedance and SECM measurements, and electrodeposition experiments.
- A consistent electron transfer rate constant was measured from the *Nicholson*

method, DigiSim simulation and impedance measurement. The rate constant measured in $Ru(NH_3)_6^{3+}$, an outer-sphere electron transfer mediator, is mostly influenced by the density of electronic states at the electrode near the formal potential of this redox mediator. The lower rate constant on heteroepitaxial diamond suggests a lower density of electronic states near the Fermi level, and is in agreement with a lower carrier density from *Mott-Schottky* characterisation.

- The heteroepitaxial diamond presents a large peak-peak separation and a very low charge transfer rate constant for $Fe(CN)_6^{4-}$, an inner-sphere redox mediator that requires sp^2 carbon impurities or oxygen surface termination to catalyse the electron transfer.
- The heteroepitaxial diamond shows a large overpotential for $MV^{+/2+}$ and $MV^{0/+}$ redox systems, and the absence of an MV^0 stripping peak, which probably originates from the band bending and wide space charge region. Both heteroepitaxial single crystalline and as-grown polycrystalline diamond demonstrate a resistance to the adsorption of ADQS, in contrast to a weak adsorption on polished polycrystalline diamond due to mechanically induced surface defects.

Overall it can be concluded that heteroepitaxial diamond is a superior electrode material than polycrystalline forms in terms of many of the characteristics noted above. However the difficulty in producing high boron doping concentrations and slow reaction kinetics in certain instances can also represent a disadvantage. The best diamond material for a given application - single crystal or polycrystalline - will thus depend exactly on that application. However certainly the heteroepitaxial form used here can overcome production and cost difficulties associated with homoepitaxial diamond.

References

[1] R.G. Compton, J.S. Foord, F. Marken, Electroanalysis 15 (2003) 1349-1363.

[2] M.C. Granger, M. Witek, J. Xu, J. Wang, M. Hupert, A. Hanks, M.D. Koppang, J.E. Butler, G. Lucazeau, M. Mermoux, Anal. Chem. 72 (2000) 3793-3804.

[3] G. Fóti, D. Gandini, C. Comninellis, A. Perret, W. Haenni, Electrochem. Solid-State Lett. 2 (1999) 228-230.

[4] E. Brillas, I. Sirés, C. Arias, P.L. Cabot, F. Centellas, R.M. Rodríguez, J.A. Garrido, Chemosphere 58 (2005) 399-406.

[5] J. Weng, J. Xue, J. Wang, J. Ye, H. Cui, F. Sheu, Q. Zhang, Adv. Funct. Mater. 15 (2005) 639-647.

[6] C. Terashima, T.N. Rao, B.V. Sarada, N. Spataru, A. Fujishima, J. Electroanal. Chem. 544 (2003) 65-74.

[7] M. Rodrigo, P. Michaud, I. Duo, M. Panizza, G. Cerisola, C. Comninellis, J. Electrochem. Soc. 148 (2001) D60-D64.

[8] D. Gandini, E. Mahé, P.A. Michaud, W. Haenni, A. Perret, C. Comninellis, J. Appl. Electrochem. 30 (2000) 1345-1350.

[9] M. Panizza, P. Michaud, G. Cerisola, C. Comninellis, Electrochem. Commun. 3 (2001) 336-339.

[10] M.C. Granger, G.M. Swain, J. Electrochem. Soc. 146 (1999) 4551-4558.

[11] J.A. Bennett, J. Wang, Y. Show, G.M. Swain, J. Electrochem. Soc. 151 (2004) E306-E313.

[12] I. Duo, A. Fujishima, C.H. Comninellis, Electrochem. Commun. 5 (2003) 695-700.

[13] L. Diederich, O. Küttel, P. Aebi, L. Schlapbach, Surf. Sci. 418 (1998) 219-239.

[14] T. Kondo, Y. Einaga, B.V. Sarada, T.N. Rao, D.A. Tryk, A. Fujishima, J. Electrochem. Soc. 149 (2002) E179-E184.

[15] R. Ramesham, Sens. Actuators, B: Chem. 50 (1998) 131-139.

[16] J. Van de Lagemaat, D. Vanmaekelbergh, J. Kelly, J. Electroanal. Chem. 475 (1999) 139-151.

[17] Y.V. Pleskov, Y.E. Evstefeeva, M. Krotova, V. Elkin, V. Mazin, V.Y. Mishuk, V. Varnin, I. Teremetskaya, J. Electroanal. Chem. 455 (1998) 139-146.

[18] Y.V. Pleskov, Y.E. Evstefeeva, M. Krotova, V.Y. Mishuk, V. Laptev, Y.N. Pal'yanov, Y.M. Borzdov, Russ. J. Electrochem. 38 (2002) 620-625.

[19] T. Bauer, S. Gsell, M. Schreck, J. Goldfuß, J. Lettieri, D. Schlom, B. Stritzker, Diamond Relat. Mater. 14 (2005) 314-317.

[20] S. Lee, Y. Lifshitz, Nature 424 (2003) 500-501.

[21] B. Stoner, J. Glass, Appl. Phys. Lett. 60 (1992) 698-700.

[22] X. Jiang, C.Ä. Klages, R. Zachai, M. Hartweg, H.Ä. Fusser, Appl. Phys. Lett. 62 (1993) 3438-3440.

[23] S. Wolter, M. McClure, J. Glass, B. Stoner, Appl. Phys. Lett. 66 (1995) 2810-2812.

[24] M. Schreck, F. Hormann, H. Roll, J. Lindner, B. Stritzker, Appl. Phys. Lett. 78 (2001) 192-194.

[25] S. Gsell, T. Bauer, J. Goldfub, M. Schreck, B. Stritzker, Appl. Phys. Lett. 84 (2004) 4541-4543.

[26] T. Teraji, physica status solidi (a) 203 (2006) 3324-3357.

[27] M. Fischer, S. Gsell, M. Schreck, R. Brescia, B. Stritzker, Diamond Relat. Mater. 17 (2008) 1035-1038.

[28] B.R. Stoner, S.R. Sahaida, J.P. Bade, P. Southworth, P.J. Ellis, J. Mater. Res. 8 (1993) 1334-1340.

[29] M.C. Granger, M. Witek, J. Xu, J. Wang, M. Hupert, A. Hanks, M.D. Koppang, J.E. Butler, G. Lucazeau, M. Mermoux, Analytical chemistry 72 (2000) 3793-3804.

[30] I. Duo, C. Levy-Clement, A. Fujishima, C. Comninellis, J. Appl. Electrochem. 34 (2004) 935-943.

[31] R. Ramesham, Thin Solid Films 322 (1998) 158-166.

[32] J.S. Foord, in: R.S. Sussmann (Ed.), CVD Diamond for Electronic Devices and Sensors, John Wiley & Sons, 2009, p. 439.

[33] S.R. Morrison, Electrochemistry at Semiconductor and Oxidized Metal Electrodes, Plenum Press, New York, 1980.

[34] E. Barsoukov, J.R. Macdonald, Impedance spectroscopy: theory, experiment, and applications, Wiley. com, 2005.

[35] N.R. Wilson, S.L. Clewes, M.E. Newton, P.R. Unwin, J.V. Macpherson, J. Phys. Chem. B 110 (2006) 5639-5646.

[36] S. Szunerits, M. Mermoux, A. Crisci, B. Marcus, P. Bouvier, D. Delabouglise, J.-P. Petit, S. Janel, R. Boukherroub, L. Tay, J. Phys. Chem. B 110 (2006) 23888-23897.

[37] K.B. Holt, A.J. Bard, Y. Show, G.M. Swain, J. Phys. Chem. B 108 (2004) 15117-15127.

[38] R.S. Nicholson, Anal. Chem. 37 (1965) 1351-1355.

[39] Z. Galus, Fundamentals of electrochemical analysis, Ellis Horwood, New York, 1994.

[40] N. Vinokur, B. Miller, Y. Avyigal, R. Kalish, J. Electrochem. Soc. 143 (1996) L238-L240.

[41] N. Maleki, A. Safavi, F. Tajabadi, Anal. Chem. 78 (2006) 3820-3826.

[42] P. Chen, R.L. McCreery, Anal. Chem. 68 (1996) 3958-3965.

[43] R.L. McCreery, K.K. Cline, C.A. McDermott, M.T. McDermott, Colloids Surf. Physicochem. Eng. Aspects 93 (1994) 211-219.

[44] K.K. Cline, M.T. McDermott, R.L. McCreery, J. Phys. Chem. 98 (1994) 5314-5319.

[45] A.E. Bohe, J.R. Vilche, K. Juttner, W.J. Lorenz, W. Paatsch, Electrochim. Acta 34 (1989) 1443-1448.

[46] Y.V. Pleskov, V.V. Elkin, M.A. Abaturov, M.D. Krotova, V.Y. Mishuk, V.P. Varnun, I.G. Teremetskaya, J. Electroanal. Chem. 413 (1996) 105-110.

[47] Y.V. Pleskov, Y.E. Evstefeeva, M.D. Krotova, V.V. Elkin, V.M. Mazin, V.Y. Mishuk, V.P. Varnin, I.G. Teremetskaya, J. Electroanal. Chem. 455 (1998) 139-146.

[48] R. Degryse, W.P. Gomes, F. Cardon, J. Vennik, J. Electrochem. Soc. 122 (1975) 711-712.

[49] J. van de Lagemaat, D. Vanmaekelbergh, J.J. Kelly, J. Electroanal. Chem. 475 (1999) 139-151.

[50] M.C. Granger, M. Witek, J.S. Xu, J. Wang, M. Hupert, A. Hanks, M.D. Koppang, J.E. Butler, G. Lucazeau, M. Mermoux, J.W. Strojek, G.M. Swain, Anal. Chem. 72 (2000) 3793-3804.

[51] R. Ramesham, Thin Solid Films 322 (1998) 158-166.

[52] M. Ito, T. Kuwana, J. Electroanal. Chem. Interfacial. Electrochem. 32 (1971) 415-425.

[53] C.L. Bird, A.T. Kuhn, Chem. Soc. Rev. 10 (1981) 49-82.

[54] F.L. Qiu, R.G. Compton, F. Marken, S.J. Wilkins, C.H. Goeting, J.S. Foord, Anal. Chem. 72 (2000) 2362-2370.

[55] J.S. Xu, Q.Y. Chen, G.M. Swain, Anal. Chem. 70 (1998) 3146-3154.

[56] M.P. Soriaga, A.T. Hubbard, J. Am. Chem. Soc. 104 (1982) 2735-2742.

[57] P.-N. Volpe, P. Muret, F. Omnes, J. Achard, F. Silva, O. Brinza, A. Gicquel, Diamond Relat. Mater. 18 (2009) 1205-1210.

[58] K.R. Kneten, R.L. McCreery, Anal. Chem. 64 (1992) 2518-2524.

[59] P.H. Chen, M.A. Fryling, R.L. Mccreery, Anal. Chem. 67 (1995) 3115-3122.

[60] S.H. Wang, G.M. Swain, J. Phys. Chem. C 111 (2007) 3986-3995.

[61] K.B. Holt, A.J. Bard, Y. Show, G.M. Swain, J. Phys. Chem. B 108 (2004) 15117-15127.

[62] M.V. Mirkin, F.R.F. Fan, A.J. Bard, J. Electroanal. Chem. 328 (1992) 47-62.

Chapter 4

Electrodeposition of Pt-PrO_x Core-shell Catalyst on Boron Doped Diamond for Methanol Electro-oxidation

4.1 Introduction

In recent decades, with significantly high energy demands, fast depletion of fossil, coal and oil resources and highly concerned pollution issues, some new effective energy systems and devices with low emissions have attracted increasing interest. Hydrogen fuel cells are considered as promising devices as they can provide very high energy without threatening the environment, with water as the resulting reaction product[1]. However, the production, storage and transportation of hydrogen are the main barriers at the current technological stage, and applications are in limited areas due in part to high cost and poor durability concerns[2]. For that reason, direct methanol fuel cells (DMFCs), using liquid and renewable methanol as the energy source, have been considered as alternative candidates to overcome the previous problems with efficient fuel utilisation along with comparatively easier strategies for fuel feeding[3, 4].

There are at least two key factors to determine the overall performance of DMFCs centred in terms of the membrane and the catalyst. The former is preferentially applied to overcome the crossover effects from methanol while the latter is broadly investigated to boost the sluggish kinetics in methanol oxidation[5]. A good catalyst candidate is mainly concerned with two aspects in terms of improved catalytic performance, *e.g.* activity, durability and reduced cost that allows practical applications.

Platinum (Pt) is always considered as a good material for various chemical and

electrochemical reactions for its excellent catalytic properties and becomes the most favourable catalyst material in DMFC application[6, 7]. However, in electro-oxidation of methanol, the oxidation is generally believed to follow a dual pathway comprising direct and indirect processes[8]. In the indirect pathway, Pt is prone to be poisoned by incompletely oxidised carbonaceous intermediates such as carbon monoxide (CO) which can be produced in methanol oxidation through stepwise dehydrogenation and harms the fuel cell performance[5, 9, 10]. The addition of a second metal is regarded as an effective approach to overcome the problem by promoting the oxidisation of adsorbed CO (CO_{ads}) and therefore alleviates the poisoning effects on the adjacent Pt nanoparticles. So far, platinum-ruthenium (Pt-Ru) binary metallic catalysts are well recognised as the most promising material in this regard[11, 12]. Ru additive to Pt can improve the tolerance of the whole structure against CO poisoning significantly through the reaction between CO_{ads} species and Ru-OH_{ads} that comes from the conversion of adsorbed water species on the Ru surface[13].

Although a Pt-Ru bimetallic catalyst is broadly used in catalysing methanol oxidation, both Pt and Ru are noble metals and are thus not totally cost-effective. Apart from alloying Pt with such oxophilic metals, employment of conductive oxides as anode materials is considered as the other viable option. Recently, certain oxides such as WO_3[14], RuO_2[15], ZrO_2[16], MgO[17] and CeO_2[18] have been observed to be able to enhance the catalytic activity in alcohol electro-oxidation using ethanol or methanol. Among them, ceria (CeO_2) shows a number of distinct characteristics that puts this series of oxides of great interest for catalytic studies. However, although CeO_2 exhibits promising properties in catalysing the alcohol electro-oxidation, the reaction mechanism is still under investigation[19]. Other rare earth oxides also tend to be studied in parallel

to find out whether they can overcome the problems above to achieve better performance. Praseodymium oxide (PrO_x)[20] is considered as a potentially competitive substitute for ceria as it has the same fluorite structure. The cation states can switch between +3 and +4, allowing the varied oxygen deficiencies to affect the methanol oxidation process significantly.

It is suggested that this oxide is deposited onto the catalyst Pt nanoparticles and partially cover the surface, forming a so-called 'core-shell' structure[21] to improve the catalytic activity of methanol electro-oxidation while it enhances the system tolerance by protecting the Pt nanoparticles underneath from being poisoned by CO_{ads} simultaneously. 'Spill-over' processes[22] are believed to occur whereby water species are adsorbed onto active oxide sites to interact with poisoning carbonaceous groups on the adjacent Pt terraces. A fully oxidised product carbon dioxide (CO_2) will be generated while clean Pt and PrO_x are released simultaneously through the 'spill-over' effects.

Although some previous work had employed PrO_x with Pt in methanol electro-oxidation studies, almost all of them used relatively complicated wet chemical approaches to synthesise the bifunctional systems[6, 23]. Hereby in this chapter, we were aiming to explore a simple electrochemical approach to prepare core-shell structures where we decorated Pt nanoparticles onto bare boron-doped diamond electrodes before its subsequent coating of a PrO_x thin film again via electrochemical deposition. As having been briefly described in *Chapter* 1, BDD is a new promising carbon substrate with excellent electrochemical properties such as a low background current, a wide potential window, chemical inertness and mechanical durability[24-26]. There is some interest in

the use of diamond in fuel cell type applications because of its stability and resistance to electrocorrosion[27, 28]. Many electrochemical approaches for the deposition of platinum based catalytic metals on BDD have been widely reported[29-31]. In this project, we utilised a particular two-stage protocol. An instantaneous nucleation began when an initial stepped potential approach was carried out, followed by a potentiostatic method[31, 32] used to enlarge nuclei into strongly adsorbed particles on the substrate surface. This specific route was found to be able to deposit more platinum nanoparticles with a higher stability compared with either single stepped potential or potentiostatic process alone. A typical electrodeposition protocol of praseodymium oxide reported by S. Shrestha *et al*[33, 34] was selected for the decoration of praseodymium oxide on platinum covered BDD, forming the supposed porous core-shell structure[35] afterwards. Once the successive electrodeposition of Pt and PrO_x was accomplished, the electrochemical performance of the modified electrodes was assessed by both CVs and chronoamperometric approaches.

4.2 Experimental

4.2.1 Materials, instruments and techniques

Free-standing un-polished polycrystalline CVD diamond with a boron-doping content higher than 10^{20} cm^3 and a grain size of ~ 50 nm was obtained from Element Six Co. and used as the working electrode in all the experiments. **Figure 4.1** shows the SEM characterisation of a clean bare BDD electrode surface. The electrodes were mounted into a home-built PTFE holder with an area of approximately 0.45 cm^2 exposed to the electrolytes.

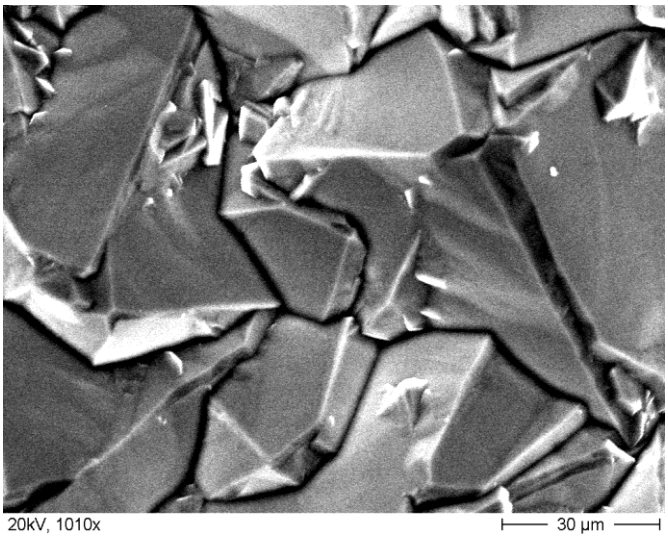


Figure 4.1 SEM of un-polished polycrystalline BDD electrode surface

As already mentioned in *Chapter* 3, all the electrochemical experiments were conducted using an Autolab electrochemical workstation (PGSTAT128N, Eco Chemie, Netherlands) at room temperature (21 °C). A standard three-electrode system comprising BDD working electrode, Pt wire counter electrode and Ag/AgCl reference electrode was also applied. SEM characterisation was operated using a Hitachi S530 SEM with a 20 kV acceleration voltage and XPS measurements were conducted by utilising a Al-Kα X-ray source at 1486.6 eV along with a hemispherical electron energy analyser.

Potassium hexachloroplatinate (IV) (K_2PtCl_6, 98%) was purchased from Alfa Aesar, and praseodymium nitrate hexahydrate ($Pr(NO_3)_3 \cdot 6H_2O$, 99.9%), hydrogen peroxide (H_2O_2, 50 wt.%) and HPLC grade methanol were purchased from Sigma-Aldrich. Platinum, nominally 20% on carbon black was obtained from Alfa Aesar. All the Diamond suspensions and alumina powders with different grades were purchased from Buehler.

4.2.2 Electrodeposition of Pt and PrO_x

Before each deposition, the BDD electrodes were polished with diamond suspension (5 μm and 1 μm respectively) and different grades of alumina (*i.e.* 5 μm, 1 μm and 0.3 μm) consecutively prior to any series of electrochemical measurements to ensure the effects of any previous electrode usage were eliminated by removing all adsorbed materials. The electrodes were then cleaned by ultrasonication with acetone and Milli-Q water sequentially to remove any alumina residues on the surface before being scanned at 0.1 V HNO_3 from -1.5 V to 2.5 V for at least 20 sweep cycles in CV to produce a chemically well-defined surface termination of the diamond.

It has been reported that Pt nanoparticles can be successfully electrodeposited by using cyclic voltammetry[36], chronoamperometry[37], potential step deposition[38] and double-pulse[39] methods. Potential step deposition (PSD), in which the potential is stepped towards more negative potential is known as an effective route to fine-tune the number of metallic sites and particle size, producing a well-dispersed and homogeneous coverage on electrode surfaces[40]. However, the depositing process is comparatively sluggish compared to the potentiostatic deposition achieved by holding the potential at a fixed appropriate value. Hereby a two-stage protocol was employed in which abundant Pt nuclei were initially synthesised on the diamond surface by PSD process, stepping the potential from 0.25 V to -0.2 V in 0.05 V steps of 10 s duration each in a solution comprising of 2 mM K_2PtCl_6 in 0.5 M H_2SO_4. After this process was accomplished, the potential was then held at a constant -0.2 V for approximate 1000 s, allowing the Pt nuclei to grow larger and more stable until the desired amount of Pt was successfully deposited on the surface as determined from coulometric calculation using the precursor solution above. A typical final Pt loading of 230 μg calculated from coulometry on the

BDD surface was applied in this chapter.

Once the Pt nanoparticles had been coated on the electrode surface, oxygen deficient praseodymium oxide was then electrodeposited as described previously[33, 34]. This procedure was carried out by CV at a negative potential range from 0 to -1.5 V at a scan rate of 0.02 V/s in 0.1 M KCl solution containing 5 mM $Pr(NO_3)_3$ and 10 mM H_2O_2 for a fixed number of sweep cycles. The local pH at the electrode surface was raised in electrolysis process due to the reduction of H_2O_2 into OH^-, resulting in the precipitation of the oxide on the surface of the modified electrode.

4.3 Characterisation of Pt and PrO_x-Pt/ BDDEs

4.3.1 Electrochemical characterisation of Pt-BDDE structures

After Pt electrodeposition using the two-stage protocol as described previously, CV studies were carried out in 0.5 M H_2SO_4 to measure the electrochemical properties of the Pt nanoparticles as shown in **Figure 4.2**. There are several typical peaks in a single cyclic scan. The prominent cathodic peak appearing at around 0.4 V is attributed to the electrochemical reduction of oxidised ionic Pt species, produced in the anodic scan, to their metallic state. The cathodic peaks around 0 to -0.2 V are due to the formation of adsorbed hydrogen produced by reduction of H^+ to form adsorbed H_2 monolayers on the surface of different facets of Pt nanoparticles[41, 42]. This is reversed in the anodic scan. These peaks are much better defined under the two-step deposition route rather than applying either single stage potentiostatic deposition or PSD as shown in **Figure 4.2** Below -0.2 V, the reduction of H^+ to gaseous hydrogen (cathodic scan) and oxidation of adsorbed hydrogen (anionic scan) is seen.

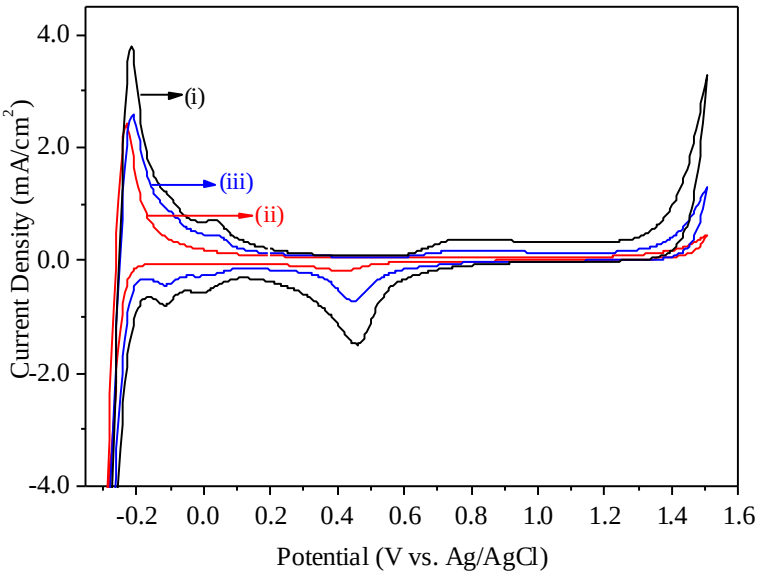


Figure 4.2 CV of the Pt modified BDD following the two-stage electrodeposition process (i) to produce a loading of approximately 230 μg at a scan rate of 0.05 V/s. The other two traces correspond to lower Pt loadings using single stage of PSD method (ii) and potentiostatic deposition method (iii)

The charge passed in the H adsorption-desorption region was integrated to 9.01 mC/cm^2 after a typical Pt deposition experiment. Since a monolayer of H adsorption corresponds to 0.21 mC/cm^2[43], the surface area of the electrodeposited Pt nanoparticles can thus be calculated as 42.90 cm^2 per cm^2 substrate, corresponding to a specific surface area S of the Pt of 8.57 m^2/g with a Pt loading of 506 μg/cm^2 as mentioned before. If all the deposited Pt nanoparticles are assumed to be of a spherical shape, the specific surface area of each particle can be explained as

$$S = 4n\pi(d/2)^2/m \qquad 4.1$$

and the whole amount of deposited Pt nanoparticles m (in weight) is therefore expressed as

$$m = \rho V = 4/3n\pi(d/2)^3\rho \qquad 4.2$$

where n is the number of deposited Pt nanoparticles, ρ is the density of Pt (21.45 g/cm^3)

and d is the particle diameter, which can be simply estimated as

$$d = 6/(\rho \times S) \quad 4.3$$

This leads to a Pt particle size of 32 nm at this loading level theoretically although much smaller particle size of approximate 5 nm could be obtained when the amount of Pt was significantly reduced, resulting in a much higher specific surface area at around 50 m^2/g. If only the single PSD process or potentiostatic deposition step was carried out, then lower loadings were produced. Somewhat as expected PSD produced the lowest loading, presumably due to slow nucleation; because of this the particle size was the smallest. Potentiostatic deposition alone produced a somewhat smaller loading than the combined two-step result. All the detailed data are shown in **Table 4.1**.

Table 4.1 Characterisation of Pt electrodeposited on diamond surfaces applying differing techniques.

	PSD	Potentiostatic	PSD + Potentiostatic
Pt loading (μg)	21.73	146.40	227.70
H desorption charge (mC/cm^2)	4.16	6.39	9.01
Electrochemical active area (ECA, cm^2/cm^2)	19.88	30.40	42.91
Specific surface area (m^2/g)	41.51	9.43	8.57
Particle size (nm)	6.74	29.66	32.64

4.3.2 Electrochemical characterisation of PrO_x-Pt deposited BDDEs

As the two-stage deposition protocol had produced stable Pt nanoparticles on a BDD surface at a desired loading, an oxygen deficient PrO_x film could thus be electrodeposited successively using the CV technique as described before[33, 34]. After PrO_x was coated, the modified electrode was then electrochemically characterised using CV in different electrolytes. Similar to the protocol applied after Pt coating, CV was firstly carried out in 0.5 M H_2SO_4 after successive PrO_x deposition from 1 to 3 sweep cycles. It is observed that the electrochemical activity of the deposited Pt nanoparticles,

as measured by means of the oxidation of the adsorbed hydrogen monolayer at around -0.2 V shown in **Figure 4.2**, attenuated rapidly as the PrO_x layer thickens with increasing number of deposition scans. The peak current in the H-desorption region is plotted as a function of the number of PrO_x deposition scans in **Figure 4.3**. After 3 deposition scans, the signal from the H-desorption peak can no longer be observed. This result suggests that the Pt nanoparticles could be effectively passivated during the PrO_x decoration, and that a too thick loading of PrO_x might entirely block the electrochemical activity of the underlying Pt.

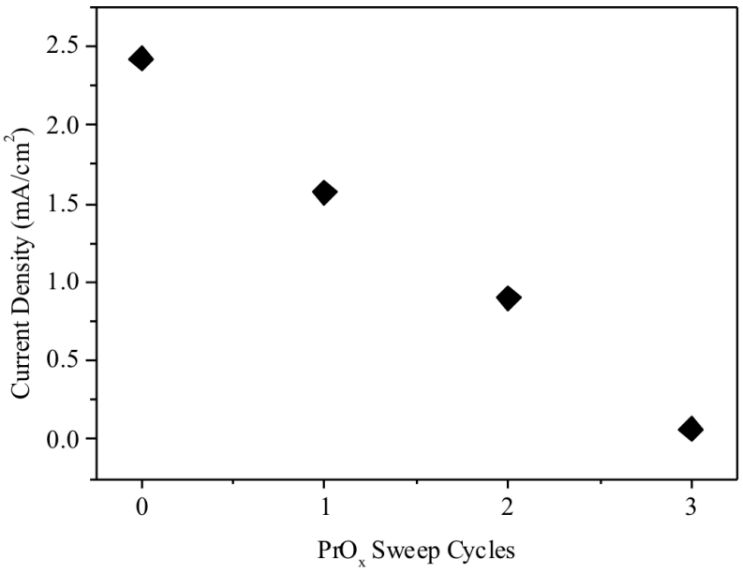


Figure 4.3 H-desorption peak current height from decorated Pt/BDD electrode in 0.5 M H_2SO_4 for differing PrO_x deposition scans.

The effect of this oxide layer on the electrochemical properties of the interface was also investigated by using different redox electrolytes, *i.e.* $Ru(NH_3)_6^{2+/3+}$, $FcCH_2OH^{0/+}$ and $IrCl_6^{2-/3-}$ representing different electrostatic charge. In **Figure 4.4**, it can be seen that the interface becomes progressively deactivated with the increasing deposition scans in both $Ru(NH_3)_6^{2+/3+}$ and $FcCH_2OH^{0/+}$ which show high activity on the bare BDD electrode surface. However, although the oxide layer covers the whole diamond surface

area, as judged by the reduced H desorption, some redox activity is still retained with these couples. The CV profiles lose their 'peaked' responses, becoming more sigmoidal as is typically observed if the electrode gains more 'microelectrode array' character, typical of small patches of active regions separated by passive electrode regions, although the hysteresis seen between the anodic and cathodic scans shows that this is only a partial conversion in character.

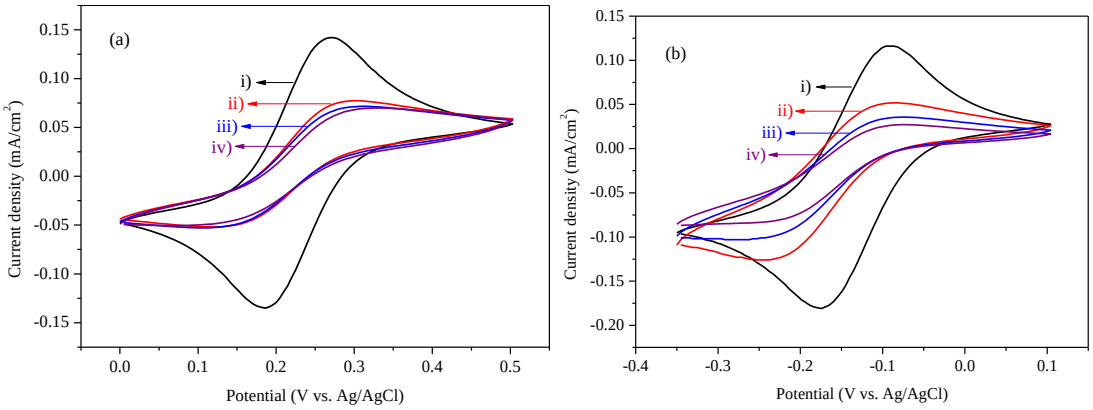


Figure 4.4 CV of 1 mM a) $FcCH_2OH^{0/+}$ and b) $Ru(NH_3)_6^{2+/3+}$ in 0.1 M KCl on clean BDD surface (i) and after 1,2 and 3 oxide deposition scans (ii, iii, iv)

The signal response is found to be enhanced in CV for anionic redox couples such as $IrCl_6^{2-/3-}$ shown in **Figure 4.5**, suggesting this oxygen deficient film can selectively adsorb certain chemical species and accumulate them in the region of the reaction interface near the electrode surface. The freshly deposited PrO_x layer was confirmed as strongly positively charged in *zeta* potential measurement (see *Chapter* 6) therefore it preferentially attracts the anionic chemical species while blocking or repelling the cationic and neutral species. The detailed surface properties of this layer and how it worked against various species will be comprehensively discussed in *Chapter* 6.

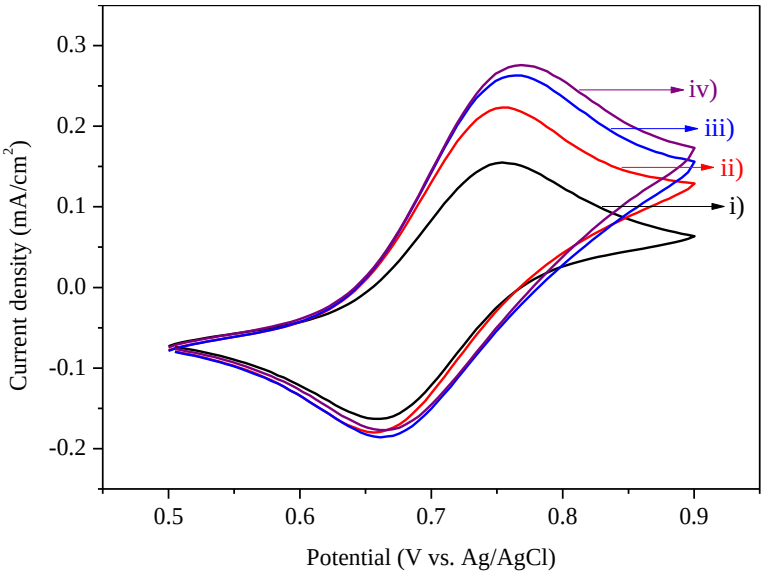
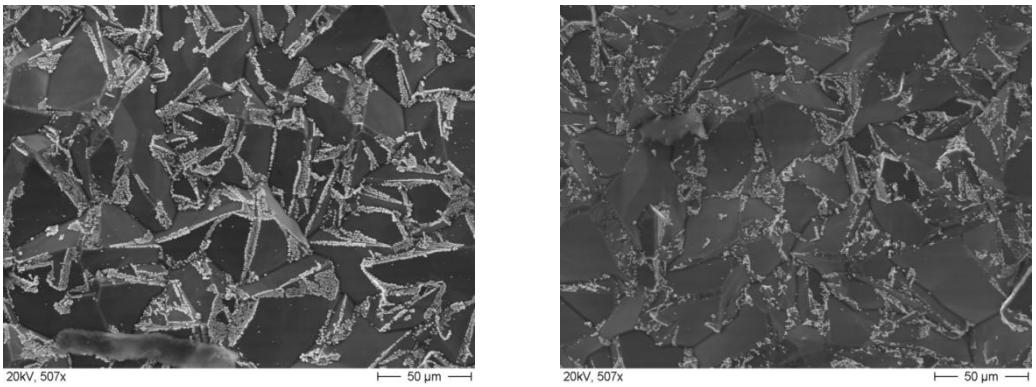


Figure 4.5 CV of 1 mM $IrCl_6^{2-/3-}$ in 0.1 M KCl on clean BDD surface (i) and after 1,2 and 3 oxide deposition scans (ii, iii, iv).

4.3.3 Surface characterisation of Pt and PrO_x/Pt coated BDD

4.3.3.1 SEM characterisation of Pt coated BDD

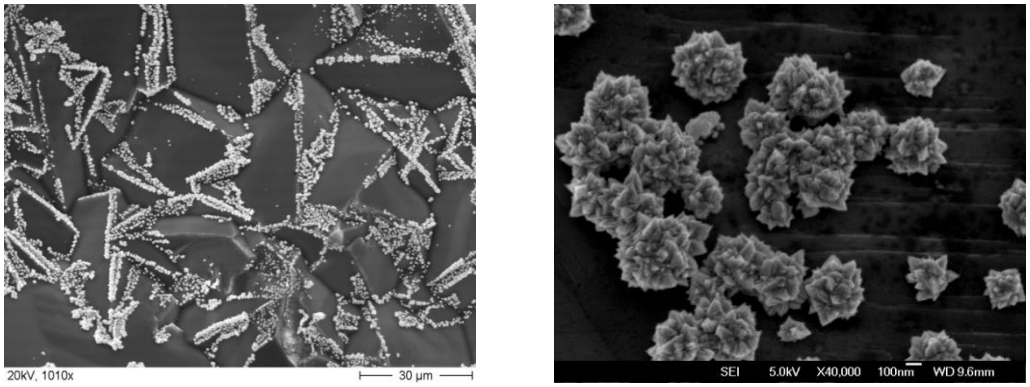
Low resolution SEM was used to characterise the electrode surface after the Pt electrodeposition. The surface morphologies of electrodes after independent single PSD and potentiostatic routes are exhibited in **Figure 4.6**, respectively. From the results in **Table 4.1** concerning Pt loading, the potentiostatic approach presents a much higher Pt loading against PSD method as expected. In both cases it can be seen that the Pt is deposited very non-uniformly on the diamond surface. This is believed to arise since the [B] dopant is incorporated during CVD in differing concentrations, depending on the crystallographic diamond facet exposed, hence some crystallites can undergo fast electrodeposition since they are highly conductive, whereas others show a slow rate of electrodeposition.[44, 45]



a) b)

Figure 4.6 Low resolution SEM of Pt deposited BDD electrode using single a) potentiostatic method and b) Potential step deposition.

For the Pt-deposited BDD under the two-stage process, SEM was operated under both low and high resolutions. Under low resolution SEM shown in **Figure 4.7** a), it actually depicts Pt at a higher loading dispersed over the diamond electrode compared with either single PSD or potentiostatic technique. The discrepancy between the estimated particle size shown in **Table 4.1** and the actual value seems to arise further. This is mainly because the Pt particles observed under the low resolution microscopy are actually crystalline aggregates rather than single particles which can be seen clearly in the high resolution micrograph in **Figure 4.7** b). Special 'nano-flower' structured Pt clusters are observed with sizes from around 100 to 350 nm. Due to the porosity of the particles and the high degree of surface roughness caused by crystalline aggregation, the actual electrochemical active area (ECA) of Pt deposits is much larger than the expected value obtained for smooth compact loadings with a spherical shape.

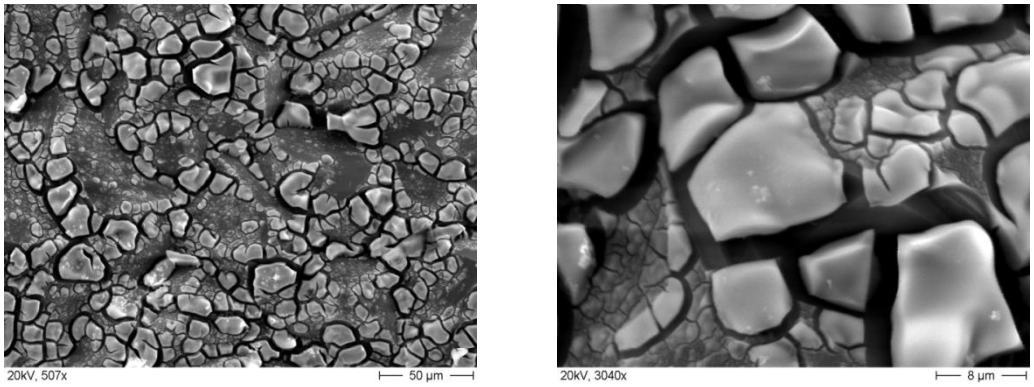


a) b)

Figure 4.7 SEM of Pt/BDD produced by the two-stage Pt deposition process at a) low and b) high resolution.

4.1.1.1 SEM characterisation of PrO_x-Pt deposited BDD

After the PrO_x deposition with differing scan numbers, the surface morphology of the modified BDD electrode was characterised again under SEM. If the depositing process lasted too long, *e.g.* more than 10 scans were carried out, the surface was observed as almost completely blocked with a significant amount of large agglomerates of PrO_x as shown in **Figure 4.8** a) at low resolution. A high resolution SEM in **Figure 4.8** b), shows the microstructure more clearly. A characteristic feature is the irregular pattern of cracking seen in the deposited layer. It is likely that this occurs in the drying process required before SEM analysis takes place. Due to the volume reduction this brings about, this is accommodated by the presumably fairly uniform layer deposited originally cracking into small crystallites. It is interesting that the marked lack of homogeneity seen in the Pt deposition is not discovered here. This is because of the differing mechanisms in the two cases. For Pt, the deposition process is driven by localised electron transfer at the diamond/electrolyte interface; for the oxide deposition, it is however driven by the diffusion of hydroxide into solution, and precipitation of the oxide, so is much less localised in nature. It is clear that at this high oxide coverage, the concept of core-shell nanostructures can scarcely be said as achieved.



a) b)

Figure 4.8 SEM of PrO_x-Pt/BDD produced by PrO_x electrodeposition for 10 CV scans under a) low and b) high resolution.

However, the layer thickening process can be controlled by reducing the number of scans used in the oxide deposition process. **Figure 4.9** depicts the SEM image of a modified BDD surface after successive electrodeposition of Pt and PrO_x, in which 3 CV scans was applied in coating PrO_x at 0.02 V/s. Now the layer can be seen to consist of particles. The particle size observed under high resolution is approximate 1µm, which is at least 2 – 3 times larger than that of the pure Pt coated BDD. This result suggests that most Pt particles are selectively and partially covered by PrO_x deposits while some tiny Pt residues might remain un-coated. This is more suggestive of the formation of coated Pt particles desired in the original aims. The structures formed are examined in more detail below using spectroscopy.

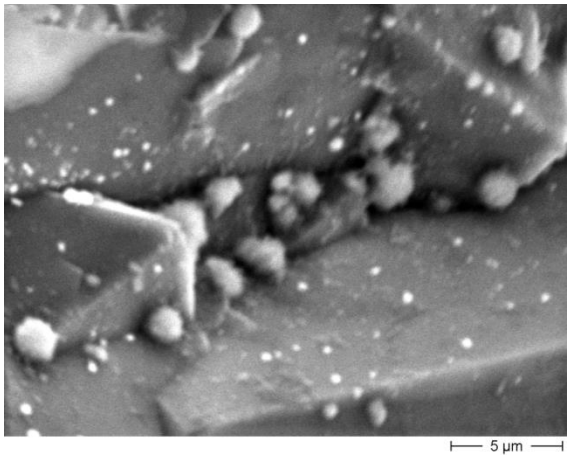


Figure 4.9 High resolution SEM of PrO_x-Pt/BDD produced by PrO_x electrodeposition for 3 CV scans.

4.3.4 XPS characterisation of Pt and PrO_x-Pt deposited BDDEs

4.3.4.1 XPS characterisation of Pt deposited BDDEs

As the surface morphology was investigated under SEM, XPS spectra were applied during stages of the deposition process to characterise the elemental composition and chemical state for both Pt and PrOx-Pt decorated BDD electrodes. **Figure 4.10** shows a typical XPS spectrum of Pt $4f_{7/2}$ and Pt $4f_{5/2}$ after electrodeposition of Pt. All the peak positions were calibrated to the standard C 1s peak at 284.6 eV. A peak appears in the Pt $4f_{7/2}$ spectral region at 71 eV, indicating Pt attached on the surface in its metallic state[46]. After the spectra fitting, an approximate 3.16% compositional ratio of Pt is estimated as shown in **Table 4.2**.

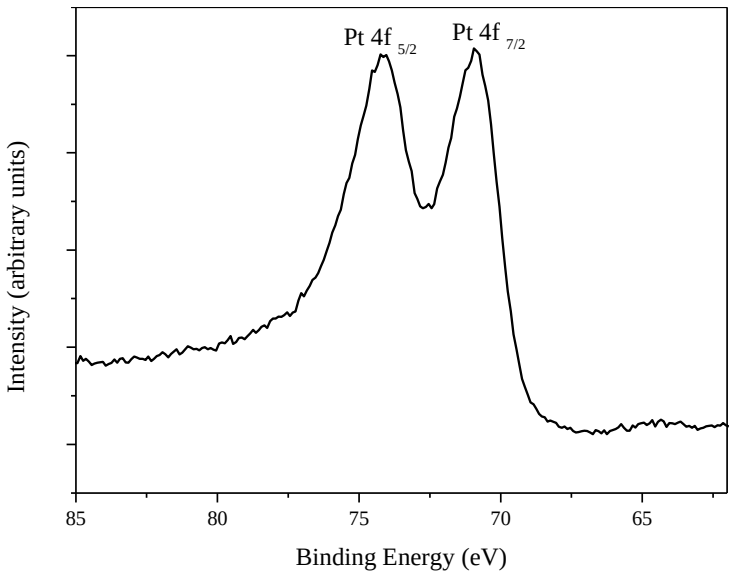


Figure 4.10 XPS spectrum of Pt 4f peaks after two-stage electrodeposition process

4.3.4.2 XPS characterisation of PrO_x-Pt deposited BDDEs

After the PrO_x electrodeposition process on the Pt modified surface, XPS was mainly utilised to investigate whether the oxide layer had been truly decorated along with the variation in Pt 4f spectra. It was found that Pt 4f spectral region shows no change in the

peak profile, however, it suffers a reduced spectral intensity down to around 20 – 25% of its initial value in the presence of the oxide layer as shown in **Figure 4.11** a). The observation confirms that with proper conditions for oxide coating, a thin PrO_x film can be deposited on the Pt with a thickness of the order of the XPS sampling depth ~ 2 nm.

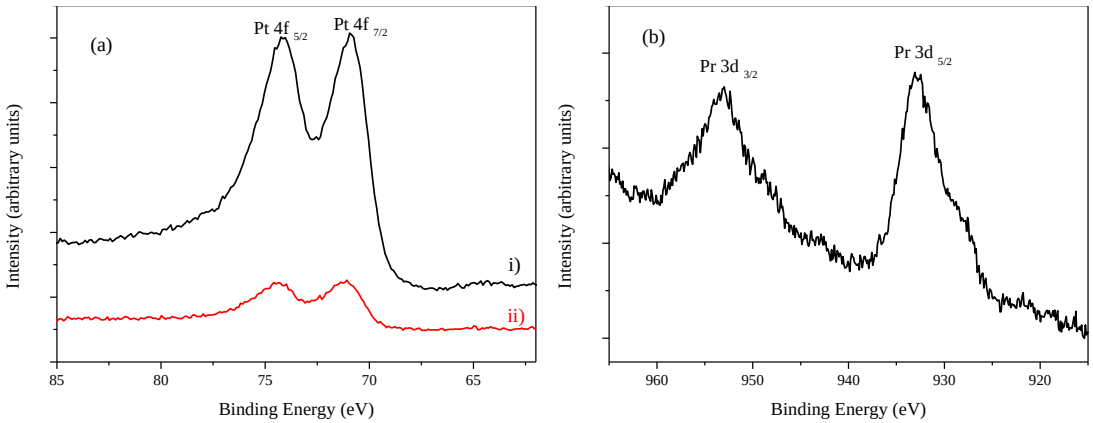


Figure 4.11 XPS spectra of a) Pt 4f spectral region before (i) and after (ii) PrO_x electrodeposition, b) Pr 3d region after PrO_x electrodeposition.

As for the deposited PrO_x, a characteristic multiplet splitting pattern is observed as expected for this oxide with the Pr $3d_{5/2}$ peak appearing at about 935 eV along with Pr $3d_{3/2}$ arising about 20 eV higher (**Figure 4.11** b)). Comparison with standard spectra show the PrO_x layer is more characteristic of Pr (III) than Pr (IV), although some low concentration of the higher oxidation state is suggested[47]. After 3 depositing scans under the conditions described above, if we assume a simple exponential decay of the Pt 4f signal due to the presence of the oxide over-layer and a mean free path of Pt 4f electrons of 1.6 nm[48], then the data suggest that an oxide layer of around 2.3 nm is present.

The compositional variation of each element after successive Pt and PrO_x electrodeposition was calculated by applying its characteristic peak area and ASF[49,

50] as represented in **Table 4.2**. The Pt content drops considerably from 3.16% to less than 0.70%, which is tightly correlated to the 20 – 25% remaining intensity observed from the spectrum. The Pr concentration in the final structure is seen to be significantly less than that of the original amount of Pt which again is consistent with a thin layer PrO_x coating in comparison with the size of the Pt particles. It is also interesting to note that whereas the Pt signal is strongly attenuated by the PrO_x deposition, the C 1s signal has little attenuation. This suggests that the PrO_x coating is preferentially associated with the Pt nanoparticles rather than the diamond electrode underneath, again in agreement with formation of Pt/PrO_x core-shell nanostructures.

Table 4.2 The elemental composition of Pt and PrO_x-Pt decorated BDD surface.

a) After two-stage of Pt electrodeposition

	Peak area	ASF	Peak area/ASF	Composition (%)
Pt 4f	32409	4.4	7284	3.16
C 1s	45958	0.24	183832	79.94
O 1s	25635	0.66	38842	16.9

b) After successive PrO_x electrodeposition by CV

	Peak area	ASF	Peak area/ASF	Composition (%)
Pt 4f	5264	4.4	1196	0.68
C 1s	33068	0.24	132273	75.62
O 1s	26334	0.66	39900	22.81
Pr $3d_{5/2}$	13850	9.0	1538	0.88

4.4 Electrochemical oxidation of methanol on PrO_x-Pt/ BDD

4.4.1 The principle of methanol electro-oxidation

The above work has confirmed that Pt could be successfully deposited onto the BDD surface through a two-stage protocol and the particles could be successfully coated by the PrO_x thin layer afterwards. The remaining part of the research comprised the measurement of this specific structure with regard to the electrochemical oxidation of

methanol to find out whether improved catalytic activity could be achieved and the well-known poisoning effects could also be alleviated with the oxide layer coverage.

CV is a most widely used technique to assess the performance of catalysed methanol electro-oxidation[51] as shown in **Figure 4.12** below and it typically exhibits two different oxidation peaks in an entire cycle. In this case CV scanning usually starts at 0 V at which no electrochemical reaction occurs and then goes towards the more positive potential before turning to the reverse pathway. The first peak arising at the comparatively higher potential is seen in the forward scan with a peak current density I_f, which is attributed to the increase of oxidation kinetics with higher potential at the electrode surface. Normally the magnitude of this peak is significantly below the diffusion limit. The ideal complete oxidation of methanol will fully generate carbon dioxide as the final product, however this process will be inevitably hindered as the electrode surface is passivated with stable adsorbed incompletely oxidised species from the real methanol oxidation process[52, 53]. After the oxidation current reaches the peak value, it begins to drop rapidly due to this effect. During the cathodic scan, another peak appears at lower potential value, which is ascribed to re-oxidisation of the adsorbed carbonaceous species as mentioned before thus reactivating the electrode surface. The peak current density I_b develops as a consequence in the backward scan process.

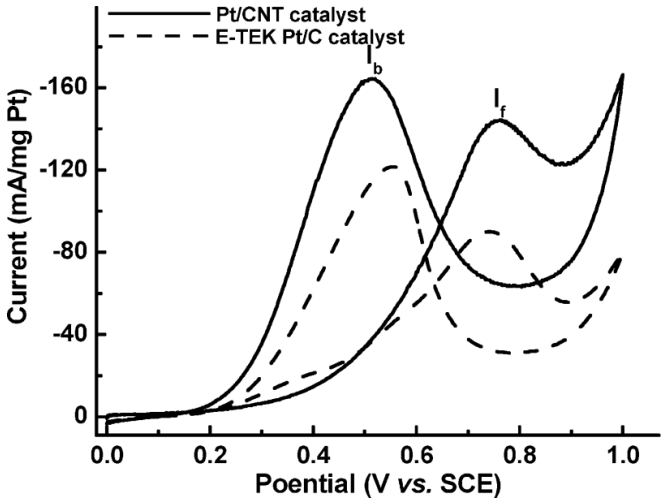


Figure 4.12 Typical electrochemical oxidation of methanol on Pt modified electrodes[51]

Hereby the overall performance of the electrode in methanol electro-oxidation can be mainly assessed by two factors. A higher I_f indicates a stronger catalytic activity of oxidising the methanol directly into carbon dioxide and a higher ratio of I_f/I_b suggests there are fewer incompletely oxidised carbonaceous species adsorbed on the electrode surface in the forward scan[51, 54, 55]. These deductions have been mainly arrived at, since electrodes which show these characteristics in CV, show good practical performance in a fuel cell. Conversely, either a low I_f or low I_f/I_b value implies the disadvantageous performance of the electrode, normally arising from excessive accumulation of carbonaceous residues on the catalyst surface. The two factors above make a combined measurement of the resistance to the poisoning effects by adsorbed species.

4.4.2 Methanol electrooxidation on Pt and PrO_x-Pt modified BDDEs

In this work, before testing the methanol electro-oxidation, a stringent cleaning pre-treatment was operated by potential-cycling in 0.5 M H_2SO_4 over the supported Pt nanoparticles initially. As shown in **Figure 4.13**, compared with the surface without any

cleaning process, the peak current intensity increases by around 40%. It is proposed that[56, 57] the potential cycling using H_2SO_4 within this range could bring a large number of oxygen-containing functional groups on the electrode surface since the potential goes high enough into the oxygen evolution region. These species might be involved in the electro-oxidation of methanol, enhancing the catalytic activity by removing the temporally adsorbed poisoning species. An enhanced area due to electrode roughening could also be involved. However, this effect seems to be attenuated rapidly with continuous CV scanning in methanol electro-oxidation testing. Both forward and backward peaks drop prominently after only 3 successive sweep cycles and even go below the initial values if more scans are applied. All the functional groups are supposed to be consumed gradually in each scanning cycle, leaving more surface area unprotected under the poisoning of the adsorbed carbonaceous species. The resistance of the electrode is weakened successively, confirming the purely Pt modified electrode is vulnerable against the poisoning effects during methanol electro-oxidation.

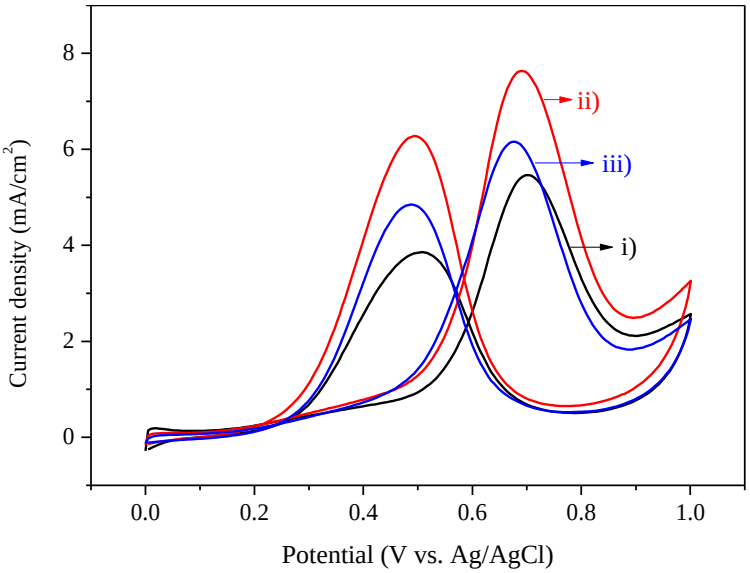


Figure 4.13 CVs of i) untreated Pt/BDD, ii) pre-treated Pt/BDD and iii) pre-treated Pt/BDD after 3 successive scans at a scan rate of 50 mV/s in 1 M CH_3OH and 0.5 M H_2SO_4.

With the PrO_x deposits on the surface, the current density signals are seen to be enhanced by about 15 – 30% compared with purely Pt covered electrodes as shown in **Figure 4.14** a) and b) respectively. The same stringent cleaning process was also carried out after Pt deposition before the series of measurements for methanol electro-oxidation on Pt and PrO_x/Pt deposited BDD electrodes. Apart from the current enhancement achieved, the electrode further modified by PrO_x presented much better reproducibility for methanol electro-oxidation measurements as the peak current intensity of either the forward or backward scan remains virtually constant as seen in the very first scan rather than decaying rapidly as on the pure Pt decorated surface.

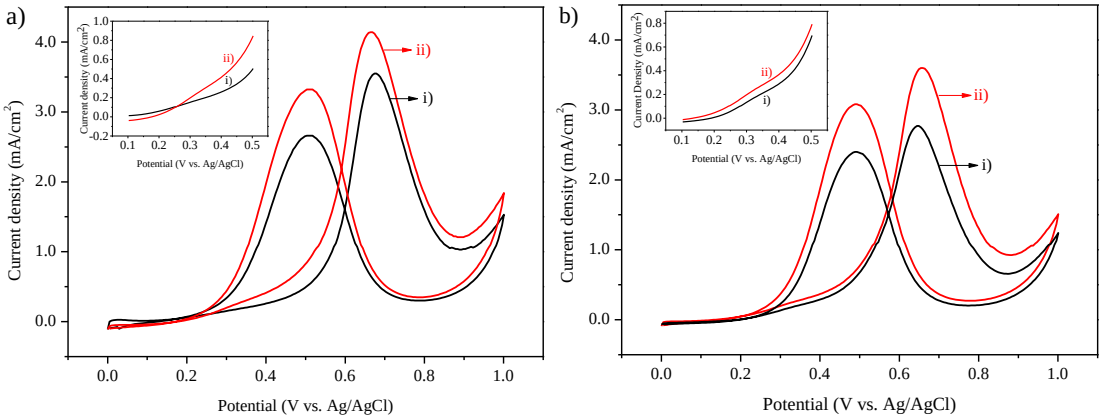


Figure 4.14 CVs of i) cleaned Pt/BDD, ii) PrO_x/Pt-BDD in 1 M CH_3OH and 0.5 M H_2SO_4 at a scan rate of 50 mV/s with a) higher peak intensity and b) smaller peak intensity (correlating to slightly differing PrO_x loadings) variation. Insets: the onset potential variation after the PrO_x electrodeposition.

Apart from the influence in controlling current density and tendency for poisoning, the variation of onset potential is the other noticeable aspect after the PrO_x coating on the surface. In both cases above, if the onset potential is defined as the potential at which 10% of the current level at the peak potential is achieved[58], its value relative to the I_f peak moves to more negative values at different extents, varying from 0.454 to 0.401 V and from 0.410 to 0.391 V, respectively, for the two samples as shown in the Insets of

Figure 4.14. This indicates that with the proper amount of PrO_x on the surface, the methanol oxidation process would start at a comparatively lower potential. **Table 4.3** lists some key factors used to judge the overall catalytic performance of Pt and PrO_x-Pt modified BDD electrodes using cyclic voltammetry correlated to **Figure 4.14**. It is clear that both I_f and I_b are enhanced considerably, where I_b increases comparatively less against I_f at the electrode modified with thinner PrO_x coverage, resulting in a higher I_f/I_b ratio. Although the onset potential only decreases by 0.019 V, which is much smaller compared with 0.053 V obtained from the thicker coverage, the overall catalytic performance is still superior to that of only Pt-deposited electrode. The usage of Pt can thus be potentially decreased to achieve competitive effects with PrO_x substitutes.

Table 4.3 Key parameters in CV of electrooxiation of methanol

a) Parameters from **Figure 4.14** a)

	I_f (mA/cm^2)	I_b (mA/cm^2)	I_f / I_b	Onset potential
Pt-BDD	3.55	2.66	1.335	0.454
PrO_x/Pt-BDD	4.14	3.32	1.247	0.401

b) Parameters from **Figure 4.14** b)

	I_f (mA/cm^2)	I_b (mA/cm^2)	I_f / I_b	Onset potential
Pt-BDD	2.77	2.40	1.154	0.410
PrO_x/Pt-BDD	3.60	3.08	1.169	0.391

As mentioned above, a stringent cleaning process was used prior to the testing of methanol electro-oxidation on Pt supported BDD electrode. The functional groups brought to the surface during the cleaning are thought to offer temporally higher catalytic activity of Pt/BDD but cannot remain stable. It was noted that without this cleaning process and after several CV scans in methanol solution, both forward and backward peak intensities decline significantly to about 20% of the value as achieved on pre-treated BDD as shown in **Figure 4.15**. The surface seems passivated to catalyse the

reaction and vulnerable to the surface poisoning caused by adsorbed carbonaceous species. However, even though the overall catalytic activity is extremely disappointing on Pt deposited BDD without any cleaning, it does not affect the performance of the electrode modified with PrO_x further. It is surprising to notice that the activity jumped approximate 200% since the same electrodeposition of PrO_x was conducted for 3 scans. The peak intensity remains fairly stable after several scans in CV for methanol electro-oxidation measurement, indicating that surface was re-activated again and became much more resistant to the poisoning effects. It should be noticed that no matter what pre-treatment was carried out before the electrodeposition process of PrO_x, the eventual overall catalytic activity stays almost the same with the coverage of this oxide layer. Clear susceptibility to poisoning is significantly reduced in the presence of the oxide layer.

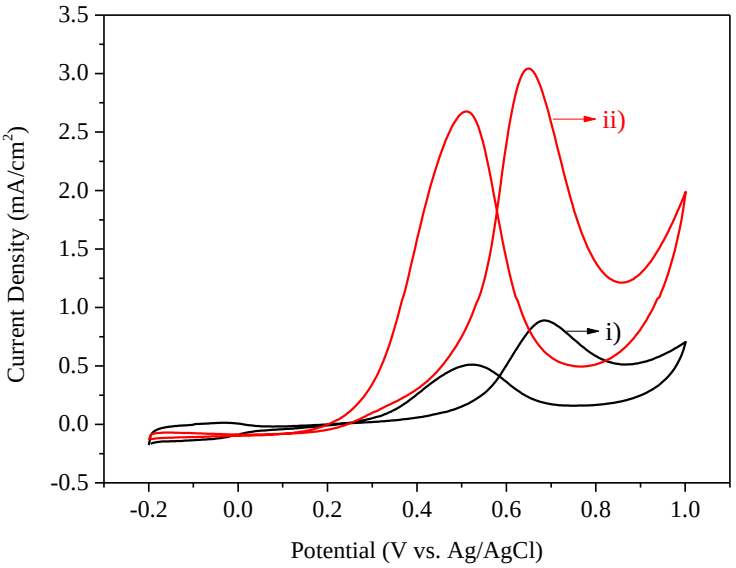


Figure 4.15 CV of i) Pt/BDD and ii) PrO_x-Pt/BDD in 1 M CH_3OH and 0.5 M H_2SO_4 at a scan rate of 50 mV/s without a stringent cleaning process applied on Pt-supported surface.

All the CV measurements above show that the PrO_x coverage provides a reliable increase of the overall catalytic activity. The I_f/I_b ratio remains at a promising level without significant fluctuation while the onset potential smoothly decays to a lower value at varied extents. Apart from the CV technique, the chronoamperometric approach was also applied to investigate the resistance of the catalytic system to the surface poisoning. In this project, a 1000 s measurement was conducted after successive electrodeposition of Pt and PrO_x respectively as shown in **Figure 4.16**. A constant potential of 0.6 V was specifically selected which is in close proximity to the potential at which the methanol rapidly oxidised on the surface. A sharp decay in current intensity is visible in both curves measured from Pt and PrO_x/Pt coated BDD electrodes in the early 200 s, which is attributed to the incompletely oxidised carbonaceous species adsorbed on the surface that would inhibit and even kill off the oxidation process as mentioned earlier[59, 60]. A smooth decay is then followed as a comparatively stabilized current is eventually achieved in either case. The current decays suggest the resistance of the modified electrode against the surface poisoning effect is improved. The signal for the Pt deposited BDD is seen to decrease towards nearly *zero* after 1000 s period, indicating the surface is almost fully occupied with the adsorbed species that cannot be reproducibly oxidised anymore. However, with the PrO_x coverage, the peak intensity in the other curve still remains at a considerably high value, proving the much stronger resistance this system has, after at a long run.

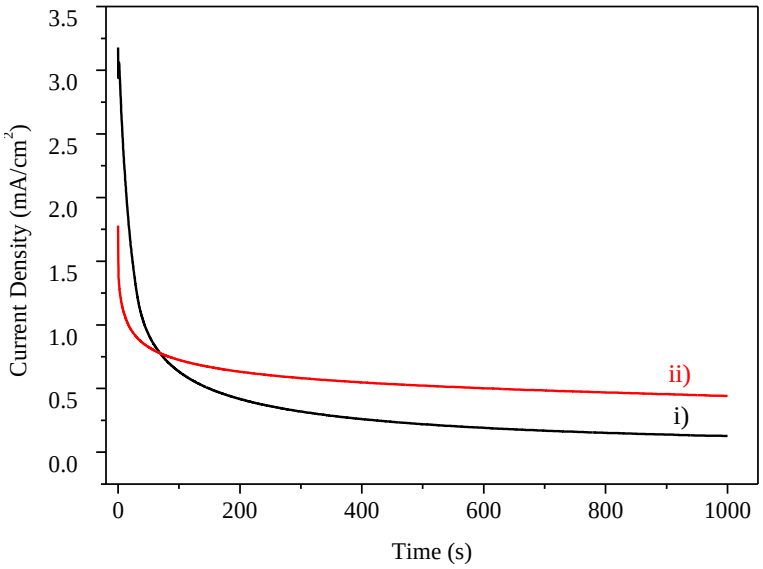


Figure 4.16 Chronoamperometric measurement in 1 M CH_3OH and 0.5 M H_2SO_4 at 0.6 V after successive electrodeposition of i) Pt and ii) Pt and PrO_x.

4.4.3 Methanol electro-oxidation on commercial catalyst based system

In view of the promising results observed above, PrO_x was further used to demonstrate its compatibility with the current commercial carbon black (CB) based platinum catalysts, which are broadly utilised in real DMFCs application. A suspension of commercial catalyst (Platinum, nominally 20% on carbon black, Alfa Aesar) was prepared by dissolving it with ethanol (2 mg/ml) and then ultrasonicated for at least 15 minutes until the sample powders were well dispersed. 50 μL of the suspension was dripped onto the BDD surface drop-wise and allowed to dry. Nafion[61, 62] was added onto the modified electrode surface until a thin visible film was synthesised after the evaporation of ethanol to stabilise the surface layers. This typical system was then studied before and after further PrO_x electrodeposition using CV. As shown in **Figure 4.17**, a prominent current increase of about 40% is achieved in both oxidation peaks even though the I_f/I_b ratio declines slightly according to the higher enhancement of peak intensity in backward scan. Similarly as observed previously, the onset potentials for the

forward peak again shifts to a less positive value with the PrO_x coating, suggesting the whole oxidation process kinetics is enhanced, allowing it to happen at lower potential values.

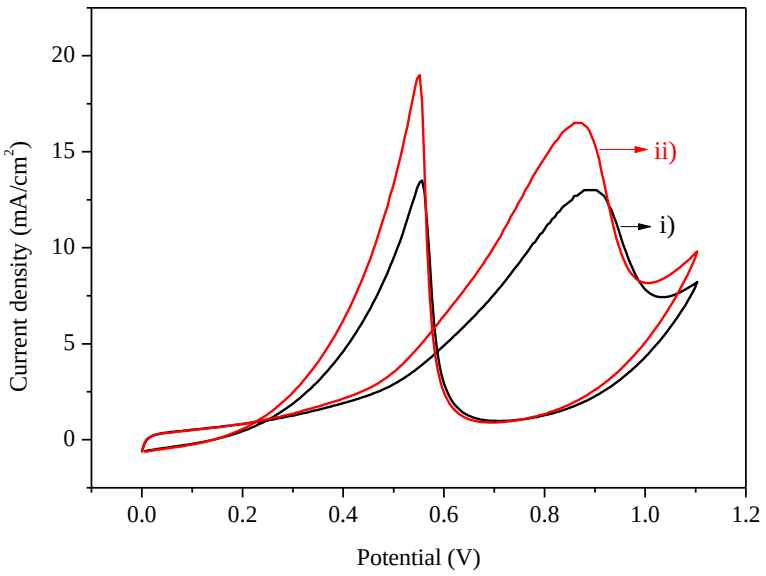


Figure 4.17 CVs of nafion/Pt-CB/BDD i) before and ii) after the electrodeposition of PrO_x in 1 M CH_3OH and 0.5 M H_2SO_4 at a scan rate of 50 mV/s.

As it was discovered that the commercial catalyst based system suffers a decrease in I_f/I_b ratio compared with the Pt supported electrode through electrodeposition, another attempt was made to see whether this disadvantageous phenomenon could be alleviated. J. Zhang *et al*[63] reported that Pt could also be used as shell material in non-noble metal - noble metal 'core-shell' structures. To mimic this approach PrO_x was therefore firstly electrodeposited onto a bare BDD electrode surface before the successive Pt decoration. However, poor results were obtained so it was not pursued further.

4.5 Summarising comments

Pt is an important electrocatalyst, used in a wide range of applications from fuel cells to electrochemical sensors. Due to its high cost, it is important to examine routes to maximize its efficiency in performance. In applications such as DMFC it is clear that surface poisoning by reaction intermediates and by-products can lead to a significant loss in efficiency. The traditional approach to this problem has been to alloy Pt with other Pt metals such as Ru. In the present work we have investigated an alternative approach using a rare earth oxide *i.e.* PrO_x, where $1.5 < x < 2$ represents a defective oxide form associated with the presence of Pr (III) and (IV) states, along with a simple electrochemical synthetic approach to form so-called core-shell nanostructures.

In particular the results presented in this chapter show that:

- A two-step method involving step potential deposition, followed by potentiostatic deposition, can be used to effectively deposit high Pt particle loadings on a diamond electrode. The layers deposited in this way show a very non-uniform dispersion with the Pt being deposited at the electrochemically most active regions on the diamond surface, which themselves are very non-uniformly distributed.
- Electrodes with Pt deposited on them can be effectively coated with PrO_x at negative potentials in a medium containing hydrogen peroxide and a soluble Pr nitrate salt, arising from precipitation of the oxide at high pH, which is generated electrochemically at the oxide surface.
- If long deposition runs are used, then the Pt at the diamond surface is buried beneath a thick PrO_x coating. However for gentler reaction conditions, SEM, XPS and electrochemical analysis suggest that thin oxide coatings can be

produced on the Pt particles, representing a successful electrochemical approach to the synthesis of core-shell nanostructures. For these thin coatings, the underlying Pt retains electrochemical activity, such as the ability to adsorb hydrogen. Indeed the PrO_x coating seems to enhance electrochemical activity for certain redox couples, emphasising that it is not simply an inert blocking layer.

- Pt/diamond electrodes decorated with PrO_x were compared to bare Pt/diamond electrodes with regard to the electrochemical oxidation of methanol under acidic conditions. Some improvements were seen in electrochemical characteristics as judged from peak currents and onset peak potentials observed in CV, by addition of PrO_x. However the most dramatic differences observed appeared to be in susceptibility to poisoning. Whereas clean Pt nanoparticles seem to lose activity easily, the PrO_x treated particles are much less susceptible to showing this characteristic.

4.6 Speculation concerning the 'spill-over' mechanism

Since catalyst poisoning is a major problem in fuel cell applications, this therefore suggests that PrO_x could be used beneficially to improve the fuel cell activity of Pt nanoparticle catalysts. As mentioned previously, it has been well recognised that intermediates such as incompletely oxidised carbonaceous species can be easily adsorbed and poison the Pt catalysts, thus declining the overall catalytic activity unexpectedly. The introduction of second metals such as Ru[64], Re[65] and Sn[66] into the Pt system to form the bi-functional catalysts was broadly considered as an effective way to alleviate the poisoning effects significantly throughout the interaction between the adsorbed -OH species on the second metal and the CO_{ads} poisoning species on the adjacent Pt site in alcohol electro-oxidation. In such kind of system, Pt adsorbs the

intermediates initially and the second metal component facilitates as shown below in equation 4.4:

$$\mathrm{Pt\text{–}CO_{ads} + M\text{–}OH \rightarrow Pt + M + CO_2 + H^+ + e^-} \qquad 4.4$$

where M is the second metal.

Apart from using the second metal, other attempts have also been made to remove such poisoning species to allow the complete methanol oxidation to proceed more smoothly. Shen and Tseung[67] had reported the electrodes modified by electrochemically co-deposited Pt/WO_3. In the acidic environment, the hydrogen is initially adsorbed on the Pt surface, however, the oxidation process actually happens on the WO_3 surface. This phenomenon is defined as 'spill-over' and leads to a significant enhancement of the electrode activity[22, 68]. The general mechanism can be represented as below:

$$\mathrm{WO_3 + Pt\text{–}H \rightarrow H\text{–}WO_3 + Pt} \qquad 4.5$$

where the hydrogen is transferred through 'spill-over' effects from Pt sites to from the hydrogen tungsten bronze. The hydrogen tungsten bronze is then oxidised to release the H^+ and tungsten bronze.

$$\mathrm{H\text{–}WO_3 \rightarrow H^+ + e^- + WO_3} \qquad 4.6$$

The 'spill-over' effects enable such Pt/WO_3 to exhibit unique advantageous properties. The Pt sites in the reaction remain comparatively clean by continuous formation and oxidation of hydrogen tungsten bronze during the de-hydrogenation process in the electro-oxidation of methanol. Moreover, as water is adsorbed onto the WO_3, it can behave in a very similar way as in the second metal case introduced above to interact with the CO poisoning species on the adjacent Pt sites to form carbon dioxide[69].

In other studies of electro-oxidation of methanol, the concept of 'spill-over' was not

only limited to the transportation of hydrogen from the Pt to the second material, but also applied to a wider range of surface groups. Jones *et al*[8] reported a possible mechanism in methanol electro-oxidation using Pt-Ru core-shell structures. Two non-CO pathways were suggested in that case. It is proposed that the 'spill-over' process actually happens between both metal sites, involving either transfer of oxygenates from Ru terraces to Pt sites or adsorbed methoxy or other derivatives from the Pt to the Ru surface in the opposite direction. Both pathways contribute to the removal of the surface poisoning species formed on Pt sites and the latter pathway is defined as a reverse 'spill-over' process.

In this chapter, as PrO_x shows improved overall performance in catalysing the methanol electro-oxidation, a similar 'spill-over' principle is suggested to happen between the Pt nanoparticles and the oxide layer on the surface. In both electrochemical and XPS characterisation after the PrO_x electrodeposition, the deposited layer is suggested as being oxygen deficient. With a large number of oxygen vacancies on the oxide layer, the surface tends to become positively charged, thereby attracting the -OH groups on it. With an ideal amount of PrO_x coverage, the well-covered oxide layer will not passivate the surface but effectively clean off the adsorbed poisoning species to reactivate the catalytic activity of Pt nanoparticles. A speculated mechanism is depicted below in **Figure 4.18**.

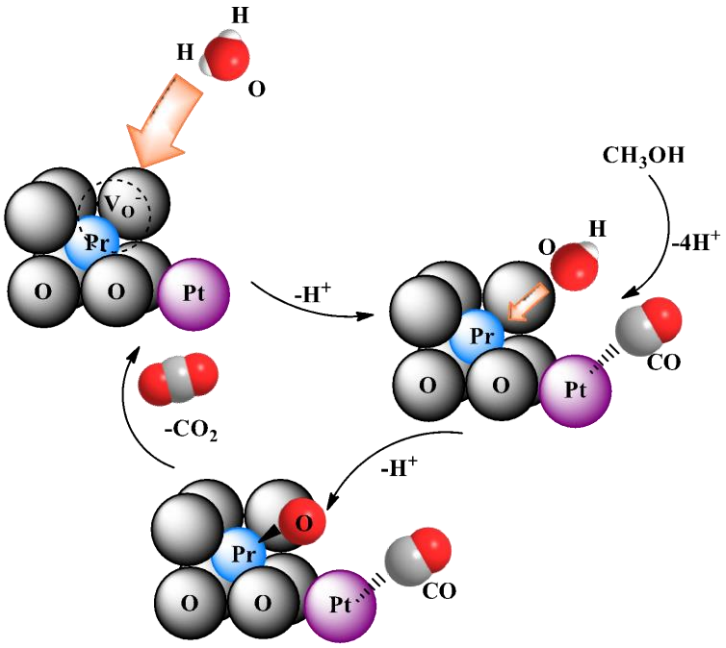


Figure 4.18 The mechanism of indirect CO pathway in PrO_x-Pt system, in which (V_o^-) represents the oxygen vacancies.

As clearly pictured, in the first step, the water species are adsorbed by PrO_x to form -OH species that occupy the initial oxygen vacancies. Since the poisoning species have been produced on the Pt sites, the interaction between the CO_{ads} and OH_{ads} on different terraces occurs at this stage. Both forward 'spill-over' process involving the transfer of adsorbed oxygenates from the PrO_x to the Pt sites and the reverse movement of carbonaceous groups from the Pt terraces towards the oxide layer surface are supposed to happen simultaneously as suggested in the Pt-Ru core-shell application. In the final step, as the poisoning species get re-oxidised again to produce carbon dioxide, both Pt and PrO_x sites are released and turned back to their initial states before the successive electro-oxidation of methanol. The overall process can be described in a series of equations as follows:

$$PrO_x \cdots V_O + H_2O \rightarrow PrO_x\text{–}OH + H^+ + e^- \quad 4.7$$

$$Pt + CH_3OH \rightarrow Pt\text{–}COH_{x\cdot ads} + (4-x)H^+ + (4-x)e^- \quad 4.8$$

$$PrO_x\text{–}OH + Pt\text{–}COH_{x\cdot ads} \rightarrow PrO_x \cdots V_O + CO_2 + (1+x)H^+ + (1+x)e^- \quad 4.9$$

where V_O represents the oxygen vacancies on PrO_x sites.

Reference

[1] X. Cheng, Z. Shi, N. Glass, L. Zhang, J. Zhang, D. Song, Z.-S. Liu, H. Wang, J. Shen, J. Power Sources 165 (2007) 739-756.

[2] L. F Brown, Int. J. Hydrogen Energy 26 (2001) 381-397.

[3] S. Wasmus, K. A, J. Electroanal. Chem. 461 (1999) 14-31.

[4] A. Arico, S. Srinivasan, V. Antonucci, Fuel cells 1 (2001) 133-161.

[5] H. Liu, C. Song, L. Zhang, J. Zhang, H. Wang, D.P. Wilkinson, J. Power Sources 155 (2006) 95-110.

[6] Z. Tang, G. Lu, Applied Catalysis B: Environmental 79 (2008) 1-7.

[7] Z. He, J. Chen, D. Liu, H. Tang, W. Deng, Y. Kuang, Mater. Chem. Phys. 85 (2004) 396-401.

[8] S. Jones, K. Tedsree, M. Sawangphruk, J.S. Foord, J. Fisher, D. Thompsett, S.C.E. Tsang, ChemCatChem 2 (2010) 1089-1095.

[9] T. Iwasita, Electrochim. Acta 47 (2002) 3663-3674.

[10] Y.X. Chen, A. Miki, S. Ye, H. Sakai, M. Osawa, J. Am. Chem. Soc. 125 (2003) 3680-3681.

[11] Y.-C. Liu, X.-P. Qiu, Y.-Q. Huang, W.-T. Zhu, J. Power Sources 111 (2002) 160-164.

[12] B. Beden, F. Kadirgan, C. Lamy, J. Leger, J. Electroanal. Chem. Interfacial. Electrochem. 127 (1981) 75-85.

[13] W. Chen, L.P. Xu, S.W. Chen, J. Electroanal. Chem. 631 (2009) 36-42.

[14] J. Shim, C.-R. Lee, H.-K. Lee, J.-S. Lee, E.J. Cairns, J. Power Sources 102 (2001) 172-177.

[15] H.M. Villullas, F.I. Mattos-Costa, L.O. Bulhões, J. Phys. Chem. B 108 (2004) 12898-12903.

[16] Y. Bai, J. Wu, J. Xi, J. Wang, W. Zhu, L. Chen, X. Qiu, Electrochem. Commun. 7 (2005) 1087-1090.

[17] C. Xu, P.K. Shen, X. Ji, R. Zeng, Y. Liu, Electrochem. Commun. 7 (2005) 1305-1308.

[18] C. Xu, P.K. Shen, Chem. Commun. (2004) 2238-2239.

[19] C. Xu, P.K. Shen, J. Power Sources 142 (2005) 27-29.

[20] H.J. Osten, J.P. Liu, E. Bugiel, H.J. Müssig, P. Zaumseil, Mater. Sci. Eng., B 87 (2001) 297-302.

[21] H. Zhao, L. Li, J. Yang, Y. Zhang, Electrochem. Commun. 10 (2008) 1527-1529.

[22] B. Hobbs, A. Tseung, Nature 222 (1969) 556-558.

[23] Y. Wang, T.S. Nguyen, C. Wang, X. Wang, Dalton Trans. (2009) 7606-7609.

[24] R.G. Compton, J.S. Foord, F. Marken, Electroanalysis 15 (2003) 1349-1363.

[25] J.H. Luong, K.B. Male, J.D. Glennon, Analyst 134 (2009) 1965-1979.

[26] J.S. Foord, W. Hao, S. Hurst, Diamond Relat. Mater. 16 (2007) 877-880.

[27] G.M. Swain, J. Electrochem. Soc. 141 (1994) 3382-3393.

[28] Q. Chen, M.C. Granger, T.E. Lister, G.M. Swain, J. Electrochem. Soc. 144 (1997) 3806-3812.

[29] I. Gonzalez-Gonzalez, D. Tryk, C.R. Cabrera, Diamond Relat. Mater. 15 (2006) 275-278.

[30] J. Wang, G.M. Swain, J. Electrochem. Soc. 150 (2003) E24-E32.

[31] F. Montilla, E. Morallon, I. Duo, C. Comninellis, J. Vazquez, Electrochim. Acta 48 (2003) 3891-3897.

[32] J. Hu, X. Lu, J.S. Foord, Q. Wang, physica status solidi (a) 206 (2009) 2057-2062.

[33] S. Shrestha, C. Yeung, F. Marken, C. Mills, S. Tsang, Sens. Actuators, B: Chem. 123 (2007) 400-406.

[34] S. Shrestha, F. Marken, J. Elliott, C. Yeung, C. Mills, S. Tsang, J. Electrochem. Soc. 153 (2006) C517-C520.

[35] S. Alayoglu, P. Zavalij, B. Eichhorn, Q. Wang, A.I. Frenkel, P. Chupas, Acs Nano 3 (2009) 3127-3137.

[36] P. He, H. Liu, Z. Li, J. Li, J. Electrochem. Soc. 152 (2005) E146-E153.

[37] J. Hu, X. Lu, J. Foord, Electrochem. Commun. 12 (2010) 676-679.

[38] H. Tang, J. Chen, S. Yao, L. Nie, Y. Kuang, Z. Huang, D. Wang, Z. Ren, Mater. Chem. Phys. 92 (2005) 548-553.

[39] M.M.E. Duarte, A.S. Pilla, J.M. Sieben, C.E. Mayer, Electrochem. Commun. 8 (2006) 159-164.

[40] S. Domínguez-Domínguez, J. Arias-Pardilla, Á. Berenguer-Murcia, E. Morallón,

D. Cazorla-Amorós, J. Appl. Electrochem. 38 (2008) 259-268.

[41] N. Furuya, S. Koide, Surf. Sci. 220 (1989) 18-28.

[42] K. Yamamoto, D. Kolb, R. Kötz, G. Lehmpfuhl, J. Electroanal. Chem. Interfacial. Electrochem. 96 (1979) 233-239.

[43] G. Tamizhmani, J.P. Dodelet, D. Guay, J. Electrochem. Soc. 143 (1996) 18-23.

[44] I. González-González, E.R. Fachini, M.A. Scibioh, D.A. Tryk, M. Tague, H.e.D. Abruna, C.R. Cabrera, Langmuir 25 (2009) 10329-10336.

[45] R. Locher, J. Wagner, F. Fuchs, M. Maier, P. Gonon, P. Koidl, Diamond Relat. Mater. 4 (1995) 678-683.

[46] C. Wagner, G. Muilenberg, Handbook of X-ray Photoelectron Spectroscopy: a reference book of standard data for use in x-ray photoelectron spectroscopy, Perkin-Elmer, Eden Prairie, MN, 1979.

[47] H. Borchert, Y.V. Frolova, V.V. Kaichev, I.P. Prosvirin, G.M. Alikina, A.I. Lukashevich, V.I. Zaikovskii, E.M. Moroz, S.N. Trukhan, V.P. Ivanov, J. Phys. Chem. B 109 (2005) 5728-5738.

[48] S. Tanuma, C.J. Powell, D.R. Penn, Surf. Interface Anal. 11 (1988) 577-589.

[49] J.F. Moulder, J. Chastain, R.C. King, Handbook of X-ray photoelectron spectroscopy: a reference book of standard spectra for identification and interpretation of XPS data, Physical Electronics Eden Prairie, MN, 1995.

[50] C.D. Wagner, L.E. Davis, M.V. Zeller, J.A. Taylor, R.H. Raymond, L.H. Gale, Surf. Interface Anal. 3 (1981) 211-225.

[51] Y. Mu, H. Liang, J. Hu, L. Jiang, L. Wan, J. Phys. Chem. B 109 (2005) 22212-22216.

[52] R. Mancharan, J.B. Goodenough, J. Mater. Chem. 2 (1992) 875-887.

[53] T. Iwasita, F.C. Nart, W. Vielstich, Ber. Bunsen-Ges. Phys. Chem. 94 (1990) 1030-1034.

[54] Z. Liu, X.Y. Ling, X. Su, J.Y. Lee, J. Phys. Chem. B 108 (2004) 8234-8240.

[55] T. Huang, J.H. Zhuang, A.S. Yu, J. Appl. Electrochem. 39 (2009) 1053-1058.

[56] Y. Shao, G. Yin, J. Zhang, Y. Gao, Electrochim. Acta 51 (2006) 5853-5857.

[57] X. Tong, G. Zhao, M. Liu, T. Cao, L. Liu, P. Li, J. Phys. Chem. C 113 (2009) 13787-13792.

[58] F. Maillard, A. Bonnefont, M. Chatenet, L. Guétaz, B. Doisneau-Cottignies, H. Roussel, U. Stimming, Electrochim. Acta 53 (2007) 811-822.

[59] A. Kabbabi, R. Faure, R. Durand, B. Beden, F. Hahn, J.-M. Leger, C. Lamy, J.

Electroanal. Chem. 444 (1998) 41-53.

[60] J. Prabhuram, T. Zhao, Z. Tang, R. Chen, Z. Liang, J. Phys. Chem. B 110 (2006) 5245-5252.

[61] V. Baglio, A. Arico, A.D. Blasi, V. Antonucci, P. Antonucci, S. Licoccia, E. Traversa, F.S. Fiory, Electrochim. Acta 50 (2005) 1241-1246.

[62] F. Bauer, M. Willert-Porada, J. Membr. Sci. 233 (2004) 141-149.

[63] J. Zhang, F. Lima, M. Shao, K. Sasaki, J. Wang, J. Hanson, R. Adzic, J. Phys. Chem. B 109 (2005) 22701-22704.

[64] H.A. Gasteiger, N. Marković, P.N. Ross, E.J. Cairns, J. Electrochem. Soc. 141 (1994) 1795-1803.

[65] J. Tayal, B. Rawat, S. Basu, Int. J. Hydrogen Energy 37 (2012) 4597-4605.

[66] T. Frelink, W. Visscher, J. Van Veen, Surf. Sci. 335 (1995) 353-360.

[67] P. Shen, A. Tseung, J. Electrochem. Soc. 141 (1994) 3082-3090.

[68] S. Abbaro, A. Tseung, D. Hibbert, J. Electrochem. Soc. 127 (1980) 1106-1107.

[69] L. Niedrach, I. Weinstock, Electrochem. Technol. 3 (1965) 270-275.

Chapter 5

Electrodeposition of a PrO_x-Pt electrocatalyst on BDD electrode for the electrochemical detection of nitric oxide

5.1 Introduction

Research concerning the role of nitric oxide (NO) in biological systems is becoming a topical area of great interests. Endogenous NO is generated from L-arginine by a family of three distinct calmodulin-dependent NO synthase (NOS) enzymes[1, 2]. It plays a very important role as a neurotransmitter[3-5] and an immune system mediator[6-8] in various physiological processes. Since it was discovered to serve as an endothelium-derived relaxing factor (EDRF) in 1980s[9, 10], a new area of biological research emerged concerning the detection of this physiological messenger molecule[11-13]. In order to get better understanding about its biological and psychological role, a comprehensive study about its production, transportation and detection is required. Therefore a sensitive, selective and quantitative *in situ* measurement is necessary.

However, the detection of NO in a biological environment is extremely difficult due to its low concentration, poor stability and high fugacity[14, 15]. The half-life of NO is reported as less than only 1 second through intact blood vessels or isolated hearts[16]. It can be readily oxidised by O_2 in the air and solution to generate NO_2^- and NO_3^-, respectively. A wide range of techniques such as chemiluminescence[17], UV-vis spectroscopy[18], and electron spin resonance (ESR) spectrophotometry[19] have been developed and investigated for the direct and selective detection of NO. Although all the above techniques have proved useful in NO detection, they still suffer some unexpected disadvantages. Chemiluminescence offers very high sensitivity in NO detection but it is

expensive, complex and requires ozone as the second reactant. UV-vis spectroscopy is particularly applied in direct detection of NO but is not suitable for *in situ* monitoring. ESR spectrophotometry can be preferentially used in complex biological systems but offers comparatively low sensitivity. In order to overcome these problems, some other techniques such as electrochemical methods have been gradually introduced[20-23], based on the direct electro-oxidation of NO at 0.7 to 0.9 V *vs.* Ag/AgCl.

$$NO + H_2O \rightarrow HNO_2 + H^+ + e^- \quad 5.1$$

$$NO + 2H_2O \rightarrow HNO_3 + 3H^+ + 3e^- \quad 5.2$$

These methods are becoming more promising for NO measurement because they are very simple, fast, direct and sensitive to NO[15]. More importantly, they are also available for *in vivo* environments with a good spatial definition. Therefore extensive efforts in developing electrochemical sensors for NO detection have been made. Although NO can be directly electro-oxidised on some conventional electrode surfaces like glassy carbon (GC), boron-doped diamond (BDD) and carbon fibres *et al*, it normally requires large overpotentials which in turn cause significant interfering effects with other molecular species at high positive potentials. Therefore, chemically modified electrodes (CMEs) have been investigated to solve this problem effectively[24-27].

In order to achieve better sensitivity in NO detection, both direct reduction and oxidation of NO have been reported by using polycrystalline and single-crystal Pt electrodes[28-31]. Since NO can be catalytically electro-reduced and electro-oxidised at a platinum surface, it is indicative that Pt alloys or related complexes may also show promising performances in NO detection. Pei *et al*[27] investigated an ultramicroelectrode modified with an electrodeposited $CuPtCl_6$ film and Wang *et al*[15] successfully fabricated an effective glassy carbon electrode modified with Pt-Fe(III)

nanoparticles. Apart from the demand of high sensitivity in NO detection as mentioned above, strong selectivity against potential interfering compounds is another important aspect. Nitrite (NO_2^-), the common oxidative product from NO, is always considered as the most important interference in NO detection as its oxidation peak appears at almost the same position against NO due to its self-disproportionation process[32]. Some other interfering products such as ascorbic acid (AA) may also significantly affect the detection accuracy, mainly attributed to its normally much higher compositional content in practical applications[33]. Nafion is sometimes applied as a membrane to address this problem as it can effectively prevent the penetration of anions to reach the active sites on the electrode surface. Previous work in NO electrochemical detection had thus been mainly concerned with nafion utilisation[14, 34, 35]. Although much better selectivity was attained as expected, severely decreased NO signal amplitudes arose from the required nafion coverage, thus producing loss of sensitivity.

In this chapter, work was concerned with exploring new approaches to electrochemical detection of NO using diamond electrodes. Since these electrodes offer high overpotential, Pt was electrodeposited following the same process as explained in *Chapter* 4 to impart electrocatalytic activity. Finally a PrO_x thin film was coated onto the Pt covered surface under CV conditions[36]. Such modifications were aimed to explore if the oxide coating was able to alleviate the interfering effects from nitrite and AA but retain a considerably high sensitivity simultaneously in comparison with nafion. Different thicknesses of the deposited PrO_x film were fine-tuned by varying the cyclic scan numbers to investigate the ideal amount of oxide for optimising the overall performance. Both CVs and SWVs were carried out on bare and modified BDD electrodes (with pure Pt and PrO_x-Pt) to display the differences after successive

electrochemical modifications.

5.2 Experimental section

5.2.1 Chemicals and materials

Praseodymium (III) nitrate hexahydrate ($Pr(NO_3)_3 \cdot 6H_2O$, 99.9%), hydrogen peroxide (H_2O_2, 50 wt.%), sodium nitrite ($NaNO_2$, ≥ 97%), L-ascorbic acid ($C_6H_8O_6$, ≥ 99%) were purchased from Sigma-Aldrich. Potassium hexachloroplatinate (IV) (K_2PtCl_6, 98%) was purchased from Alfa Aesar and nitric oxide (NO, 75 L cylinder, 99.99%) was ordered from BOC gas. All the solutions were prepared and relative dilutions were carried out using Milli-Q water (> 18 MΩ cm). 0.1 M Phosphate buffered saline (PBS) was chosen as the counter electrolyte in all relevant NO detection experiments. The PBS with a pH of 7.4 comprises of 8.01 g/L sodium chloride (NaCl), 0.20 g/L potassium chloride (KCl), 1.78 g/L sodium phosphate dibasic dihydrate ($Na_2HPO_4 \cdot 2H_2O$) and 0.27 g/L potassium phosphate monobasic (KH_2PO_4).

5.2.2 Preparation of nitric oxide solution

NO standards with different concentrations were prepared by series of dilutions from a saturated NO solution. Since NO is extremely sensitive to oxygen and can be easily converted into its different oxidative forms in both aqueous and non-aqueous environments, the meticulous exclusion of O_2 was essential by bubbling a 10 ml 0.1 M PBS (pH = 7.4) solution with pure N_2 for about 20 minutes prior to the preparation. A small bottle was well sealed with a rubber seal on the top to ensure rigorous airproof properties. A syringe needle connected with a gas pipeline was applied for gas injection by piecing the rubber lid. The other syringe needle connected with the atmosphere was placed nearby in case of excessive pressure throughout the bubbling process. After the

oxygen residues were fully removed and the solution was well protected under N_2, it was further bubbled with 99.99% NO for about another 20 minutes to make it saturated with a NO concentration of 1.8 mM at 20 °C according to the literature[37]. All the dilutions to make various concentrations of NO solutions were carried out by applying an air-tight syringe to transfer the solution sequentially. In order to ensure precision in all electrochemical characterisations, the syringe needle was preferentially re-assembled by replacing the original syringe with an adjustable pipette with more precise measuring ranges. The saturated solution was well sealed-off and re-bubbled for a while with fresh NO prior to each experiment.

5.2.3 Preparation of PrO_x/Pt-BDD electrodes

As stated in *Chapter* 4, Pt nanoparticles were initially electrodeposited onto the BDD surface with 2 mM K_2PtCl_6 in 0.5 M H_2SO_4 via a two-stage pathway combining (1) a potential step deposition (PSD), which stepped the potential from 0.25 to -0.2 V in 0.05 V steps of a 10 s duration and (2) a potentiostatic method at -0.2 V with an approximately 20 minutes length for each stage until a proper amount of about 230 μg, *i.e.* 506 μg/cm^2 Pt was decorated. For the electrochemical coating of PrO_x, 0.5 mM $Pr(NO_3)_3$ combined with 5 mM H_2O_2 in 0.1 M KCl was used as the precursor in CV. The number of scans used was adjusted to varying extents of electrodeposition for optimising both sensitivity and selectivity in electrochemical detection of NO.

5.3 Results and discussion

5.3.1 Characterisation of Pt/BDD and PrO_x-Pt/BDD

5.3.1.1 Electrochemical characterisation of Pt/BDD and PrO_x-Pt/BDD electrodes

Similar to *Chapter* 4, CVs were conducted in 0.5 M H_2SO_4 immediately after the

electrodeposition of Pt nanoparticles and PrO_x thin film to feature the variation of electrochemical responses with successive modifications to the electrode surface. As exhibited in **Figure 5.1**, on the cathodic scan, it is clear to observe (1) an ionic Pt reduction signal at about 0.4 V, (2) peaks associated with H adsorption onto Pt crystallites in the range of 0 to -0.25 V and (3) hydrogen evolution at even more negative potential. After the Pt coated electrode was scanned for 20 CV cycles in the $Pr(NO_3)_3$ and H_2O_2 mixed precursor solution, a decay in the Pt signal response was achieved as displayed *via* the dashed line. A decreased but still visible Pt reduction peak suggests the deposited oxide film partially covers the Pt nanoparticles underneath. Similarly the H underpotential peaks are also very much attenuated. However hydrogen evolution is still observed, suggesting some preserved catalytic action of Pt.

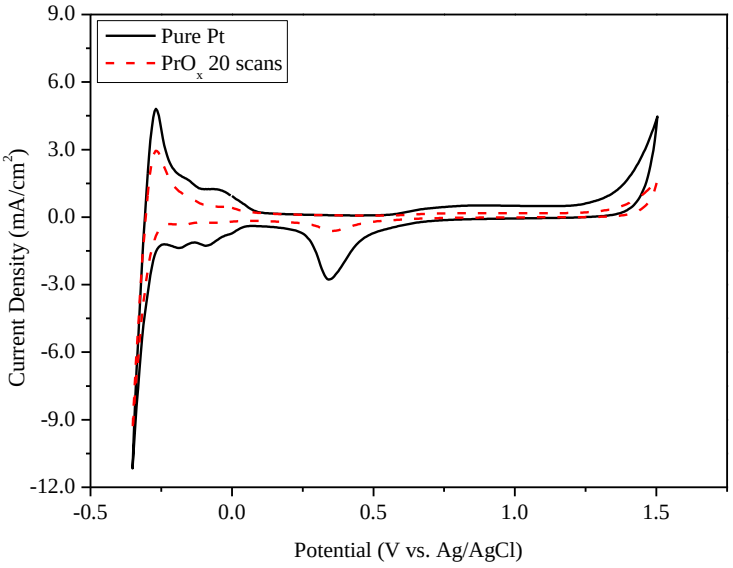
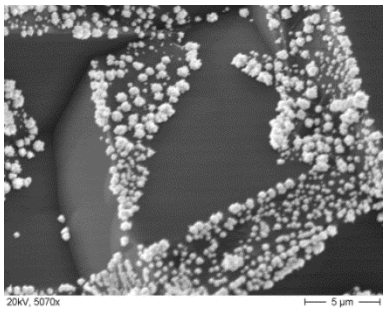


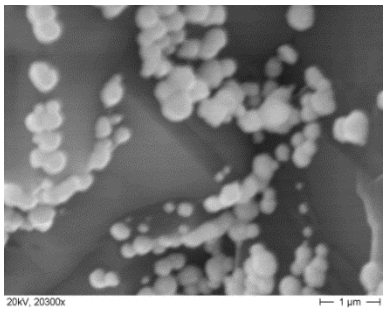
Figure 5.1 CVs in 0.5 M H_2SO_4 on pure Pt and PrO_x-Pt coated BDD at a scan rate of 50 mV/s.

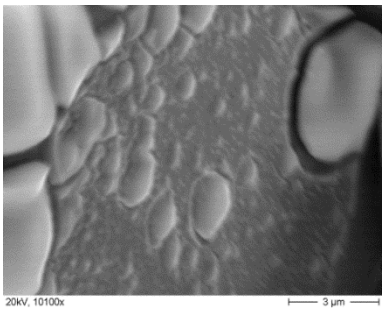
5.3.1.2 SEM characterisation of Pt/BDD and PrO_x-Pt/BDD electrodes

SEM characterisation was also carried out and exhibited comparable results as obtained in *Chapter* 4. **Figure 5.2** shows the topography variation before and after the electrochemical coating of the oxide layer on Pt decorated BDD. It is apparent that the Pt nanoparticles are preferentially electrodeposited onto specific areas, *i.e.* (111) facets, while adjacent surfaces present very low coverage. This observation is fairly similar to that in *Chapter* 4 and is probably mainly associated with [B] inhomogeneity in the grown diamond layer. The particle size is seen as increasing after the PrO_x electrodeposition for a few CV scans, suggesting the oxide material has been selectively coated onto the active metallic sites as shown in **Figure 5.2** b). However, much larger oxide agglomerations are obtained after more scan numbers were applied as depicted in **Figure 5.2** c), which is suggestive that the Pt modified electrode can also be completely passivated when the oxide coverage exceeds a certain extent. All the characteristic results observed are similar to those achieved previously in *Chapter* 4, suggesting the electrodeposition routes for both Pt and PrO_x are hereby reproducible and controllable.



a)





b) c)

Figure 5.2 SEM of a) pure Pt coated BDD, b) lower and c) higher PrO_x coverage modified Pt/BDD electrodes.

5.3.1.3 XPS characterisation of Pt/BDD and PrO_x-Pt/BDD

To study the variation of elemental composition after successive electrodeposition of Pt and PrO_x, XPS was also conducted as explained in *Chapter* 4. Pr 3d characteristic peaks were clearly observed when the intensity of the Pt 4f spectral region was attenuated, suggesting the Pt nanoparticles were partially covered with the deposited oxide layer. The Pt intensity was seen as 20 – 25% of the initial value after around 4 CV scans, suggesting an oxide thickness at the order of double the inelastic mean free path, *i.e.* 3 nm. In comparison, the modified electrode with a thicker coverage of the oxide layer as shown in **Figure 5.3** shows much greater attenuation of Pt 4f region intensity, confirming rather thick oxide layers could be deposited. In particular it is clear that there is little tendency for self-limiting thin film formation.

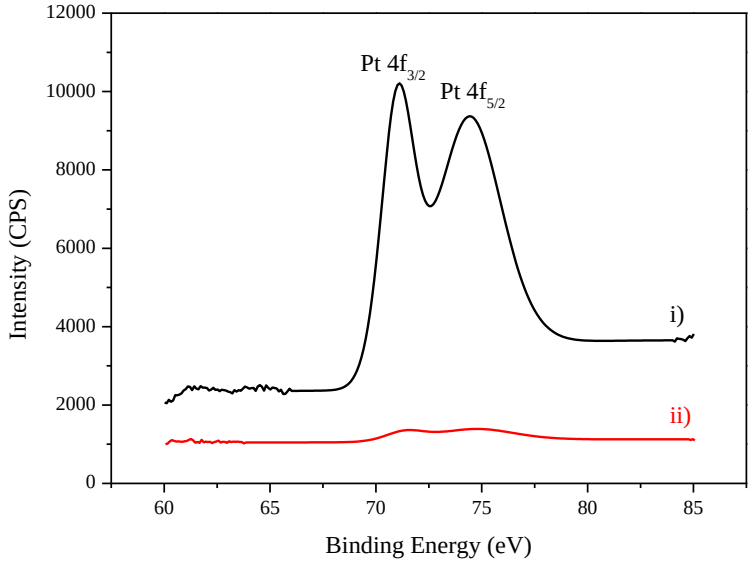


Figure 5.3 XPS spectra of Pt 4f spectral region before i) and after ii) thicker PrO_x deposition by 40 CV scans with 0.5 mM $Pr(NO_3)_3$ and 5 mM H_2O_2 in 0.1 M KCl on Pt/BDD.

5.3.2 Electrochemical detection of NO on bare-BDD and Pt-BDD

CVs with different concentrations of NO, *i.e.* 1.8×10^{-5}, 3.6×10^{-5} and 9.0×10^{-5} M in

0.1 M PBS were carried out on both bare and Pt-coated BDD electrodes, which are illustrated in **Figure 5.4**. On the bare diamond electrode, although an increase in current intensity with enhanced NO concentration above ~ 1.0 V is seen, no clean oxidation peaks are observed as shown in **Figure 5.4** a). It thus reveals that NO is only oxidised at high overpotentials on the clean diamond electrode. These potentials are close to those for the oxidation of water, and are unlikely to be useful for NO detection, given a wide range of chemical species which are oxidised in this regime. In contrast, with the Pt coating on the surface after the two-stage electrodeposition, highly discernible peaks appear and increase along with higher NO concentration. It is also noticeable that the oxidation potential of NO shifts towards a much more negative value by about 0.4 V as observed in **Figure 5.4** b) compared with that achieved on the bare BDD electrode. This suggests that with a stable coverage of these electrochemically decorated Pt nanoparticles, much greater catalytic activity was obtained and NO could be oxidised much easier at lower potential values. Wang and Lin[15] reported Pt-Fe(III) alloyed nanoparticles on a glassy carbon (GC) electrode were particularly active in NO oxidation. However the peak current density of NO oxidation at a pure Pt covered BDD electrode fabricated here is around 8 times higher than that observed by Wang and Lin for the same NO concentration at similar oxidation potentials, suggesting that alloying with Fe (III) is not necessarily required. Comparing with the work of Wang and Lin, it can be seen that the overpotential on clean diamond for NO oxidation is about 0.2 V greater than on GC. It is also discovered that the bare GC can also catalyse the NO oxidation even though with a comparatively lower peak current at a higher potential. The signal responses from both deposited materials and the electrode may overlap and disturb the detection accuracy especially at precise levels for *in vivo* applications. Conversely, BDD has exhibited its great electrochemical inertness in NO detection,

making this supporting electrode material a promising candidate for featuring the accelerated reaction kinetics by any further surface modification.

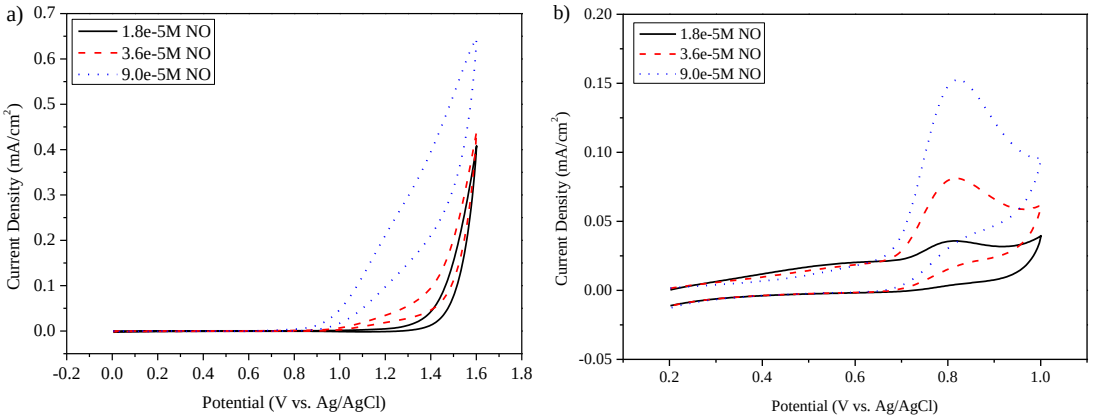


Figure 5.4 CVs of 1.8 $\times 10^{-5}$, 3.6 $\times 10^{-5}$ and 9.0 $\times 10^{-5}$ M NO in 0.1 M PBS (pH = 7.4) at a scan rate of 50 mV/s on a) bare and b) Pt-coated BDD.

Apart from the changes obtained from different concentrations, the effects of scan rate were also investigated by using a fixed NO concentration of 3.6 $\times 10^{-5}$ M in 0.1 M PBS on the Pt covered electrode. CVs were conducted at 20, 50, 100 and 200 mV/s respectively on the Pt/BDD with fresh NO in PBS electrolyte each time. A series of oxidation faradaic responses are plotted as a function of the potential as shown in **Figure 5.5**. It can be seen that although presumably the electrochemistry is driven by the Pt nanoparticles, nevertheless a typical cyclic voltammetry 'peaked' response is seen due to the overlapping diffusion fields from the adjacent Pt particles, which tend to be clustered in particular regions of the electrode as seen in SEM. Unsurprisingly however, a simple (scan rate)$^{1/2}$ relationship expected for diffusion control at a large planar electrode is not seen in view of the very heterogeneous electrode structure.

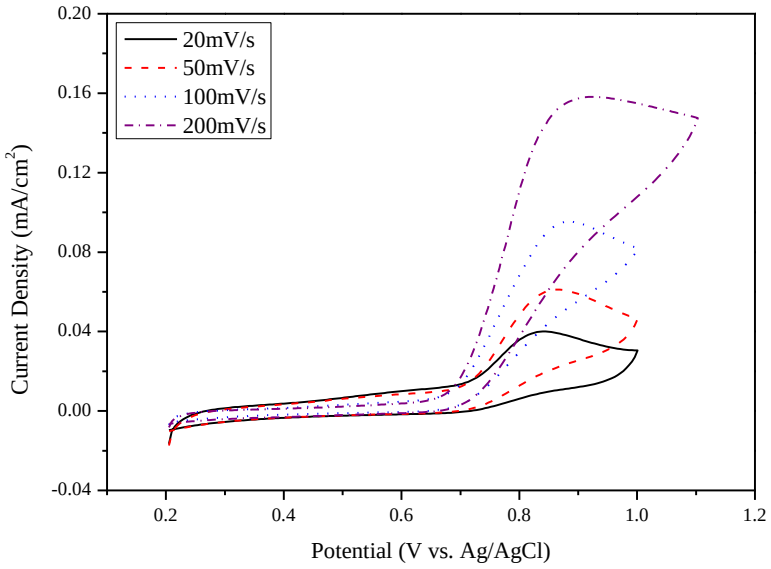


Figure 5.5 CVs of 3.6 × 10^{-5} M NO in 0.1 M PBS (pH = 7.4) on Pt-coated BDD at different scan rates of 20, 50, 100 and 200 mV/s

As part of this initial overview, square wave voltammetry (SWV) was also performed since this is often preferred in sensitive analytical applications due to the ability to minimise background signal contributions. (Data are shown in **Figure 5.6**) For both un-modified and Pt deposited BDD, the peak SWV current increases along with enhancing NO concentration. However, with the electrodeposited Pt nanoparticles, the modified electrode presents a comparable signal response with a 10 times lower NO content against that achieved on bare electrodes at the highest NO concentration. Also it can be seen that the SWV signal on the Pt coated electrode is well-separated from the water oxidation region, whilst it is not achieved on the bare diamond electrode. This would therefore reveal that the latter would perform poorly at trace NO levels where the contribution will be lost to the background even in SWV. The results clearly suggest that the capability of using Pt-modified electrodes in NO detection throughout a wide concentration range.

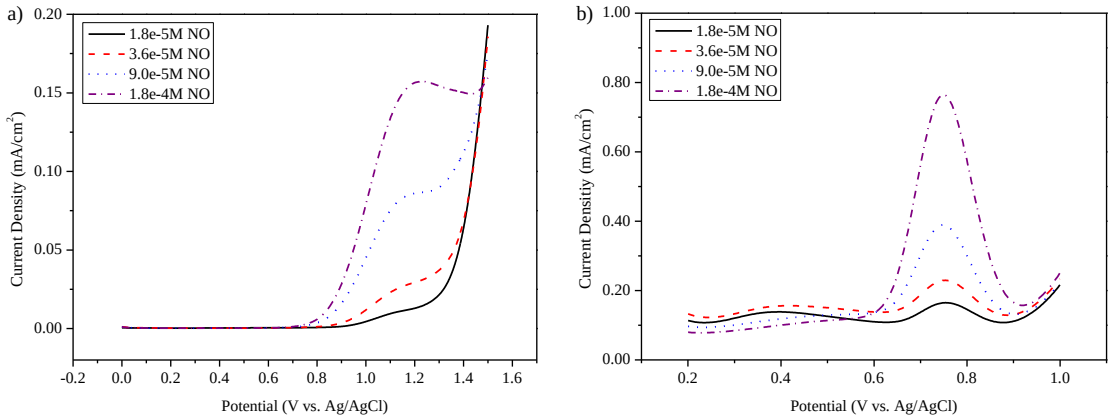


Figure 5.6 SWV of NO at concentrations of 1.8×10^{-5}, 3.6×10^{-5}, 9.0×10^{-5} and 1.8×10^{-4} M in 0.1 M PBS (pH = 7.4) at a frequency of 10 Hz along with a 0.002 V step potential and a 0.05 V amplitude on a) bare and b) Pt-covered BDD

5.3.3 Interfering compounds in NO detection

Although the Pt modified BDD electrode displays promising feasibility in NO electrochemical detection by showing significantly enhanced faradic response along with prominently lower potential required for NO oxidation compared with that of its bare BDD counterpart, the usefulness in an analytical context can be enhanced if any selectivity towards NO can be imparted, to minimise interference from compounds other than NO. As the oxidation potential of NO is ~ 0.8 V on Pt/BDD electrodes, there are a lot of potential interfering compounds that may affect NO detection. In this work, two significant interfering compounds in NO detection are especially of concern, namely nitrite (NO_2^-) and ascorbic acid (AA). The former is recognised as the most important interference in NO detection as an oxidation peak appears at almost exactly the same position as NO due to the disproportionation reaction which generates free NO, especially at acidic pH values[32]. In mixtures comprising both NO and NO_2^-, it is thus barely possible to determine the origin of the 'NO' if nitrite is in the vicinity of the electrode. As for ascorbate, as it normally has a comparatively high concentration in

biological systems and is easily oxidised, the strong background current arising can make it difficult to detect the weak signal currents from NO.

5.3.3.1 NO detection in the presence of NO_2^-

As described above, NO_2^- is one of the crucial interfering products in the NO detection. In order to achieve much better selectivity against it, almost all the studies to date preferentially apply nafion as an effective membrane coated upon the modified electrode. Nafion is well acknowledged for its unique ionic properties as a proton exchange membrane that only allows the cationic protons to penetrate through. In the NO and NO_2^- co-existing system, the negatively charged NO_2^- species are hereby significantly passivated while the neutral NO molecules can still pass the membrane to reach the active Pt sites underneath to some extent. It has been broadly proved that with a stable coverage of nafion film, the NO_2^- signal responses can be completely eliminated even with a much higher concentration compared with its NO counterpart. Although this seems to solve the selectivity problem, an apparent disadvantage is the attenuated detection sensitivity of NO due to blocking effects. In the present work we therefore explored if an oxide coating with PrO_x could enhance selectivity without loss of sensitivity since it was observed previously that PrO_x could induce selectivity against ascorbate[38].

Results are compared in **Figure 5.7**. A solution comprising 9.0×10^{-5} M NO, with and without 20-fold NO_2^-, *i.e.* 1.8×10^{-3} M in 0.1 M PBS were measured respectively using SWV as shown in **Figure 5.7** at two different electrodes. On the pure Pt-coated BDD electrode, the mixed solution shows a higher current response due to the signal contributions from both NO and NO_2^- compositions than in a solution containing only

NO. It is noticeable that although the NO_2^- presence is approximately 20 times higher than that of NO in the mixed solution, it only exhibits a comparable signal response to NO, showing that even the Pt/BDD electrode at neutral pH has some selectivity due to limited disproportionation of nitrite. Varied loadings of the PrO_x layer were investigated by operating the electrodeposition with different cyclic scan numbers using conditions described in *section* 5.2 above, and data in the **Figure 5.7** b) refers to a thick oxide coverage produced by 40 CV scans in the solution containing Pr^{3+}. For this thick oxide coating, the NO signal is attenuated by a factor of 2. However the signal response in the presence of nitrite is essentially the same as in its absence, indicating that good selectivity against nitrite is imparted by the oxide layer.

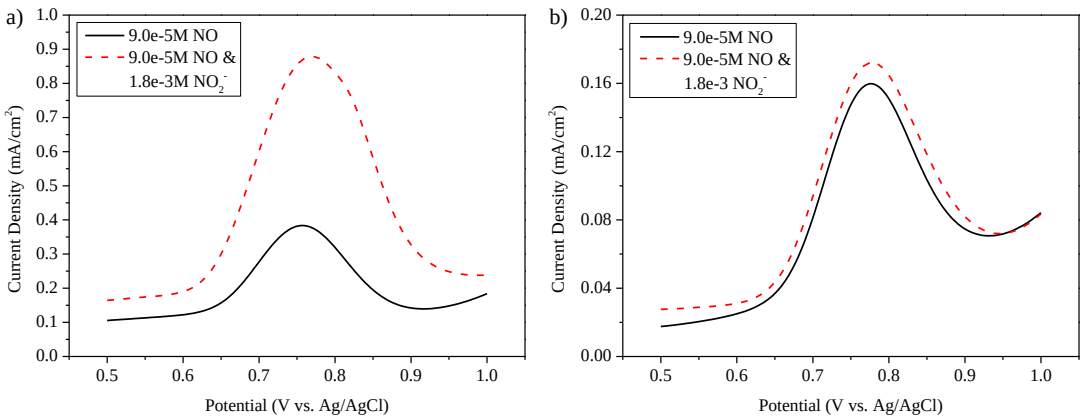


Figure 5.7 SWVs of 9.0 $\times 10^{-5}$ M NO, and its mixed solution with 1.8 $\times 10^{-3}$ M NO_2^- in 0.1 M PBS (pH = 7.4) at a frequency of 10 Hz along with a 0.002 V step potential and a 0.05 V amplitude on a) Pt/BDD and b) PrO_x-Pt/BDD after 40 cyclic scans in the electrodeposition of PrO_x

Optimal performance is expected when the PrO_x coating is thick enough to impart selectivity but sufficiently thin to maintain sensitivity. In order to modify the thickness of the deposited oxide layer, the scan numbers in CV deposition were decreased by half to 20 instead and data are presented in **Figure 5.8** a) and b) for the same Pt-loaded BDD electrode with and without oxide. As displayed in **Figure 5.8** a), qualitatively similar to

Figure 5.7 a), the addition of nitrite to a solution containing NO results in an increased signal due to the problems with selectivity. Clearly much better selectivity is seen in **Figure 5.8** b), when PrO_x decorates the surface. However for the thinner oxide coating, no attenuation is seen in NO signal when the oxide layer is added to the surface. Indeed a small increase in NO signal is actually observed. The PrO_x coating therefore seems to offer uniquely advantageous properties in that it eliminates the response to nitrite (similar to nafion) whilst leaving the NO signal unaffected (unlike nafion). The proposed reasons of why the oxide layer shows such distinct features will be discussed later in this chapter. However, it is obvious that the thickness of the deposited film plays a crucial role in NO detection to determine whether the catalytic activity for NO will be boosted or attenuated, in spite of always attenuating NO_2^- responses.

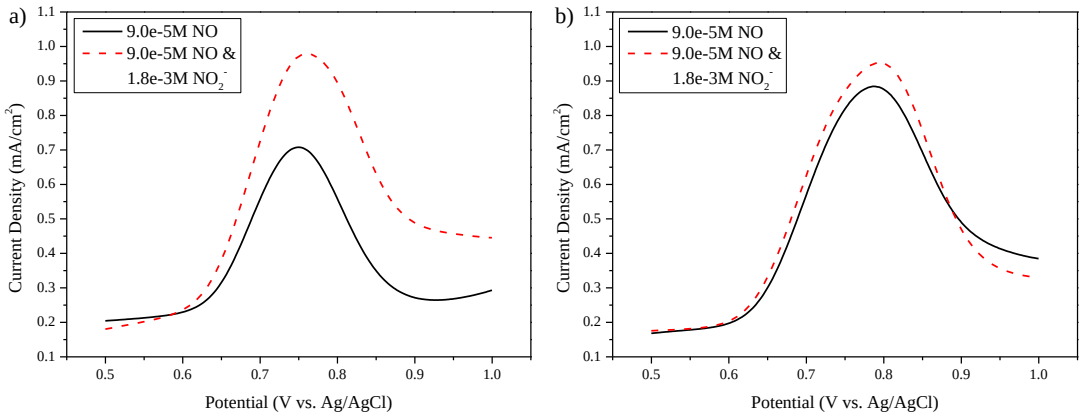


Figure 5.8 SWVs of 9.0 × 10^{-5} M NO, and its mixed solution with 1.8 × 10^{-3} M NO_2^- in 0.1 M PBS (pH = 7.4) at a frequency of 10 Hz along with a 0.002 V step potential and a 0.05 V amplitude on a) Pt/BDD and b) PrO_x-Pt/BDD after 20 cyclic scans in the electrodeposition of PrO_x

5.3.3.2 NO detection in the presence of AA

Ascorbate is the other main interference in the electrochemical detection of NO and other *in vivo* applications due to its ease of oxidation and relatively concentrated presence in many living systems. CVs were hereby carried out with 5.4 × 10^{-5} M NO

and 1.8 × 10^{-3} M AA in 0.1 M PBS, respectively, to see their activity variations after the PrO_x layer coating was deposited on the Pt-modified diamond electrode as shown in **Figure 5.9**. As the normal AA concentration range is around 2.3 to 8.5 × 10^{-5} M[39] while the NO level is approximately 0.91 to 3.46 × 10^{-5} M[40], respectively, in healthy individuals, this high ascorbate to NO ratio used here can further optimise the accuracy for realistic testing even in a much larger presence of interfering product. **Figure 5.9** b) compares data for ascorbate on the oxide free and oxide coated Pt-diamond electrode. Without the oxide, an oxidation peak is seen at about 0.3 V as expected for ascorbate[41], significantly lower than that seen on diamond because of the electrocatalytic effect of Pt. An irreversible oxidation wave is also discovered at ~ 0.6 V, which is typical for ascorbate oxidation on diamond, presumably occurring in regions of the electrode as seen in SEM where Pt is at low concentration. Virtually complete attenuation of these signals is seen in the presence of PrO_x. The results are thus somewhat similar to that seen for nitrite; some decay of the NO signal occurs as exhibited in **Figure 5.9** a) but the comparative attenuation of the anionic nitrite or ascorbate is much greater.

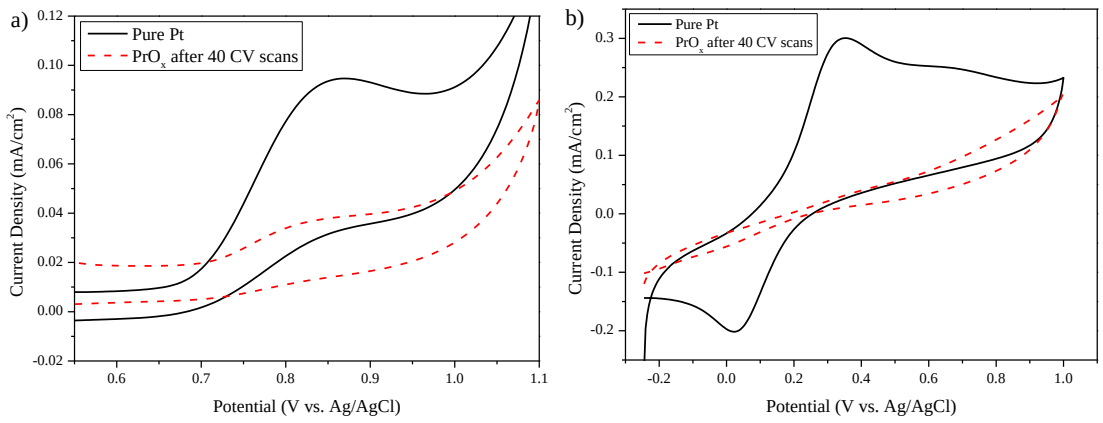


Figure 5.9 CVs of a) 5.4 × 10^{-5} M NO and b) 1.8 × 10^{-3} M AA in 0.1 M PBS (pH = 7.4) at a scan rate of 50 mV/s on Pt/BDD and PrO_x-Pt/BDD after 40 cyclic scans in the electrodeposition of PrO_x

In order to investigate the behaviours of NO and AA co-existing in the same system, CVs were further carried out with a mixed solution comprising of 9.0×10^{-5} M NO and 1.8×10^{-3} M AA in 0.1 M PBS on the BDD electrode modified with pure Pt and after successive 20 and 40 cyclic scans for PrO_x deposition as exhibited in **Figure 5.10**. For the very thick oxide coating (40 scans), complete attenuation of the redox signals associated with ascorbate seems to occur, and some broadening and attenuation of the oxidation wave of NO also arises. For the thinner oxide coating (20 scans), some residual redox behaviour of ascorbate is seen, however the NO signal is signifncantly enhanced. The thickness of the oxide layer can thus be used to fine-tune the relative signal responses from ascorbate and NO to desired values.

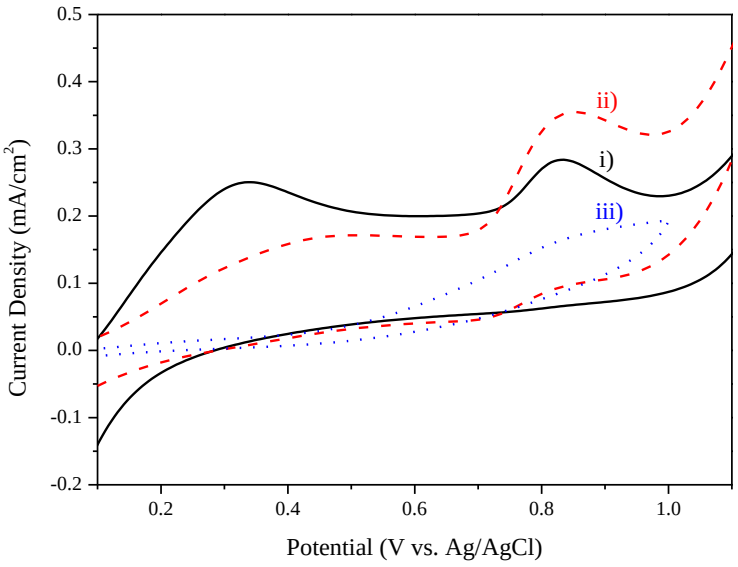
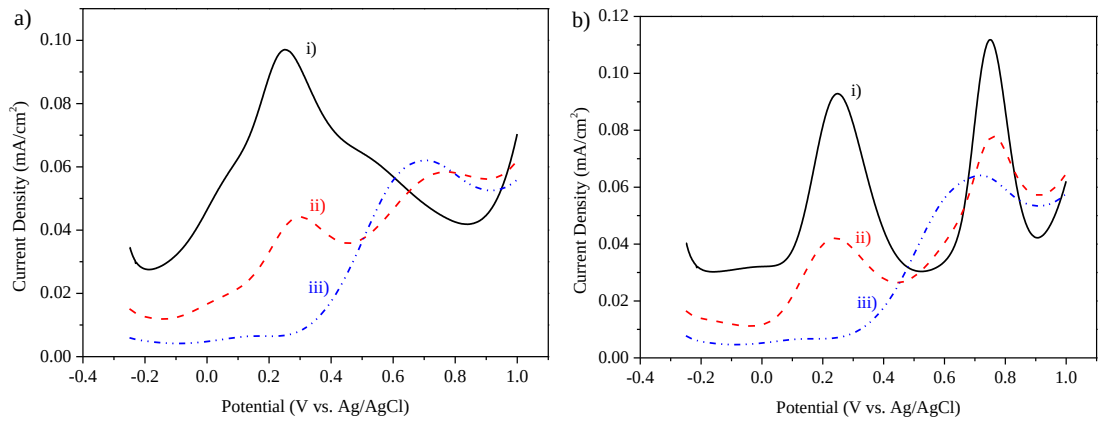


Figure 5.10 CVs of the mixed solution of 9.0×10^{-5} M NO and 1.8×10^{-3} M AA in 0.1 M PBS (pH = 7.4) at a scan rate of 50 mV/s on i) pure Pt and Pt-PrO_x coated BDD electrode after ii) 20 and iii) 40 cyclic scans in the electrodeposition of PrO_x.

Similar results using SWV at a frequency of 10 Hz along with a 0.002 V step potential and a 0.05 V amplitude are illustrated in **Figure 5.11**. The concentration of interfering AA was fixed at a very high level of 1.8×10^{-3} M as used in CVs above but the NO

concentrations were varied from 1.8 × 10^{-5} to 1.8×10^{-4} M in 0.1 M PBS electrolyte. With the largest concentration disparity between these analytes, the NO oxidation signal cannot be easily observed at the concentration of 1.8 × 10^{-5} M on the pure Pt-coated BDD electrode as depicted in **Figure 5.11** a) since a strongly varying background is seen, most probably linked to the oxidation of ascorbate at high overpotentials on bare diamond. Even with a very thin oxide layer, prepared from only 2 CV scans, PrO_x is sufficient to attenuate this background contribution to permit the NO signal at this concentration to be observed using SWV although the 'cleanest' NO response is seen with the thick oxide layer. Similar phenomena are achieved throughout the whole range of NO presences displayed in **Figure 5.11** b), c) and d) as the NO peak current remains at a certainly visible level while AA is entirely passivated even if with a much larger presence. It is also discovered however that although the NO responses vary corresponding to the different concentrations, a final state with a fairly close intensity value is obtained on the modified electrode after 40 CVs electrodeposition of PrO_x in all cases. This suggests that with the same thick oxide loading, only a certain amount of NO molecules were involved in the catalytic oxidation, which is correlated with barely changed current responses irrelevant of the actual NO concentrations.



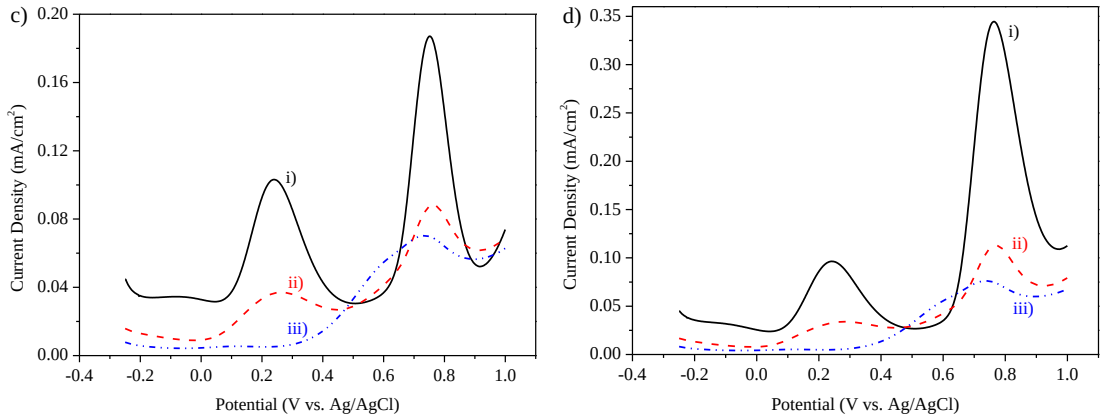


Figure 5.11 SWVs of the mixed solution comprising of 1.8 × 10^{-3} M AA with a) 1.8 × 10^{-5} M, b) 3.6 × 10^{-5} M, c) 9.0 × 10^{-5} M and d) 1.8 × 10^{-4} M NO in 0.1 M PBS (pH = 7.4) at a frequency of 10 Hz along with a 0.002 V step potential and a 0.05 V amplitude on i) Pt and PrO_x-Pt coated BDD electrode after ii) 2 and iii) 40 cyclic scans in the electrodeposition of PrO_x

The same experiments were conducted with less PrO_x coverage deposited from 20 CV scans instead. Two different NO concentrations of 3.6 × 10^{-5} and 9.0 × 10^{-5} M were respectively applied along with the fixed AA presence of 1.8 × 10^{-3} M mentioned before in 0.1 M PBS as demonstrated in **Figure 5.12**. With the somewhat thinner coating of the oxide layer, the AA peak response is attenuated by over 90% but not fully eliminated, as a broad response in the characteristic region is still visible. The SWV NO signal intensity however now tracks the NO concentration much more faithfully. This observation is contrary to that achieved on the modified electrode with thicker coverage of PrO_x as all the signals are restricted into a certain level, which is not especially related to the NO concentration. This 'proper' oxide deposition is supposed not to simply block the diffusion of anionic AA from reaching the Pt nanoparticles but is also involved in the interaction with NO molecules such that the oxidation rate is directly related to their concentrations. One can only speculate at present why this situation might arise. But for example a thin oxide coating might be expected to permit efficient transport of NO from solution to the electroctive sites leading to a response that tracks NO concentration. In contrast for a very thick oxide layer, perhaps the detected NO

reflects the concentration of NO in the outermost oxide layers, the binding sites of which saturate very easily leading to a constant detected signal independent of the concentration in solution.

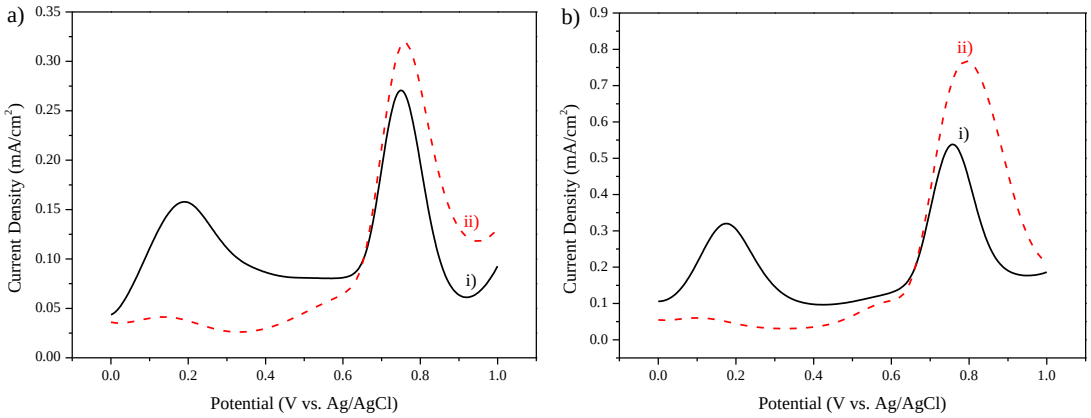


Figure 5.12 SWVs of the mixed solution of 1.8 × 10^{-3} M AA with a) 3.6 × 10^{-5} M and b) 9.0 × 10^{-5} M NO in 0.1 M PBS (pH = 7.4) at a frequency of 10 Hz along with a 0.002 V step potential and a 0.05 V amplitude on i) pure Pt and ii) Pt-PrO_x coated BDD electrode after 20 cyclic scans in electrodeposition.

5.3.3.3 NO detection in the presence of both NO_2^- and AA

Since NO has been detected in the presence of NO_2^- or AA respectively, further investigation aimed to feature how the signal responses would vary in the mixed solution comprising of all these three analytes above. The chronoamperometric technique is broadly utilised in various sensing works in chemical and biological systems and was hereby applied here at a fixed potential of 0.8 V, which was almost the same value that NO is electrochemically oxidised under CV characterizations. The measurement was operated in stirred 0.1 M PBS blank solution after stabilisation for approximately 200 seconds prior to the injections of analytes. Different concentrations of NO_2^- (1.8 × 10^{-3} M), NO (3.6 × 10^{-5} to 9.0 × 10^{-5} M) and AA (0.9 and 1.8 × 10^{-3} M) were added sequentially at 100-second intervals until the experiment ended at 1000 seconds. Typical data is shown in **Figure 5.13** i) for the bare Pt-BDD electrode. Very

strong responses from both NO_2^- and AA are expectedly achieved with the large concentrations injected although detected NO signals at the μM level can be seen despite these interfering chemicals. After being further modified with an 'ideal' amount of PrO_x after 20 cyclic scans electrodeposition, both anionic interfering products suffer large attenuations in signals, decreasing to approximately 10 – 20% of their original values. This is tightly correlated with the observations in previous CV and SWV characterisations, suggesting these negative charged species are quite vulnerable to the passivation effects associated with the oxide layer. Conversely, the NO responses are increased, showing the dominant intensity at the concentration of 9.0×10^{-5} M. It is also seen that the current enhancements fairly faithfully track the NO concentration in solution. As seen in CV/SWV, it can be confirmed that the presence of the PrO_x layer can be used to effectively block interference from nitrite and ascorbate, whilst enhancing signal contributions from NO. This is therefore likely to prominently improve NO detection limits in the large presence of these interfering compounds.

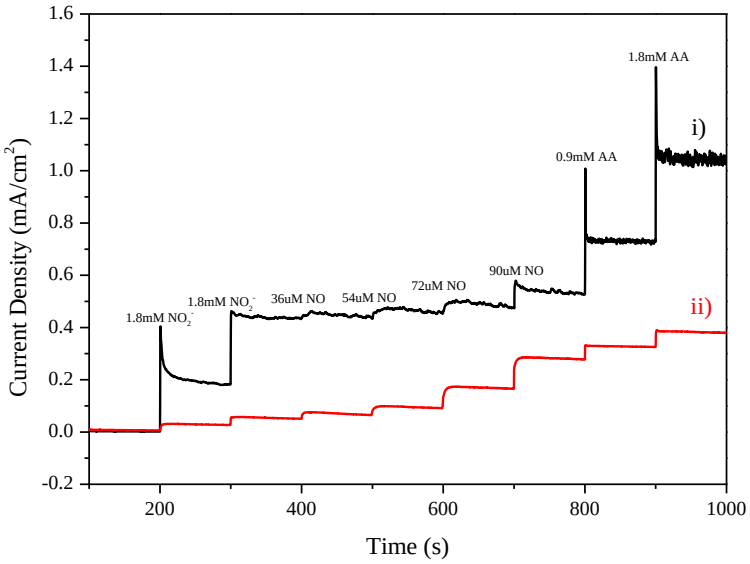


Figure 5.13 Chronoamperometric measurement at 0.8 V *vs.* Ag/AgCl in 0.1 M PBS (pH = 7.4) for 1000 seconds with successive injections of NO_2^-, NO and AA with varied concentrations on i) pure Pt/BDD and ii) Pt-PrO_x/BDD after 20 cyclic scans in electrodeposition.

5.3.4 Detection limit

All the previous results have proved the promising properties of the PrO_x/Pt structure in the electrochemical detection of NO with large presence of other anionic interfering compounds. However, all the characterisations were conducted with the NO concentration around 10^{-5} to 10^{-4} M level, which is slightly higher than the expected detection requirements of 0.91 to 3.46 × 10^{-5} M in the chemical or biological systems[40]. Therefore the detection limit is also considered as a key factor to judge the overall performance of the modified electrode for *in vivo* applications. In all electrochemical characterisations operated under analytical instruments, tiny signals described as the noise level will be inevitably produced even with the blank electrolyte. The detection limit is hereby identified as the analyte concentration that is minimally required to produce a signal at least three times higher than the noise level (S/N = 3). The amperometric technique is introduced again to feature this value on both Pt-coated and PrO_x further modified electrodes at the potential of 0.8 V as mentioned previously.

In order to prepare lower concentrations of NO solutions suitable for the detection limit investigations, the preparation initially started from diluting the saturated NO solution (1.8 × 10^{-3} M) 10 times to achieved a 1.8 × 10^{-4} M NO in 0.1 M PBS (pH = 7.4) electrolyte which was kept well-sealed for further operations. Successive dilutions were conducted similarly, until fairly low stock concentrations of 1.8 × 10^{-8} M were eventually achieved which was used in chronoamperometric experiments. At these low concentrations some difficulty was experienced in achieving stable responses due to a combination of factors including some or all of electrolytic depletion of NO from the electrode region, loss to the gas phase and non-electrochemical oxidation. Nonetheless useful chronoamperometric traces in **Figure**

5.14 were recorded in the 10^{-7} M range. Given the typical noise levels from this and similar data, the detection limit of 9.0×10^{-8} and 4.6×10^{-8} M for Pt/BDD and PrO_x-Pt/BDD respectively was estimated, where the latter improvement reflects the enhanced signal strength due to the catalytic properties of PrO_x in the NO oxidation step.

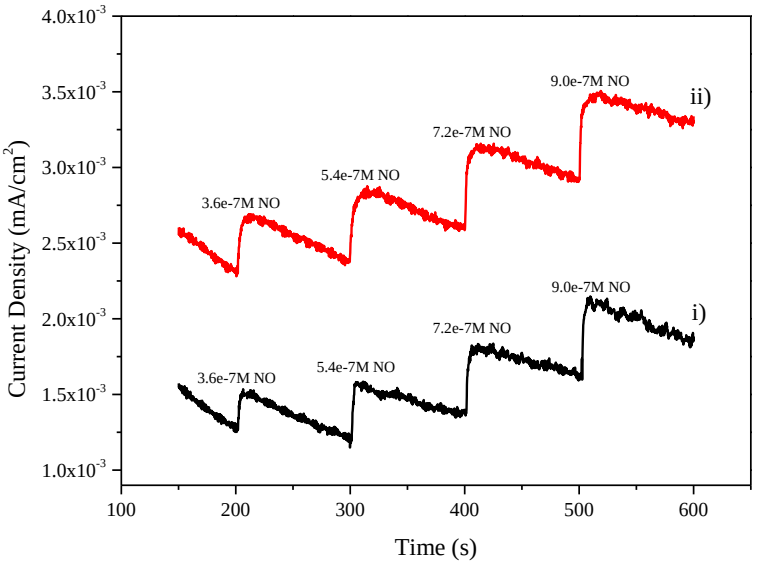


Figure 5.14 Chronoamperometric measurement at 0.8 V *vs.* Ag/AgCl in 0.1 M PBS (pH = 7.4) for 600 seconds with successive injections of NO from its aqueous solution at a concentration of 1.8×10^{-5} M on i) Pt/BDD and ii) PrO_x-Pt/BDD after 20 cyclic scans in electrodeposition.

5.3.5 Mechanism of NO electrochemical oxidation on PrO_x-Pt/BDD

According to all the results above, the electrodeposited PrO_x has exhibited features clearly associated with enhancing electrochemical signal intensities associated with NO oxidation whilst attenuating these with regards to nitrite and ascorbate. Although the latter features are similar to nafion, the former is not since nafion very significantly attenuates NO signals leading to poor sensitivity[15, 42]. As described elsewhere in this thesis (see *Chapter* 6), PrO_x can be thought of as an oxygen deficient material which carries a positive surface charge in many environments due to the presence of coordinativley unsaturated Pr (III)/(IV) species. If anions such as ascorbate and nitrite

can be bound to the oxide, then a negatively charged film may arise if sufficient accumulation occurs. Thus although the film eventually shows comparable behavior with its nafion counterpart, it is instead achieved by the accumulation of other species rather than the natural properties shown of the oxide. A schematic mechanism is depicted in **Figure 5.15** as below.

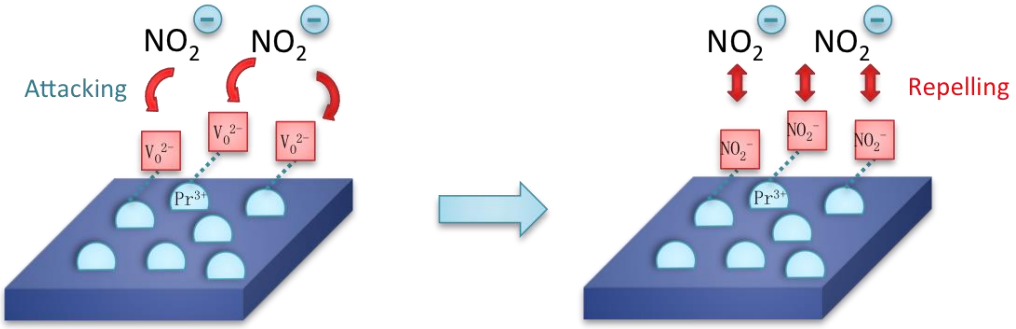


Figure 5.15 Proposed interaction mechanism between the PrO_x layer and anionic interfering compounds, *e.g.* NO_2^-

Similar to the speculations on the repelling effects against the interference, oxygen vacancies are also thought to play a crucial role in boosting the catalytic activity. Mart ńez-Arias *et al*[43] and Niwa *et al*[44] both introduced the reaction mechanism of adsorbed NO on the cerium oxide, forming a diamagnetic chelating nitrite species. As PrO_x has fairly close structural features with CeO_x, NO species are hereby suggested to attack the oxygen vacancies and are thus chemically activated and concentrated at the PrO_x/Pt interface, leading to enhanced electrochemistry. Of course detailed investigations would be required to deduce the exact surface sites and adsorbed species. The essential point however is that the oxide is essentially acting as an active electrochemical promoter rather than an inert passivated filter.

5.4 Summarising comments

The feasibility of using the Pt and PrO_x modifications to a diamond electrode described in *Chapter* 4 to advantageously modify diamond for electrochemical sensing of NO has been investigated.

- Pt coated BDD exhibits superior catalytic activity for NO electrochemical oxidation compared with the bare BDD electrode, as reflected in the useful reduction in the high overpotential which NO oxidation exhibits on clean diamond, resulting in a peak close to the water electrolysis limit. However the electrode is not especially selective since interfering compounds such as nitrite and ascorbate are also easily oxidised.
- A PrO_x coating displays similar properties to the previously used nafion film in this area in terms of reducing sensitivity to NO_2^- and AA. However in marked contrast to nafion, this oxide material coating can actually enhance the signal response to NO if the thickness of the oxide layer is optimised. If the coating is too thick, then some NO signal attenuation is observed, and the signal 'saturates' hence does not reflect NO in bulk solution. A mechanism has been suggested whereby anions bond to oxygen vacancies in the oxide layer leading to the development of a negative charge, thereby repelling anions such as nitrite and ascorbate. In contrast it is suggested that these active sites can bind and chemically activate the NO analyte.
- The detection limit was estimated with a chronoamperometric method using a series of NO solutions throughout a wide concentration range. The value is determined to be 9.0×10^{-8} M with pure Pt deposits and further optimised to a more sensitive level of 4.6×10^{-8} M with proper PrO_x coating. Although even

lower detection values were probably achievable, the difficulty in accurately controlling NO concentration in bulk dilute solutions introduced uncertainties in this area.

References

[1] B.S. Masters, K. McMillan, E.A. Sheta, J.S. Nishimura, L.J. Roman, P. Martasek, The FASEB journal 10 (1996) 552-558.

[2] H. Bult, G.E. Boeckxstaens, P.A. Pelckmans, F.H. Jordaens, Y.M. Van Maercke, A.G. Herman, Nature 345 (1990) 346-347.

[3] M.G. Belvisi, C. David Stretton, M. Yacoub, P.J. Barnes, Eur. J. Pharmacol. 210 (1992) 221-222.

[4] S.H. Snyder, Science (New York, NY) 257 (1992) 494.

[5] S.R. Vincent, Prog. Neurobiol. 42 (1994) 129-160.

[6] E. Moilanen, H. Vapaatalo, Ann. Med. 27 (1995) 359-367.

[7] E. Änggård, The Lancet 343 (1994) 1199-1206.

[8] C. Bogdan, Nat. Immunol. 2 (2001) 907-916.

[9] R.M. Palmer, A.G. Ferrige, S. Moncada, Nature 327 (1987) 524-526.

[10] L.J. Ignarro, G.M. Buga, K.S. Wood, R.E. Byrns, G. Chaudhuri, Proc. Natl. Acad. Sci. USA 84 (1987) 9265-9269.

[11] T.M. Dawson, V.L. Dawson, S.H. Snyder, Ann. Neurol. 32 (1992) 297-311.

[12] T. Nguyen, D. Brunson, C.L. Crespi, B.W. Penman, J.S. Wishnok, S.R. Tannenbaum, Proc. Natl. Acad. Sci. USA 89 (1992) 3030-3034.

[13] E.M. Schuman, D.V. Madison, Science 254 (1991) 1503-1506.

[14] X. Zhang, L. Cardosa, M. Broderick, H. Fein, J. Lin, Electroanalysis 12 (2000) 1113-1117.

[15] S. Wang, X. Lin, Electrochim. Acta 50 (2005) 2887-2891.

[16] L.J. Ignarro, Hypertension 16 (1990) 477-483.

[17] A. Fontijn, A.J. Sabadell, R.J. Ronco, Anal. Chem. 42 (1970) 575-579.

[18] C. Tang, S. Zou, M.W. Severson, M.J. Weaver, J. Phys. Chem. B 102 (1998) 8546-8556.

[19] T. Akaike, M. Yoshida, Y. Miyamoto, K. Sato, M. Kohno, K. Sasamoto, K. Miyazaki, S. Ueda, H. Maeda, Biochemistry 32 (1993) 827-832.

[20] T. Malinski, Z. Taha, Nature 358 (1992) 676-678.

[21] M. Pallini, A. Curulli, A. Amine, G. Palleschi, Electroanalysis 10 (1998) 1010-1016.

[22] F. Bedioui, N. Villeneuve, Electroanalysis 15 (2003) 5-18.

[23] N. Imanaka, A. Oda, S. Tamura, G.-y. Adachi, J. Electrochem. Soc. 151 (2004) H113-H116.

[24] N. Diab, W. Schuhmann, Electrochim. Acta 47 (2001) 265-273.

[25] Y. Xian, W. Zhang, J. Xue, X. Ying, L. Jin, J. Jin, Analyst 125 (2000) 1435-1439.

[26] M. Maskus, F. Pariente, Q. Wu, A. Toffanin, J.P. Shapleigh, H.D. Abruna, Anal. Chem. 68 (1996) 3128-3134.

[27] J. Pei, N.-T. Yu, X.-Y. Li, Anal. Chim. Acta 402 (1999) 145-155.

[28] A.C.A. De Vooys, M.T.M. Koper, R.A. Van Santen, J.A.R. Van Veen, J. Catal. 202 (2001) 387-394.

[29] G.L. Beltramo, M.T.M. Koper, Langmuir 19 (2003) 8907-8915.

[30] S. Ye, H. Kita, J. Electroanal. Chem. 346 (1993) 489-495.

[31] D. Dutta, D. Landolt, J. Electrochem. Soc. 119 (1972) 1320-1325.

[32] F. Bedioui, S. Trevin, V. Albin, M. Guadalupe, G. Villegas, J. Devynck, Anal. Chim. Acta 341 (1997) 177-185.

[33] C. Fan, G. Li, J. Zhu, D. Zhu, Anal. Chim. Acta 423 (2000) 95-100.

[34] F.-H. Wu, G.-C. Zhao, X.-W. Wei, Electrochem. Commun. 4 (2002) 690-694.

[35] T. Malinski, Z. Taha, S. Grunfeld, A. Burewicz, P. Tomboulian, F. Kiechle, Anal. Chim. Acta 279 (1993) 135-140.

[36] S. Shrestha, F. Marken, J. Elliott, C.M.Y. Yeung, C.E. Mills, S.C. Tsang, J. Electrochem. Soc. 153 (2006) C517-C520.

[37] A.R. Butler, D.L.H. Williams, Chem. Soc. Rev. 22 (1993) 233-241.

[38] M. Sawangphruk, Electrochemical deposition and properties, of nanostructured materials, Oxford University, 2010.

[39] http://www.merckmanuals.com/home/appendixes/common_medical_tests/common_medical_tests.html.

[40] D. Fareed, O. Iqbal, M. Tobu, D.A. Hoppensteadt, J. Fareed, Clin. Appl. Thromb. Hemost. 10 (2004) 357-364.

[41] J. Weng, J. Xue, J. Wang, J. Ye, H. Cui, F. Sheu, Q. Zhang, Adv. Funct. Mater. 15 (2005) 639-647.

[42] C.M. Li, J. Zang, D. Zhan, W. Chen, C.Q. Sun, A.L. Teo, Y. Chua, V. Lee, S. Moochhala, Electroanalysis 18 (2006) 713-718.

[43] A. Martínez-Arias, J. Soria, J.C. Conesa, X.L. Seoane, A. Arcoya, R. Cataluña, J. Chem. Soc., Faraday Trans. 91 (1995) 1679-1687.

[44] M. Niwa, Y. Furukawa, Y. Murakami, J. Colloid Interface Sci. 86 (1982) 260-265.

Chapter 6

Investigations on the Properties of Electrodeposited Praseodymium Oxide (PrO_x)

6.1 Introduction

Rare earth oxide materials have attracted notable attentions in various areas of electrochemical catalysis[1-3]. They are well acknowledged to exhibit a fast oxygen ion mobility, a high surface basicity along with various interesting semiconductor properties which are considered crucial in their applications[4]. The majority of previous work in this field has preferentially focused on cerium oxide (ceria), CeO_2.

For most rare earth oxide materials, the trivalent oxidised state *i.e.* Ln_2O_3 (where Ln stands as rare earth element) is thought to be the most stable[5]. However for cerium, the fourth ionisation potential is more favourable[6]. In general applications, cerium will be oxidised to different extents, leading to the co-existence of several non-stoichiometric phases in the oxidised product CeO_x, where *x* fluctuates between 1.5 to 2, representing the oxygen-deficient and oxygen-rich states respectively. Pure stoichiometric cerium oxide has a typical calcium fluoride (fluorite) crystal structure with $Fm\bar{3}m$ space group throughout the whole temperature range from room temperature to its melting point[7]. This structure allows a rapid diffusion of oxygen atoms to form or eliminate varied amounts of oxygen vacancies in the whole structural system, resulting in a high 'oxygen storage capacity'[8]. As the number of these vacancies increases, a higher mobility of oxygen atoms is achieved, allowing this oxide to oxidise or reduce other species or incorporate with other catalytic molecules on its surface due to the conversion of two ionization potentials[9]. It has been suggested that the catalytic activity of ceria-based

material is directly associated with the number of oxygen vacancies in the oxide[10]. The ratio of two ionisation states, *i.e.* Ce^{3+} and Ce^{4+} can therefore be detected under XPS, exhibiting the extent of oxidisation in certain products.

Ceria is well acknowledged as a good candidate in solid oxide fuel cell (SOFC) applications either as electrolyte or anode. Yahiro *et al* investigated a high temperature SOFC using Y_2O_3 doped ceria as the electrolyte[11] while He *et al* described Cu and YSZ incorporated ceria as an optimistic anode material for SOFC[12]. Ceria has been broadly reported for its advantageous properties in association with other catalysts in treating exhaust gases. Wu *et al* reported ceria modified MnO_x/TiO_2 catalyst in selective catalytic reduction (SCR) of NO_x to clean this main air pollutant from stationary sources[13]. Sayle *et al* stated the function of oxygen vacancies in promoting the oxidation of carbon monoxide into harmless carbon dioxide by computer simulation[14]. More recently, ceria was economically co-deposited with pure Pt to prohibit the Pt surface being poisoned by the carbonaceous intermediate species due to incomplete methanol oxidation in fuel cell applications[15, 16]. It is suggested that CO was removed by oxygen attached on Ce (IV) oxide to form CO_2, leaving an oxygen ion vacancy on the surface, associated with the reduction from (IV) oxidative state into (III)[17].

Similar with ceria, stoichiometric praseodymium oxide (PrO_2) has the same fluorite structure. It has been observed that its finite electrical conductivity is ascribed to the electron hopping between the two ionisation states, *i.e.* Pr^{3+} and Pr^{4+} in the lattice[4]. It indicates that this oxide may follow similar mechanisms with the ceria counterpart in many applications due to a high mobility of oxygen vacancies in the crystal structure,

activating the reduction or oxidation of certain species, associated with the variation of ionic valence between Pr^{3+} and Pr^{4+}.

As stated in previous chapters, oxygen deficient praseodymium oxide (PrO_x) can be applied as a catalyst promoter with noble platinum nanoparticles to improve the catalytic activity of Pt in various applications such as DMFCs and electrochemical detection of NO. The oxide film is considered as being able to adsorb hydroxyl groups that accelerate the 'spill-over' mechanism[18] to eliminate the poisoning carbonaceous molecules in methanol oxidation. The surface is also believed to be positively charged due to the existence of various oxygen vacancies.

At present, the most commonly applied techniques for the formation of oxide film consisting of chemical vapor deposition[19], vacuum evaporation[20], electron beam evaporation[21] and spin coating[22] are all generally based on the physical deposition of certain materials onto a substrate surface. However, when used for electrocatalyst modifications, electrodeposition is more attractive - it is fully compatible with the electrochemical environment and deposition can be preferentially focused on the electrochemically active regions.

While some insight into the electrochemical properties of PrO_x have been presented earlier in this thesis, this chapter aims to address this area through a series of more detailed electrochemical and surface characterisation studies. Both CV and SWV were used to investigate the behaviour of the PrO_x surface in contact with various redox species including cationic $Ru(NH_3)_6^{2+/3+}$, anionic $Fe(CN)_6^{3-/4-}$ and neutral $FcCH_2OH^{0/+}$. XPS was selected to study the elemental compositional information of the substrate

surface. Dynamic Light Scattering (DLS) method combined with *zeta* potential measurement was complementarily chosen to examine the surface charge of praseodymium oxide and the size distribution in its own suspension. Further investigations were carried out by testing with biological molecules such as dopamine (DA) to explore in the context of biosensing devices.

6.2 Experimental

6.2.1 Materials, instruments and techniques

The electrochemical and surface characterisations were conducted under the same conditions as being stated in *Chapter* 3 and 4. DLS and *zeta* potential measurement was carried out with a Malvern Zetasizer Nano ZS instrument, electrophoresis and dynamic light scattering technique was selected respectively to feature the surface charge and the size distribution in the colloidal suspension of PrO_x.

Praseodymium nitrate hexahydrate ($Pr(NO_3)_3{\cdot}6H_2O$, 99.9%), hydrogen peroxide (H_2O_2, 50wt.%), hexaammineruthenium(III) chloride ($Ru(NH_3)_6Cl_3$, 98%), potassium ferrocyanide ($K_4Fe(CN)_6$, 98.5%), potassium ferricyanide ($K_3Fe(CN)_6$, 99.99+%), potassium iridium chloride (K_2IrCl_6, 99.99%), ferrocene methanol ($C_{11}H_{12}FeO$, 97%), L-Ascorbic acid ($C_6H_8O_6$, ≥ 99%), Dopamine hydrochloride ($C_8H_{11}NO_2{\cdot}HCl$) were all purchased from Sigma-Aldrich. All the solutions were prepared using milli-Q water (> 18 MΩ cm) and 0.1 M KCl was chosen as the counter electrolyte in all relevant electrochemical characterisations.

6.2.2 Electrodeposition of PrO_x

The electrodeposition of PrO_x has already been described in *Chapter* 4 by conducting

CV in a negative potential range from 0 to -1.5 V in 0.1 M KCl containing PrO_x and H_2O_2. However as it was carried out on the bare BDD electrode without any Pt coating instead in this project, both concentrations of PrO_x and H_2O_2 precursors and scan numbers in CV electrodeposition were selectively varied to investigate how the coverage would be affected by these factors.

6.3 Results and discussion

6.3.1 Electrochemical characterisations of bare BDD

In order to distinguish PrO_x modified and bare BDD, a series of electrochemical characterisations were first carried out by using several different mediators on a bare BDD electrode substrate. $Ru(NH_3)_6^{2+/3+}$ and $FcCH_2OH$ were selected as positively charged and neutral redox probes while $Fe(CN)_6^{3-/4-}$ and $IrCl_6^{2-/3-}$ were rather chosen as the anionic counterparts. CVs were firstly conducted at a fixed concentration of electrolytes with different scan rates.

As stated in *Chapter* 3, $Ru(NH_3)_6^{2+/3+}$ is well acknowledged as a typical outer sphere electron transfer redox mediator and is insensitive to the electrode surface[23, 24]. CVs of 100 μM $Ru(NH_3)_6Cl_3$ in 0.1 M KCl at varied scan rates from 0.02 to 1.0 V/s are shown in **Figure 6.1** a). The peak-peak potential separation (ΔE_p) is greater than 57 mV at the scan rate of 0.02 V/s and even goes larger gradually as the higher scan rates are applied, showing a quasi-reversible like behaviour (although in part this could be due to the uncompensated resistance of the electrode). However, the peak-peak potential separation is observed not to exceed 100 mV with all the scan rates. The peak current density is proportional to the square root of the scan rate, meaning the redox reaction is controlled by semi-infinite linear diffusion.

CVs were also recorded using 100 μM neutral $FcCH_2OH$ in 0.1 M KCl at the same scan rate range from 0.02 to 1.0 V/s as exhibited in **Figure 6.1** b). Similar to the observations from $Ru(NH_3)_6^{2+/3+}$, this cyclic voltammogram of this mediator electrolyte shows a mean ΔE_p of about 75 mV although the value is slightly higher with increasing scan rates, suggesting fast but quasi-reversible electron transfer kinetics. The diffusional controlled mechanism is also achieved, as the peak current is in linear correlation with square root of the scan rate.

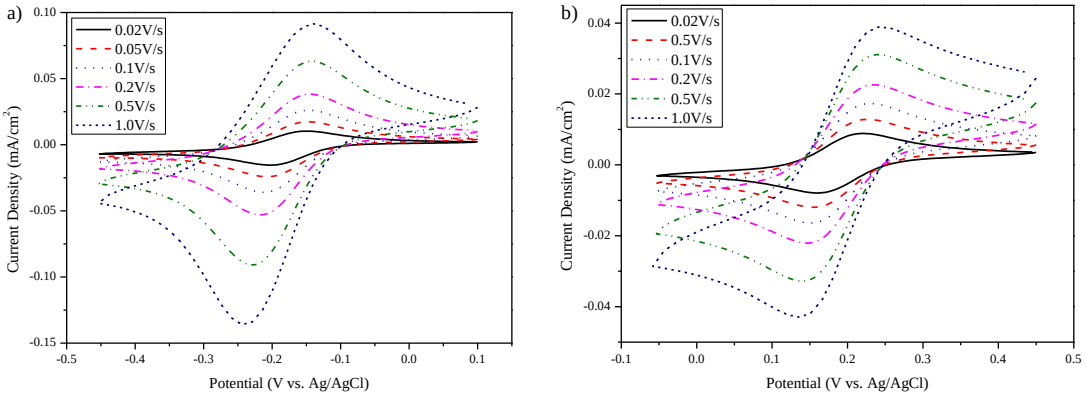


Figure 6.1 CVs of 100 μM a) $Ru(NH_3)_6Cl_3$ and b) $FcCH_2OH$ in 0.1 M KCl on bare BDD at varied scan rates from 0.02 to 1.0 V/s.

Two different anionic species *i.e.* $Fe(CN)_6^{3-/4-}$ and $IrCl_6^{2-/3-}$ were also measured under analogous conditions. As mentioned in *Chapter* 3, $Fe(CN)_6^{3-/4-}$ has some 'inner-sphere' electron transfer mediator characteristics, and as such is sensitive to the surface functionalities, impurities and defects[25, 26]. 100 μM $K_3Fe(CN)_6$ was cyclically scanned in 0.1 M KCl at 0.02 to 1.0 V/s and the peak current is still in line with the square root of the scan rate as displayed in **Figure 6.2** a), suggesting the redox reaction is also controlled by the diffusion of the analyte molecules. The ΔE_p exceeds 100 mV at 0.02 V/s and even gets much bigger at higher scan rates, indicating fairly sluggish electron transfer kinetics for this species. However, different from

other two mediators as discussed above, the results for $Fe(CN)_6^{3-/4-}$ are not always reproducible since this molecule is rather sensitive to the exact chemical state of the electrode surface. Further CVs were conducted by measuring 1 mM $K_3Fe(CN)_6$ solution with consecutively increasing scans from 5 to 500 in 0.1 M KCl at 0.1 V/s, as depicted in **Figure 6.2** b). It is found that the peak current gradually decreases as more scans are conducted. The overall peak current intensity drops by approximately 20% after 500 scans and the redox peaks str*etc*h out to enlarge the ΔE_p by about 100 mV. This suggests the surface may change termination and become deactivated after a long time scanning in $Fe(CN)_6^{3-/4-}$.

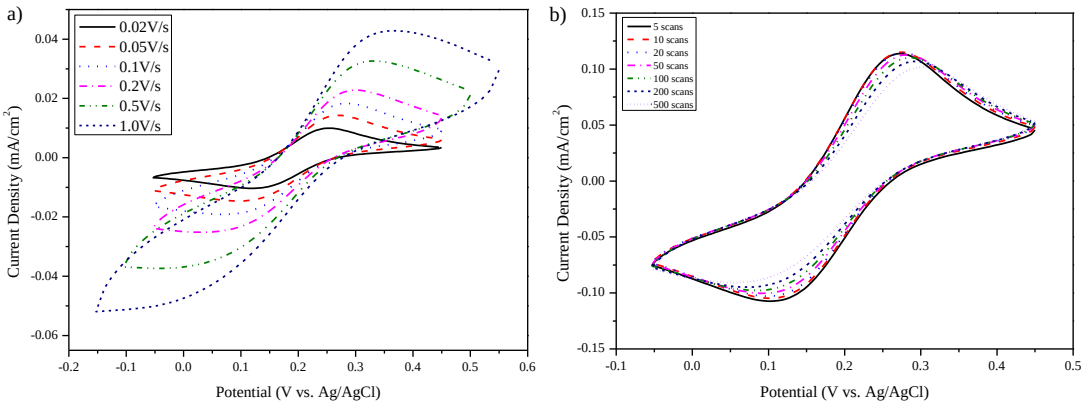


Figure 6.2 CVs of a) 100 µM $K_3Fe(CN)_6$ at varied scan rates from 0.02 to 1 V/s and b) 1 mM $K_3Fe(CN)_6$ after consecutive *n* scans (n = 5 to 500) at 0.1 V/s in 0.1 M KCl on bare BDD.

In comparison, the other anionic redox couple, $IrCl_6^{2-/3-}$ was also measured under CV with 100 µM K_2IrCl_6 in 0.1 M KCl at 0.02 to 0.2 V/s as shown in **Figure 6.3**. The ΔE_p is fairly independent to the scan rate *v* that is applied. Different from its anionic counterpart, $IrCl_6^{2-/3-}$ exhibited reproducible results even though more scans were conducted, indicating this mediator is not as sensitive as $Fe(CN)_6^{3-/4-}$ to the surface chemistry and microstructure but behaves mostly like $Ru(NH_3)_6^{2+/3+}$, whose electron transfer kinetics is mainly determined by the electronic properties of the electrode, *e.g.*

the boron up-take and charge carrier concentration. Similar with the three other mediators above, a semi-infinite diffusional mechanism is also achieved as judged from the scan rate square root dependence of the peak current.

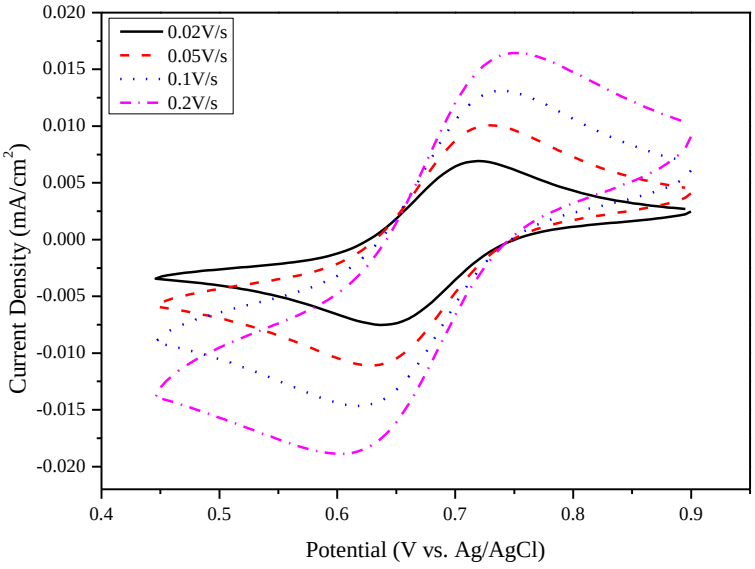


Figure 6.3 CVs of 100 μM K_2IrCl_6 in 0.1 M KCl at varied scan rates from 0.02 to 0.2 V/s on bare BDD

6.3.2 Electrochemical characterisations of PrO_x/BDD

To compare the behaviour of PrO_x modified BDD against that of the bare BDD, electrochemical deposition of PrO_x was carried out following the conditions[27] used in the previous *Chapter* 4. Different from being coated onto the surface with catalytic Pt nanoparticles, the oxide film was rather deposited directly on the BDD surface, which is much less conductive. After cyclic scanning in the precursor solutions containing 25 mM $Pr(NO_3)_3$ and 5 mM H_2O_2 in 0.1 M KCl, a thin layer with light green colour (even lighter at smaller $Pr(NO_3)_3$ content of 5mM) can be seen covering the surface. In order to understand how the oxide layer can affect the behaviour of electrodes facing different electrolytes, the deposition conditions were accordingly varied and some further treatments were operated as being discussed later in this chapter.

6.3.2.1 PrO_x deposition with high concentration of $Pr(NO_3)_3$

25 mM $Pr(NO_3)_3$ and 5 mM H_2O_2 were initially used for PrO_x deposition with only 1 scan in CV at 0.05 V/s to compare the variation of the electrochemical behaviour after the oxide film coating. It is notable to observe that the redox peaks of 100 µM $Ru(NH_3)_6^{2+/3+}$ almost disappear as shown in **Figure 6.4** a), indicating the negligible activity for this mediator with such coverage of the oxide layer. The signal response is still barely discernible even if the concentration increases by 10 times to 1 mM, suggesting the electrode is passivated. Compared with $Ru(NH_3)_6^{2+/3+}$, $FcCH_2OH$ exhibits similar behaviour on this PrO_x covered electrode surface as seen in **Figure 6.4** b). However, the redox peak intensity from this neutral mediator is still somehow visible at higher concentrations, suggesting the attenuation is not as great.

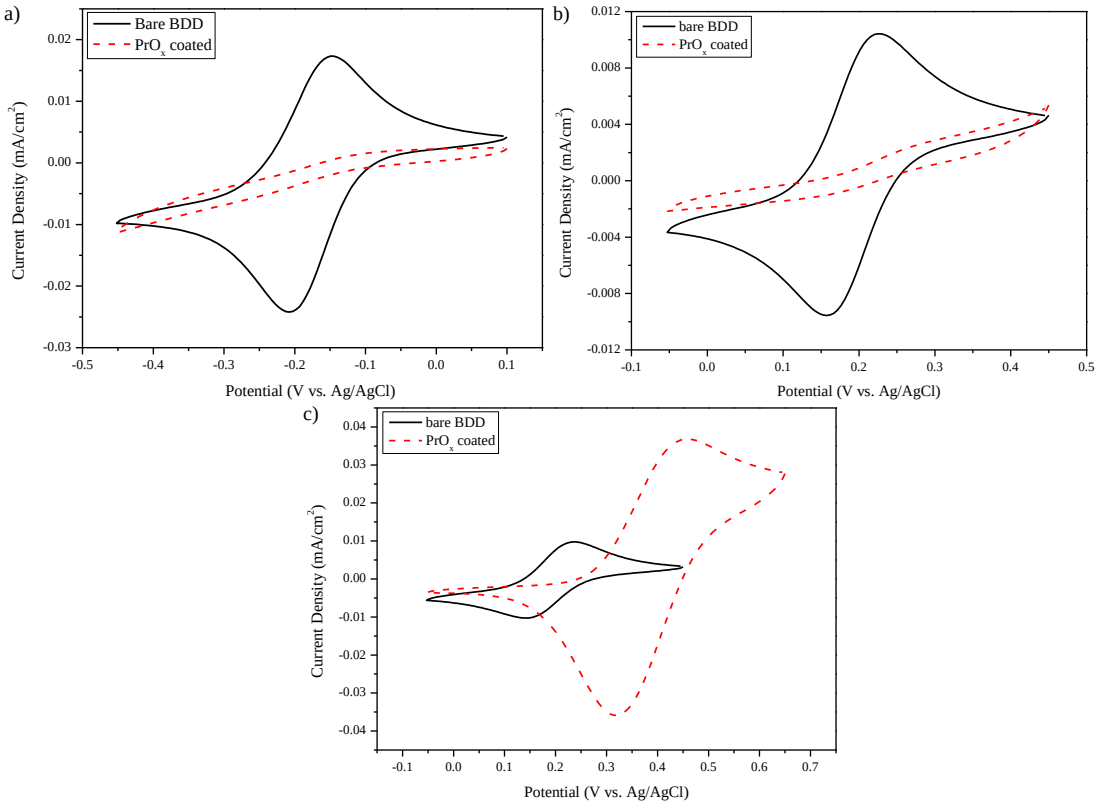


Figure 6.4 CVs of 100 µM a) $Ru(NH_3)_6^{3+}$, b) $FcCH_2OH$ and c) $Fe(CN)_6^{3-}$ in 0.1 M KCl at 0.05 V/s on bare and PrO_x coated BDD electrode after the electrodeposition in 25 mM $Pr(NO_3)_3$ and 5 mM H_2O_2 for 1 scan.

Entirely converse results are observed by measuring the negatively charged $Fe(CN)_6^{3-}$ after the same deposition process. The current peak intensity for this mediator on the modified surface is boosted by a factor of 2 as large as that on the bare BDD as shown in **Figure 6.4** c). The oxide film seems very sensitive to this redox couple which enhances the overall reaction activity significantly. The other highly noticeable variation by using this anionic mediator is the large potential shift after the decoration of the oxide layer. The half wave potential $E_{1/2}$ shifts by approximately 0.2 V towards more positive values from around 0.2 to 0.4 V showing that $Fe(CN)_6^{4-}$ is stabilised relative to $Fe(CN)_6^{3-}$. Overall it is clear from these experiments that the PrO_x layer is electrochemically active and is not simply a blocking layer.

6.3.2.2 PrO_x deposition with low concentration of $Pr(NO_3)_3$

As strong passivation effects are exhibited using a high concentration of $Pr(NO_3)_3$ precursor in the electrochemical deposition, further work was carried out to determine how the oxide film thickness alters the electrocatalytic properties . The deposition process was operated in the same manner as described above, however with a much lower concentration of 5 mM $Pr(NO_3)_3$ along with a diluted H_2O_2 content of 1 mM. Gradually increasing scan numbers were applied to investigate how the consecutive deposition can affect the overall performance.

Only one scan was initially operated as having been used at the higher concentration of 25 mM $Pr(NO_3)_3$. The attenuated peak current intensity is achieved for $FcCH_2OH$ but not quite discernible for both $Ru(NH_3)_6^{3+}$ and $Fe(CN)_6^{3-}$ at 100 μM in 0.1 M KCl as

shown in **Figure 6.5**. The film is considered too thin to modify activity for these mediators. After a further 5 scans, more significant modification effects are observed with prominent attenuations in peak currents for both $Ru(NH_3)_6^{3+}$ and $FcCH_2OH$ throughout the whole concentration range from 1 μM to 1 mM. The overall activity decreases by about 50% for both mediators above with larger peak-peak separations showing more sluggish reaction kinetics with this oxide film coating. It is observed that the initial current intensity is quite comparable for both cationic and neutral mediator analytes. However, with the oxide coverage formed after 6-scan CV deposition, the activity seems to decrease more with $Ru(NH_3)_6^{3+}$ than $FcCH_2OH$.

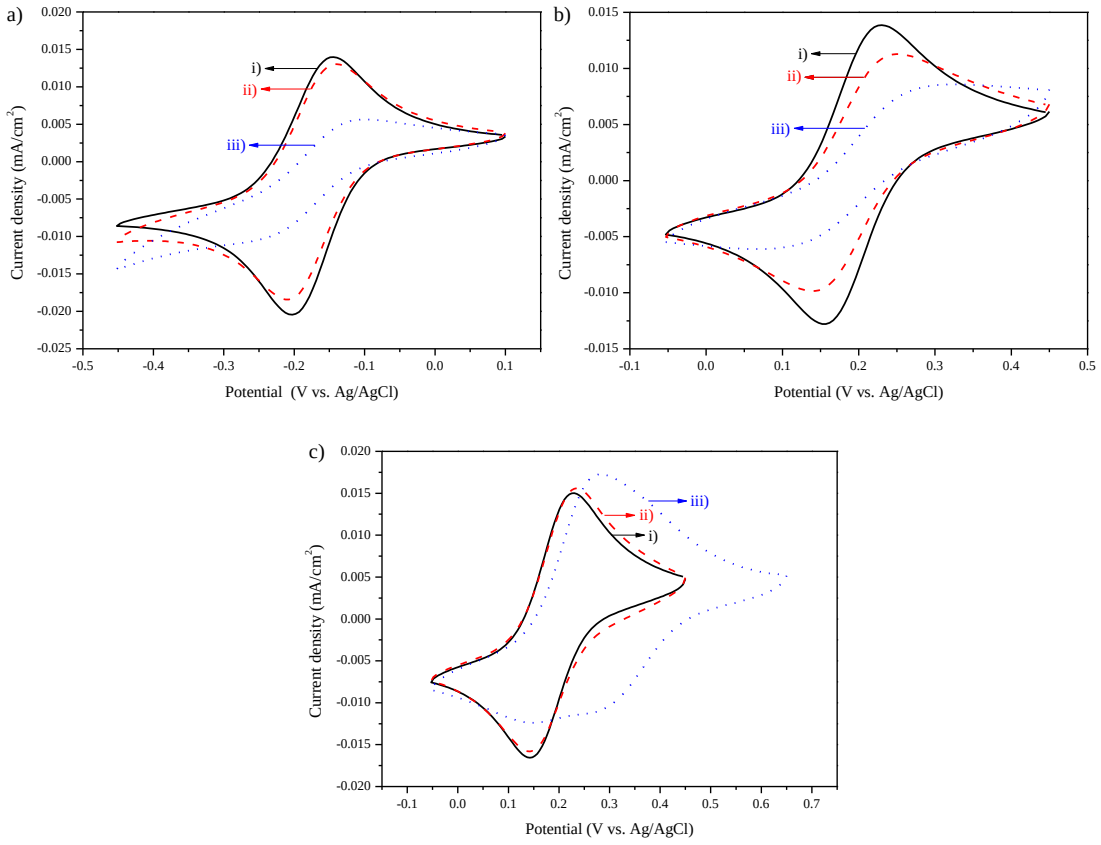


Figure 6.5 CVs of 100 μM a) $Ru(NH_3)_6^{3+}$, b) $FcCH_2OH$ and c) $Fe(CN)_6^{3-}$ in 0.1 M KCl at 0.1 V/s on i) bare and PrO_x coated BDD electrode after the electrodeposition in 5 mM $Pr(NO_3)_3$/1 mM H_2O_2 in 0.1 M KCl electrolyte for ii) 1 and iii) 6 scans.

More complicated behaviour is observed with $Fe(CN)_6^{3-}$ after the 6 scan deposition process as depicted in **Figure 6.5** c). Two split peaks are seen; one component is at the position observed on the un-modified bare BDD electrode with the other component shifts to more positive potentials as noted above. Changes with gradually increasing oxide thickness are shown in more detail in **Figure 6.6** a). The enhancements in peak currents are more identifiable at a lower concentration of 10 μM of redox couple than at a higher concentration, (see **Figure 6.6** b)).

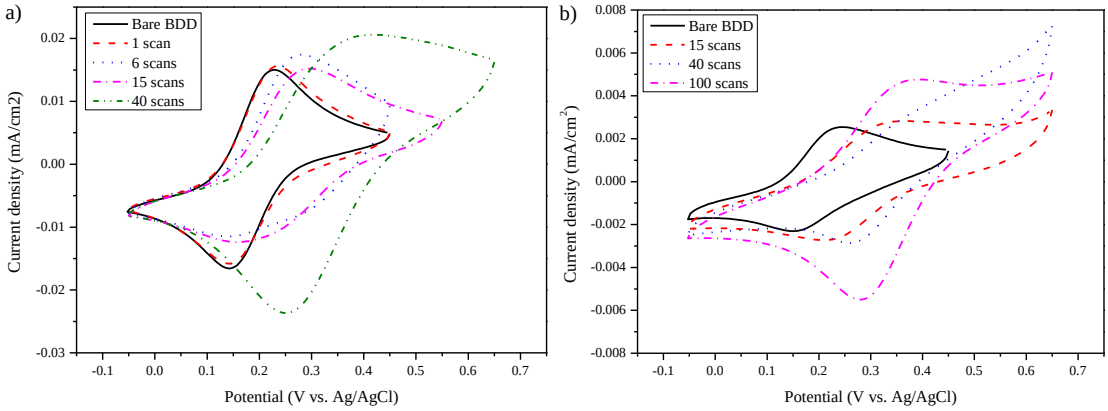


Figure 6.6 CVs of a) 100 μM and b) 10 μM $Fe(CN)_6^{3-}$ in 0.1 M KCl at 0.1 V/s on bare and PrO_x modified BDD after varied cyclic numbers in the deposition of PrO_x at 0.05 V/s.

From the measurements presented above, it is possible to suggest that the PrO_x acts as a thin film coating with limited porosity and with positive charge. Due to electrostatic repulsion, cationic redox species are excluded from the oxide layer so electrochemical signals are sharply attenuated. In contrast, anionic redox couples such as $Fe(CN)_6^{3-/4-}$ is rebound in the layer and pre-concentrated there. Hence enhanced electrolytic currents are observed with marked shifts in potential due to the strong interaction of the redox species with the oxide surface.

Further studies were carried out with anionic redox couples to further investigate this hypothesis. It can be seen from **Figure 6.7** that the electrochemical behaviour of the bare and PrO_x modified BDD are qualitatively similar for both $Fe(CN)_6^{3-}$ and $Fe(CN)_6^{4-}$ systems. This seems to rule out models suggested previously to describe the action of certain thin film modifiers, where the enhanced peak currents have been ascribed to the ability of the film to recycle the oxidised form of a couple into its reduced form, thereby forming a catalytic cycle which leads to enhanced (in this example) oxidation currents[28]. Rather the working hypothesis above seems more applicable.

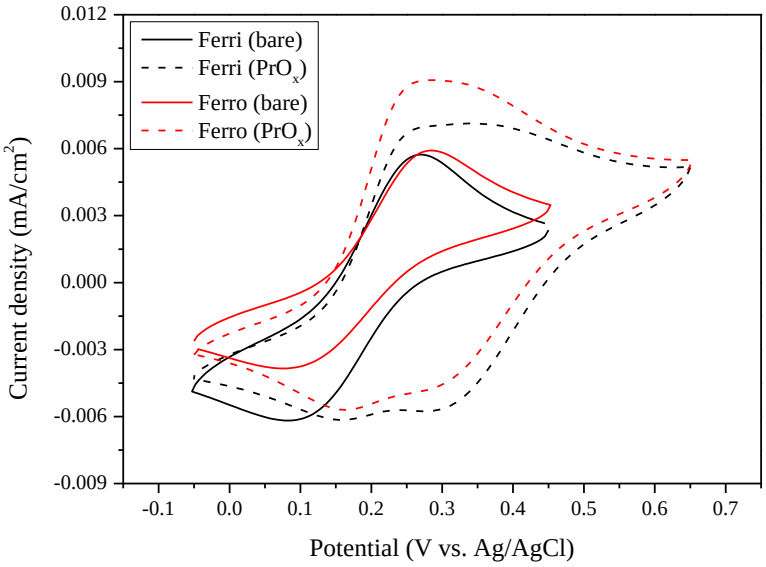


Figure 6.7 CVs of 100 μM $Fe(CN)_6^{3-}$ and $Fe(CN)_6^{4-}$ in 0.1 M KCl at a scan rate of 0.02 V/s on bare and modified BDD electrode after 20 cyclic numbers in the deposition of PrO_x at 0.05 V/s.

$IrCl_6^{2-}$ also shows an enhanced electrolysis current in CV as shown in **Figure 6.8** a). However differences arise from the behaviour of $Fe(CN)_6^{3-}$ and $Fe(CN)_6^{4-}$ above. The redox peaks remain at almost the same potential as on bare BDD. In addition, the oxidation current is considerably more enhanced than the reduction current, indicating a selectivity in the phenomenon causing the observation. It seems the $IrCl_6^{3-}$ ions

generated from the reduction process become concentrated in the layer leading to large oxidation currents. In contrast $IrCl_6^{2-}$ forms are expelled from the layer so enhanced reduction currents are not observed. However the model proposed by Holt[28] could also be applicable here; if the PrO_x can spontaneously reduce $IrCl_6^{2-}$ to $IrCl_6^{3-}$ then again enhanced oxidation currents would be seen. Either way inherent electrochemical activity of the PrO_x layer is suggested. The effect of the scan rates was also explored further as exhibited in **Figure 6.8** b). Unlikely in the $Fe(CN)_6^{3-/4-}$ system, there is no peak splitting observed at any scan rate and larger signal responses are achieved with increasing scan rates. The reduction current is plotted as proportional to the square root of scan rates, suggesting a semi-infinite diffusion for this mediator species on this modified electrode as presented in the inset of **Figure 6.8** b). Although the film seems to influence analyte concentrations within it, diffusion to the active electrode surface still seems rate-limiting.

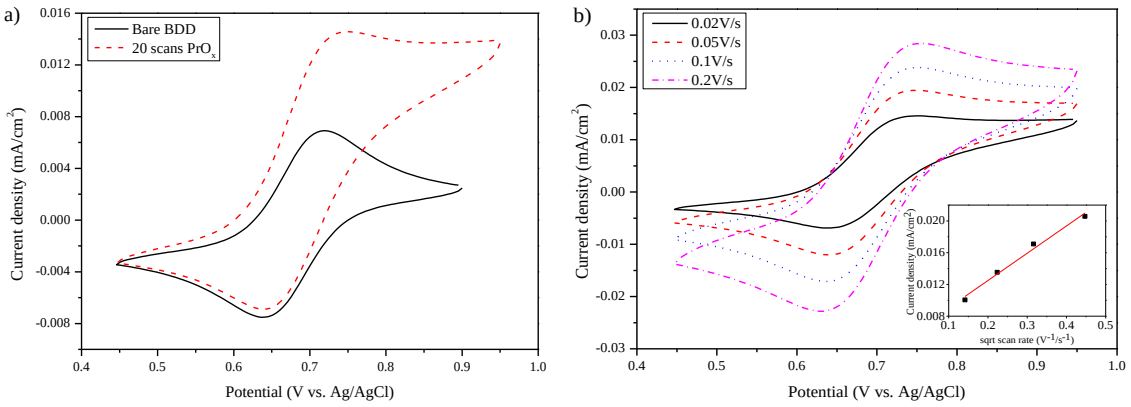


Figure 6.8 CVs of 100 μM $IrCl_6^{2-}$ in 0.1 M KCl on a) bare and PrO_x modified BDD (after 20 scans in CV electrodeposition) at 0.02 V/s and b) PrO_x modified BDD (after 20 scans in CV electrodeposition) with varing scan rates from 0.02 to 0.2 V/s, Inset: linear plot of cathodic currents *vs.* square root of scan rates.

6.3.3 Post-treatment of the deposited PrO_x film

After the electrochemical deposition from the $Pr(NO_3)_3$ precursor, the oxygen deficient oxide layer PrO_x (x = 1.5 to 2) was coated on the surface. Since x in this product is uncertain depending on the deposition conditions and environment, several treatments can be operated to transfer its formation to different states for investigations on the varied behaviours the oxide film may present. In our project, the fresh modified BDD electrodes were left overnight in the air before being annealed in hydrogen plasma and air respectively, and all the cases were comprehensively compared in parallel. The aim was to understand if chemical changes to the oxide layer would influence the observations noted above.

100 μM $Fe(CN)_6^{4-}$ was preferentially selected to compare the CV curves under four different conditions in 0.1 M KCl at 0.02 V/s as shown in **Figure 6.9**. After 20 cyclic scans in fresh electrochemical deposition of PrO_x, the observations are similar to those as reported above. Two pairs of nearly symmetric redox peaks are observed simultaneously in which one set of peaks appears at approximately the same position as obtained on the bare BDD while the other shifts by 0.15 V towards more positive potential value as explained previously. If the modified electrode is left in air, pronounced changes are seen in the voltammetry. Most clearly, the shifted redox couple no longer appears. It therefore reveals that this must be especially associated with the as-deposited oxide layer. After oxidation in air, the chemically defective state is removed thereby destroying the special interaction with the redox couple. Although attempts to reactivate the defective state using a hydrogen plasma to reduce the oxide forms were made, this was unsuccessful.

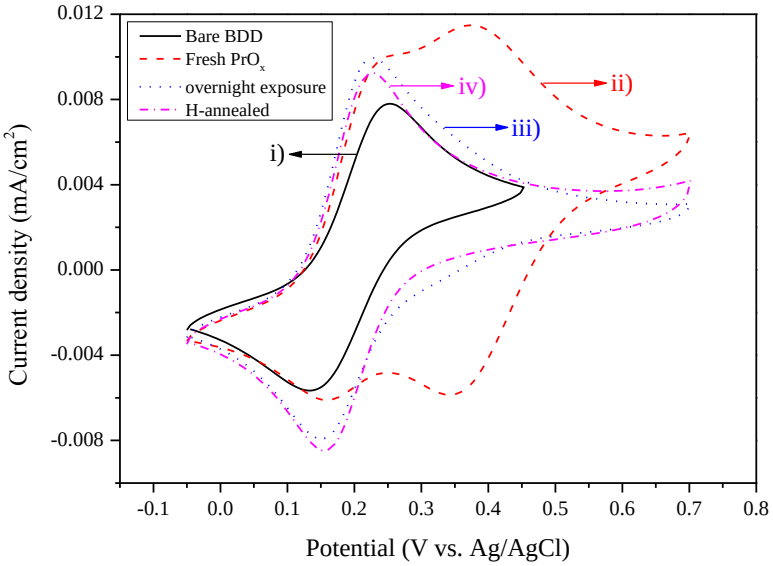


Figure 6.9 CVs of 100 μM $Fe(CN)_6^{4-}$ at a scan of 20 mV/s on i) bare BDD and after several treatments: ii) PrO_x freshly deposited, iii) after air-exposured, annealed and iv) after annealed in hydrogen plasma.

Although defective PrO_x is oxidised partially in air at room temperature, higher oxidation temperatures are needed to form the pure dioxide PrO_2[29]. Another altered annealing process was therefore used whereby the oxide was heated in an oven at 473 K for 2.5 hours. CVs were carried out afterwards using different redox couples as shown in **Figure 6.10**. The effects are quite significant, in particular qualitatively similar for all three redox couples as reduced peak currents are observed. This is somewhat similar to what might have been naively expected – the oxide behaves as a somewhat impermeable blocking layer hence it reduces the diffusional access of the analytes to the electrode surface. It is therefore the only highly oxygen-deficient oxide layer which is freshly deposited shows the high chemical activity leading to distinctive changes in the electrochemistry as noted in this chapter above and earlier in this thesis.

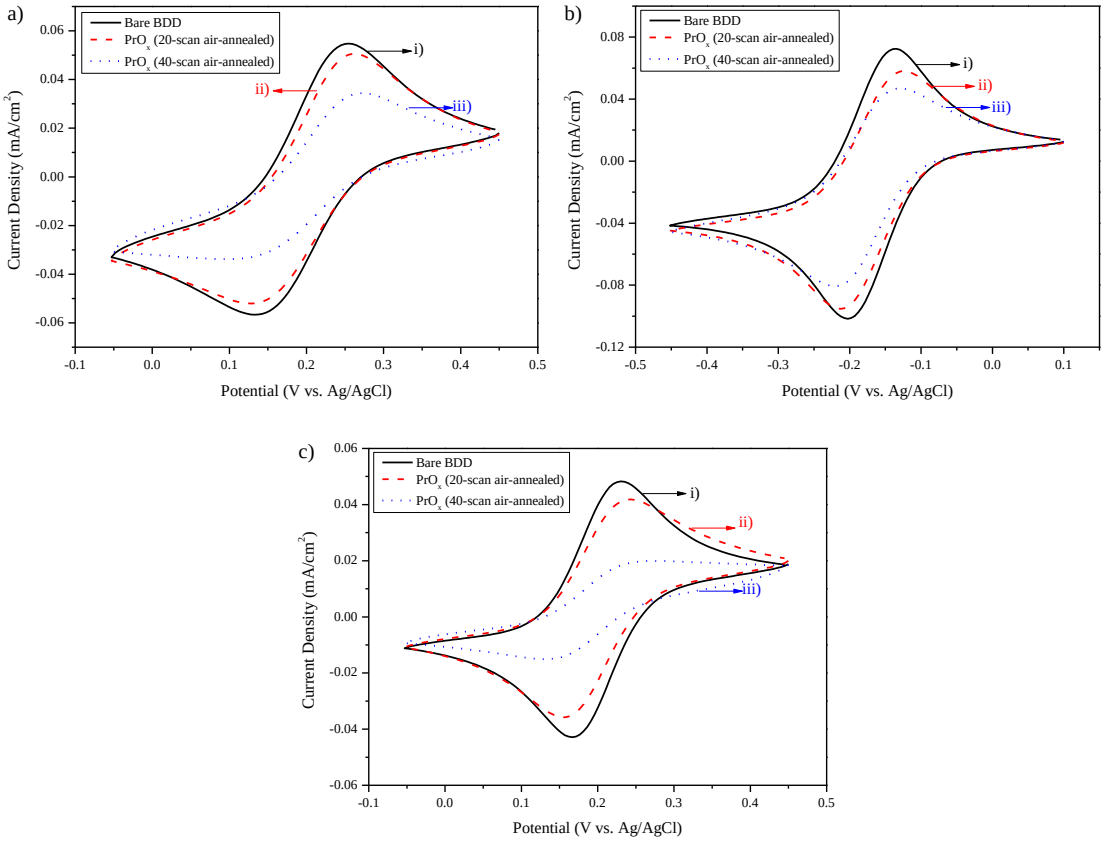


Figure 6.10 CVs of 1 mM a) $Fe(CN)_6^{3-}$, b) $Ru(NH_3)_6^{3+}$, c) $FcCH_2OH$ in 0.1 M KCl at 0.02 V/s on i) bare BDD, and PrO_x coated and air-annealed BDD with ii) 20 scans and iii) 40 scans in CV electrodeposition of PrO_x.

6.3.4 XPS characterisations of PrO_x modified electrodes with different treatments

In order to understand further about the variation of formation after different treatments to the oxide film, XPS was carried out on the deposited oxide. All the samples were characterised directly after deposition and relevant treatments without being used in any electrochemical measurement. **Figure 6.11** shows a typical wide scan XPS spectrum of the fresh PrO_x film deposited with 60 CV scans in 5 mM $Pr(NO_3)_3$/1 mM H_2O_2 at 0.05 V/s before being removed from solution dried and analysed. Characteristic Pr 3d peaks

are seen at the region from approximately 930 to 950 eV, confirming the oxide film is successfully deposited onto the surface. As expected oxygen is also detected as well as carbon. It is not clear whether this is due to residual contamination, or from the underlying diamond.

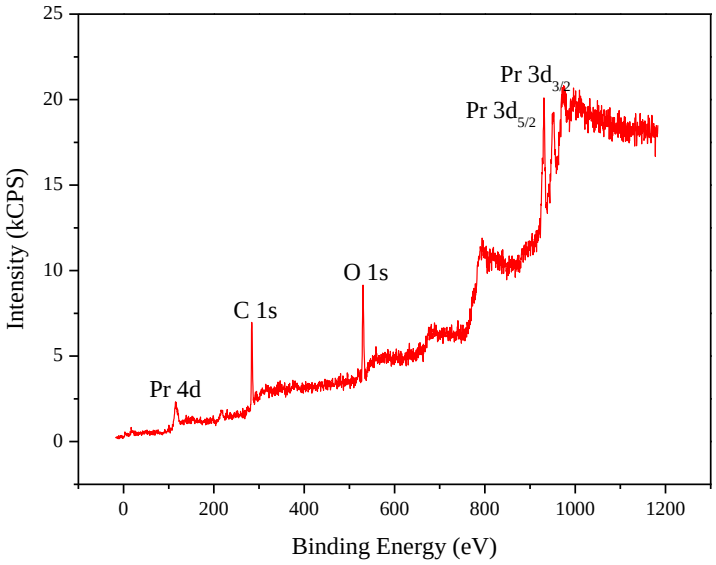


Figure 6.11 XPS survey spectrum of PrO_x film as freshly electrodeposited after 20 CV scans with 5 mM $Pr(NO_3)_3$/1 mM H_2O_2 in 0.1 M KCl at 0.05 V/s

Figure 6.12 a) exhibits the narrow spectrum of Pr 3d containing both $3d_{3/2}$ and $3d_{5/2}$ components with a spin orbit splitting energy of 20.5 eV, which is very close to the value of 20.2 eV reported in the literature[30]. The observed XPS shows three core components peaks *a*/*a*', *b*/*b*' and *c*/*c*' for Pr $3d_{5/2}$ and Pr $3d_{3/2}$ respectively as noted elsewhere[31]. There is also an intensity rise *t*' on the higher binding energy value for $3d_{3/2}$ component which is absent in the $3d_{5/2}$ characteristic region due to the multiplet effect[32]. Although the peak *c* in Pr $3d_{5/2}$ is strongly overlapped with the peak *a*' in Pr $3d_{3/2}$, the peak *c*' at the high energy tail of approximately 965 eV is weakly visible which is reported as the characteristic peak that only appears in the fully oxidised PrO_2

formation[33]. Overall in the light of previous XPS work it is likely the electrodeposited oxide layer analysed may have both Pr (III) and Pr (IV) in existence simultaneously.

Apart from the Pr XPS spectrum, O is the other element mainly concerned after the deposition of oxide film and varied treatments. A typical O1s spectrum for the freshly deposited PrO_x coating with 60 CV scans in 5 mM $Pr(NO_3)_3$/1 mM H_2O_2 at 0.05 V/s is shown in **Figure 6.12** b). There are three peaks appearing in the characteristic region. The first one at the highest binding energy of 531.6 eV is attributed to the $O^{\delta-}$ species, which mainly comes from the Pr-O-C bonding structure. The main peak exhibited at a relatively lower energy value of 530.2 eV instead refers to the -OH species existing in both hydroxide and hydrated forms of Pr deposits, while a very small and weak peak is also observed at an even lower energy of 527.5 eV, corresponding to the appearance of O^{2-} species in the PrO_x formation[34].

The large peak area for the $-OH^-$ species suggests a large amount of hydroxide present along with the adsorption and dissociation of water on the freshly deposited sample, which is in line with the very small presence of the O^{2-} characteristic peak in the XPS spectrum. The result reveals an intermediate oxidation state comprising a mixed praseodymium hydroxide, praseodymium hydrate, along with small Pr_2O_3 and PrO_2 contents where Pr(III) is the dominant metal species rather than its (IV) counterpart by using $Pr(NO_3)_3$ as the precursor in the deposition process.

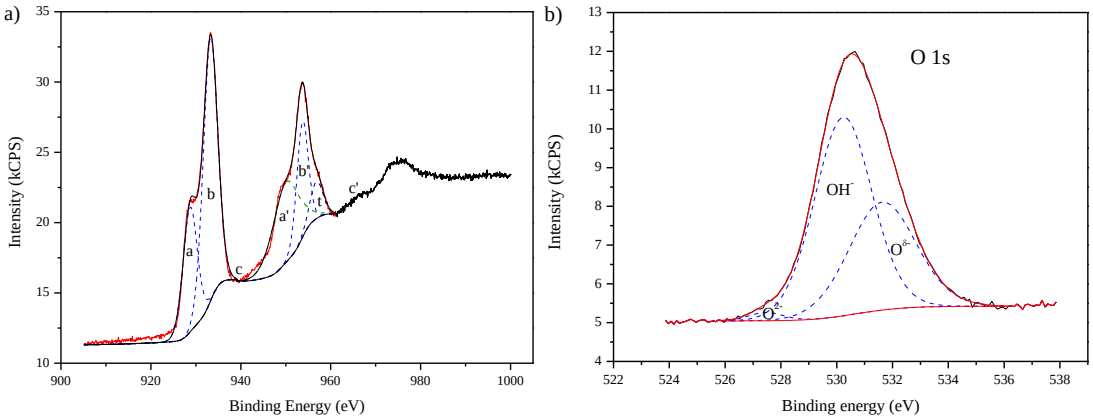


Figure 6.12 Narrow scan XPS spectra of a) Pr 3d with three core components peaks *a*/*a*', *b*/*b*' and *c*/*c*' for Pr $3d_{5/2}$ and Pr $3d_{3/2}$ respectively and a rise *t*' on the higher binding energy value for $3d_{3/2}$ component due to the multiplet effect[32] and b) O1s with three component peaks for O^{2-}, OH^- and $O^{\delta-}$ after the PrO_x film was freshly electrodeposited after 20 CV scans with 5 mM $Pr(NO_3)_3$/1 mM H_2O_2 in 0.1 M KCl at 0.05 V/s.

XPS spectra of Pr 3d were also recorded after the annealing treatments in hydrogen and air respectively as shown in **Figure 6.13**. The changes in the Pr 3d region from the as-grown film are rather subtle somewhat highlighting the difficulties in analysing defective Pr oxides with XPS.

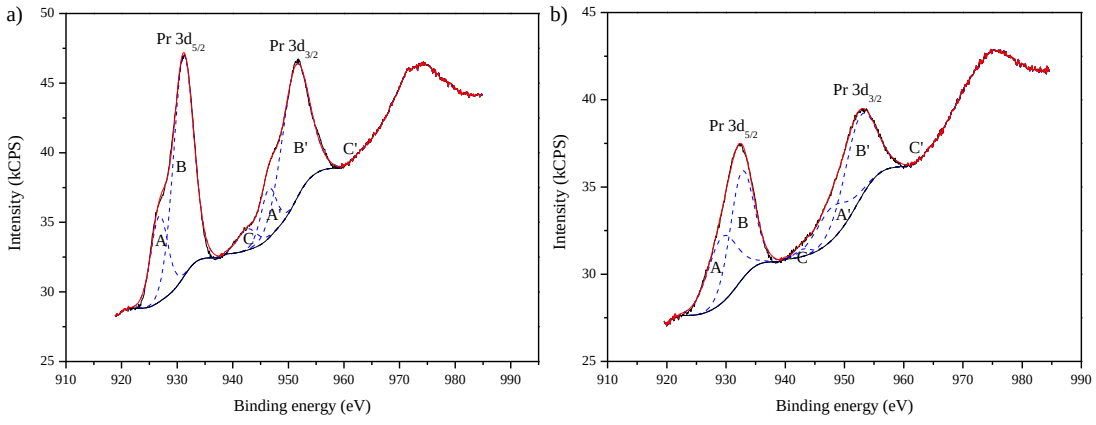


Figure 6.13 Narrow scan XPS spectra of Pr 3d with three core components peaks *A*/*A*', *B*/*B*' and *C*/*C*' for $Pr3d_{5/2}$ and $Pr3d_{3/2}$ respectively for a) hydrogen annealed and b) air annealed PrO_x deposits on BDD produced after 20 CV scans in 5 mM $Pr(NO_3)_3$/1 mM H_2O_2 at 0.05 V/s

The O 1s peak spectra were also characterised in parallel. Three core component peaks are still observed for both annealed samples even though the intensity varies much with different treatments. As exhibited in **Figure 6.14** a), the characteristic peak of $O^{\delta-}$ seems to remain the same as achieved on the freshly coated sample either for intensity or position. The main variation is rather discovered for O^{2-} and OH^- peaks as their intensities are enhanced and decreased, respectively. Since a high temperature is applied in the annealing, a dehydration process should be going on thoroughly to eliminate the adsorbed water phase. A considerable amount of praseodymium hydroxide will also be converted into its oxide state simultaneously. However, as shown in **Figure 6.14** b), $O^{\delta-}$ peak seems decreasing significantly to approximately 10% of its initial intensity, indicating the Pr-O-C structure is vulnerable at annealing with air. It is noticeable that the intensity of the O^{2-} characteristic peak is significantly enhanced, which can be tightly associated with a rapid hydration process and further conversion towards the fully oxidised PrO_2 forms. Variation is also discernible but to a smaller extent for OH^- peak, indicating the existence of some hydroxide residues.

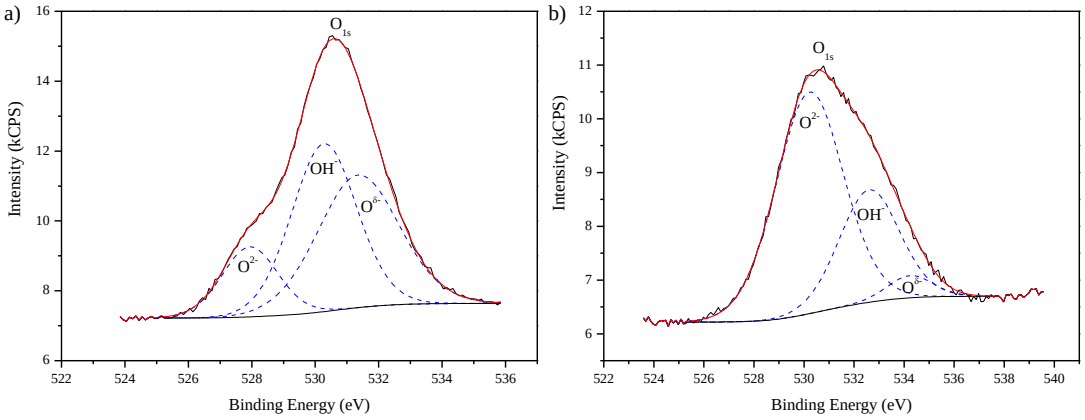


Figure 6.14 Narrow scan XPS spectra of O 1s with three component peaks for O^{2-}, OH^- and $O^{\delta-}$ for a) hydrogen annealed and b) air annealed PrO_x deposits on BDD produced after 20 CV scans in 5 mM $Pr(NO_3)_3$/1 mM H_2O_2 at 0.05 V/s

Clearly it is difficult to provide a totally definitive composition of the oxide for the different pre-treatments. Overall a picture emerges of a complex defective composition comprising Pr (III), Pr (IV), O^{2-} and OH^-. Changes in this defective state with pre-treatment have a drastic effect on the electrochemical properties as noted above.

6.3.5 Dynamic light scattering (DLS) and *zeta* potential characterisation of the PrO_x suspension

As mentioned before, the catalytic activity variation observed for all the mediator electrolytes may be mainly attributed to the surface charge effects associated with the oxygen vacancies in the deposited film structure. In order to examine this hypothesis in more detail, the suspension of electrodeposited PrO_x was measured by using a DLS technique combined with a *zeta* potential technique as described below. In order to prepare the colloidal suspension of freshly deposited PrO_x, a slightly revised deposition procedure was carried out by replacing the BDD working electrode with a pure Pt wire. The electrodeposited PrO_x on the BDD surface is stable and cannot be scratched off very easily, so the Pt wire was instead chosen as a suitable alternative to provide sufficient amount of PrO_x deposits that can be formed and collected easily from this more conductive material without being firmly attached. The electrodeposition route was carried out by scanning in the precursor solution containing 5 mM $Pr(NO_3)_3$ and 1 mM H_2O_2 in 0.1 M KCl at 0.05 V/s for 50 scans. The Pt wire was seen to become coated with oxide, which was then removed by scraping. These were then washed in pure water several times before a final suspension in pure water was made for DLS analysis.

The particle size distribution is displayed in **Figure 6.15** as shown below. It is clear to see that most common particle size is between 80 and 200 nm when 105.7 nm sized particle represents the highest proportion of around 28%. There are also some much larger particles ranging from 200 to 800 nm with smaller presence in the suspension. These particle sizes from the scrapings to some extent probably reflect the crystallite sizes in the initially deposited film, since it is unlikely the gentle scraping process would significantly break down the particles initially prepared.

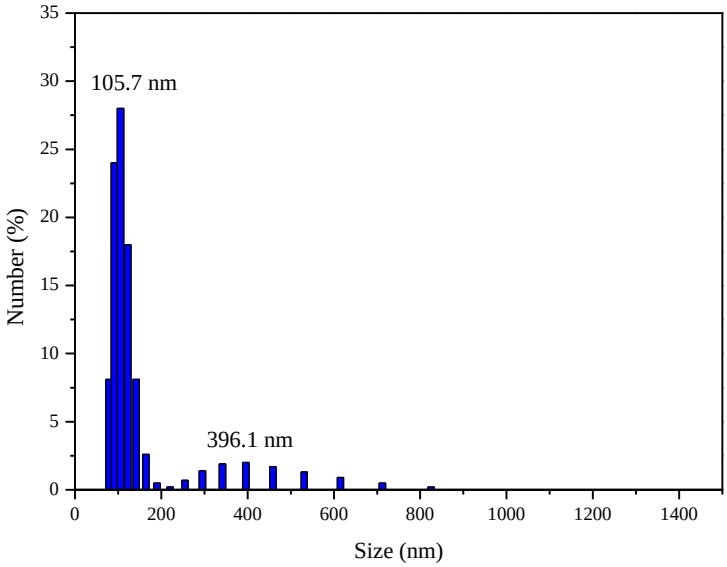


Figure 6.15 Dynamic light scattering histogram of PrO_x suspension prepared by fresh electrodeposition using 5 mM $Pr(NO_3)_3$ and 1 mM H_2O_2 in 0.1 M KCl at 0.05 V/s for 50 scans on pure Pt wire. (A bin size proportional to particle size has been employed)

Zeta potential measurements were then recorded. The *zeta* potential values from all the samples were found to be positive, with an average peak charge of approximately 43.9 mV in a range from 42.9 to 44.7 mV in neutral water. This observation indicates a strongly cationic surface for the PrO_x particles as supposed from the CV characterisations with different mediators. A typical *zeta* potential distribution plot is exhibited in **Figure 6.16**.

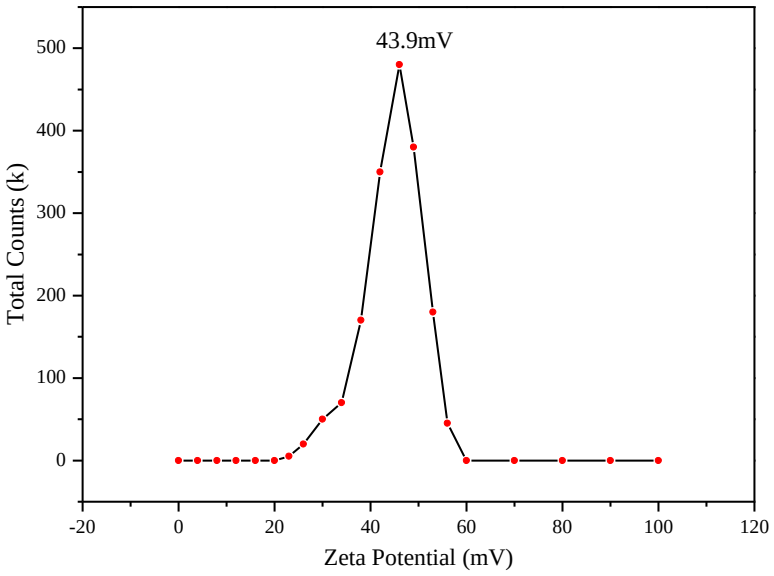


Figure 6.16 *Zeta* potential distribution plot for fresh PrO_x suspension (in pure water, pH=7.0) produced from 5 mM $Pr(NO_3)_3$ and 1 mM H_2O_2 in 0.1 M KCl at 0.05 V/s for 50 scans on pure Pt wire.

6.3.6 Electrochemical detection of dopamine

In order to extend the investigation on the electrochemical properties of the praseodymium oxide coating, some further preliminary experiments were recorded to examine the performance of the modified diamond electrode in solutions of dopamine (DA) and ascorbic acid (AA). DA is a neurotransmitter playing an important role in renal, and hormonal systems thus its presence and measurement in the blood is crucial [35, 36], as its abnormal concentrations can be an indicator of several diseases such as Parkinson's disease[37]. However, since both DA and AA molecules mentioned above co-exist in the bio-system with closely overlapped characteristic oxidation peak regions[38], various studies have been focused on resolving the peaks since the normally much higher concentration of AA can mask the DA response. The electrochemistry was carried out in a 0.1 M phosphate buffer solution, whose pH (7.4)

is close to the *in vivo* applications. It should be noticed that at this pH level, with the different pKa values, *i.e.* 8.87 and 4.1 for DA and AA respectively[39], the former is likely to be cationic whereas the latter is completely dissociated to the anionic form. In view of the electrostatic effects explained in *Chapter* 5 in repelling the anionic response from PrO_x-Pt modified diamond electrodes, and the interesting effects seen in this chapter, it was of interest to examine in further detail whether PrO_x could help improve the selective discrimination of DA in the presence of AA. Indeed, preliminary studies using chronoamperometry[29] have suggested that the sensitivity of the electrode to AA is reduced by the presence of the oxide layer.

The CV characterisations were carried out with 1 mM DA and 10 mM AA separately in 0.1 M PBS at 0.1 V/s on both bare and PrO_x deposited BDD as shown in **Figure 6.17**. It is surprising to observe that the signal responses from both molecules decrease with PrO_x coverage after 10 scans in electrodeposition using 5 mM $Pr(NO_3)_3$ and 1 mM H_2O_2 in 0.1 M KCl at 0.05 V/s. So no obvious selectivity changes can be seen in CV. However subtle effects are observed. In particular the oxidation peak positions for DA and AA appear to move apart from each other as the AA peak shifts towards a more positive potential value while that of DA almost remains the same.

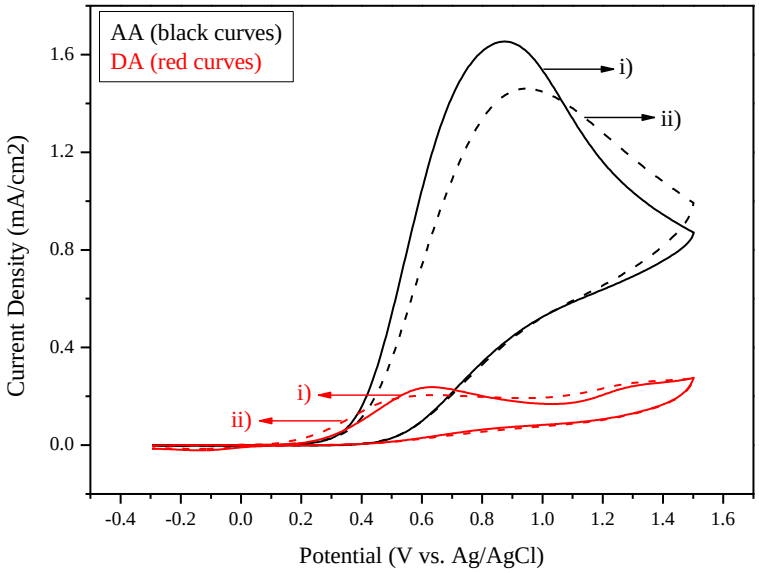


Figure 6.17 CVs of 10 mM AA and 1 mM DA in 0.1 M PBS at 0.1 V/s on (i) bare and (ii) PrO_x coated BDD (dashed line) produced by 10 cyclic scans in 5 mM $Pr(NO_3)_3$ and 1 mM H_2O_2 in 0.1 M KCl at 0.05 V/s

In order to further investigate any analytical advantage of the increasing peak separation as observed separately for the two molecules, electrochemical measurements were carried out by conducting SWV in the mixed solution with increasing concentrations of AA (from 0.1 to 1 mM) in the presence of fixed concentration of DA (0.1 mM) on bare and PrO_x coated BDD respectively as shown in **Figure 6.18**. On bare BDD, the two peaks are not able to be resolved at all until the AA concentration is 5 times higher than that of DA. However, with the proper amount of PrO_x loading after 10 CV scans mentioned above, the well-separated peaks become discernible even if the concentrations of DA and AA are comparable at 0.1 mM. The positive peak shift in the AA potential is probably responsible for the observations in chronoamperometry that selectivity can be improved by the use of PrO_x[29] since the corresponding AA signal will drop if the oxidation peak is shifted to more positive values than used in the experiment.

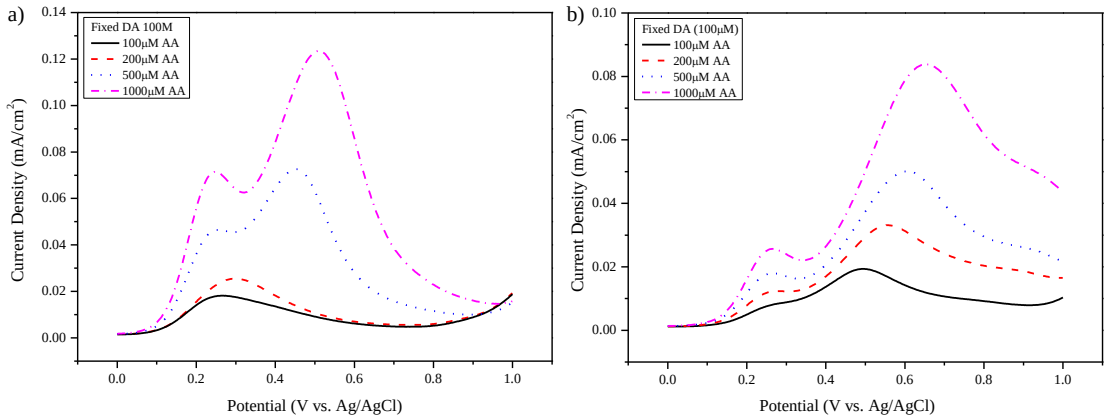


Figure 6.18 SWVs of AA and DA mixed solution with increasing concentrations of AA at 0.1, 0.2, 0.5 and 1 mM in the presence of a fixed DA concentration of 0.1 mM at a frequency of 10 Hz along with a 0.002 V step potential and a 0.05 V amplitude on a) un-modified bare and b) PrO_x coated BDD produced by 10 cyclic scans in 5 mM $Pr(NO_3)_3$ and 1 mM H_2O_2 in 0.1 M KCl at 0.05 V/s

It is discovered that the DA signal increases along with the enhanced concentration of AA, which is consistent with the known EC' mechanisms[40]. DA is initially oxidised into its dopamine-o-quinone form in the presence of AA before being reduced by AA, which will result in a homogeneous catalytic oxidation of AA. Since some oxidative DA molecules are reduced in the process above and can be re-oxidised at the electrode surface, the signal responses are observed as increasing along with higher AA concentrations even though the DA content is fixed. The supposed mechanism is therefore depicted in **Figure 6.19** as below.

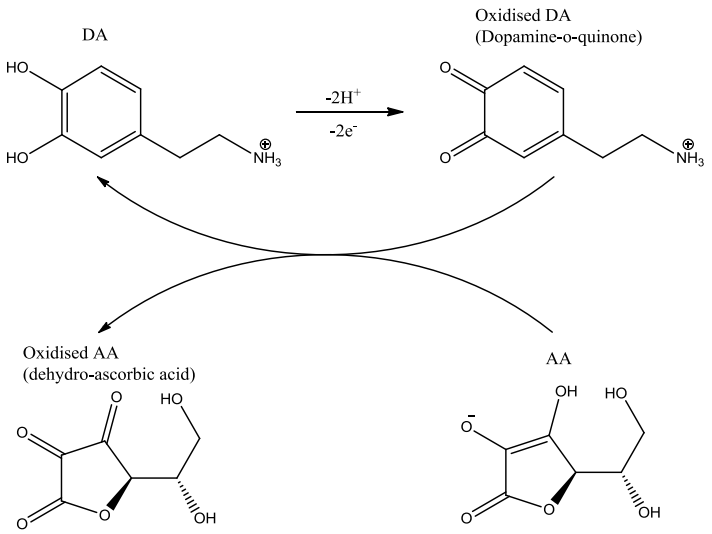


Figure 6.19 Electrocatalytic oxidation of AA by oxidised DA

6.4 Summarising comments

- In this chapter, PrO_x is specifically electrodeposited on the bare BDD without being coated with any other catalyst such as Pt in the previous studies to investigate its own electrochemical and mechanical properties. Freshly deposited, overnight exposed, hydrogen plasma treated and air annealed samples are measured by various techniques.
- CV characterisation was carried out with four different mediator electrolytes, *i.e.* cationic $Ru(NH_3)_6^{2+/3+}$, neutral $FcCH_2OH$ and anionic $Fe(CN)_6^{3-/4-}$ and $IrCl_6^{2-/3-}$. For the neutral and cationic species, the freshly deposited PrO_x seemed to serve as a simple blocking layer, partially reducing the electrochemical currents which could be recorded under given conditions at the electrode. However very different results were observed with the anionic species - enhanced electrochemical currents were measured, suggesting concentration of the species in the oxide layer. Significant redox potential shifts were seen along with selective enhancements of oxidation currents, all pointing to significant electrochemical activity of the oxide

film.

- The above observations were consistent with the measurement of positive *zeta* potential at PrO_x surfaces, which could give rise to an electrostatic interaction with anionic species in solution. They were also somewhat consistent with XPS measurements which suggested variable stoichiometry associated with the presence of Pr (III) and Pr (IV) cationic species, O^{2-} and OH^- anionic species. Interestingly if the as-deposited layer was oxidised into a more stoichiometric PrO_2 layer, then the active chemical effects noted above were found to disappear as replaced by simple blocking behaviour.
- Electrochemical characterisation of dopamine and ascorbate at the PrO_x modified surface was also studied, in the light of earlier work in this thesis which showed reduced anionic response at PrO_x-Pt modified electrodes, and previous work which suggested that ascorbate sensitivity at an electrode could be reduced by the presence of PrO_x. Somewhat surprisingly no prominent loss of sensitivity to ascorbate was seen, although a positive shift in the oxidation potential was observed which could explain the previous results in chronoamperometric measurements.

References

[1] Z. Tang, G. Lu, J. Power Sources 162 (2006) 1067-1072.

[2] K. Eguchi, J. Alloys Compd. 250 (1997) 486-491.

[3] X. Cui, H. Zhang, X. Dong, H. Chen, L. Zhang, L. Guo, J. Shi, J. Mater. Chem. 18 (2008) 3575-3580.

[4] S. Chi Tsang, C. Bulpitt, Sens. Actuators, B: Chem. 52 (1998) 226-235.

[5] L. Marsella, V. Fiorentini, Phys. Rev. B 69 (2004) 172103.

[6] N. Haraguchi, Y. Okaue, T. Isobe, Y. Matsuda, Inorg. Chem. 33 (1994) 1015-1020.

[7] M. Mogensen, N.M. Sammes, G.A. Tompsett, Solid State Ionics 129 (2000) 63-94.

[8] C.T. Campbell, C.H. Peden, Science 309 (2005) 713-714.

[9] S. Fabris, G. Vicario, G. Balducci, S. de Gironcoli, S. Baroni, J. Phys. Chem. B 109 (2005) 22860-22867.

[10] P. Dutta, S. Pal, M. Seehra, Y. Shi, E. Eyring, R. Ernst, Chem. Mater. 18 (2006) 5144-5146.

[11] H. Yahiro, K. Eguchi, H. Arai, Solid State Ionics 36 (1989) 71-75.

[12] H. He, R.J. Gorte, J.M. Vohs, Electrochem. Solid-State Lett. 8 (2005) A279-A280.

[13] Z. Wu, R. Jin, Y. Liu, H. Wang, Catal. Commun. 9 (2008) 2217-2220.

[14] T. Sayle, S. Parker, C. Catlow, Surf. Sci. 316 (1994) 329-336.

[15] C.L. Campos, C. Roldán, M. Aponte, Y. Ishikawa, C.R. Cabrera, J. Electroanal. Chem. 581 (2005) 206-215.

[16] S.-Y. Huang, C.-M. Chang, C.-T. Yeh, J. Catal. 241 (2006) 400-406.

[17] T. Jin, T. Okuhara, G. Mains, J. White, J. Phys. Chem.;(United States) 91 (1987).

[18] B. Hobbs, A. Tseung, Nature 222 (1969) 556-558.

[19] J. Hu, R.G. Gordon, J. Appl. Phys. 71 (1992) 880-890.

[20] T. Tsutsumi, Jpn. J. Appl. Phys. Vol 9 (1970) 735-739.

[21] T. Ishida, H. Kobayashi, Y. Nakato, J. Appl. Phys. 73 (1993) 4344-4350.

[22] Y. Natsume, H. Sakata, Thin Solid Films 372 (2000) 30-36.

[23] N. Vinokur, B. Miller, Y. Avyigal, R. Kalish, J. Electrochem. Soc. 143 (1996) L238-L240.

[24] M.C. Granger, M. Witek, J. Xu, J. Wang, M. Hupert, A. Hanks, M.D. Koppang, J.E. Butler, G. Lucazeau, M. Mermoux, Anal. Chem. 72 (2000) 3793-3804.

[25] N. Maleki, A. Safavi, F. Tajabadi, Anal. Chem. 78 (2006) 3820-3826.

[26] P. Chen, R.L. McCreery, Anal. Chem. 68 (1996) 3958-3965.

[27] S. Shrestha, F. Marken, J. Elliott, C.M.Y. Yeung, C.E. Mills, S.C. Tsang, J. Electrochem. Soc. 153 (2006) C517-C520.

[28] K.B. Holt, D.J. Caruana, E.J. Millán-Barrios, J. Am. Chem. Soc. 131 (2009) 11272-11273.

[29] M. Sawangphruk, Electrochemical deposition and properties, of nanostructured materials, DPhil Thesis, Oxford University, 2010.

[30] S. Lütkehoff, M. Neumann, A. Ślebarski, Phys. Rev. B 52 (1995) 13808.

[31] A. Bianconi, A. Kotani, K. Okada, R. Giorgi, A. Gargano, A. Marcelli, T. Miyahara, Phys. Rev. B 38 (1988) 3433.

[32] H. Ogasawara, A. Kotani, R. Potze, G. Sawatzky, B. Thole, Phys. Rev. B 44 (1991) 5465.

[33] H. Borchert, Y.V. Frolova, V.V. Kaichev, I.P. Prosvirin, G.M. Alikina, A.I. Lukashevich, V.I. Zaikovskii, E.M. Moroz, S.N. Trukhan, V.P. Ivanov, J. Phys. Chem. B 109 (2005) 5728-5738.

[34] M.S. Hassan, M.S. Akhtar, K.-B. Shim, O.-B. Yang, Nanoscale Res. Lett. 5 (2010) 735-740.

[35] M. Wei, L.G. Sun, Z.Y. Xie, J.F. Zhii, A. Fujishima, Y. Einaga, D.G. Fu, X.M. Wang, Z.Z. Gu, Adv. Funct. Mater. 18 (2008) 1414-1421.

[36] L.I. Goldberg, Pharmacol. Rev. 24 (1972) 1-29.

[37] P. Damier, E. Hirsch, Y. Agid, A. Graybiel, Brain 122 (1999) 1437-1448.

[38] Y. Zhang, G. Jin, Z. Yang, H. Zhao, Microchimica Acta 147 (2004) 225-230.

[39] Y. Wang, Y. Li, L. Tang, J. Lu, J. Li, Electrochem. Commun. 11 (2009) 889-892.

[40] L. Zhang, X. Jiang, J. Electroanal. Chem. 583 (2005) 292-299.

Chapter 7

Electrochemical detection of riboflavin (VB2) on carbon black modified BDD electrode

7.1 Introduction

Riboflavin, which is also known as Vitamin B2 (VB2), is a water-soluble biological compound broadly existing in food and pharmaceutical products and working as precursor of cofactors in enzymes[1]. In order to analyse the VB2 composition both sensitively and selectively and exclude interfering species, several techniques such as spectrophotometric[2, 3], high performance liquid chromatography (HPLC)[4, 5], chemiluminescence[6] and fluorescence[7] methods have been preferentially applied. And recently, a cyclodextrin-based sensor with high sensitivity and selectivity was developed for the VB2 determination in pharmaceutical applications[8].

It is generally considered that the electrochemical detection of VB2 can be based on an accessible redox couple, each component of which consists of two overlapping one electron-one proton transfer steps (discussed further below)[9]. There have been only a few studies on using electroanalytic methods to investigate the electrochemical properties of VB2. They were usually carried out by adsorptive stripping voltammetry (ASV) at mercury electrodes[10], which however suffered from rapid decomposition in alkaline medium under ambient light[11]. VB2 was observed to show poor adsorption on various solid electrodes such as carbon paste, gold and platinum[12]. However, electrochemically pre-treated glassy carbon (GC) electrodes have been considered as potential candidates to adsorb and detect the presence of VB2[13]. Unfortunately as the surface structure and chemistry are relatively complex for such electrodes, the modified

surface states may vary prominently under different pre-treatment conditions[14, 15]. Therefore it is difficult to achieve a stable surface that can exhibit a reproducible performance in the electrochemical characterisation of VB2 on GC.

Boron doped diamond (BDD) is a very reproducible electrode material so could overcome these problems[16]. However, pure polycrystalline diamond is not fully advantageous in VB2 detection as the electrode shows only weak adsorption of VB2 and generally a very poor electrode response is seen unless very low quality diamond with high sp^2 content is used[16]. Such electrode materials are themselves quite ill-defined so the reliable detection of VB2 using diamond itself is quite difficult. In the present work an alternative approach involving commercial diamond electrodes is used, which involves the modification of the diamond electrode with carbon black.

Carbon black (CB), which is widely known as a successful electrocatalyst support in DMFC applications[17, 18] and a promising material in gas sensing[19, 20], was explored by Compton's group for its advantageous properties as a much cheaper alternative electrode modifier compared with multi-walled carbon nanotube in adsorptive stripping voltammetry for nicotine detection.[21] It is also likely to have advantageous properties in VB2 electrochemical detection as it can adsorb abundant VB2 molecules thus enhance the sensitivity significantly. With a homogeneous coating of CB on the surface, the redox reaction signals are more likely to be reproducible, without being varied significantly on the glassy carbon electrode due to the pre-treatments required.

In this chapter, both CV and SWV techniques were thus applied to investigate the

feasibility of using this cheap material as a suitable promoter in VB2 electrochemical detection by drop-drying the CB suspension onto the BDD surface firmly with a homogeneous coverage.

7.2 Experimental

7.2.1 Materials, instruments and techniques

The electrochemical characterisations including both CV and SWV measurements were operated under the analogous conditions as being described in *Chapter* 3-5. Commercial Monarch® 430 carbon black CB powder (27 ± 10 nm diameter) was obtained from Cabot Corporation. Riboflavin ($C_{17}H_{20}N_4O_6$, ≥ 98%), folic acid ($C_{19}H_{19}N_7O_6$, ≥ 97%) and L-Ascorbic acid ($C_6H_8O_6$, 99.9%) were all purchased from Sigma-Aldrich.

7.2.2 Deposition of CB on BDD

Similar to that explained in the previous chapters, the bare BDD electrode was potential scanned in 0.1 M HNO_3 prior to use to remove all organic pollutants from the surface. Some works[22] have suggested that strongly oxidised diamond can be advantageous so to this end some samples were anodically treated using a potentiostatic mode by holding the potential at 2 V *vs.* Ag/AgCl reference electrode for 90 s after the cleaning process.

The native CB powder, with a diameter of 27 ± 10 nm as mentioned before, has been characterised under XPS by Panchompoo *et al*[23] as shown in **Figure 7.1**. In this chapter, CB was dispersed in 10 ml ethanol with a weight/volume ratio of 2:1. The suspension was then ultrasonicated until a homogeneous form was achieved. It was drop-coated carefully using a 10 – 100 μL pipette onto the electrode gradually to ensure a uniform coverage was obtained. The coated BDD electrode was left in air to dry

before all the electrochemical characterisations. The CB coating on the surface proved both mechanically and electrochemically stable during measurements and rinsing processes.

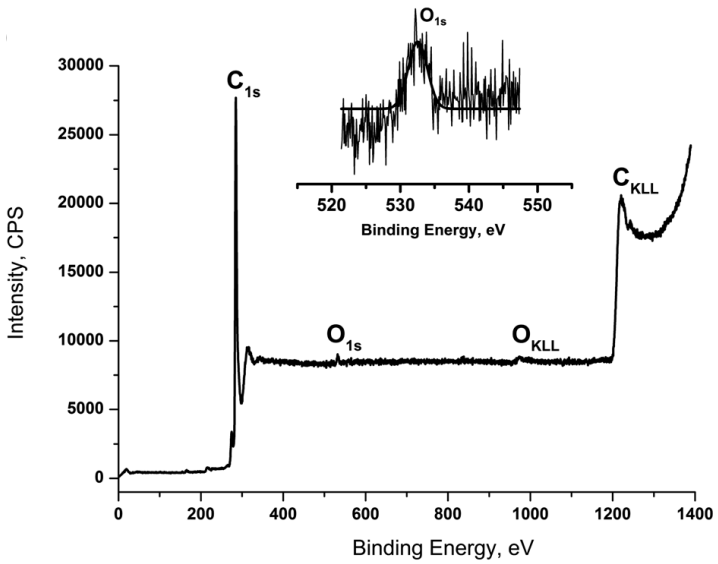


Figure 7.1 Survey XPS spectrum of native CB[23]

7.3 CV characterisations of CB modified BDD

7.3.1 Redox reaction of riboflavin

The VB2 redox reaction is considered to effectively involve a two-electron and two-proton reversible process where the two unsaturated nitrogen atoms in the quinone forms attract a hydrogen atom each, forming the hydroquinone counterpart[16] as shown in **Figure 7.2** below. The net charge on the species involved in the redox couple is influenced by protonation/deprotonation as determined by the pKa values involved. The overall electrochemical behaviour is expected to be influenced by pH variation, which will be discussed further in section **7.3.4**.

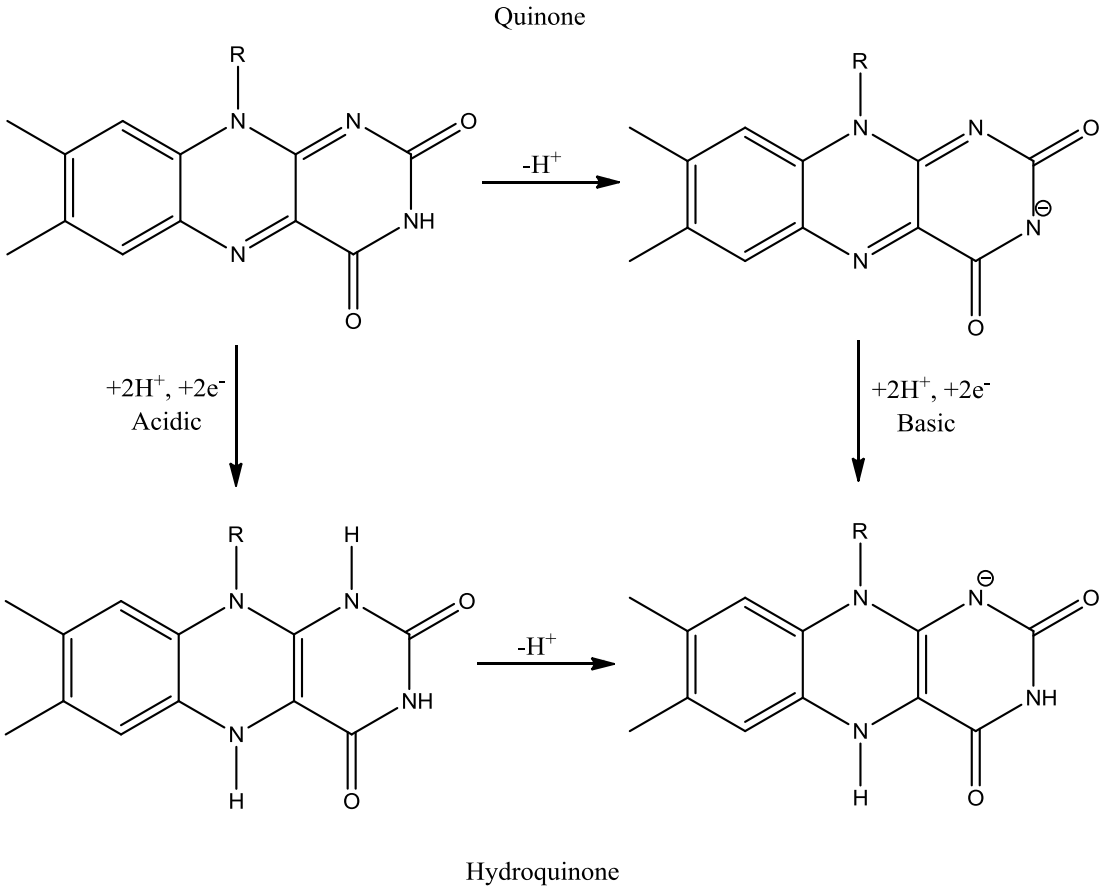


Figure 7.2 The redox reactions of VB2 between its quinone and hydroquinone forms[16]

7.3.2 Effects of CB coating

To investigate how the CB loading affected the electrochemical features, CVs were conducted on both bare and CB modified BDDs in comparison. 30 μL CB suspension was dry coated onto the electrode surface successively using 3 × 10 μL aliquots, with drying in between since this produced the best uniformity. A visible black film was seen formed in the circle central area of the electrode, which was exposed to the electrolyte solutions afterwards.

On bare BDD, the peak potential separation is observed as 58 mV at a scan rate of 20 mV/s, which is almost the same theoretical value for reversible one-electron transfer

system. The value however grows to 97.7 mV with a 10-times higher scan rate of 200 mV/s, indicating quasi-reversible behaviour on the bare BDD electrode as shown in **Figure 7.3** a). The peak current was proportional to the square root of the scan rate throughout the range from 20 to 200 mV/s, suggesting a diffusion controlled process on the unmodified BDD electrode surface. After the CB loading on the BDD surface, a significantly enhanced electrocatalytic activity is achieved with almost 15 times larger redox peak currents observed compared with the bare BDD as exhibited in **Figure 7.3** b). The peak-peak separation is however only approximately 34 mV at the lowest scan rate of 20 mV/s. The peak currents were plotted out against the scan rate and their relative square root values, respectively, but no linear correlation was observed for either of them. The cathodic peak currents were selected and plotted in double logarithmic coordinates, showing a linear dependence with a slope of 0.83, which is between 0.5 and 1.0 for the electron transfer processes controlled by diffusion and adsorbed layer of electroactive species respectively in the inset of **Figure 7.3** b). This observation therefore suggests the mixed behaviour of the VB2 system intermediating the two processes mentioned above. The peak profiles are more reminiscent of adsorption control.

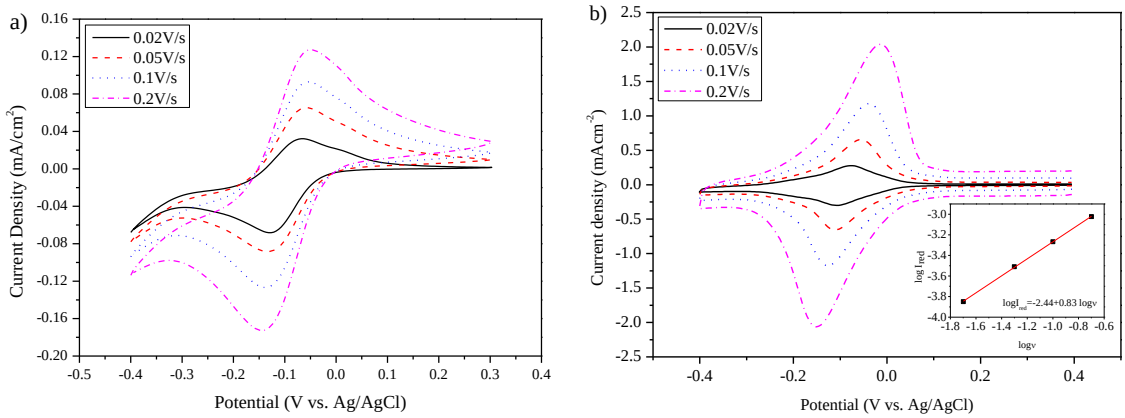


Figure 7.3 CVs of a) anodically treated bare BDD and b) 30 μL CB coating modified BDD at varying scan rates from 20 to 200 mV/s in 0.1 mM VB2 and 0.5 M H_2SO_4. (Inset: linear fitting of cathodic peak currents against scan rates in the double logarithmic manners)

As the reaction on the CB modified BDD seems at least partially controlled by the adsorbed VB2 molecules on the surface, the adsorption effects were investigated on bare and CB coated BDD electrodes respectively as exhibited in **Figure 7.4**. On the clean diamond surface, after being characterised in 0.1 mM VB2 and carefully rinsed afterwards, a much smaller anodic signal response is obtained while the reduction peak is not discernible on bare BDD as shown in **Figure 7.4** a), suggesting a very weak adsorption onto the un-modified electrode probably attributed to the interaction of VB2 molecules with the oxygen containing groups introduced by the initial anodic treatments. However, one can note that the redox peaks still remains at a fairly comparable level after the rinsing process on CB coated BDD as seen in **Figure 7.4** b) instead. As the CV was measured in pure H_2SO_4, this strong signal response is fully assigned to the electron transfer within the tightly attached thin layer of VB2 on the surface. Since the current peak does not decay after various sweeping scans, a considerable and uniform amount of VB2 seems to be firmly adsorbed on the surface and remains mechanically and electrochemically stable.

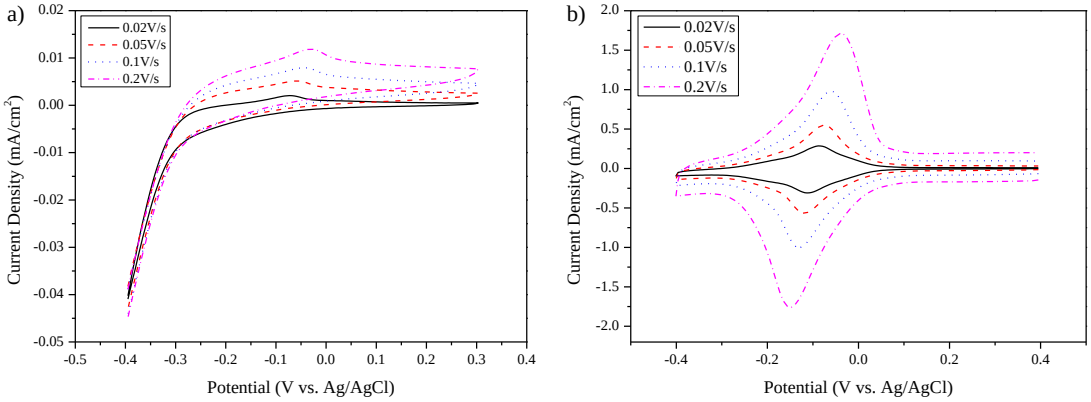


Figure 7.4 CVs of a) anodically treated bare BDD and b) 30 µL CB coating modified BDD in 0.5 M H_2SO_4 at varying scan rates from 20 to 200 mV/s after being characterised in 0.1 mM VB2 and 0.5 M H_2SO_4 and carefully rinsed.

Since the CB loading has been observed to change the electrochemical activity, the effects of different amounts of CB coverage and the scan rates in CV characterisations were further investigated as well. As mentioned previously, the successive drop coating process was still applied by adding 10 μL CB suspension onto the electrode surface each time. CVs were carried out after each coating step. A series of CVs with different CB loadings are plotted out in **Figure 7.5**. It is seen that the current response for VB2 is improved with the increasing CB loading. The current peak density increases from about 0.25 to 0.7 mA/cm^2 at a scan rate of 50 mV/s with 10 μL and 30 μL CB suspension loading respectively, where the latter one is roughly 10 times higher than that on the bare BDD. The electrode modified with even higher loading levels was also characterised, but increased currents became much less a feature, indicating that VB2 could only penetrate a limited distance into the CB layer.

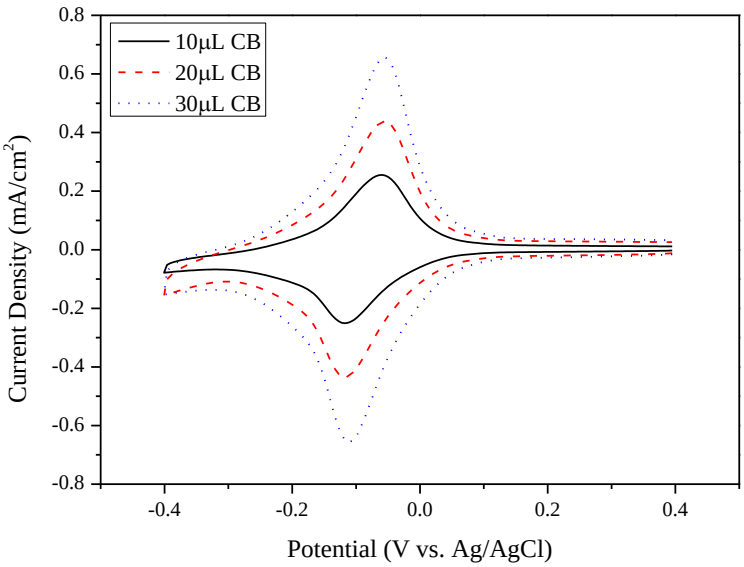


Figure 7.5 CVs of modified BDD electrode with different CB loadings (10 to 30 μL) in 0.1 mM VB2 and 0.5 M H_2SO_4 at a scan rate of 50 mV/s.

The effects of scan rate were also studied. Although the usual single oxidation and reduction peak as noted above is seen at slow scan rates, a peak splitting as shown in

Figure 7.6, which was not observed on un-modified BDD appeared at higher scan rates using the CB modified electrode. This peak splitting seemed to be a particular feature associated with the homogeneity of the CB coating. If the entire CB loading was deposited in one drop, then a prominent peak splitting arose; in contrast much more regular voltammetry was seen if the CB was deposited in several aliquots which visually seemed to produce a much more even layer. This suggests that the peak splitting is somehow associated with the structure of the CB layer rather than the intrinsic electrochemistry of VB2. This possibly arises from the mixed adsorption-diffusion regime suggested by the scan rate dependence noted above. At low scan rates, VB2 or the reduced form in the 'thick' regions of the CB layer in poor contact with the underlying electrode has sufficient time to diffuse to the most active regions so is rapidly reduced/oxidised. At high scan rate, this does not take place, so reduction/oxidation takes place at higher overpotential. This implies that the most uniform CB layers are likely to yield the best results in terms of analytical electrochemistry.

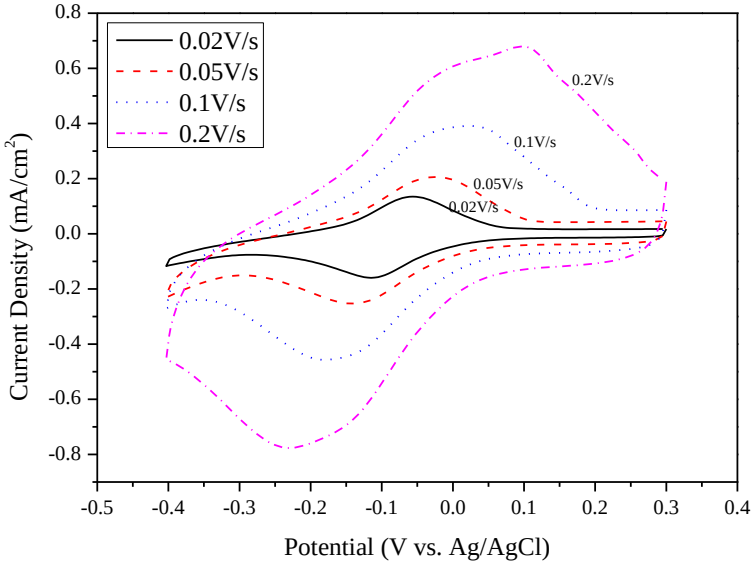


Figure 7.6 CVs of modified BDD with 40 µL CB loading in 0.1 mM VB2 and 0.5 M H_2SO_4 at varied scan rates from 20 to 200 mV/s.

Further evidence for the dependence of the voltammetry on the physical form of the coating also emerged. Non-reproducibility in the voltammetry was traced back to the exact preparation routine to prepare the CB drop coating solution, which was typically done by ultrasonication of the as received CB in ethanol. **Figure 7.7** exhibits typical CV plots for the electrode undergoing three different ultrasonication times to the CB suspension prior to the drop coating of 10 μL CB. The peak-peak separation varies significantly, reducing to 73.2 mV with a few seconds ultrasonication, which is nearly half the initial value of 146.5 mV, as the ultrasonication increases to 30 minutes. Clearly the best electrode performance is seen with the longer ultrasonication associated with better uniformity of CB coverage. Presumably agglomerates exist in the as-received CB which seems to degrade the voltammetry. A longer ultrasonication time might be able to produce a more uniform coating, which seems to improve electrochemical performance. Overall it is clear that some care is needed in preparing the CB coating. If this is not done, then irreproducible results are obtained.

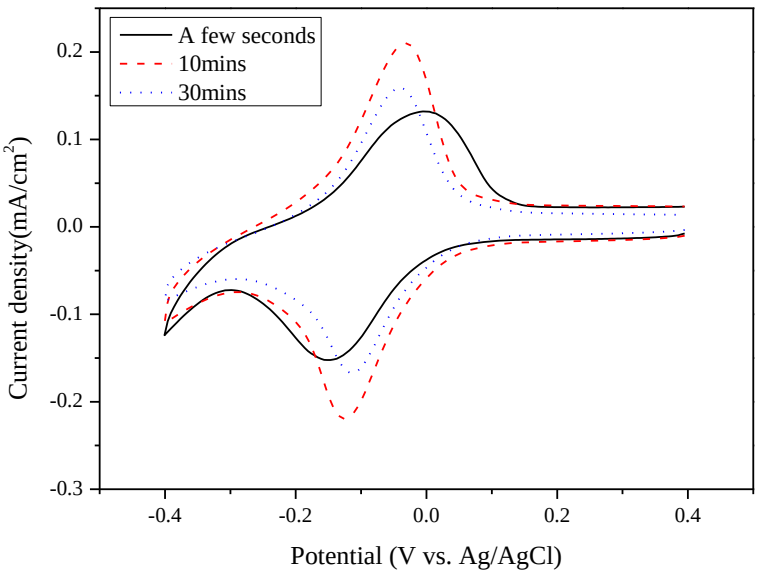


Figure 7.7 CVs of anodically treated and 0.1 mM VB2-immersed BDD coated with 10 μL CB in 0.5 M H_2SO_4, with varing ultrasonication times of a few seconds, 10 and 30 minutes at a scan rate of 50 mV/s.

7.3.3 Electrochemical behaviour of VB2 affected by exposure time

It has been suggested by Chatterjee[16] that the behaviour of CB modified BDD is controlled by the exposure time of the electrode to the VB2 solution, using low quality diamond electrodes, presumably due to slow adsorption. Hereby in this chapter, it was also supposed that the varied exposure time might contribute to different signal responses from such electrode, given that adsorption of VB2 in the CB layers seems to be implicated. CB (10 μL) coated BDD was immersed in 0.1 mM VB2 solution for 15, 30 and 60 minutes respectively prior to CV characterisations in pure H_2SO_4 as shown in **Figure 7.8**. Stable voltammetric responses are seen independent of the immersion time. The adsorption remains at a comparatively 'saturated' state, exhibiting almost the same catalytic activity even with longer exposure time. The data therefore indicates that the adsorption occurs on a relatively fast time scale, presumably within a few seconds of the electrode being immersed in the analyte solution.

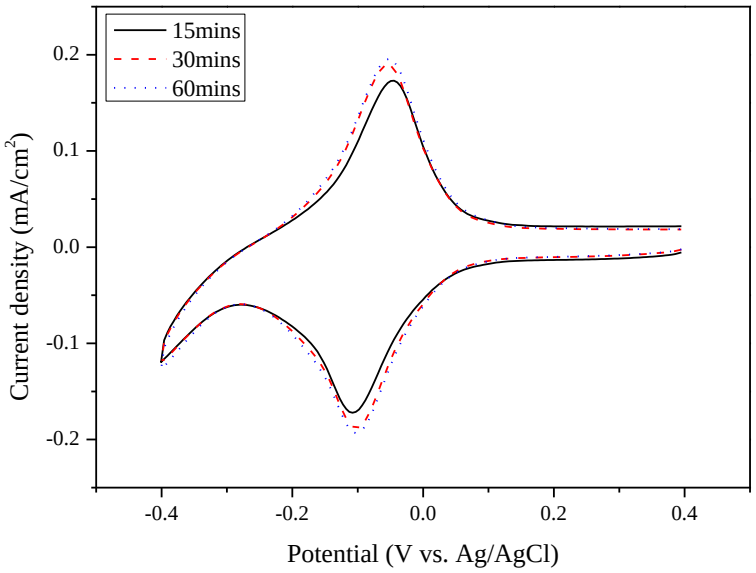


Figure 7.8 CVs of anodically treated and 0.1 mM VB2-immersed BDD coated with 10 μL CB in 0.5 M H_2SO_4, with varing VB2 immersion times of 15, 30 and 60 minutes at a scan rate of 50 mV/s.

7.3.4 pH dependence

In all previous tests, 0.5 M H_2SO_4 was used as the electrolyte to sustain an acidic pH. Since the observed electrochemistry involves coupled proton transfer and species which change chemical form with pH, the pH dependence was studied by recording CVs in a phosphate buffer solution over a wide range of pH values from 2.0 to 12.0. A series of CVs show a successive potential shift towards more negative voltages with increasing pH of buffer solutions as shown in **Figure 7.9** as expected qualitatively from the redox couple. Redox responses are observed on both un-modified and CB coated BDD electrodes but seem more symmetric for the latter one. It should be noticed that the peak currents become much broader and less discernible with higher pH values for both electrodes.

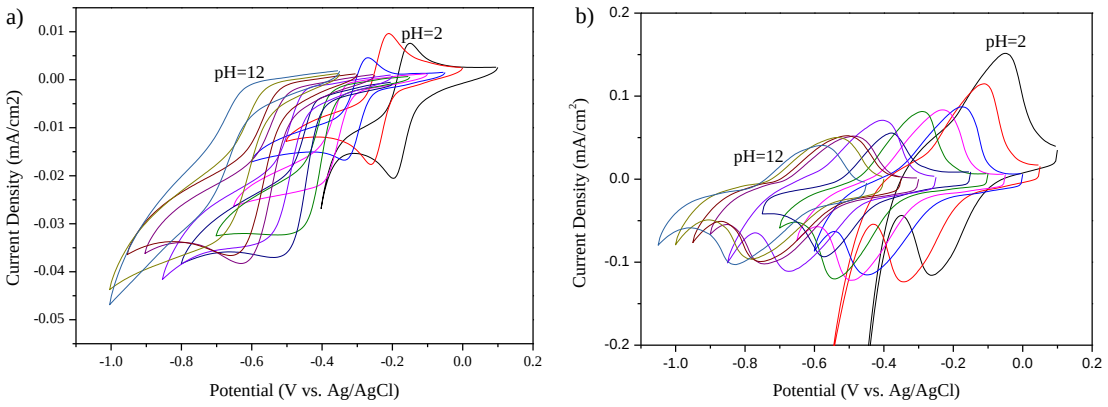


Figure 7.9 CVs of a) un-modified bare and b) CB coated BDD over a pH range from 2.0 to 12.0 in 0.1 mM VB2 with 0.1 M phosphate buffer solution at a scan rate of 50 mV/s.

The plots of the anodic peak potential dependence on pH with both bare and CB modified BDD electrodes are shown in **Figure 7.10**. A clear linear relationship is seen in the acidic pH range from 2.0 to 6.0, with an approximately 60 mV decay per pH unit throughout this region. At these pH values, due to the existence of abundant protons,

both quinone and hydroquinone forms of VB2 stay in their electrically natural states thus can undergo a reversible Nernstian linear correlation, which is strongly dependent on the pH with the same number of transferred protons and electrons (**Figure 7.2**). A similar tendency is also observed when the pH exceeds around 10 where both quinone and hydroquinone forms mentioned above are entirely converted into their negatively charged states by losing a proton in the alkaline solution. The hydroquinone form of reduced VB2 has a pKa of 6.2 while the quinone having a comparatively higher pKa of 9.62. Consequently in the pH range of 6.0 – 10.0, the chemical forms of the reduced and oxidised VB2 species change with pH and a simple linear dependence is not seen in this intermediate range.

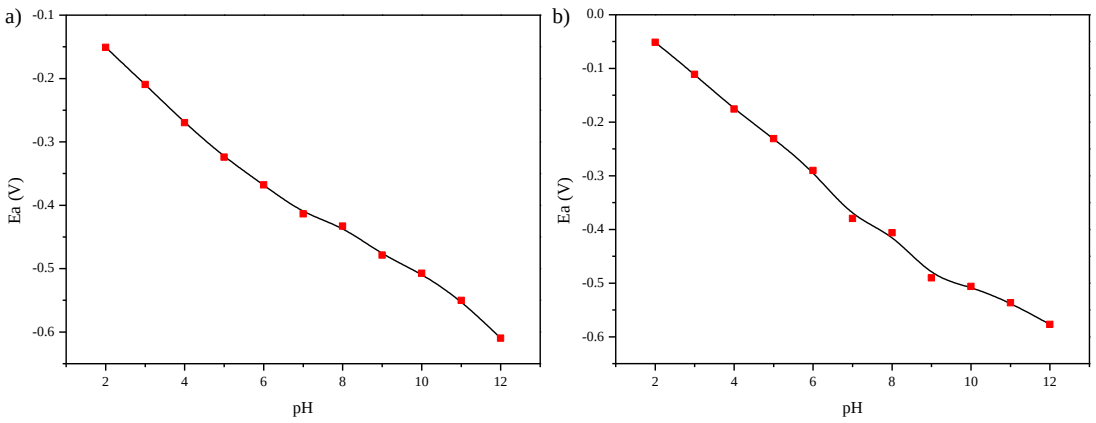


Figure 7.10 Plots of E_a against pH for 0.1 mM VB2 in 0.5 M H_2SO_4 on a) un-modified bare and b) CB coated BDD.

Overall it can be concluded that the pH dependence seen at the electrodes used is fairly well-behaved. The data suggest the best-developed redox peaks are seen at low pH where the best analytical performance might be therefore expected, although detection across the entire pH range seems feasible.

7.4 Detection limit and interfering effects

7.4.1 Detection limit

Having characterised the basic voltammetry at the modified diamond electrode, work was carried out to study the analytical performance, primarily using square wave voltammetry. 0.5 M H_2SO_4 was chosen as the electrolyte since it can provide better characteristic signals in CV measurements, as discussed above. Current responses from both bare and CB coated BDD are exhibited in **Figure 7.11** at differing VB2 concentrations for the reduction of VB2. Although the reduction peak of VB2 appears at nearly the same potential, *i.e.* -0.1 V for both electrodes throughout the concentration range from 10^{-7} to 10^{-4} M and 10^{-8} to 10^{-5} M for bare and modified electrodes respectively, the signal intensity varies significantly between them. Although both CB coated and un-modified electrodes show noticeable responses at all concentration levels and a good dependence of current against concentration, the un-modified one gives relatively much weaker signals, which are around one magnitude smaller even with 10 times higher analyte concentration and not able to be easily defined for concentrations below 2×10^{-7} M. Characteristic concentration changes below this value are not discernible above the background. In comparison, the modified BDD exhibits a greatly improved and stable detection limit to approximately 2×10^{-8} M, which is approximately 10 times higher than the bare counterpart, even with only 10 μL CB loading. If desired, the detection limit could be further-optimised with higher CB loadings, although as noted above, only to a limited extent since the surface reaches the 'saturated' state, and higher CB loading tends to enhance background noise simultaneously.

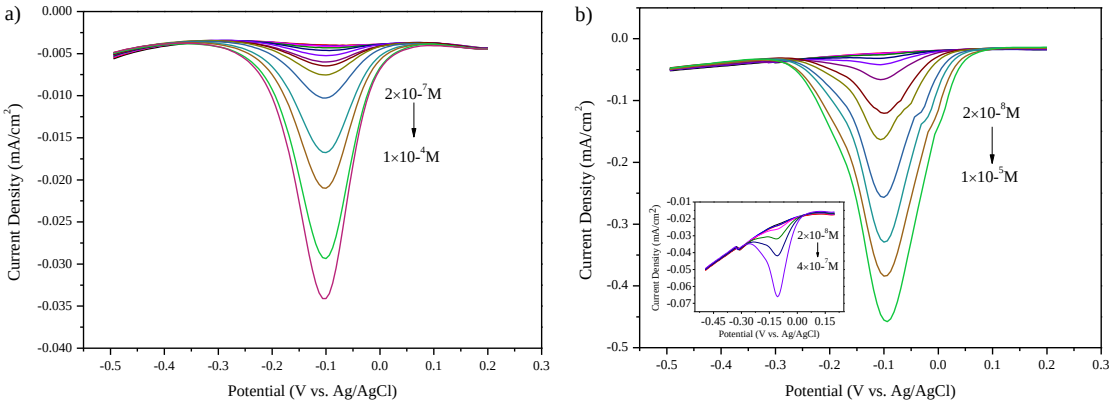


Figure 7.11 SWV of varying VB2 concentrations in 0.5 M H_2SO_4 on a) bare and b) 10 µL CB coated BDD from cathodic direction at a frequency of 10 Hz along with a 0.002 V step potential and a 0.05 V. Inset: SWV of VB2 at 2×10^{-8} to 4×10^{-7} M.

7.4.2 The simultaneous determination of VB2 with other vitamins

From previous results, optimistic electrochemical behaviour in VB2 detection has been shown by CB modified electrode. However, since VB2 is only part of the multivitamin system, its determination is always accompanied by other species with various concentrations. Folic acid and ascorbate are preferentially investigated here, as the former normally co-exists with VB2 as part of vitamin B complex and is commonly found together in other vitamin supplements while the latter is a concerned interfering compound in a large variety of sensing applications due to its high presence and background current level[24] as mentioned in NO electrochemical determination. Although the simultaneous detections of either VB2/FA[25] or VB2/AA[26] have been reported, there are few explorations on a system containing these three species, especially using BDD electrodes. As the normal presences of VB2, FA and AA in clinical blood tests are 106-638 nM, 340-1020 nM and 23-85 µM, respectively[27, 28], 0.5 µM VB2, 1 µM FA and 50 µM AA were preferentially prepared in simultaneous SWV characterisations at a frequency of 10 Hz along with a 2 mV step potential and a

50mV amplitude as shown in **Figure 7.12**. It can be seen that the performance of the bare diamond electrode is poor as only VB2 presents a weak faradic response at its characteristic potential. However on CB modified BDD, all the peaks for these three species are well separated as VB2 shows a dominant peak compared with the other two compounds simultaneously. Since the reduction process is mainly concerned in VB2 characterisations, the well-recognized oxidation peak of AA used to be discovered in previous chapters is replaced by a less discernible reduction response in the cathodic direction although clearer signal can be expected in the anodic scan. From the results above, it can be judged that the simultaneous detection of mixed VB2, FA and AA is applicable on the CB coated BDD, showing well-defined peaks for all species.

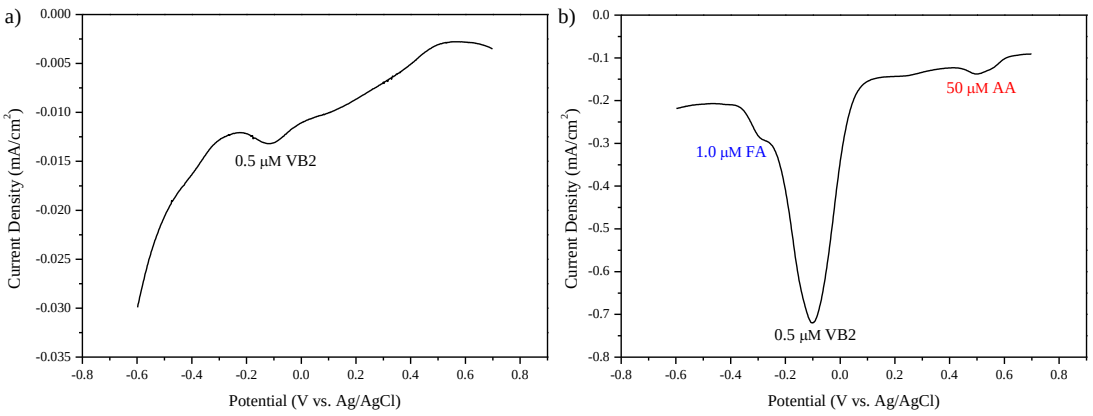


Figure 7.12 SWVs of 0.5 µM VB2, 1.0 µM FA and 50 µM AA in 0.5 M H_2SO_4 at a frequency of 10 Hz along with a 0.002 V step potential and a 0.05 V amplitude on a) un-modified bare and b) 10 µL CB coated BDD in cathodic direction.

7.5 Summarising comments

Diamond presents a poor electrochemical response to VB2 unless used in poorly defined impure form, so the aim of the present chapter was to assess if a simple modification with CB could improve performance.

- A simple drop-dry process was developed to prepare the modified commercial diamond electrodes, which were used in this work. Investigations showed that prolonged ultrasonication of the CB suspensions used, prior to use, improved the reproducibility and quality of the data, suggesting good uniformity was needed in the coating layer to optimize performance. The electrochemical response was also found to increase with CB loading, up to particular loading value. Above this a constant response is observed, suggesting that the interaction with the VB2 analyte solution is limited to a certain depth of CB coating. Above this loading the main effect of CB is to increase the background signal.
- The VB2 electrochemical response seen at the pure diamond electrodes used in this work is not useful analytically. A very broad signal ill-defined reduction wave is seen on the cathodic scan, and a weak wave close to background is seen on the anodic scan. In contrast clearly defined and enhanced reduction and oxidation waves are seen on the CB treated electrodes. The wave characteristics suggest adsorptive or mixed adsorptive diffusional electrochemistry takes place, with a pH response compatible with the expected redox processes and the pKa values of the oxidised and reduced forms.
- Some experiments were perfomed to establish the electrode performance in dilute VB2 solution. Whereas the bare diamond electrode exhibited essentially background response, below about 400 nM VB2, the CB treated electrode exhibited a useful response down to at least 1 order of magnitude lower concentration. Electrochemistry in mixed VB2/ascorbic acid/folic acid solutions also indicated the ability of the CB modified electrode to function successfully in solutions containing mixed redox active species.

References

[1] S. Hustad, P.M. Ueland, S.E. Vollset, Y. Zhang, A.L. Bjørke-Monsen, J. Schneede, Clin. Chem. 46 (2000) 1065-1071.

[2] T. Perez-Ruiz, C. Martínez-Lozano, V. Tomás, O. Val, Analyst 119 (1994) 1199-1203.

[3] J.J.B. Nevado, J.R. Flores, M.J.V. Llerena, Fresenius J. Anal. Chem. 350 (1994) 610-613.

[4] G.M. Greenway, N. Kometa, Analyst 119 (1994) 929-935.

[5] É. Barna, E. Dworschák, J. Chromatogr. 668 (1994) 359-363.

[6] T. Pérez-Ruiz, C. Martínez-Lozano, A. Sanz, V. Tomás, Analyst 119 (1994) 1825-1828.

[7] E. Sikorska, A. Gliszczyńska-Świgło, M. Insińska-Rak, I. Khmelinskii, D. De Keukeleire, M. Sikorski, Anal. Chim. Acta 613 (2008) 207-217.

[8] Z. Gong, Z. Zhang, Analyst 121 (1996) 1119-1122.

[9] H. Zhang, J. Zhao, H. Liu, H. Wang, R. Liu, J. Liu, Int. J. Electrochem. Sci 5 (2010) 295-301.

[10] B. Janik, P.J. Elving, Chem. Rev. 68 (1968) 295-319.

[11] A. Safavi, N. Maleki, H. Ershadifar, F. Tajabadi, Anal. Chim. Acta 674 (2010) 176-181.

[12] L. Gorton, G. Johansson, J. Electroanal. Chem. Interfacial. Electrochem. 113 (1980) 151-158.

[13] H.-Y. Gu, A.-M. Yu, H.-Y. Chen, Anal. Lett. 34 (2001) 2361-2374.

[14] N.R. Vettorazzi, L. Sereno, M. Katoh, M. Ota, L. Otero, J. Electrochem. Soc. 155 (2008) F110-F115.

[15] R.L. McCreery, in: A.J. Bard (Ed.), Electroanalytical Chemistry, Marcel Dekker, New York, 1991, pp. 221-374.

[16] A. Chatterjee, J.S. Foord, Diamond Relat. Mater. 18 (2009) 899-903.

[17] M. Carmo, A.R. Dos Santos, J.G.R. Poco, M. Linardi, J. Power Sources 173 (2007) 860-866.

[18] K. Han, J. Lee, H. Kim, Electrochim. Acta 52 (2006) 1697-1702.

[19] J.R. Li, J.R. Xu, M.Q. Zhang, M.Z. Rong, Carbon 41 (2003) 2353-2360.

[20] M.C. Lonergan, E.J. Severin, B.J. Doleman, S.A. Beaber, R.H. Grubbs, N.S. Lewis, Chem. Mater. 8 (1996) 2298-2312.

[21] T.W. Lo, L. Aldous, R.G. Compton, Sensors and Actuators B: Chemical 162 (2012) 361-368.

[22] N.R. Wilson, S.L. Clewes, M.E. Newton, P.R. Unwin, J.V. Macpherson, J. Phys. Chem. B. 110 (2006) 5639-5646.

[23] J. Panchompoo, L. Aldous, M. Baker, M.I. Wallace, R.G. Compton, Analyst 137 (2012) 2054-2062.

[24] C. Fan, G. Li, J. Zhu, D. Zhu, Anal. Chim. Acta 423 (2000) 95-100.

[25] S. Çakir, İ. Atayman, O. Çakir, Microchimica Acta 126 (1997) 237-240.

[26] K. Mielech, J. Trace Microprobe Tech. 21 (2003) 111-121.

[27] A. Kratz, M. Ferraro, P.M. Sluss, K.B. Lewandrowski, New Engl. J. Med. 351 (2004) 1548-1564.

[28] E. Descombes, A.B. Hanck, G. Fellay, Kidney Int. 43 (1993) 1319-1328.

Chapter 8
Electrodeposition of Pt nanoparticles on Boron-doped Diamond (BDD) for the electrochemical oxidation of nitrite

8.1 Introduction

Nitrite (NO_2^-) is frequently found as a pollutant or contaminant in various fields such as environmental, industrial and food sciences[1, 2]. Since these ions can interact with amines to form nitrosamines, which are well-recognised carcinogenic molecules in human bodies[3, 4], there have been increasing interest in the quantitative determination of NO_2^- in biological systems. A broad range of techniques such as spectrophotometry[5, 6], liquid chromatography[7], gas chromatography[8], chemiluminescence[9, 10] and capillary electrophoresis[11] have been accordingly applied. Although most of these approaches exhibit considerably high efficiency in NO_2^- characterisations, they are also usually time-costly and complex to conduct. For that reason, recently, there has been an upsurge in the exploration of electrochemical techniques in NO_2^- analysis as these methods are comparatively faster, cheaper and more convenient to be carried out for reliable analytical sensing at low NO_2^- concentrations[2, 12]. Both electrochemical reduction and oxidation, which was explored here, can be used.

The traditional electrochemical characterisations of NO_2^- have been reported by using both bare glassy carbon (GC)[13] and platinum electrodes[14, 15]. As noted in previous chapters, BDD is another promising electrode material assigned to its superior properties such as a wide potential window, a low background current, mechanical

durability and chemical inertness[16, 17]. All these advantageous features also enable it to be an alternative electrode candidate for NO_2^- detection. Although NO_2^- may be electro-active at bare electrodes, its oxidation (to nitrate) usually requires high overpotentials. The process is hence prone to be interfered with by other species that can be readily oxidized simultaneously. In order to alleviate these effects and to achieve stronger sensitivity, some modifications to the bare electrode surface such as utilising metallophthalocyanines[18] and metalloporphyrins[19], series of porous materials[20] and enzymes[21] were essentially proposed. However, many of such chemically modified electrodes suffered a low stability of the coated film, which can be a severe limitation.

Recently and more helpfully therefore, noble metal nanoparticle materials have been observed to present strong catalytic properties in the electrochemical oxidation of NO_2^-. Wang *et al*[12] reported concerning the Pt-Fe(III) binary nanoparticles produced by CV deposition on GC electrode while Huang *et al*[22] have extensively studied the properties of gold nanoparticle modified electrodes in catalysing the oxidation of NO_2^- molecules. Work with nanoparticles on diamond in this application has not been reported, so the aim of the present chapter is to study the oxidation of NO_2^- using the Pt functionalised diamond surface prepared as described earlier.

8.2 Experimental

8.2.1 Chemicals and materials

Sodium nitrite ($NaNO_2$) (≥ 97%), L-ascorbic acid ($C_6H_8O_6$, ≥ 99%) and potassium iodide (KI, 99%) were purchased from Sigma-Aldrich. Potassium hexachloroplatinate(IV) (K_2PtCl_6, 98%) was purchased from Alfa Aesar. All the

solutions were prepared and relative dilutions were carried out using Milli-Q water (> 18 MΩ cm). 0.1 M Phosphate buffered saline (PBS) comprising of 8.01 g/L sodium chloride (NaCl), 0.20 g/L KCl, 1.78 g/L sodium phosphate dibasic dihydrate ($Na_2HPO_4 \cdot 2H_2O$) and 0.27 g/L potassium phosphate monobasic (KH_2PO_4) was chosen as the counter electrolyte with a pH of 7.4.

8.2.2 Preparation of Pt modified BDD electrode

Since Pt nanoparticles produced by the two-stage electrodeposition route combining both PSD and potentiostatic methods have been proved to show useful catalytic properties in DMFC and electrochemical oxidation of NO, the similar process was carried out in this chapter, starting with a 10-minute PSD by stepping the potential from 0.25 to -0.2 V in 0.05 V steps of 10 s duration each in 2 mM K_2PtCl_6 with 0.5 M H_2SO_4 as the electrolyte. A further 10-minute potentiostatic process was then conducted in the same solution to enlarge and stabilise the tiny nuclei into firmly attached nanoparticles onto the BDD electrode surface. The two separate deposition routes comprising of either single PSD or potentiostatic technique were also utilised in parallel to compare the overall catalytic performance.

8.3 Results and discussion

8.3.1 Preparation and Electrochemical characterisations of Pt/BDD

After Pt particles were electrodeposited with the three different approaches mentioned above, the modified electrodes were then electrochemically characterised in 0.5 M H_2SO_4 at a scan rate of 0.05 V/s as shown in **Figure 8.1**. As explained in *Chapter* 4, the cathodic response at approximately 0.4 V is assigned to the reduction of ionic Pt into the metallic forms while the cathodic and anodic peaks at 0 to -0.25 V are attributed to the

adsorption/desorption of hydrogen monolayers on the Pt nanoparticles[23, 24] along with bulk hydrogen evolution/reduction at the most negative potentials. The single stage deposition with either PSD or potentiostatic technique exhibits smaller responses in the hydrogen desorption region, which is indicative for a considerably smaller electrochemical active area compared with the combined process. This must result from a larger particle size (so smaller specific area) or lower Pt loadings.

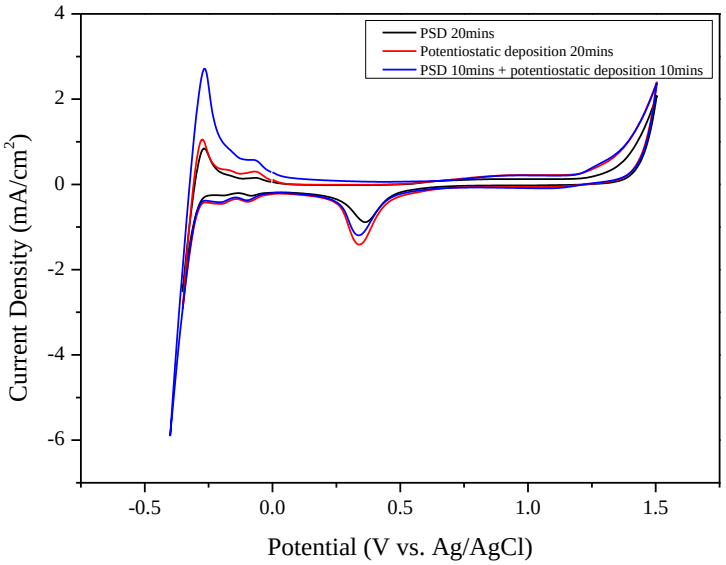


Figure 8.1 CVs of modified BDD electrodes in 0.5 M H_2SO_4 at a scan rate of 0.05 V/s after i) 20-minute PSD, ii) 20-minute potentiostatic deposition and iii) 10-minute PSD followed by 10-minute potentiostatic deposition.

After the successful two-stage electrodeposition, the surface topography of modified electrode was also characterised under SEM as depicted in **Figure 8.2** with an average particle size of around 100 nm. This size is still larger than that is theoretically calculated in *Chapter* 4 under the same deposition protocol with longer operation time, which is thought to be due to porosity of deposited particles and high surface roughness caused by the crystal aggregation. Most Pt nanoparticles seem to be preferentially deposited onto certain areas of the BDD electrode as noted and explained in *Chapter* 4.

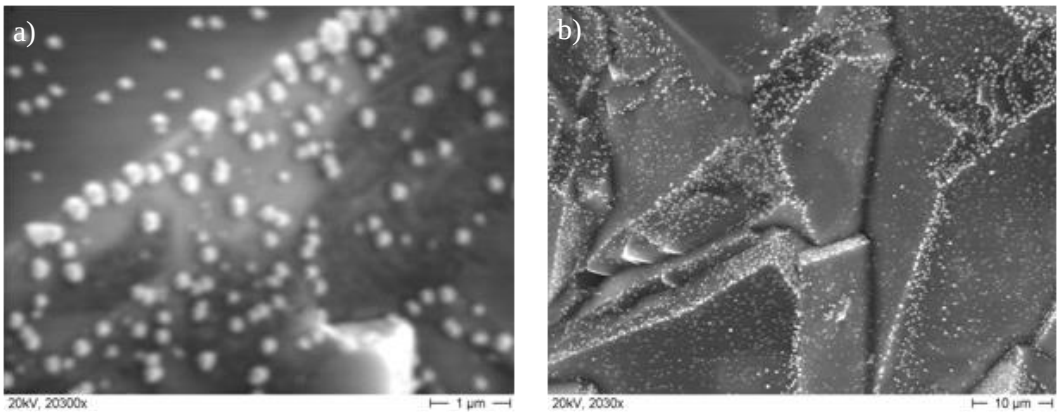


Figure 8.2 SEM of Pt modified BDD electrode with a) high and b) low resolution after the two-stage electrodeposition comprising of 10-minute PSD followed by 10-minute potentiostatic deposition.

8.3.2 Electrochemical oxidation of NO_2^- on bare BDD and Pt/BDD

Since the BDD electrodes have been modified with three different electrodeposition routes respectively, CVs were then conducted with 1×10^{-3} M NO_2^- in 0.1 M PBS (pH = 7.4) at a scan rate of 0.05 V/s to find out how these deposits could optimise the electrochemical oxidation of NO_2^- compared with undecorated bare BDD electrode as exhibited in **Figure 8.3**. It is seen that the signal response is barely discernible on the bare BDD electrode as only an extremely wide and weak anodic slope appears at approximately +1.0 V. Clearly diamond is a poor electrode material for the detection of nitrite. However, significantly higher peaks are instead observed after the coating of Pt nanoparticles by all the three depositing processes described above along with a prominent potential shift of about 0.2 V towards a more negative value of around 0.8 V. This is associated with the oxidation of nitrite to nitrate[25]. The magnitude of the oxidation peaks varies with the Pt deposition route and seems to follow the trend noted for Pt surface area as seen in previous section. This indicates that at these nanoparticle functionalised electrodes, the availability of surface sites and transport to them seems to be rate-limiting. Conversely the oxidation potential seems to be independent of the Pt

deposition route. Although the nitrite to nitrate oxidation wave is the main feature, it can be seen although ill-defined features appear at more negative potentials. The cathodic signal appearing at ~ 0 V is probably attributed to the oxygen reduction as was observed on Pt/MWCNTs electrodes in a neutral system[26] while a higher background current in the anodic curve may be assigned to the re-oxidation of some incompletely reduced forms (*e.g.* H_2O_2) from O_2 reduction. These features are also observed at different pH values, as exhibited in **Figure 8.5** a).

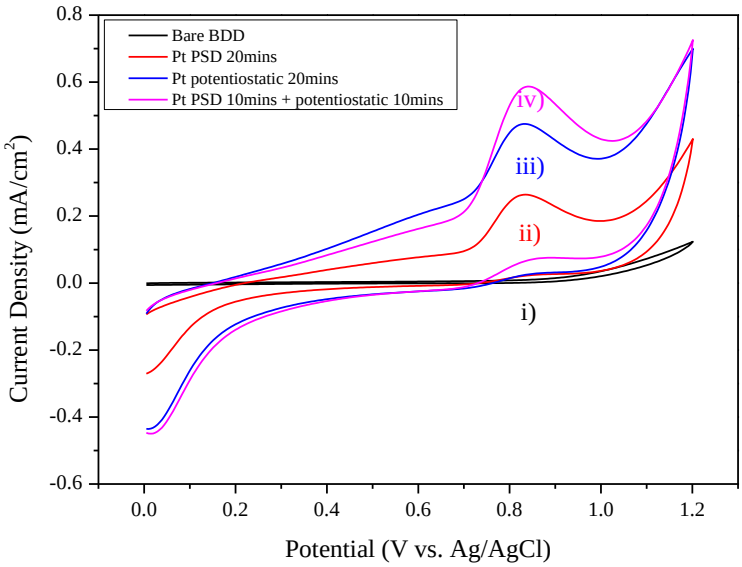


Figure 8.3 CVs of 1×10^{-3} M NO_2^- in 0.1 M PBS (pH = 7.4) at a scan rate of 0.05 V/s on i) bare and modified BDD electrodes after ii) 20-minute PSD, iii) 20-minute potentiostatic deposition and iv) 10-minute PSD followed by 10-minute potentiostatic deposition.

In order to determine the electron transfer process in the electrochemical oxidation of NO_2^-, various scan rates from 0.02 to 0.2 V/s were selected in the CV characterisations carried out with 1×10^{-3} M NO_2^- in 0.1 M PBS (pH = 7.4) as exhibited in **Figure 8.4**. A simple square root dependence of the peak current with scan rate is seen in **Figure 8.4**, confirming that diffusion of species to the electrode surface rather than oxidation of adsorbed species is the rate-limiting factor. This is simpler behaviour than was observed

in *Chapter* 5, where the complicated effects from the overlapping of diffusion fields from the neighbouring nanoparticles gave a relatively complicated dependence of peak current on scan rate instead.

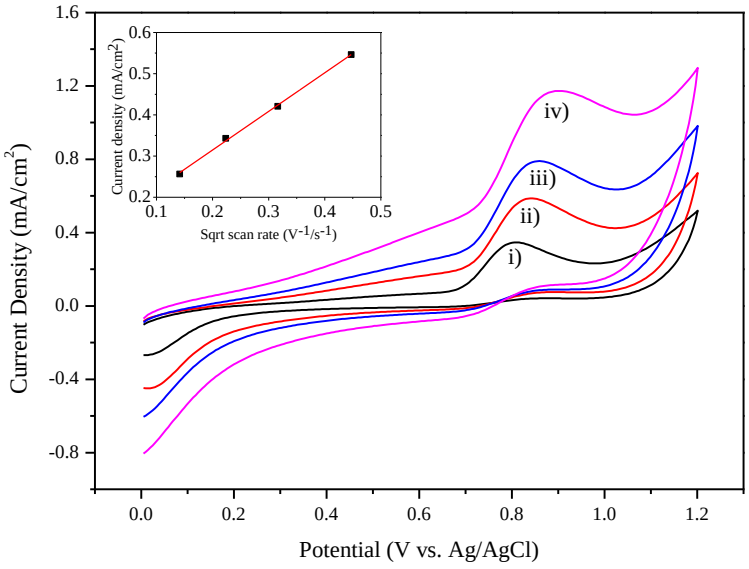


Figure 8.4 CVs of 1×10^{-3} M NO_2^- in 0.1 M PBS (pH = 7.4) at i) 0.02 V/s, ii) 0.05 V/s, iii) 0.1 V/s and iv) 0.2 V/s on the Pt coated BDD electrode after 10-minute PSD followed by 10-minute potentiostatic deposition. Inset: linear fitting of peak current *vs.* square root of scan rate.

8.3.3 pH effects in the NO_2^- detection on Pt modified electrode

Apart from the investigation on the electron transfer process associated with the scan rate above, the pH effects were also explored to find out how this variation could affect the electrochemical detection of NO_2^-. A series of CV measurements were carried out in phosphate buffer solution with a pH range from 3.0 to 10.0 at a fixed scan rate of 0.05 V/s as depicted in **Figure 8.5** a). A significant peak shift to lower pH values is seen as the pH rises from 3.0 to 6.0. A clear linear relationship between the peak potential *vs.* pH is observed in the pH region from 3.0 to 6.0 as displayed in the Inset of **Figure 8.5** a) in which the slope value is 0.0363 V per pH unit. The half reaction of NO_2^- electrochemical oxidation above the pKa limit of 3.4 where nitrite is demonstrated

below in Equation 8.1.

$$NO_2^- + H_2O \rightarrow NO_3^- + 2H^+ + 2e^- \quad 8.1$$

The oxidation peak potential E at different pH values can be presented as below:

$$E = E_0^{'} + \frac{RT}{nF} ln \frac{[H^+]^2[NO_3^-]}{[NO_2^-]} = E_0^{'} - \frac{2.303RT}{F} pH + \frac{RT}{nF} ln \frac{[NO_3^-]}{[NO_2^-]} \quad 8.2$$

where E_0' is the formal potential, R is the gas constant, T is the temperature (K), n is the number of electrons transferred in the reaction (n = 2 in this case) and F is the Faraday constant. $[H^+]^2$, $[NO_3^-]$ and $[NO_2^-]$ are the equilibrium concentrations of these species at the interface, respectively.

Although the expected trend in reduction in potential with increase pH is seen, the Nernstian limit of 59 mV per pH unit is not observed. There are probably two reasons for this. Firstly the quantitative prediction only applies to a reversible couple which is not applicable to the present case[27]. Secondly NO_2^- is relatively unstable so can undergo a self-disproportionation process[28] as below:

$$3NO_2^- + 2H^+ \rightleftharpoons 2NO + NO_3^- + H_2O \quad 8.3$$

Homogeneously this is important at low pH but it also can be kinetically driven in the presence of catalytic species such as Pt. The pH-dependent behaviour exhibited in this pH range is thus indicative that the electrochemical reaction is thus probably dominated by kinetics rather than thermodynamics[29]. Above pH of 6.0, the oxidation potential becomes relatively insensitive to pH, suggesting that the chemical species remain essentially constant in this range.

Meanwhile, it is also worthy to notice the gradual decrease of the oxidation peak signal response throughout the whole pH range as illustrated in **Figure 8.5** b). NO_2^- is fairly stable in neutral and alkaline systems in spite of the decomposition in acidic

environment assigned to its self-disproportionation process[28] as explained above. This observation is clearly important from the point of view of electroanalysis since the signal intensity decays by an order of magnitude at high pH values. The origin of the behaviour is not entirely clear. One possibility mechanistically is that nitrite is scarcely oxidised at the electrode surface but rather one of the disproportionation products such as NO is actually the active species. At high pH nitrite stability rises so the signal from the disproportionation drops[30, 31]. This is especially notable above neutral pH.

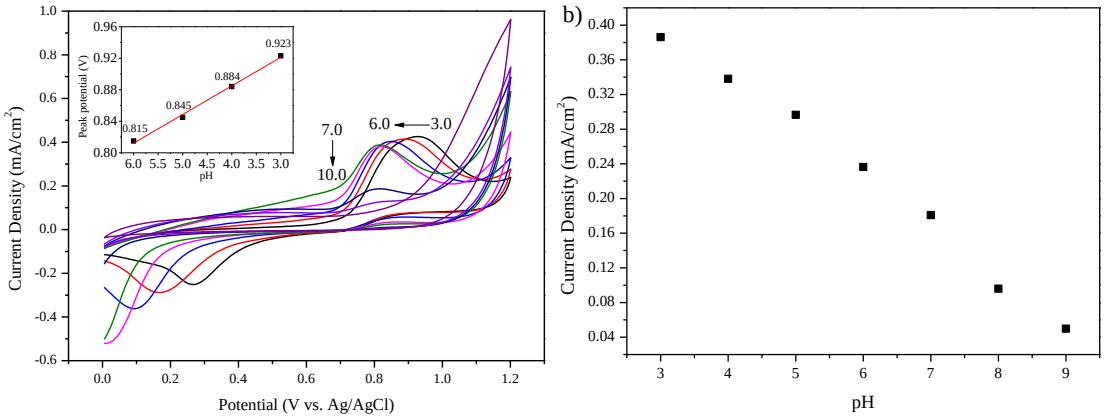


Figure 8.5 a) CVs of 1×10^{-3} M NO_2^- in phosphate buffer solution at different pH values from 3.0 to 10.0 at a scan rate of 0.05 V/s on Pt modified BDD after the two-stage electrodeposition of Pt nanoparticles. Inset: linear correlation between NO_2^- oxidation peak potential *vs.* pH from 3.0 to 6.0. b) The relationship between the NO_2^- oxidation peak current density *vs.* pH from 3.0 to 9.0.

8.3.4 Detection limit of NO_2^- on Pt modified BDD

In order to investigate the capability for using this modified electrode in the measurements with various NO_2^- concentrations, CVs were selectively operated in 0.1 M PBS (pH = 7.4) at 0.05 V/s with a NO_2^- concentration range from 1×10^{-4} to 1×10^{-3} M as exhibited in **Figure 8.6**. The anodic signal responses are observed to track the higher NO_2^- concentrations and it is clear to find an excellent linear relationship between them in this concentration range as shown in the Inset. The linear regression is

hereby obtained as $i_{pa} = 0.169C_{NO_2^-}$ with the correlation coefficient of 0.9989.

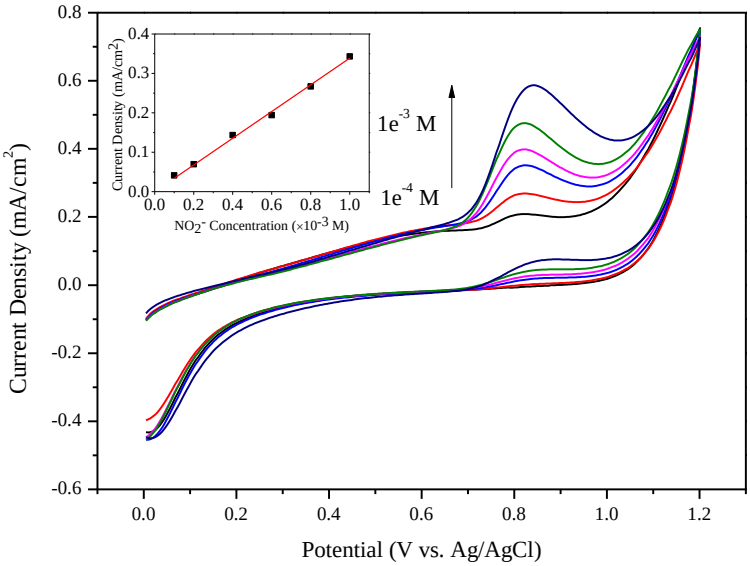


Figure 8.6 CVs of 0.1 M PBS (pH = 7.4) in the presence of 1×10^{-4}, 2×10^{-4}, 4×10^{-4}, 6×10^{-4}, 8×10^{-4} and 1×10^{-3} M NO_2^- at a scan rate of 0.05 V/s on Pt/BDD electrode. Inset: linear correlation between the peak current density *vs.* the NO_2^- concentration.

However, even though CVs have shown useful results in such range above, the high pseudo-capacitive background current limits the usefulness in highly diluted solutions. Similar to the scheme adopted in *Chapter* 5 for the characterisations of NO electrochemical oxidation, the SWV technique was also selected as an effective alternative approach that could be applied in a broader range of NO_2^- detection by presenting much weaker faradic currents even at the smaller presences of NO_2^- molecules. It was conducted with NO_2^- solutions at various concentrations in 0.1 M PBS (pH = 7.4) at a frequency of 10 Hz along with a 0.002 V step potential and a 0.05 V amplitude, respectively, as demonstrated in **Figure 8.7** a). The oxidation peak current of NO_2^- is observed as almost perfectly proportional to the NO_2^- concentration as well as the observations from previous CV measurements, however at a much wider range from

2×10^{-5} to 4×10^{-3} M, which is comparatively broader than some values reported from either CV measurement[32] or amperometric analysis using flow injection[33] in the literature. The linear regression equation is then presented as $i_{pa} = 0.0887C_{NO_2^-}$ with a correlation coefficient of 0.9977 in this case. The signal response becomes barely discernible when the concentration falls below 2×10^{-5} M, the detection limit (S/N = 3) is estimated as approximately 2×10^{-6} M, which is also competitive against some other modified electrodes as reported[29, 34, 35].

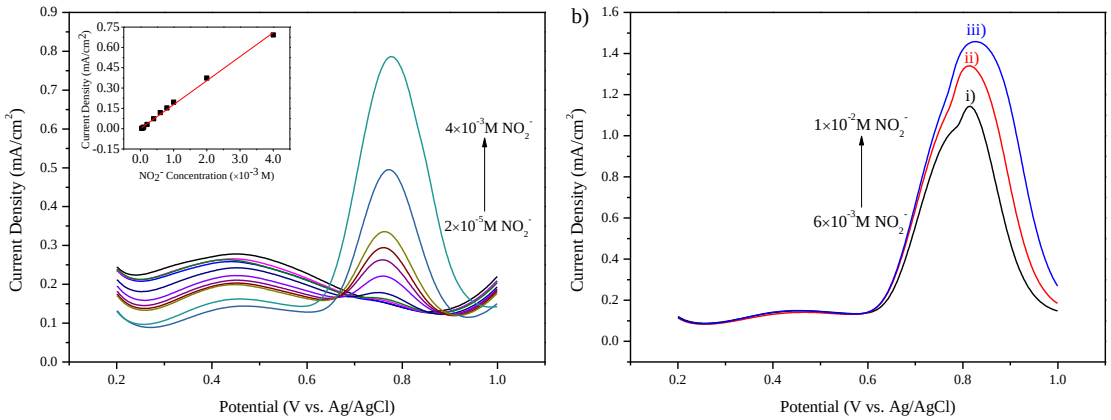


Figure 8.7 SWVs of 0.1 M PBS (pH = 7.4) with different NO_2^- presenses from a) 2×10^{-5} to 4×10^{-3} M and b) 6×10^{-3} to 1×10^{-2} M in 0.1 M PBS (pH = 7.4) at a frequency of 10 Hz along with a 0.002 V step potential and a 0.05 V amplitude. a) Inset: linear relationship between the oxidation peak current density *vs.* the NO_2^- concentration.

It was meanwhile noticed that when the concentration went beyond 4×10^{-3} M, the linear correlation between the faradic response and the NO_2^- presence cannot be achieved any more as the peak intensity seems to be limited, with the SWV peak becoming distorted as shown in **Figure 8.7** b). Again the underlying cause could be related as much to the disproportionation of nitrite and fundamental electrode properties.

8.3.5 Interferences in NO_2^- electrochemical detection

Further to the above work, the influence of potential interfering compounds was also investigated. It is understood that most common inorganic ions do not affect the NO_2^- detection even when in large 100× excess[29, 36]. However in biological systems, easily oxidised species such as ascorbate are problematic so this exemplar species was briefly investigated here.

Typical data are shown in **Figure 8.8**. CV was conducted with 1×10^{-4} M NO_2^- and 50-fold AA in 0.1 M PBS (pH = 7.4) at a scan rate of 0.05 V/s. Although the formal oxidation potential of AA is much more negative than the nitrite signal, the fairly high background current presented by AA rather can be seen to mask the signal response from nitrite, although it is expected SWV could be used to partially alleviate this problem as exhibited.

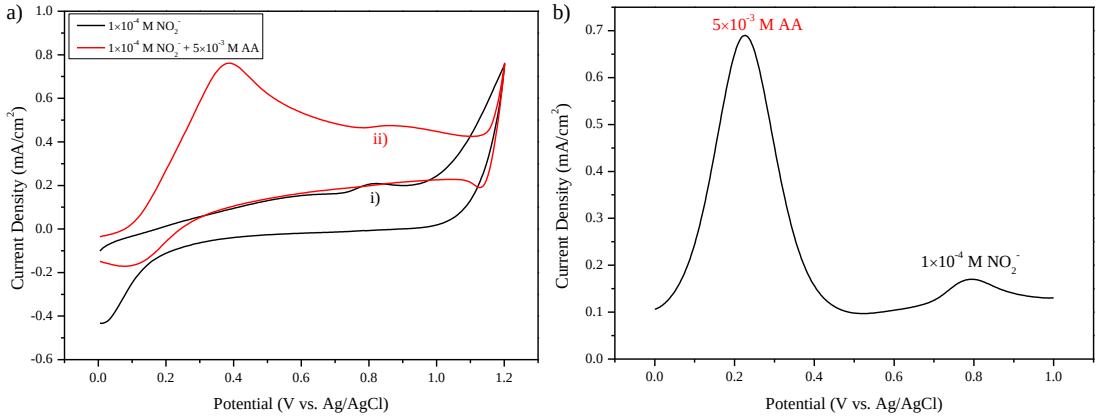


Figure 8.8 CVs of a) 1×10^{-4} M NO_2^- i) without and ii) with 50-fold AA in 0.1 M PBS (pH = 7.4) at a scan rate of 0.05 V/s on Pt/BDD and b) SWV of 1×10^{-4} M NO_2^- and 50-fold AA in 0.1 M PBS (pH = 7.4) at a frequency of 10 Hz along with a 0.002 V step potential and a 0.05 V amplitude on Pt/BDD.

The co-presence of iodide was also looked at. According to Equation 8.4 and 8.5[1].

$$2NO_2^- + 3I^- + 4H^+ \rightarrow I_3^- + 2H_2O + 2NO \quad 8.4$$

$$I_3^- + 2e^- \rightarrow 3I^- \quad 8.5$$

Nitrite undergoes a spontaneous redox reaction with iodide, resulting the formation of I_3^-, which itself is redox active at many electrodes, along with iodide.

$$2I^- - 2e^- \rightarrow I_2 \quad 8.6$$

$$3I^- - 2e^- \rightarrow I_3^- \quad 8.7$$

$$2I_3^- - 2e^- \rightarrow 3I_2 \quad 8.8$$

The influence of the presence of I^- on the CV scan of nitrite electro-oxidation is shown in **Figure 8.9**. Large oxidation current enhancements are seen which completely mask the expected current from the oxidation of nitrite. The first anodic peak observed at around 0.5 V is attributed to the oxidation from I^- into I_3^-[37, 38], while two adjacent peaks at higher potential values are assigned to the conversion from $I^-$and I_3^- species towards I_2 respectively[37, 38]. It is thus evident that I^- is a crucial interference in direct NO_2^- electrochemical oxidation.

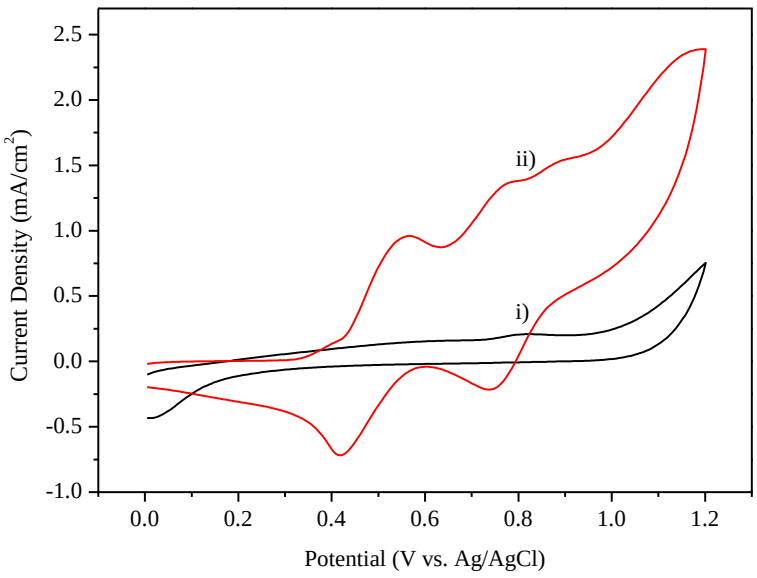


Figure 8.9 CVs of 1×10^{-4} M NO_2^- i) without and ii) with 50-fold I^- in 0.1 M PBS (pH = 7.4) at a scan rate of 0.05 V/s on Pt/BDD.

8.4 Summarising comments

A number of useful deductions can be presented concerning the short study presented above.

- Pt nanoparticles are successfully electrodeposited onto a BDD electrode surface throughout a two-stage protocol comprising of successive PSD and potentiostatic technique. The particles produced under this deposition route, exhibit useful catalytic properties in electrochemical oxidation of NO_2^- .
- Bare and Pt modified BDD electrodes have been used in NO_2^- electrochemical detection respectively in which the former behaves as almost completely inert in catalysing the NO_2^- oxidation while the latter significantly boosts the signal response and shifts the oxidation potential towards a more negative value by approximately 0.2 V.
- With the Pt nanoparticles deposited, the modified BDD electrode presents a good linear correlation between the peak current *vs.* concentration level in 1×10^{-4} to 1×10^{-3} M from CVs along with the capability for NO_2^- detection in a broader range from 2×10^{-5} to 4×10^{-3} M as confirmed by SWVs. The detection limit is estimated as 2×10^{-6} M (S/N = 3), which is competitive against similar studies undergoing more complicated electrode modifications[29, 34, 35].
- It is recognised that the detection of nitrite is complicated by disproportionation and degradation reactions, particularly at low pH or when catalysed by active species such as Pt. Unsurprisingly therefore the electrochemistry measured is significantly dependent on pH. In particular a shift to lower oxidation potential is seen at higher pH, but more unexpectedly, the signal intensity meanwhile drops dramatically, therefore practical analysis should avoid these pH extremes.

- Brief studies of interfering effects from other species are reported. In particular in the presence of ascorbate or iodide, the oxidation signal in CV from nitrite is shown to be completely masked.

References

[1] M.J. Moorcroft, J. Davis, R.G. Compton, Talanta 54 (2001) 785-803.

[2] L. Jiang, R. Wang, X. Li, L. Jiang, G. Lu, Electrochem. Commun. 7 (2005) 597-601.

[3] W. Lijinsky, S.S. Epstein, Nature 225 (1970) 21-23.

[4] I.A. Wolff, Wasserma.Ae, Science 177 (1972) 15-&.

[5] I.T. Bae, R.L. Barbour, D.A. Scherson, Anal. Chem. 69 (1997) 249-252.

[6] K.M. Miranda, M.G. Espey, D.A. Wink, Nitric Oxide 5 (2001) 62-71.

[7] J.R. Thayer, R.C. Huffaker, Anal. Biochem. 102 (1980) 110-119.

[8] D. Tsikas, R.H. Böger, S.M. Bode-Böger, F.M. Gutzki, J.C. Frölich, J. Chromatogr. B: Biomed. Sci. Appl. 661 (1994) 185-191.

[9] C. Garside, Mar. Chem. 11 (1982) 159-167.

[10] P.H. MacArthur, S. Shiva, M.T. Gladwin, J. Chromatogr. B 851 (2007) 93-105.

[11] A.M. Leone, P.L. Francis, P. Rhodes, S. Moncada, Biochem. Biophys. Res. Commun. 200 (1994) 951-957.

[12] S. Wang, Y. Yin, X. Lin, Electrochem. Commun. 6 (2004) 259-262.

[13] A.Y. Chamsi, A.G. Fogg, Analyst 113 (1988) 1723-1727.

[14] R. Guidelli, F. Pergola, G. Raspi, Anal. Chem. 44 (1972) 745-755.

[15] S.M. Silva, C.R. Alves, S.A.S. Muchado, L.H. Mazo, L.A. Avaca, Electroanalysis 8 (1996) 1055-1059.

[16] R.G. Compton, J.S. Foord, F. Marken, Electroanalysis 15 (2003) 1349-1363.

[17] J.S. Foord, W. Hao, S. Hurst, Diamond Relat. Mater. 16 (2007) 877-880.

[18] C.A. Caro, F. Bedioui, M.A. Páez, G.I. Cárdenas-Jiron, J.H. Zagal, J. Electrochem. Soc. 151 (2004) E32-E39.

[19] J.N. Younathan, K.S. Wood, T.J. Meyer, Inorg. Chem. 31 (1992) 3280-3285.

[20] Z. Dai, X. Xu, H. Ju, Anal. Biochem. 332 (2004) 23-31.

[21] B. Strehlitz, B. Gründig, W. Schumacher, P.M.H. Kroneck, K.-D. Vorlop, H. Kotte, Anal. Chem. 68 (1996) 807-816.

[22] X. Huang, Y. Li, Y. Chen, L. Wang, Sens. Actuators, B: Chem. 134 (2008) 780-786.

[23] N. Furuya, S. Koide, Surf. Sci. 220 (1989) 18-28.

[24] K. Yamamoto, D.M. Kolb, R. Kötz, G. Lehmpfuhl, J. Electroanal. Chem. Interfacial. Electrochem. 96 (1979) 233-239.

[25] S.-M. Chen, J. Electroanal. Chem. 457 (1998) 23-30.

[26] H.-F. Cui, J.-S. Ye, W.-D. Zhang, J. Wang, F.-S. Sheu, J. Electroanal. Chem. 577 (2005) 295-302.

[27] R.G. Compton, C.E. Banks, Understanding voltammetry, World Scientific, 2007.

[28] A. Samouilov, P. Kuppusamy, J.L. Zweier, Arch. Biochem. Biophys. 357 (1998) 1-7.

[29] Y. Cui, C. Yang, W. Zeng, M. Oyama, W. Pu, J. Zhang, Anal. Sci. 23 (2007) 1421-1425.

[30] O.A. Petrii, T.Y. Safonova, J. Electroanal. Chem. 331 (1992) 897-912.

[31] A.N. Frumkin, O.A. Petrii, Electrochim. Acta 20 (1975) 347-359.

[32] S. Liu, H. Ju, Analyst 128 (2003) 1420-1424.

[33] V. Biagiotti, F. Valentini, E. Tamburri, M.L. Terranova, D. Moscone, G. Palleschi, Sens. Actuators, B: Chem. 122 (2007) 236-242.

[34] X. Chen, C. Ruan, J. Kong, J. Deng, Anal. Chim. Acta. 382 (1999) 189-197.

[35] M.H. Pournaghi-Azar, H. Dastangoo, J. Electroanal. Chem. 567 (2004) 211-218.

[36] K. Zhao, H. Song, S. Zhuang, L. Dai, P. He, Y. Fang, Electrochem. Commun. 9 (2007) 65-70.

[37] H. Tang, A. Kitani, M. Shiotani, J. Appl. Electrochem. 26 (1996) 36-44.

[38] H. Tang, A. Kitani, M. Shiotani, J. Appl. Electrochem. 26 (1996) 45-50.